Insights into high-temperature mineral reactions of calcium silicate materials revealed in operando by in situ Raman spectroscopy

Dissertation

zur

Erlangung des Doktorgrades (Dr. rer. nat.)

der

Mathematisch-Naturwissenschaftlichen Fakultät

der

Rheinischen Friedrich-Wilhelms-Universität Bonn

vorgelegt von

Nadine Susanne Böhme

aus

Köln

Bonn, 2022

Angefertigt mit Genehmigung der Mathematisch-Naturwissenschaftlichen Fakultät
der Rheinischen Friedrich-Wilhelms-Universität Bonn

1. Gutachter: Prof. Dr. Thorsten Geisler-Wierwille
2. Gutachter: Prof. em. Dr. Michael Raith

Tag der Promotion: 29.06.2022
Erscheinungsjahr: 2022

PREFACE

This thesis is submitted for obtaining the Ph.D. degree in Natural Sciences (Dr. rer. nat.) at the University of Bonn. The work described in this thesis was conducted at the Institute of Geosciences at the University of Bonn, under the supervision of Prof. Dr. Geisler-Wierwille. The project was financially supported by the RWE Power AG, Niederaußem, in cooperation with Dr. Manuela Neuroth. The present dissertation follows the cumulative approach in accordance with the guidelines of the University of Bonn and contains the following articles:

a) **Böhme N**, Hauke K, Neuroth M, Geisler T. In situ Raman imaging of high-temperature solid-state reactions in the $CaSO_4$–SiO_2 system. *Int Coal Sci Technol* **2019**, 6, 247–259.

https://doi.org/10.1007/s40789-019-0252-7

b) **Böhme N**, Hauke K, Neuroth M, Geisler T. In Situ Hyperspectral Raman Imaging of Ternesite Formation and Decomposition at High Temperatures. *Minerals* **2020,** 10, 287.

https://doi.org/10.3390/min10030287

c) **Böhme N**, Hauke K, Dohrn M, Neuroth M, Geisler T. High-temperature phase transformations of hydroxylapatite and the formation of silicocarnotite in the hydroxylapatite - quartz - lime system studied in situ and in operando by Raman spectroscopy. *J Mater Sci* **2022**. Submitted.

Another co-authored publication was also written during the Ph.D. period and deals with the general topic of the thesis. Article d) was used as a basis for the introduction (Chapter 1) of the thesis.

d) Hauke K, Kehren J, **Böhme N**, Zimmer S, Geisler T. In Situ Hyperspectral Raman Imaging: A New Method to Investigate Sintering Processes of Ceramic Material at High-temperature. *Appl Sci* **2019**, 9, 1–23.

https://doi.org/10.3390/app9071310

The following work was also carried out as part of the project:

e) **Böhme N**, Stange K, Geisler T, Neuroth M. Untersuchungen versinterungs- und verschlackungskritischer Mineralreaktionen mithilfe der bildgebenden konfokalen Ramanspektroskopie. In: Beckmann M und Hurtado A (Hrsg.): Kraftwerkstechnik 2017, Strategien, Anlagentechnik, SAXONIA Standortentwicklungs- und -verwaltungsgesellschaft mbH, Freiberg, **2017**, 703–732.

ABSTRACT

Knowledge of high-temperature calcium silicate materials is becoming increasingly interesting for industry in different ways. On the one hand, their application in the construction, cement, refractory, and ceramics industry is well established due to, in particular, their high melting point, thermal stability, fluxing characteristics, acicular shape, and bioactivity. However, these minerals also form as sinter deposits in industrial kilns and may cause serious and expensive problems during kiln operation. It follows that a detailed understanding of solid-state or solid-melt mineral reactions that form calcium silicate materials as well as the knowledge about their thermal stability are essential to optimize industrial processes, i.e., to fully exploit their technical advantages and to ensure synthesis under optimal conditions.

In this project, the high-temperature mineral reactions and transformations of calcium silicate materials in the $CaO\text{-}SiO_2(\text{-}SO_3/Al_2O_3/P_2O_5)$ system and subsystems were studied in both single- and multi-phase experiments by *in situ* Raman spectroscopy. The green bodies of multi-phase experiments mainly consisted of calcium oxide (lime) and quartz, and sulfate/aluminate/phosphate components were systematically added or replaced. During firing the samples to temperatures between about 660 and 1100 °C, the decomposition and formation processes of mineral phases were monitored and visualized at the micrometer-scale and *in operando*, i.e., while the reactions were running. For instance, the formation of mono- and dicalcium silicates was found to occur at different in situ temperatures via different reaction pathways. In addition, the polymorphs pseudowollastonite and $\alpha'_L\text{-}Ca_2SiO_4$ were identified. The latter transformed to $\beta\text{-}Ca_2SiO_4$ (larnite) during cooling and remained metastable at room temperature.

The formation and temperature stability of ternesite and silicocarnotite, i.e., the sulfate- and phosphate-containing end member of a solid solution series, were studied. Both mineral phases are formed by reactions involving dicalcium silicate. In particular, the grain boundary migration of ternesite by replacing a large quartz grain was observed. With increasing temperature (and time), $\alpha'_L\text{-}Ca_2SiO_4$ formed new reaction rims around ternesite, producing a layered texture with quartz in the center, ternesite in the middle, and $\alpha'_L\text{-}Ca_2SiO_4$ in the outer layer. The heating study with a natural ternesite crystal revealed a phase transformation to $\alpha'_L\text{-}Ca_2SiO_4$ between 730 and 1120 ± 1 °C and confirms that both the ternesite and dicalcium silicate domains can co-exist in this temperature range. It generally depends on the course of the reaction whether ternesite or larnite is detected after quenching to room temperature. Furthermore, two reaction pathways were found to form silicocarnotite between about 1050 and 1150 °C, i.e., at significantly lower in situ temperatures than previously proposed. In addition, a heating study with a natural silicocarnotite crystal was performed for the first time. This experiment revealed, for instance, that the position of the $v_1(PO_4)$ band shifted from 951 ± 1 cm^{-1} to ~930 cm^{-1} at 1200 ± 1 °C. Moreover, the transformation of hydroxylapatite to tricalcium phosphate was investigated and gave new insights into the complex process of the loss of surface hydroxyl groups bound to HAp nanocrystals.

The advantages of in situ hyperspectral Raman imaging compared to conventional experimental and analytical methods, where the sample has to be quenched to room temperature before being analyzed, are clearly demonstrated. This new analytical method is a powerful tool for studying sinter reactions with a high temperature, time, and spatial resolution and offers a wide range of possibilities to study ceramic systems for industrial applications.

ZUSAMMENFASSUNG

Das Wissen über Hochtemperatur-Calciumsilikat-Materialien wird für die Industrie in verschiedener Hinsicht zunehmend von Bedeutung. Einerseits ist ihre Anwendung in der Bau-, Zement-, Feuerfest- und Keramikindustrie aufgrund ihres hohen Schmelzpunkts, ihrer thermischen Stabilität, ihrer Flussmitteleigenschaften, ihrer nadelförmigen Gestalt und ihrer Bioaktivität weit verbreitet. Allerdings bilden diese Minerale auch Sinterablagerungen in Industrieöfen und können beim Ofenbetrieb ernsthafte und teure Probleme verursachen. Daraus folgt, dass ein detailliertes Verständnis möglicher Festkörper- bzw. Schmelzmineralreaktionen sowie die Kenntnis der thermischen Stabilitätsbereiche von Kalziumsilikaten unerlässlich sind, um industrielle Prozesse zu optimieren, d. h. um ihre technischen Vorteile voll auszuschöpfen und die Synthese unter optimalen Bedingungen zu gewährleisten.

In diesem Projekt wurden die Hochtemperatur-Mineralreaktionen und -Umwandlungen von Kalziumsilikat-Materialien im $CaO\text{-}SiO_2(\text{-}SO_3/Al_2O_3/P_2O_5)$-System sowohl in Einphasen- als auch in Mehrphasenexperimenten mittels *in situ* Raman-Spektroskopie untersucht. Die Grünkörper der Mehrphasenexperimente bestanden hauptsächlich aus Calciumoxid (Branntkalk) und Quarz, und Sulfat/Aluminium/Phosphat-Komponenten wurden systematisch hinzugefügt oder ersetzt. Während des Aufheizens der Proben bei Temperaturen zwischen etwa 660 und 1100 °C wurden die Zersetzungs- und Bildungsprozesse der Mineralphasen *in operando*, d. h. während der laufenden Reaktionen, im Mikrometerbereich überwacht und visualisiert. So wurde beispielsweise festgestellt, dass die Bildung von Mono- und Dicalciumsilikaten bei unterschiedlichen Temperaturen *in situ* über verschiedene Reaktionswege erfolgen kann. Darüber hinaus wurden die Polymorphe Pseudowollastonit und α'_L-Ca_2SiO_4 identifiziert. Letzteres wandelte sich beim Abkühlen in β-Ca_2SiO_4 (Larnit) um und blieb bei Raumtemperatur metastabil.

Die Bildung und Temperaturstabilität von Ternesit und Silicocarnotit, d. h. dem sulfat- und phosphathaltigen Endglied einer Mischkristallreihe, wurden untersucht. Beide Mineralphasen werden durch Reaktionen mit Dicalciumsilikat gebildet. Insbesondere wurde die Korngrenzenwanderung von Ternesit durch das Ersetzen eines großen Quarzkorns beobachtet. Mit zunehmender Temperatur (und Zeit) bildete α'_L-Ca_2SiO_4 neue Reaktionsränder um Ternesit, wodurch eine Schichtstruktur mit Quarz im Zentrum, Ternesit in der mittleren und α'_L-Ca_2SiO_4 in der äußeren Schicht entstand. Die Erhitzungsstudie mit einem natürlichen Ternesit-Kristall ergab eine Phasenumwandlung zu α'_L-Ca_2SiO_4 zwischen 730 und 1120 ± 1 °C und bestätigte, dass sowohl die Ternesit- als auch die Dicalciumsilikat-Domäne in diesem Temperaturbereich koexistieren können. Im Allgemeinen hängt es vom Fortschritt der Reaktion ab, ob nach dem Abschrecken auf Raumtemperatur Ternesit oder Larnit nachgewiesen wird. Des Weiteren wurden zwei Reaktionswege zur Bildung von Silicocarnotit zwischen 1050 und 1150 °C gefunden, d. h. bei deutlich niedrigeren *in situ* Temperaturen als bisher angenommen. Außerdem wurde zum ersten Mal eine Erhitzungsstudie mit einem natürlichen Silicocarnotit-Kristall durchgeführt. Dabei zeigte sich zum Beispiel, dass sich die Position der $v_1(PO_4)$ Bande bei 1200 ± 1 °C von 951 ± 1 cm^{-1} auf ~930 cm^{-1} verschoben hat. Darüber hinaus wurde die Umwandlung von Hydroxylapatit in Tricalciumphosphat untersucht, was neue Einblicke in den komplexen Prozess des Verlusts der an HAp-Nanokristallen gebundenen Hydroxylgruppen an der Oberfläche ermöglichte.

Die Vorteile der *in situ* hyperspektralen Raman-Bildgebung im Vergleich zu herkömmlichen experimentellen und analytischen Methoden, bei denen die Probe vor der Analyse auf Raumtemperatur abgekühlt werden muss, werden deutlich aufgezeigt. Diese neue Analysemethode ist ein leistungsfähiges Instrument zur Untersuchung von Sinterreaktionen mit hoher Temperatur-, Zeit- und Ortsauflösung und bietet eine breite Reihe von Möglichkeiten zur Untersuchung keramischer Systeme für industrielle Anwendungen.

TABLE OF CONTENT

ABBREVIATIONS

AQ	anhydrite-quartz
AQC	anhydrite-quartz-CaO
AQG	anhydrite-quartz-gehlenite
acq. time	acquisition time
Anh	anhydrite
Cal	calcite
CHRI	confocal hyperspectral Raman imaging
CLS	classical least squares
DiC	dicalcium silicate
DTA	differential thermal analysis
EM-CCD	electron-multiplier charge-coupled device
exp.	experiment
HAp	hydroxylapatite
HT	high-temperature
ICDD	International Centre for Diffraction Data
LWD	long-working distance
NA	numerical aperture
PWo	pseudowollastonite
QM	quadrupole mass measurement
Qz	quartz
RT	room temperature
TCP	tricalcium phosphate
TG	thermogravimetric analysis
TQC	tricalcium phosphate-quartz-CaO
Wo	wollastonite
XRD	X-ray diffraction
XRF	X-ray fluorescence

GENERAL INTRODUCTION

Calcium silicates such as $CaSiO_3$, Ca_2SiO_4, Ca_3SiO_5, and $Ca_3Si_2O_7$ form at high temperatures within the CaO-SiO_2 system [1,2]. Therefore, the use of materials containing CaO and SiO_2 in the operation of industrial furnaces, such as in quicklime and cement production or coal combustion, leads to sinter deposits consisting mainly of these calcium silicates, which cause problems during kiln operation [3–6]. Furthermore, as part of the debate about coal combustion, significant attention is currently being paid to alternative fuels such as biomasses and sewage sludge. The residues from thermal combustion processes of these fuels primarily consist of calcium phosphates [7]. In general, the operating temperature and the chemical and mineralogical composition of fuels or the materials used mainly control the agglomeration mechanisms, which involve a complex interaction of phenomena that include aspects of hydrodynamics, chemical transformations, and particle interaction mechanisms [8]. However, once this complexity of influencing factors is understood and, in particular, the range of thermal stability of the deposited minerals is known, calcium silicates can serve as a temperature indicator that can help furnace operators to optimize combustion temperatures.

Furthermore, the industrial application of high-temperature (HT) minerals like calcium (alumina) silicates is essential and is becoming increasingly important. They have established their use as building materials like glass, cement, tile, and fireproof ceilings [9]. In particular, their high melting point and thermal stability make them of great importance for the ceramic industry. Calcium silicates are well-known phases in the cement industry [10–12]; especially, there has recently been a great interest in a sulfate-containing calcium silicate phase [13]. Other potential applications of calcium silicates are in biomedicine due to their excellent bioactivity and biocompatibility [14–16]. In this context, calcium phosphates play an important role in the use of bone substitutes [e.g., 17], whereby highly promising studies with silicon-substituted calcium phosphates have shown that silicon is an essential trace element for bone mineralization and can improve the bioactivity of calcium phosphate materials [18–23]. Obviously, both calcium (alumina) silicates and silica-/calcium phosphates have many positive properties for industrial applications.

In all cases, a detailed understanding of the thermodynamics and kinetics, and thus the mechanisms of high-temperature solid-state and melting reactions within the large field in the CaO-SiO_2(-SO_3/Al_2O_3/P_2O_5) system and subsystems as well as of pure phases is essential in order (i) to fully exploit their technical advantages, (ii) to predict sinter reactions in industrial processes at a given temperature, and (iii) to find the optimal synthesis conditions. The mineral reactions of the sequential subsystems were investigated *in situ* and *in operando*, i.e., while they are running, using a modern confocal Raman spectrometer system with an integrated heating stage. This new analytical method, its application, and the evaluation of data are described in Chapter 1. The results of experiments with synthetically prepared samples have been published in or submitted to peer-reviewed international journals and are presented in Chapters 2 to 4. Chapter 5 contains a comprehensive chemical and mineralogical analysis and initial insights into a sintering study of a real combustion sample used as an alternative fuel. Chapter 6 is a summary discussion of the present results and the final Chapter 7 provides a short conclusion and an outlook on the potential of confocal hyperspectral Raman imaging of HT mineral reactions.

1 The analytical method

In this work, we combined the advantages of in situ high-temperature (HT) Raman spectroscopy with the possibility of 2-dimensional Raman imaging with a micrometer-scale resolution as a powerful tool for in situ investigations of solid-state and solid-melt sintering processes. The results highlight the power of confocal hyperspectral Raman imaging (CHRI) as an analytical tool that can deliver in situ information about the growth and breakdown of distinct phases, including the detection of metastable or intermediate phases, without the necessity to quench the sample to room temperature (RT). Raman images can be taken during heating and cooling with a high temperature, time, and spatial resolution, enabling the kinetics of individual reaction steps to be quantified. A single experiment, therefore, contains the information of a multitude of conventional sintering experiments, involving heating and quenching of different samples. In this work, a novel approach to in situ study the sintering processes of different calcium (alumina) silicates as well as of silica-/calcium sulfates/phosphates by CHRI is presented. In the following, the analytical method is described in detail based on the results described and discussed in the co-authored publication with the title "*In situ hyperspectral Raman imaging: A new method to investigate sintering processes of ceramic material at high-temperature*", published in 2019 in *Applied Sciences* [24].

1.1 Raman spectroscopy

Raman spectroscopy is based on the interaction between electromagnetic radiation and the atoms of sample material. When a small part of the laser light is scattered by a molecule with an energy different from that of the incident photon, inelastic scattering occurs. The observed scattering intensities (Raman bands) at different frequencies depend on the symmetry of the molecular groups or crystal lattice, the bond strength, and the mass of the atoms involved. Thus, the vibrational spectrum provides information about the structure and composition of the material irradiated. Because of this dependence, each compound has its characteristic Raman spectrum ("fingerprint"). This makes it possible to clearly identify both crystalline and amorphous solids (but also gases and liquids) in most cases if reference spectra are available. Furthermore, Raman spectroscopy provides a range of crystallographic chemical and physical information, which can also be 2-dimensional visualized by scanning the sample surface. One of the major advantages of Raman spectroscopy is the ability to obtain spectral information non-destructively. Therefore, Raman studies can be an interesting alternative to other analytical methods for industrial applications.

All Raman data presented in this work were collected with two different Raman spectrometers (Horiba Scientific HR800/HR800 Evolution*,* Kyōto, Japan*)* both equipped with an electron-multiplier charge-coupled device (EM-CCD) detector, an Olympus BX41 microscope, and a Nd:YVO_4 laser (λ = 532.11 nm) and a Nd:YAG laser (λ = 532.09 nm), respectively. Both laser offer a maximum power of 2 W, which is significantly lower at the sample surface [24]. To correct for any spectrometer shift during long-time measurements, the intense Ne line that occurs in the spectra at a Raman shift of 1707.36 or 1707.06 cm^{-1} depending on the laser excitation, was continuously monitored by placing a Ne lamp alongside the beam path of the scattered light. A 50x long-working distance (LWD) objective with a numerical aperture (*NA*) of 0.5 and a working distance of 10.6 mm was used for all experiments. Because the width of a Raman band usually broadens with increasing temperature to values of up to several tenths of wavenumbers, the spectral resolution was not a major issue. Therefore, we used a

grating with 600 groves/mm, so the wavenumber ranges from about 100 to 1730 cm^{-1} could be measured in a single spectral window. With this grating, the spectral resolution was ~3.5 cm^{-1}, as given by the width of the Ne line. The LabSpec 6.4.4.15 software was used to control the instrument, the heating, soaking, and cooling cycles, to refine the data, and to create hyperspectral Raman images.

1.1.1 Experimental setup

Figure 1 shows the experimental setup including the Raman spectrometer system, the microscope equipped with a Ne lamp, and a TS1500 (Linkam Scientific Instruments, Surrey, UK) heating stage with a connected water-cooling system.

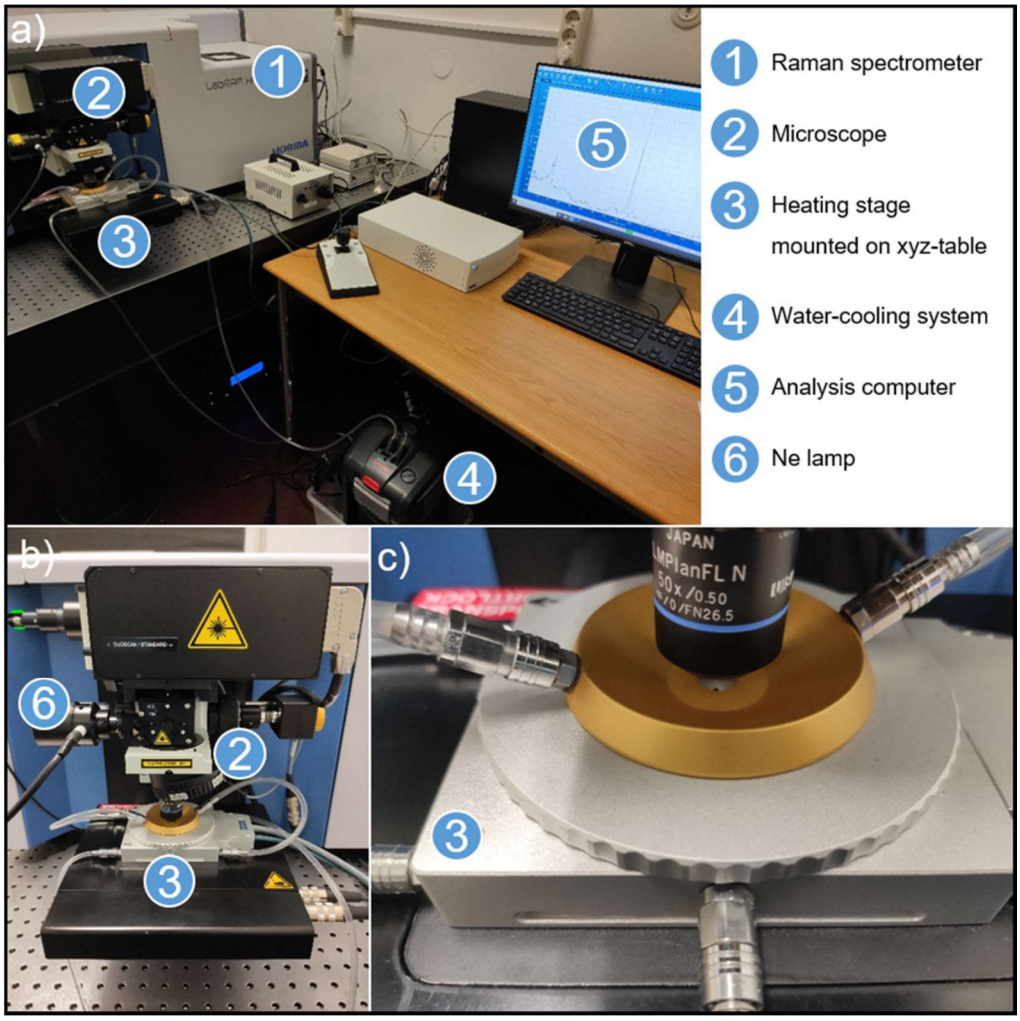

Figure 1: (a) The experimental setup that includes a Raman spectrometer system (here: Horiba Scientific HR800 Evolution, Kyōto, Japan) equipped with (b) an Olympus BX41 microscope, and (c) a TS1500 (Linkam Scientific Instruments, Surrey, UK) heating stage.

For all experiments, cylindrical samples were placed in the heating chamber (Figure 2), which was mounted on an automated x-y-z stage below the microscope objective (Figure 1b). This allows the heating stage to be moved in all three directions with a reproducibility of ± 0.5 µm in x and y and ± 0.25 µm in z-direction and thus to acquire hyperspectral Raman images at high temperatures. The temperature of the heating device can be varied between RT and 1500 °C with temperature stability of ± 1 °C and a maximal heating rate of 200 °C/min [25]. A platinum resistor sensor, accurate within ± 0.01 °C, measures the temperature at the bottom of the cell. The ceramic sample holder has a

diameter of 7 mm and a height of 6 mm. A second ceramic ring with insulation wool in between surrounds the cup to reduce heat loss (Figure 2). A heating shield with a pinhole aperture of 1 mm diameter is mounted above the heating stage to moderate the black body radiation reaching the objective (Figure 1c). Due to the height and volume of the sample cylinder, a strong temperature gradient occurs within the furnace. This gradient was empirically determined following the approach described by Stange and colleagues [26], who used a natural diamond for temperature calibration exhibiting a first-order Raman mode near 1332 cm^{-1} (at RT) that shows a strong frequency shift with increasing temperature. This temperature-dependent frequency shift of this first-order band was measured with high precision as a function of temperature up to 800 °C at the bottom of the cell as well as at the top of a green body with a height of 3.1 mm. From these data, the temperature gradient could be determined [26], which was also used here to determine the actual temperature at the sample surface with an error of about ± 1 °C for a sample height of < 1 mm and an error of about ± 5 °C for a sample height of ~3 mm.

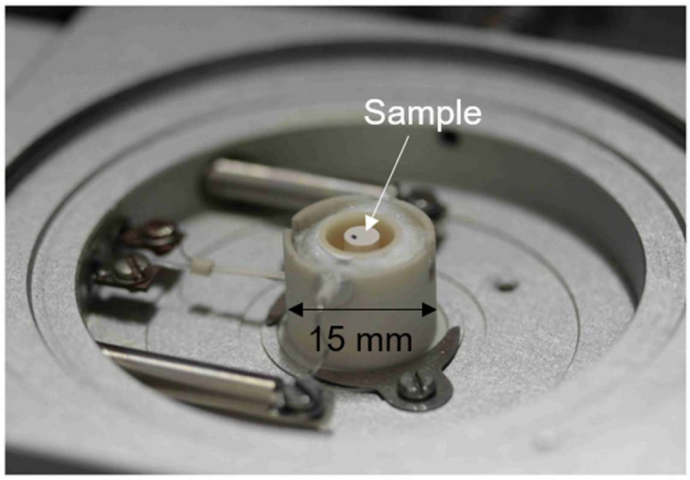

Figure 2: Detailed view of the Linkam furnace with sample. The cylindrical sample pellet placed within the oven cup of a TS1500 heating stage. The outer ceramic ring with insulation wool in between surrounds the cup to reduce heat loss.

1.2 Experimental series

Three types of experiments were performed in this work that are listed in Table 1. The experiments differ from each other in that studies were performed on single phases (heating studies) as well as on multi-component systems. In the following the details of the experimental series are described.

Table 1: Types of experiments.

Experiment	Type of Experiment		T range [°C]
E#1	heating study	in situ	RT–1400 (max)
E#2	multi-component sintering exp.	in situ	RT, x–1200, RT *
E#3	multi-component sintering exp.	in situ/quench	RT, x–1200, RT *

* x ≙ first temperature step; detailed experimental conditions are described in Chapters 2–4.

1.2.1 Mineral heating studies

In general, mineral phases are identified by the characteristic wavenumber positions and relative intensities of their fundamental Raman bands. With increasing temperature, the Raman bands of a mineral phase usually shift to lower wavenumbers and their width (given as full width of half-maximum) increases. The interpretation of in situ heating experiments based on high-temperature data becomes of great importance, in particular, due to the fact that reference Raman spectral

databases, such as, e.g., the RRUFF database [27], only contain RT spectra that usually differ significantly from their high-temperature (HT) counterparts. Therefore, a comprehensive database of HT reference spectra is essential for the evaluation of high-temperature experiments and has been collected to be used as in-house input data for the data evaluation procedure.

The first series of experiments (E#1) contained heating studies with pure mineral phases that occur in calcium silicate and calcium phosphate materials (Table 2). These experiments were carried out to obtain high-temperature in-house reference spectra to (i) determine the relative phase proportions from a mixed Raman spectrum, (ii) identify individual high-temperature phases in such mixed spectra, and (iii) visualize mineral reactions at high temperature. The heating studies were performed with both single crystals and powder pellets that were placed at the bottom of the cell close to the thermocouple. The powdered minerals used for the heating studies were pressed with 10 kPa in a wolfram carbide press into cylinders with a diameter of 3 mm and a height of less than 1 mm to minimize the temperature deviation caused by the temperature gradient in the heating stage. For the heating studies with single crystals, the samples were also prepared to a cylinder (Ø: 3 mm, h: < 1 mm). Both single crystals and powder pellets show a flat surface. Although Raman spectroscopy is a non-destructive analytical method, the flatness of the sample surface can be crucial, because light scattering at uneven surfaces may negatively affect the quality of the spectra.

Table 2: Relevant minerals that were used for the heating studies E #1.

Mineral	Sample material	Origin/Company
Anhydrite	Crystal/pellet	Tirol, Austria
Calcite	Crystal/pellet	Alfa Aesar
CaO	Pellet	Merck, Darmstadt, Germany
Gehlenite	Pellet	Tirol, Austria
Gehlenite	Crystal	Fassa Valley, Italy
Hydroxylapatite	Pellet	VWR, Darmstadt, Germany
Larnite	Crystal	Mayen, Germany
MgO	Pellet	Merck, Darmstadt, Germany
Ternesite	Crystal	Mayen, Germany
Pseudowollastonite	Pellet	Synth. from Wo (1250 °C)
Silicocarnotite	Crystal	Har Parsa, Israel, YV-415
Tri-Calciumphospate	Pellet	Synth. from HAp (1350 °C)
Quartz	Crystal/pellet	Natural, unknown
Wollastonite	Crystal/pellet	Baja California, Mexico

Raman spectra of single crystals compared to those of powders reveal differences in the width and intensity of the fundamental Raman bands due to temperature and/or quantum confinement effects. In particular, both local heating due to the focused laser light and a decrease in particle size normally result in an increase in band broadening [24,28]. In addition, for anisotropic crystals, the intensity of a Raman band depends on the angle of incidence of the laser beam in relation to crystal lattice orientation, bond polarizabilities, and the state of polarization of the incident laser beam. Therefore, relative intensities of a mineral phase change with crystal orientation, whereas the band shape and position are independent of crystal orientation [24]. Figure 3 shows, using anhydrite ($CaSO_4$) as an example, that the intensity of the fundamental Raman bands varies with the different orientations of the crystal plane oriented perpendicular to the incident laser beam. The Raman bands observed within the frequency range 100–300 cm^{-1} represent lattice modes due to Ca^{2+}-SO_4^{2-} vibrations. The bands between 400 and 500 cm^{-1} are attributed to the v_2 bending modes of the SO_4 tetrahedra [29]. The band at 416 cm^{-1} is also assigned to $v_2(SO_4)$, but clearly appears only in measurements when the incident laser beam was oriented perpendicular to the (010) crystal plane. The group of bands between 600 and 675 cm^{-1} and the bands located at frequencies higher than 1100 cm^{-1} are assigned to anti-symmetric v_4 bending and v_3 stretching modes of the SO_4 tetrahedra, respectively [29]. In the spectra

of anhydrite crystals, which were measured with a laser beam incident perpendicular to the (001) and (100) crystal planes, only two of three bands of the respective group can be clearly identified. A spectrum measured in random crystallographic orientation with respect to the laser polarization is also shown. All measured band positions are consistent in all spectra. The most intense symmetric $v_1(SO_4)$ stretching mode at 1016 cm^{-1} is non-polarized and is thus important for mineral identification. In the powder spectrum, all Raman modes can be seen due to the random orientation of the individual grains/crystals.

To account for such orientation effects in the identification and quantification procedure, reference spectra from minerals with relatively large orientation effects, like anhydrite or gehlenite, were recorded in a number of different orientations and implemented in the evaluation and quantification procedure. However, when sufficient material was available, reference spectra were preferentially recorded from pellets prepared from powdered samples with grain sizes between 5 and 30 µm rather than from single crystals.

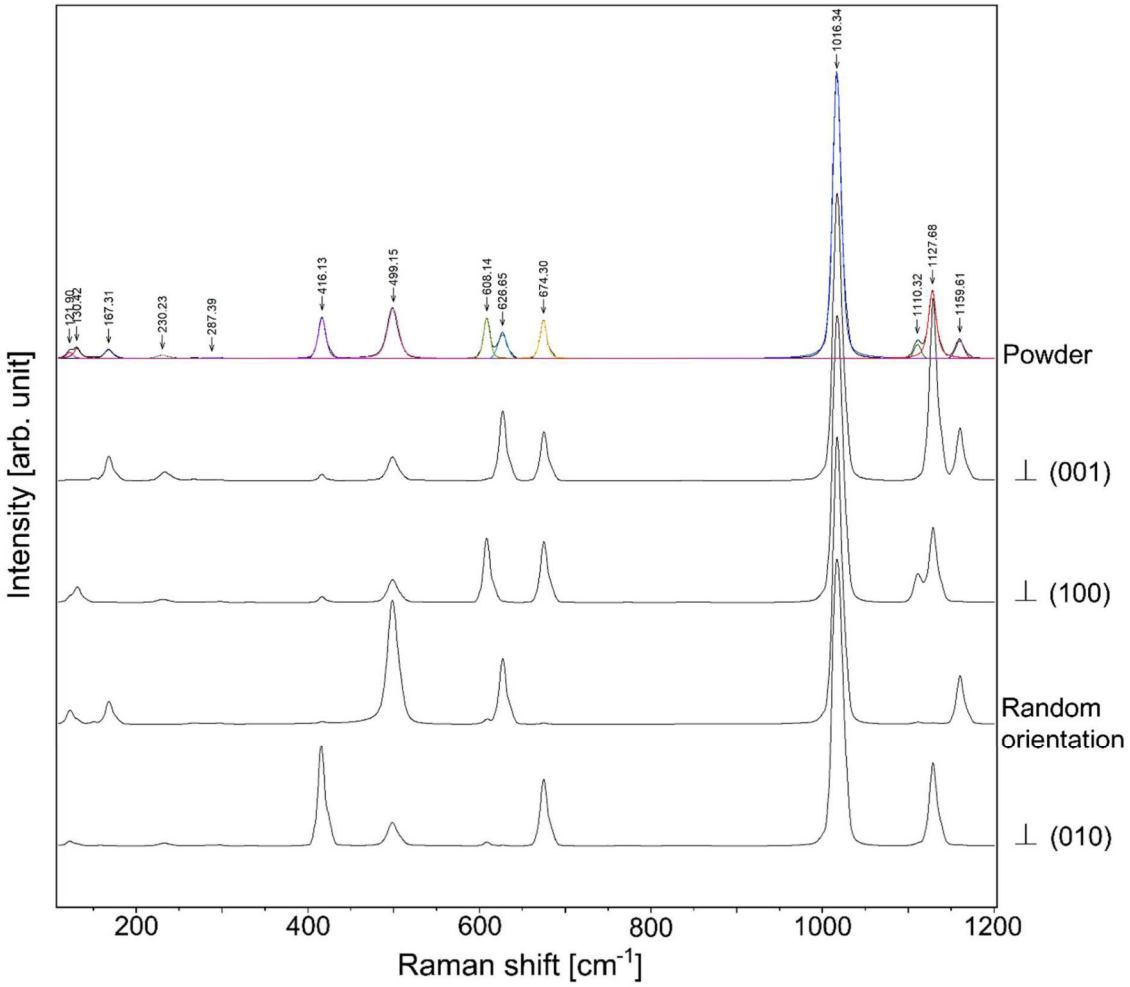

Figure 3: Room temperature (RT) unpolarized Raman spectra of selected anhydrite crystals and powdered material under ambient conditions. The v_2, v_3, and v_4 bands of SO_4 tetrahedra vary in intensity depending on the different crystalline planes oriented perpendicular to the incident laser beam. In the powder spectrum, all Raman bands that may occur are clearly identifiable. Note that the intensity of the main $v_1(SO_4)$ mode is about the same in all spectra.

In general, pure phase Raman spectra were recorded in a frequency range between 100 and 1730 cm^{-1}. For minerals such as lime (CaO) and hydroxylapatite, where OH or H_2O bands were expected, a spectral range from 100 to 4000 cm^{-1} was investigated. The spectra were recorded every 10 °C from RT to a

maximum temperature of 1400 °C with a total acquisition time of 100 s and an output laser power of 2 W. The long acquisition time was chosen to obtain high-resolution reference spectra, but also to visualize possible structural or chemical changes reflected in the width and frequency of a Raman band. The heating rate was 10 °C/min. After having recorded a spectrum at maximum temperature, the sample was cooled to RT with a cooling rate of 10 °C/min and the last spectrum was recorded. At each temperature step, depth profiles were acquired (auto-focus function) after an equilibration time of 300 s to obtain an optimal signal-to-noise ratio and a measure of reaction- and temperature-related shrinking or expansion effects. One example for the temperature-related expansion effect is the decomposition reaction of calcite to CaO and CO_2 between about 650 and 950 °C, which could be followed by spectral depth profiling (Figure 4) [24].

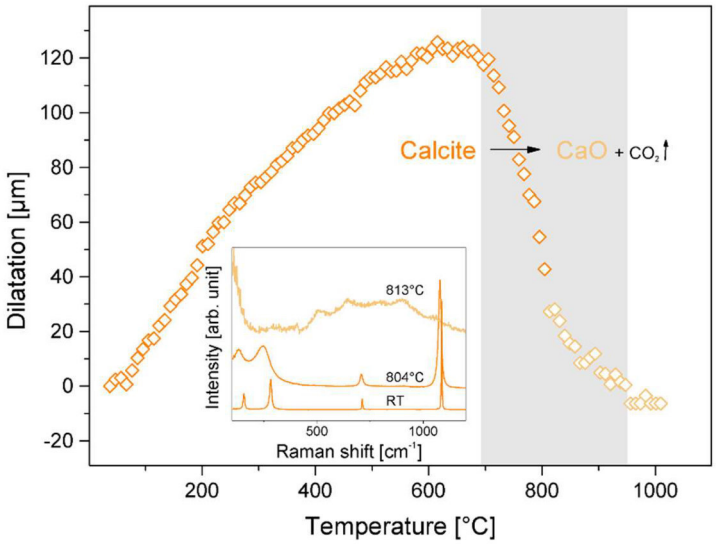

Figure 4: Dilatation of a pellet composed of calcite powder as a function of temperature. The dilatation was measured during the automated measurements by depth profiling. Note the dramatic shrinkage above 740 °C due to the decarbonation of calcite. The decarbonation is taking place between 700 and 950 °C, which can be followed by the shrinkage of the sample. At 804 °C, the calcite bands broaden and are shifted to lower wavenumbers (inset). Above 813 °C, calcite at the sample surface is fully decomposed to CaO (lime) that only shows a second-order Raman spectrum. Note that the Raman spectra were recorded at the sample surface [24].

With increasing temperature, the spectra change due to band positions, intensities, and widths. As an example, Figure 5 shows the heating study of a natural gehlenite sample ($Ca_2Al_2SiO_7$) performed in horizontal orientation with respect to (001) crystal plane orientation (cf. R060841.4 [27]). It is common practice to normalize Raman spectra to the maximum intensity to compare different spectra [30], but in doing so information about the intensity change of the v_1 mode with increasing temperature is lost. Thus, the stacked spectra are shown in a normalized and non-normalized representation. Within the frequency region between 100 and 400 cm^{-1}, Raman bands of lattice modes of stiff AlO_4 tetrahedra and Ca^{2+} ions occur. The bands between 400 and 550 cm^{-1} as well as the band near 800 cm^{-1} can be assigned to vibrational modes of the AlO_4 units. The most intense Raman bands are located in the frequency ranges 600 to 660 and 900 to 930 cm^{-1}, which can be assigned to the symmetric stretching v_1 modes of bridging oxygen of the pyrosilicate anions (T: Al or Si) and the non-bridging oxygen of the pyrosilicate group ($Si_2O_7^{-6}$), respectively [31,32]. Obviously, the measurement parallel to crystal plane orientation (001) leads to the occurrence of two strong non-equivalent v_1(T–O) modes at 906 and 927 cm^{-1} in the RT spectrum (blue spectra in Figures 5a and b).

Both the non-normalized and normalized representation show a change of the position and width of each Raman band with increasing temperature. In the normalized representation, the relative change in Raman shift of each band position with increasing temperature is highlighted. The observed bands become broader and slightly shift to lower frequencies when heated up to 1170 °C compared to the spectrum recorded at RT. The non-equivalent v_1(T–O) and v_1(T–O–T) modes merge at about 600 °C (orange spectra) and 1100 °C (red spectra), respectively. Note, however, that the change in intensity of the maximum band is observable only in the non-normalized representation (Figure 5a). After the v_1(T–O–T) modes are merged at about 1100 °C, the band intensity decreases significantly.

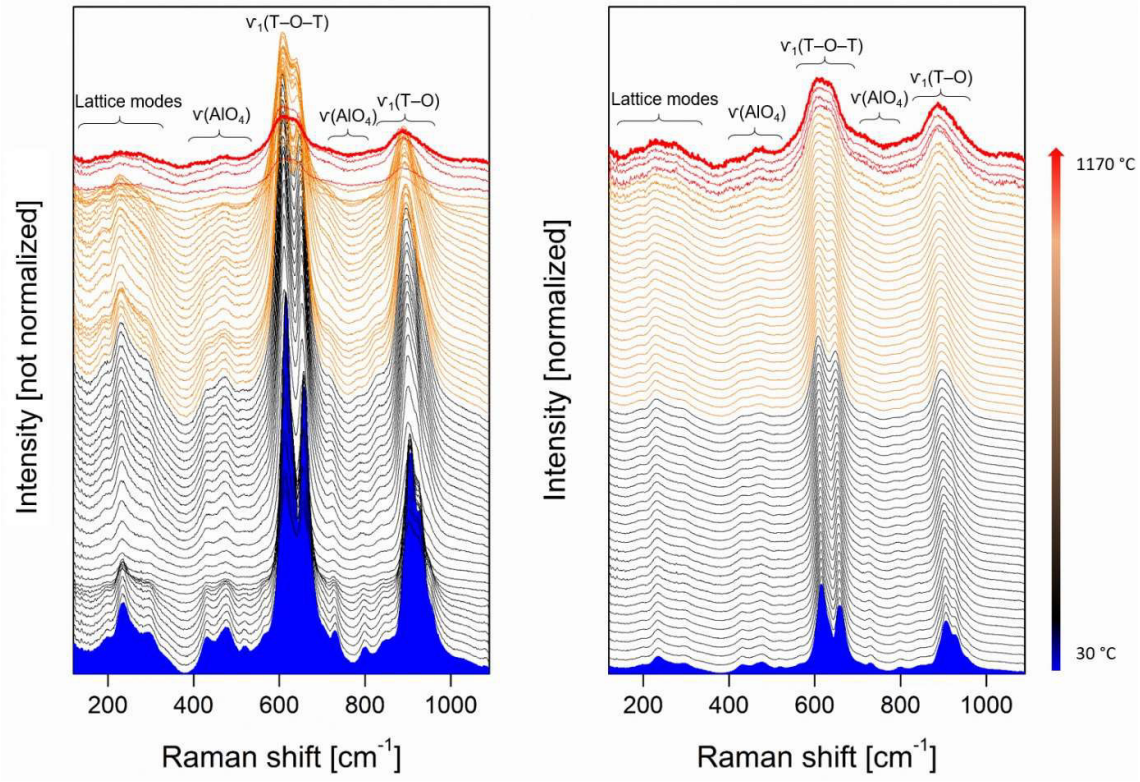

Figure 5: Stacked Raman spectra of a gehlenite sample recorded between 30 and 1170 ± 5 °C (approx. 10 °C-steps) presented (a) before and (b) after normalization to the maximum intensity (T≙ Al or Si). The double bands within the frequency ranges 900 to 930 and 600 to 660 cm^{-1} merge at about 600 °C (orange spectra) and 1100 °C (red spectra), respectively. Note that only in the non-normalized representation the change of relative band intensities becomes obvious.

It makes a difference whether the reference spectra are normalized to the maximum intensity before using them for data interpretation or not. The effect becomes apparent in the visualization of the hyperspectral Raman images, but plays a minor role in phase identification. The normalization of the spectra neglects the Raman scattering cross sections of the mineral phases and therefore phases with low cross sections (e.g., CaO) will be underrepresented in the image as shown in Figure 6a. In order to consider the Raman scattering cross sections of the individual mineral phases, all reference spectra are recorded at the same measurement setup (i.e., laser power, acquisition time, internal Ne lines, etc.) and are not normalized before using them for data analysis.

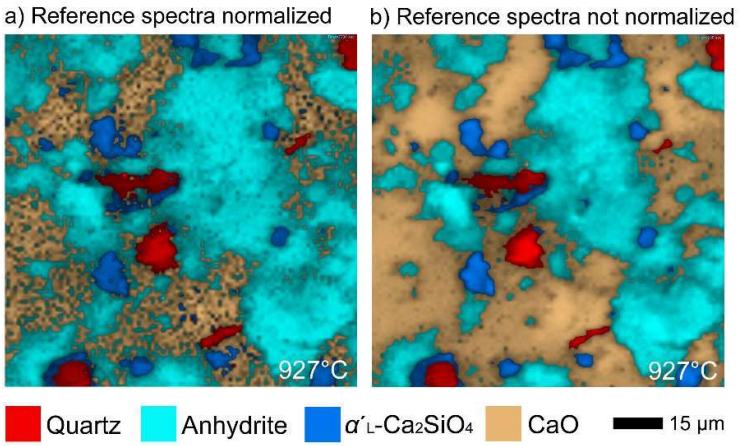

Figure 6: Hyperspectral Raman images recorded at 927 °C using the classical least-squares (CLS) fitting method (cf. 1.3.2.1) and in-house reference spectra that are (a) normalized and (b) not normalized before loading. The reference spectra in (b) are recorded at the same measurement setup and thereby the Raman cross sections of the individual mineral phases are considered [24].

1.2.1.1 Second-order Raman spectra

Lime (CaO) and periclase (MgO) crystallize in rock-salt structure with inversion symmetry and thus yield no first-order Raman spectrum [33,34], but show second-order Raman features. Despite the fact that it is difficult to assign second-order spectra at high temperatures, house-intern reference spectra of CaO and MgO were successfully used for data processing. At RT, CaO can be identified by Raman features near 540, 670, 740, and 900 cm^{-1} [24] (spectrum not shown here). The heating study of MgO is presented in Figure 7. In the RT spectrum of MgO, Raman features are observed at about 740, 1040, and 1090 cm^{-1} [34]. The two weak, but distinct bands at 276 and 442 cm^{-1} can possibly be assigned to first-order scattering due to microcrystals [35]. They disappear above 300 °C, whereas a weak band appears at 497 cm^{-1} and the most intense band at 1090 cm^{-1} decreases. The significant spectral change is marked by a dashed line in Figure 7a. As the temperature increases up to 1000 °C, the band at 1090 cm^{-1} continues to decrease, whereas the bands at 740 and 1040 cm^{-1} remain constant in intensity and position. In addition, the band at 497 cm^{-1} increases in intensity. Until 1000 °C, the HT spectra can be used to identify MgO within multi-phase sintering experiments.

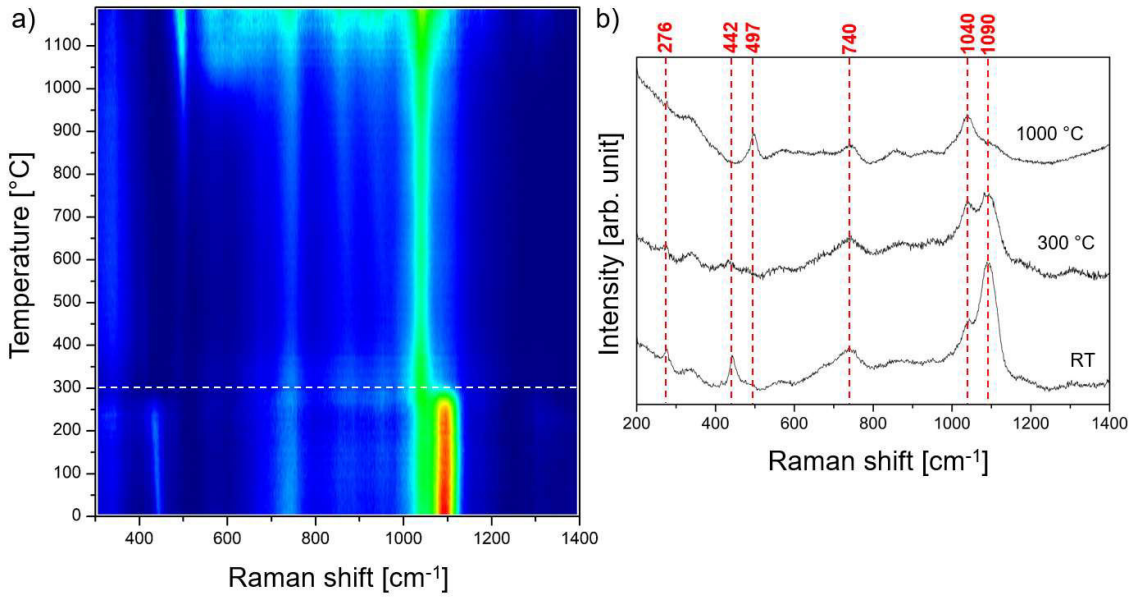

Figure 7: (a) Color-coded Raman intensity as a function of Raman shift and temperature (red and blue colors represent high and low intensities, respectively) and (b) second-order Raman spectra of pressed MgO powder recorded at RT, 300, and 1000 °C..

1.2.2 Multi-component sintering experiments

The second test series (E#2) involved multi-component sintering experiments with green bodies that were produced by compacting between about 20 and 50 mg of powdered precursor material into cylinders (Ø: 3 mm, h: 1.5–2.7 mm) at a pressure of 10 kPa, which resulted in a flat sample surface. All multi-component sintering experiments were performed under very similar conditions as the experiments with pure reference phases, except for the acquisition time per spectrum/pixel. After selecting a representative area of the sample surface, a hyperspectral Raman image was first recorded at RT. The sample was then fired with a heating rate of 10 °C/min to different high temperatures, where two in situ hyperspectral Raman images were subsequently recorded before heating the sample to the next temperature step. The detailed temperature profiles are described in the respective article or chapter of this thesis. After taking the last HT image at the chosen maximum sintering temperature of the experiment, the sample was cooled to RT with a cooling rate of 10 °C/min and a final image was

acquired. In the third experimental series (E#3) the images were recorded in situ at HT and after cooling down at RT for each temperature step to study the effect of quenching. The RT maps form the basis for the interpretation of conventional sintering experiments, wherein the sample has to be quenched before analysis at RT.

1.3 Experimental conditions

1.3.1 Lateral and axial resolution

The spatial resolution is an essential factor for interpreting hyperspectral Raman images and is governed mainly by the diffraction of light and therefore depends on the laser wavelength (λ) as well as on the numerical aperture (*NA*) of the objective [24,36]. In a first approximation, the theoretical lateral (d_l) and axial (d_a) resolution is linearly dependent on the wavelength of the incident laser and inversely proportional to the numerical aperture of the objective. It follows that a high spatial resolution can be achieved with lasers at shorter wavelengths and objectives with a large *NA*.

With the 50x long-working distance objective (*NA* = 0.5) used in this study, the diffraction-limited theoretical lateral and axial resolution at the sample surface is 1.3 and 8.5 µm, as given by $d_l \approx 1.22\,\lambda/NA$ and $d_a \approx 4\lambda/NA^2$, respectively, where λ is the excitation wavelength [37]. In practice, the real resolution is certainly worse than the theoretically calculated values, i.e., in the order of 2 µm lateral and 15 µm axial, due to (i) an imperfect optics, (ii) light scattering at the surface and interfaces of the sample, and (iii) light refraction at the top window of the heating stage [24,26]. The axial resolution can principally be improved by using a confocal aperture, reducing the volume from which the scattered light is collected by blocking radiation generated from the surrounding volume [38]. A convenient side effect is the reduction of the black body radiation, which is emitted by the sample at elevated temperatures by reducing the confocal aperture. A drawback of narrowing the confocal hole is that the overall intensity becomes lower. Both the black body radiation and the setting of the confocal hole affect the background of Raman spectra (cf. Section 1.3.1.1).

To interpret hyperspectral Raman images and especially to interpret the spectrum arising from a specific point in the map (for example grain boundaries), it is essential to know how much of the observed Raman signal originates within the focal volume and how the response tails off with depth [39]. Two factors are primarily important for the depth resolution, the volume of the laser focus, and how Raman photons generated within this volume are relayed back into the spectrometer via the confocal aperture [36]. The axial resolution obtainable in confocal microscopy can be calculated by the following equation [40]:

$$d_a = \frac{2.2\,n\lambda}{2\pi NA^2} \tag{1}$$

where *n* is the refractive index of the immersion medium. This equation is only valid with the optical focus at the surface of the sample.

Based on the theoretic consideration, Everall [36] showed that the true laser focus is always deeper within a transparent sample than the so-called nominal depth (Δ), i.e., the distance below the surface given by the *z* drive of the stage. The axial laser focus also broadens upon moving deeper into the sample. The depth resolution gets worse linearly with the nominal depth [38] and can be estimated from:

$$d_a = \Delta\left[\left[\frac{NA^2(n^2-1)}{(1-NA^2)} + n^2\right]^{\frac{1}{2}} - n\right] \tag{2}$$

Apart from the point of focus also the depth of focus increases with increasing nominal depth. In general, due to the limited spatial resolution it is impossible to obtain "pure" spectra at interfaces [37].

1.3.1.1 Spectral background

Two fundamental background contributions often occur within a frequency range of 100 to 1750 cm^{-1} that are related to sample fluorescence and black body radiation. The latter effect is electromagnetic radiation emitted by the furnace material and the sample at temperatures above ~800 °C [41]. Fluorescence can be caused by the presence of specific fluorescing cations (e.g., Cr^{3+}, Fe^{2+}, etc.) [41] that are incorporated into the crystal structure. Fortunately, fluorescence effects are more significant at lower temperatures [24]. Significant portions of the black body radiation are in the region of Raman-active vibrations and therefore partly hide the Raman signals [42]. Figure 8a shows an increasing intensity of black body radiation at higher temperatures. Each spectrum was recorded at the beginning of each temperature step, while the acquisition parameters were identical, except that the laser did not excite the sample.

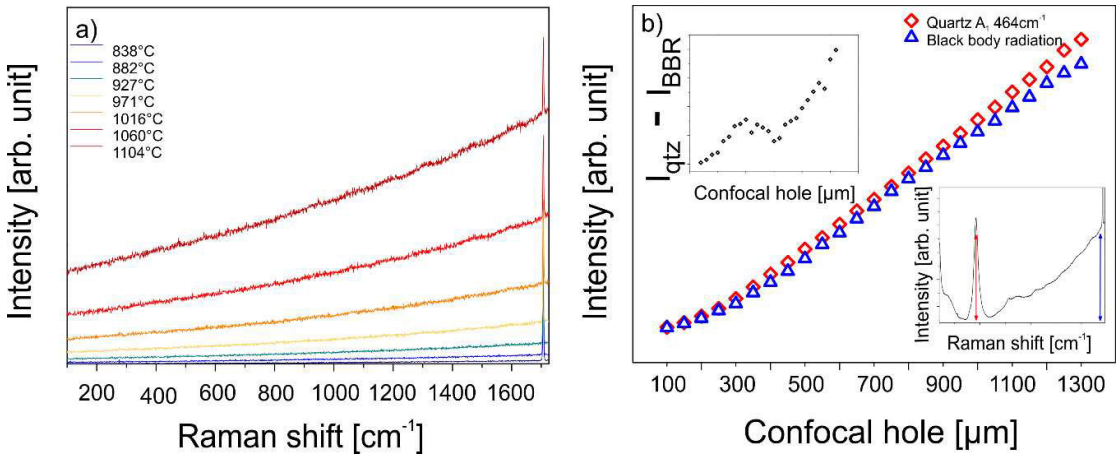

Figure 8: (a) The black body radiation as a function of temperature. (b) The Raman intensity of the A_1 quartz band near 464 cm^{-1} (lower inset diagram) and the intensity of the black body radiation at 1100 °C as a function of the confocal pinhole [24].

The black body radiation was reduced by (i) the addition of a radiation shield located between heating chamber and objective, (ii) working with a small heating system, and by (iii) decreasing the confocal pinhole, which however also decreases the Raman signal. To study the influence of the confocal hole on the depth resolution, Hauke and co-workers [24] recorded a series of hyperspectral Raman images at the same location with a different confocal pinhole (100 to 1300 µm). With decreasing pinhole aperture, the depth resolution increases at the expense of intensity. Small mineral grains are clearly distinguishable within the Raman images recorded with a confocal hole of up to 400 µm, whereas they appear to have "grown" together in images recorded with a larger confocal aperture. Furthermore, due to the overall lower intensity of the images recorded with a confocal hole smaller than 300 µm most of the grain boundaries are blurry. Another study shows that with increasing confocal pinhole, the intensity of the A_1 band of quartz near 464 cm^{-1} at RT increases linearly in the range of 400 to 1300 µm (Figure 8b). A pinhole larger than 1000 µm increases the intensity of the black body radiation to a lesser extent than the intensity of the quartz band, which leads to a better signal-to-noise ratio. Considering the intensity, closing the confocal pinhole is only a benefit if the spatial resolution of the measurement is of concern as it is for Raman imaging of multi-component sintering reactions. All measurements were thus performed with a confocal pinhole of 300 µm, which appears to be the best compromise between spatial resolution, overall image recording time, and signal-to-noise ratio [24].

1.3.1.2 Focus

It is important to note that the axial resolution at the surface also depends on the absorption properties of the material investigated. To study this dependence, a series of hyperspectral Raman images of a ceramic sample at different nominal depths (*z* drive) were recorded [24]. As expected, the intensity of the Raman bands of the individual phases decreases with increasing nominal depth. A Raman intensity loss of 20 to 40 % is observed within the first ten micrometers, whereas within the first 20 µm, which is a typical grain diameter, already about half of the intensity of the Raman bands is lost. At a depth of about 50 µm, Raman signals from any of the analyzed phases are hardly detectable anymore due to strong absorption of the incident and scattered light (Figure 9).

This is also reflected by the observation that the Raman images recorded at different nominal depths from the surface (z = 0 µm) to a depth of z = −15 µm are very similar [24]. As a matter of fact, the statistical variations of the average mineral fractions, obtained from all images, are in the same order of magnitude of those that were estimated from multiple images recorded from the same area (volume) with identical focus. It follows that slight variations of the focus among different images do not significantly affect the recorded mineral fractions and morphological details [24].

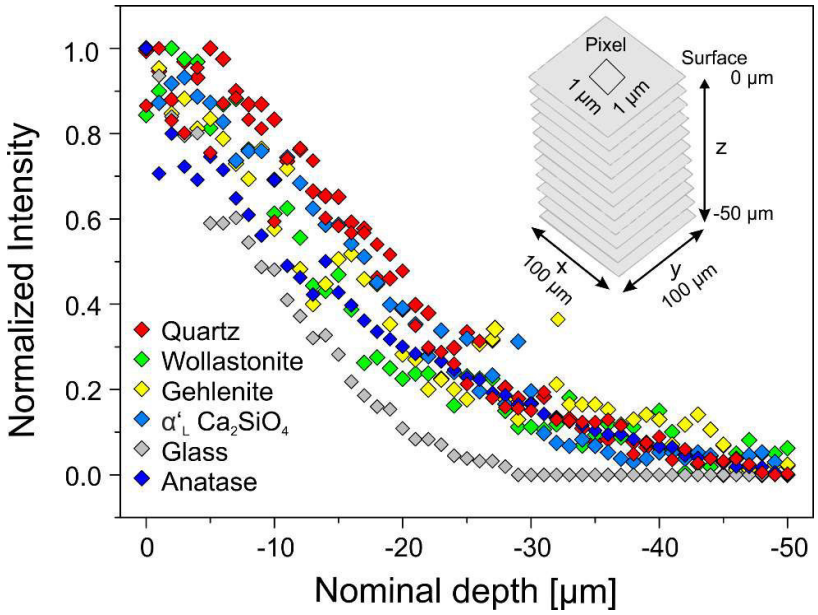

Figure 9: Normalized intensities of the main Raman band of the respective phase at six x-y positions as a function of nominal depth (z = 0; focus at the sample surface). The data was extracted from 50 hyperspectral Raman images of a fired ceramic that were acquired at RT at a focal depth between 0 and −50 µm (z-axis) with a step size of 1 µm (inset diagram) and a confocal hole of 300 µm [24].

The position of sample surface can change significantly due to reaction- and temperature-related shrinking or expansion effects during firing. Depth profiles were acquired manually and/or with the auto-focus procedure (depth profiling) before recording the first image at each temperature step to monitor such effects and to obtain an optimal signal-to-noise ratio. The "tilt at limits" mode acquires depth profiles of the image center and the four corners and determines the best focus regarding the Raman signal from which the focus at each position (pixel) in the image is interpolated. Thereby an inclined sample surface can be compensated [24]. Figure 10 shows the effects of expansion and shrinkage of green bodies, containing anhydrite, quartz, and calcite (AQC), due to increasing and decreasing temperature, respectively. In the in situ experiments AQC-1.1 and AQC-1.2 (Figure 10a), the green body was first fired to 927 or 659 ± 5 °C, respectively, with a heating rate of 10 °C/min. Subsequently, each sample was fired stepwise (~50 °C-steps) every four hours to 1104 ± 5 °C and then

cooled down to RT. In the in situ/quench experiment AQC-2, the green body was first fired to 927 ± 5 °C and cooled down to RT before firing to the next temperature step (~50 °C-steps). Comparing the change in focus during the experimental series, it becomes clear that a longer heating period leads to a stronger expansion (Figure 10a). Furthermore, heating/quenching significantly affects the focus only at high temperatures (Figure 10b), indicating that mainly reversible processes have occurred in this example.

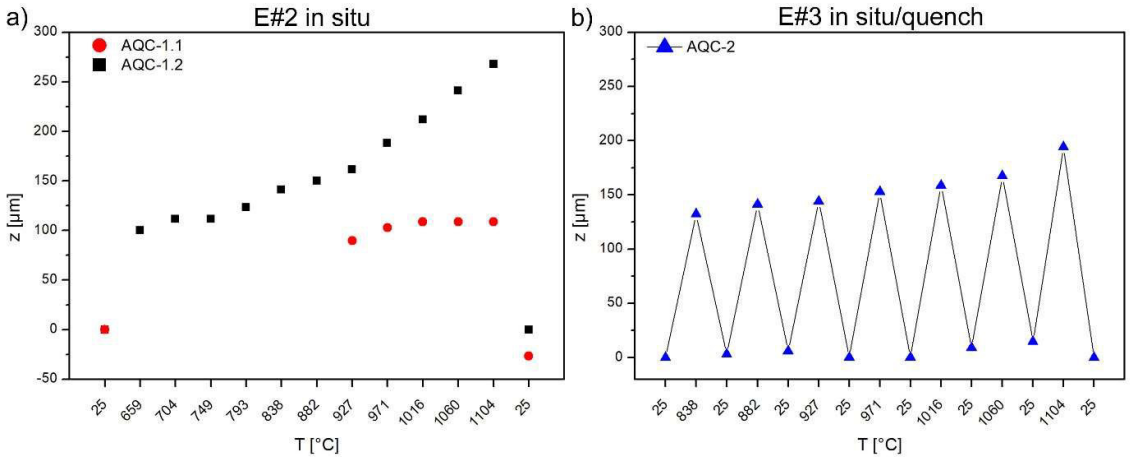

Figure 10: The depth of focus (z) as a function of temperature for (a) the in situ studies AQC-1.1 and AQC-1.2 and (b) the in situ/quench experiment AQC-2. Note that the dwell time at each temperature step was about 4 h.

1.3.2 Hyperspectral Raman imaging

1.3.2.1 Map programming

The quality of the Raman spectra and therefore also of the Raman images depends on a number of instrumental parameters (e.g., laser power, acquisition time, quality of the lenses, grating, sensitivity of the detector, the size of the confocal hole, the microscope objective) and sample characteristics (e.g., surface roughness, color, heterogeneity, the refractive index of the sample) [30]. In general, superior spectral quality can be obtained using a point-by-point mapping approach, as data sets can benefit from longer acquisition times. Hauke and colleagues [24] compared two maps recorded in the fast scanning mode (SWIFT© mode, 0.6 s per spectrum, recording time of 50 min) and in the point-by-point mode with an acquisition time of 10 s per spectrum (recording time of 8 h 43 min), respectively [24]. They conclude that the large increase in acquisition time has only a minor influence on the quality of a hyperspectral Raman image. Thus, even poor-quality spectra usually provide sufficient detail for phase identification and a semi-quantitative estimate of the increase or decrease of a mineral fraction within the analyzed volume as a function of temperature and time is still reliable. Generally, analytical parameters (e.g., image size and EM-CCD settings) are always a compromise between (i) the required signal-to-noise ratio that depends on the spectral details to be imaged, (ii) the spatial resolution necessary to separate chemical, structural, and/or textural features, and (iii) the total imaging time that should be significantly faster than the progress of the reaction under investigation [24].

Raman spectra were collected during continuous x-y stage movement with a speed of 1.6 µm/s (SWIFT© mode). During movement, Raman intensities were recorded for 0.5 s in the frequency range from 100 to 1730 cm^{-1}. All acquired HT images comprised an area of 100 × 100 $µm^2$ in size. For RT spectra, a larger area (140 x 140 $µm^2$ or 160 x 160 $µm^2$) was usually chosen so that the same area could be investigated at all temperature steps. The step size was 1 µm, yielding 10,000 pixels (spectra) per HT image. Despite the short acquisition time per spectrum, the total exposure time was still about two

hours for a single image. Hence, an image is not always an accurate snapshot in time, which has to be considered when interpreting hyperspectral Raman images.

1.3.2.2 Data reduction

As a first step, undesirable spectral features have to be separated from the Raman bands. This preprocessing step has to be done with care, because it is easy to introduce but not necessary to detect artifacts in a Raman image [43]. All spectra were corrected for (i) the wavelength-depended instrumental sensitivity (white light correction), (ii) a possible spectrometer shift by using "internal" Ne light lines as frequency standard, (iii) cosmic spikes, and (iv) background contributions (cf. 1.3.1.1). First, the white-light spectrum measured by the manufacturer was used to correct every spectrum of an image for the wavelength-dependent instrumental response or sensitivity. Then, each spectrum was corrected for a possible spectrometer shift during long-time image acquisition using the position of the intense Ne line at 1707.36 or 1707.06 cm^{-1}, respectively, depending on the excitation (λ). For this, a Gaussian function was fitted to this Ne spectral line and the line position was then used to correct for any frequency shift during long-time imaging. With such an internal standard, the propagated precision of the frequency of a Raman band, obtained by least-squares fitting, was usually between ± 0.05 and ± 0.10 cm^{-1} for RT spectra. The accuracy is thereby coupled to the precision of the Ne line wavelength determination at 585.24878 nm, which is better than ± 10^{-5} nm [44].

As a next step, all spectra acquired in the SWIFT© mode, excluding the spectra taken at RT, were corrected for cosmic spikes by the spike correction function implemented in the LabSpec software. This procedure identifies all signals with a full width of half maximum (FWHM) smaller than six CCD pixels as cosmic signals, which are automatically removed. The analyzed spectral range was then reduced to the frequency range 100–1200 cm^{-1} to simplify the following band fitting procedures. This area covers the main rocking and bending (between 100 and 700 cm^{-1}) and stretching vibrations (between 700 and 1200 cm^{-1}) of all mineral phases of interest. For quantification and image visualization, the spectra had to be further corrected for background contributions. The black body spectrum that was recorded at the beginning of each temperature step was usually subtracted from every spectrum of the image before a 2nd order polynomial baseline function was fitted to the spectrum and subtracted to further correct the spectrum for fluorescence and any background noise.

1.3.2.3 Quantification and image generation

The classical least squares (CLS) fitting procedure was used to determine the phase proportion at each pixel of an image and was performed with the LabSpec software. This method is based on the assumption that a polyphase spectrum is a linear mixture of the spectra from the pure phases. Within the multidimensional spectral array, the CLS fitting procedure finds a linear combination of reference spectra from the pure phases, which best fits the raw spectrum at each position (pixel). The resulting image is created by false-coloring each pixel of the image relative to the fraction of each component in the spectrum. This means that in the unmixed color-coding algorithm used in this work, the pixel is displayed in the color of the phase that dominates in the Raman spectrum [26]. The brightness of the color represents the overall intensity of the spectrum (pixel). While a dark color reflects low intensity, a bright color signifies high intensity. Additionally, the analyzed hyperspectral Raman images are smoothed, which improves the visualization of grain boundaries as shown in the work of Hauke and colleagues [24]. Such a procedure is straightforward if pure reference spectra are available. Due to the small grain size of the mineral phases and the limits of the spatial resolution, most spectra of an image are composed of contributions from multiple phases. Therefore, the temperature-dependent in-house reference spectra were used as input reference spectra for the CLS fitting routine.

As already described (cf. 1.2.1), all reference spectra are recorded with the same analytical conditions (i.e., laser power, acquisition time, internal Ne lines, etc.) to consider the Raman scattering cross sections of the individual mineral phases. However, if the Raman cross sections of the analyzed phases are very different, the image will appear black except for small bright spots where phases (e.g., anatase) with a high Raman cross section are located. This is because the intensity of the Raman spectrum here is extremely high, unlike all other spectra where the dominant phases have lower Raman intensities. Therefore, the Raman CLS images were normalized to 100 % for each pixel.

2 In situ Raman imaging of high-temperature solid-state reactions in the $CaSO_4$–SiO_2 system

PREFACE

The main focus of the first study was to analyze the decomposition processes and mineral reactions of anhydrite ($CaSO_4$) and quartz (SiO_2), and potentially newly formed calcium silicates during firing using confocal hyperspectral Raman imaging. The minerals of the $CaSO_4$-SiO_2 system are of particular interest due to the fact that they are typical components of brown coal ashes and sintering reactions between these phases at high temperatures may lead to adherent soiling and poorly removable sintering crusts inside the boiler of power stations [3–6]. On the other hand, if their formation and decomposition temperatures are known, they can act as indicators to estimate the real temperature conditions during the combustion of lignite. Furthermore, wollastonite ($CaSiO_3$) is an important mineral in the ceramic and building industry, because of its high melting point, thermal stability, and high electrical resistivity [45]. Due to its acicular structure, wollastonite improves the mechanical properties of building components and is used as a filler in polymers. Other potential applications exist in the paint and varnish industry due to its white color [12]. Both wollastonite and dicalcium silicate (Ca_2SiO_4) are cement-relevant phases [10,11] and moreover, show excellent bioactivity for biomedical applications [14–16]. The present study includes sintering experiments with samples of anhydrite and quartz, demonstrating the possibilities of in situ Raman imaging to study high-temperature sintering reactions. Since gehlenite ($Ca_2Al_2SiO_7$) is also a common mineral phase in lignite ash[3] and is used as a regular constituent of ceramic materials [46,47], one experiment was carried out with additional gehlenite.

The following publication is reprinted from "Böhme N, Hauke K, Neuroth M, Geisler T. In situ Raman imaging of high-temperature solid-state reactions in the $CaSO_4$–SiO_2 system. *Int J Coal Sci Technol* **2019**, 6, 247–259" [48].

Author contributions:

The planning of the experiments, the procurement of the sample material, and the sample preparation were performed by Nadine Böhme. All Raman measurements, data processing, and analysis were also performed by Nadine Böhme with the help of Kerstin Hauke. In addition, literature research and the preparation of the original draft were done by Nadine Böhme with the assistance of Kerstin Hauke. Manuela Neuroth provided information on high-temperature mineral reactions during the coal combustion process. Thorsten Geisler commented and proofread the manuscript, while all authors contributed to the final version of the manuscript. All co-authors agree to the use of the publications for this dissertation and to the identification of the doctoral student's contribution.

Int J Coal Sci Technol (2019) 6(2):247–259
https://doi.org/10.1007/s40789-019-0252-7

In situ Raman imaging of high-temperature solid-state reactions in the $CaSO_4$–SiO_2 system

Nadine Böhme[1] · Kerstin Hauke[1] · Manuela Neuroth[2] · Thorsten Geisler[1]

Received: 12 June 2018 / Revised: 9 April 2019 / Accepted: 10 May 2019 / Published online: 27 May 2019

Abstract The deposition of mineral phases on the heat transfer surfaces of brown coal power plants may have a negative effect on power plant boilers. The paragenesis of these deposits contains information about the actual temperature prevailed during the combustion of lignite, if the temperature-dependences of distinct mineral transformations or reactions are known. Here, we report results of a sintering study (to ~ 1100 °C) with samples containing anhydrite, quartz, and gehlenite, which are typical components of Rhenish lignite ashes. Thermal decompositions and solid-state reactions were analyzed (1) in situ and (2) both in situ and after quenching using confocal hyperspectral Raman imaging. This novel application of confocal Raman spectroscopy provides temperature- and time-resolved, 2-dimensional information about sintering processes with a micrometer-scale resolution. In the course of the sintering experiments with anhydrite and quartz with a weight ratio of 2:1 both polymorphs wollastonite and pseudowollastonite were identified in situ at about 920 and 1000 °C, respectively. The formation of pseudowollastonite was thus observed about 120 °C below the phase transition temperature, demonstrating that it can form metastably. In addition, α'_L-Ca_2SiO_4 was identified at about 1100 °C. In samples containing equal weight fractions of anhydrite and quartz that were quenched after firing for 9 h at about 1100 °C, β-Ca_2SiO_4 (larnite) crystallized as rims around anhydrite grains and in direct contact to wollastonite. We furthermore observed that, depending on the ratio between quartz and anhydrite, wollastonite replaced quartz grains between 920 and 1100 °C., i.e., the higher the quartz content, the lower the formation temperature of wollastonite.

Keywords Ash deposition · Calcium silicate · Calcium sulfate · High-temperature · Raman imaging

1 Introduction

During the combustion process of lignite in a brown coal power plant, the deposition of mineral phases on the heat transfer surfaces may have a negative effect on power plant boilers. Such ash deposition, including fouling and slagging, can reduce the heat conductibility and consequently the efficiency of the power station. The temperature at which sintering reactions take place strongly depends on coal composition. Therefore, it is important to determine the mineralogical composition of brown coal before firing it. Furthermore, it is of great interest to understand the mechanism of ash transformation of different coals worldwide (Nankervis and Furlong 1980; Vuthaluru and Zhang 2001; Kostakis 2011; Li et al. 2016, 2017). Currently, there exists a wide range of analytical techniques to classify varieties of brown coals according to its combustion behavior, such as X-ray fluorescence (XRF), scanning electron microscopy (SEM), and X-ray diffraction (XRD). These methods have also frequently been applied to study mineral reactions associated with the burn up of brown coals (e.g., Nankervis and Furlong 1980; Li et al.

✉ Nadine Böhme
nadine.boehme@uni-bonn.de

[1] Institut für Geowissenschaften und Meteorologie, Universität Bonn, Poppelsdorfer Schloss, Meckenheimer Allee 169, 53115 Bonn, Germany

[2] RWE Power AG, F und E, Kraftwerk Niederaußem, Bergheim, Germany

2016, 2017) as well as with natural lignite combustion deposits (Kostakis 2011).

Anhydrite, quartz, and gehlenite are typical components of Rhenish brown coal ashes. Sintering reactions between these phases at high temperature may lead to adherent soiling and poorly removable sintering crusts inside the boiler of power stations. Anhydrite has, in combination with sodium sulfate, adhesive properties and supports ash deposition (Kostakis 2011; Li et al. 2016). Li et al. (2016, 2017) have studied ash depositions formed on an air-cooled probe and pointed out that early deposits consist of fine Ca/S particles that connect coarser fragments and initiate ash accumulation. On the other hand, CaO helps to capture gaseous SO_2/SO_3 (Li et al. 2017). Anhydrite is the main sulfur-containing mineral phase in the solid combustion waste from 500 °C until its decomposition temperature of about 1200 °C (e.g., Hofman and Mostowitsch 1909) and the main crystalline phase involved in the sulfur retention in the combustion waste. A considerable proportion of SO_2/SO_3 would not be emitted into the flue gas at firing temperatures lower than the decomposition temperature of anhydrite. However, the decomposition temperature of anhydrite changes in the presence of other minerals (Mihara et al. 2007). For example, quartz can suppress fouling at low temperatures (Li et al. 2016), but also leads to the formation of calcium silicates at high temperatures when in contact to CaO-bearing minerals. It was found as main component of fouling and slagging deposits (Nankervis and Furlong 1980; Kostakis 2011). Calcium silicates play a major role not only during power plant operation. Wollastonite ($CaSiO_3$) and dicalcium silicates (Ca_2SiO_4) are important minerals for a number of industrial applications. The main applications of wollastonite are in the ceramic and building industry, because of its high melting point, thermal stability, and fluxing characteristics. Due to its acicular structure, wollastonite particularly improves the mechanical properties of building components. Both wollastonite and dicalcium silicate are also cement-relevant phases. For instance, dicalcium silicate is an important ingredient of Portland cement clinker. Other potential applications exist in biomedicine due to its excellent bioactivity (e.g., Mohammadi et al. 2014).

Due to the importance of calcium silicate minerals, numerous sintering experiments with CaO-bearing minerals and quartz have been performed to synthetize wollastonite and dicalcium silicate (e.g., Remy et al. 1997; Rashid et al. 2014). However, none of the experiments, with two exceptions (Stange et al. 2018; Hauke et al. 2019), were carried out in situ as a function of temperature and time. Modern confocal Raman spectrometer systems with integrated heating stages allow the 'visualization' of mineral reactions and textures even at high temperatures with a spatial resolution of a few micrometers (Stange et al. 2018; Hauke et al. 2019). Therefore, it is an exceptional method to in situ follow high-temperature phase transformations and reactions. The advantages of confocal Raman spectroscopy compared to conventional experimental and analytical methods, where the sample has to be quenched to room temperature (RT) before being analyzed, has clearly been demonstrated by Stange et al. (2018). These authors were the first, who have investigated solid–solid reactions in calcite-bearing kaolin during high-temperature sintering by hyperspectral Raman imaging. One important result of their study was that in an in situ experiment calcite decomposition occurred at temperatures below 750 °C, whereas in a quench experiment calcite was still detectable at temperature above 1000 °C, because calcite recrystallized during cooling. A detailed understanding of thermodynamics and kinetics of high-temperature solid-state and melting reactions and thus the mechanism of mineral reactions and transformations is essential to predict sinter reactions in brown coal blocks at a given temperature.

In the present study, samples of anhydrite, gehlenite, and quartz were fired to about 1100 °C and the reactions were analyzed in situ by hyperspectral Raman imaging. The aim was to visualize phase reactions between these minerals and gain kinetic and thermodynamic information about mineral growth and breakdown. In order to use mineral phases as indicators to estimate temperature conditions during the combustion of lignite, it is necessary to understand their reaction behavior at high temperatures. Taking into account all calcium phases that can potentially form during firing, different weight and molar ratios of the raw materials were used for the experiments. Of particular interest was to investigate the formation of wollastonite and dicalcium silicate as a function of the quartz content in the anhydrite-quartz system. The prime questions were: (1) does quartz affect the decomposition behavior of anhydrite, (2) does sulfate promote the crystallization of calcium silicates, (3) does temperature influence the formation of different calcium phases, and (4) does quenching have an effect on the sintering products. Additionally, we aim to demonstrate the power of in situ Raman imaging of high-temperature sintering reactions.

2 Materials and methods

2.1 Sample preparation

To study the influence of composition on the formation temperature of the calcium silicates in the quartz-anhydrite system, several sintering experiments with varying quartz-anhydrite composition ratios were carried out (Table 1). Additionally, gehlenite was added in one experiment to the

Table 1 Experimental conditions

Exp.	Anh:Qtz(:Geh) (wt%)	Type of experiment	T range (°C)	T steps (°C)	T rate (°C/min)	Acquisition time (s)	Dwell time (h)
AQ-1	1:1	in situ	815, 850–1200	50	10 ↗↘	2 × 1	6.5
AQ-2.1	2:1	in situ	500–800, 900–1200	100	10 ↗↘	1 × 0.5	2 × 2 (4)[a]
AQ-2.2	2:1	in situ/quench	900–1200	100	10 ↗↘	1 × 0.5	2 × 2 (4)[a]
AQ-3.1	4.5:1	in situ	950–1250	50	10 ↗↘	1 × 0.5	2 × 2 (4)[a]
AQ-3.2	4.5:1	in situ/quench	900–1200	100	10 ↗; 50 ↘	1 × 0.5	2 × 2 (4)[a]
AQG-1	1:1:1	in situ	450, 900	450	10 ↗↘	1 × 0.5	3 × 2 (6)[a]

[a]During a dwell time of 4 or 6 (AQG-1) h, two respectively three (AQG-1) Raman images with a recording time of about 2 h were recorded

anhydrite-quartz system to study the influence of (1) an additional Ca source and (2) Al added to the system (Table 1: exp. AQG-1). The sample mixtures were prepared from natural crystals of anhydrite, quartz, and gehlenite. These crystals were obtained from the Mineralogical Museum of the University of Bonn, Germany. The anhydrite and gehlenite crystals stem from Tirol, Austria. The origin of the quartz crystal is unknown. Light microscopic images of anhydrite and quartz revealed no contamination of other minerals. The gehlenite, however, was partly overgrown by grossular, which was confirmed by a XRD analysis. The minerals were ground in an agate mortar to obtain different grain sizes between about 20 and 60 µm. Several green bodies were produced by compacting 50 mg of precursor material into cylinders (3 mm × 3 mm) at a pressure of 10 kPa. Before firing, all samples were checked for with the occurrence of initial calcium silicates.

2.2 Raman spectroscopy

The Raman measurements were carried out using a Horiba Scientific HR800 Raman spectrometer equipped with a 2 W Nd:YAG laser (λ = 532.09 nm), an electron-multiplier CCD detector, and an Olympus BX41 microscope. A 50 × long-working distance objective with a numerical aperture (*NA*) of 0.5, a grating with 600 grooves/mm, and a 100 µm spectrometer entrance slit were used for the measurements. The lateral and axial (depth) resolution of a Raman measurements with the focus at the sample surface is usually estimated from the theoretical diffraction limit given by $d_l \approx 1.22\lambda/NA$ and $d_a \approx 4\lambda/NA^2$, yielding 1.3 and 8.5 µm, respectively. However, these values should be understood as the best resolution theoretically possible. The real lateral and axial resolution may rather be in the order of $d_l \approx 2$ µm and $d_a \approx 15$ µm, respectively. It is important to note that the axial resolution at the surface also depends on the absorption properties of the material investigated. A Raman intensity loss of 20% to 40% is observed within the first ten micrometers, whereas within the first 20 µm, which is a typical grain diameter, already about half of the intensity of the Raman bands is lost (Hauke et al. 2019). The spectral resolution was 3.5 cm^{-1}, as given by the line width of a Ne line at 1707.062 cm^{-1} that was recorded as "internal" frequency standard in all spectra. For the sintering experiments, a LINKAM TS 1500 heating stage was mounted on an automated *x*–*y*–*z* stage. Due to the height and the volume of the sample cylinder, a strong temperature gradient occurs within the furnace. This gradient was empirically determined by a procedure that is described in detail in Stange et al. (2018). With this procedure, the corrected temperatures are accurate within ± 5 °C. In the following, the corrected temperatures are given.

In general, in situ hyperspectral Raman images were recorded from an area of 100 µm × 100 µm with a 1 µm step size (100 µm × 100 µm = 10,000 pixel per image) in *x* and *y* direction. The individual Raman spectra were collected during continuous *x*–*y* stage movement with a speed of 2 µm/s (SWIFT© mode). During movement, Raman intensities were recorded for 0.5 s in the wavenumber range from 100 to 1730 cm^{-1}. The total exposure time was about 2 h for a single image. Two types of Raman experiments were performed to study the effect of quenching the sample to room temperature (RT) before Raman imaging. However, experiments AQ-1 and AQ-2.1 were the first experiments that were performed. These experiments contain a few individual trials to figure out the best experimental conditions for further experiments. The experimental conditions of each experiment are

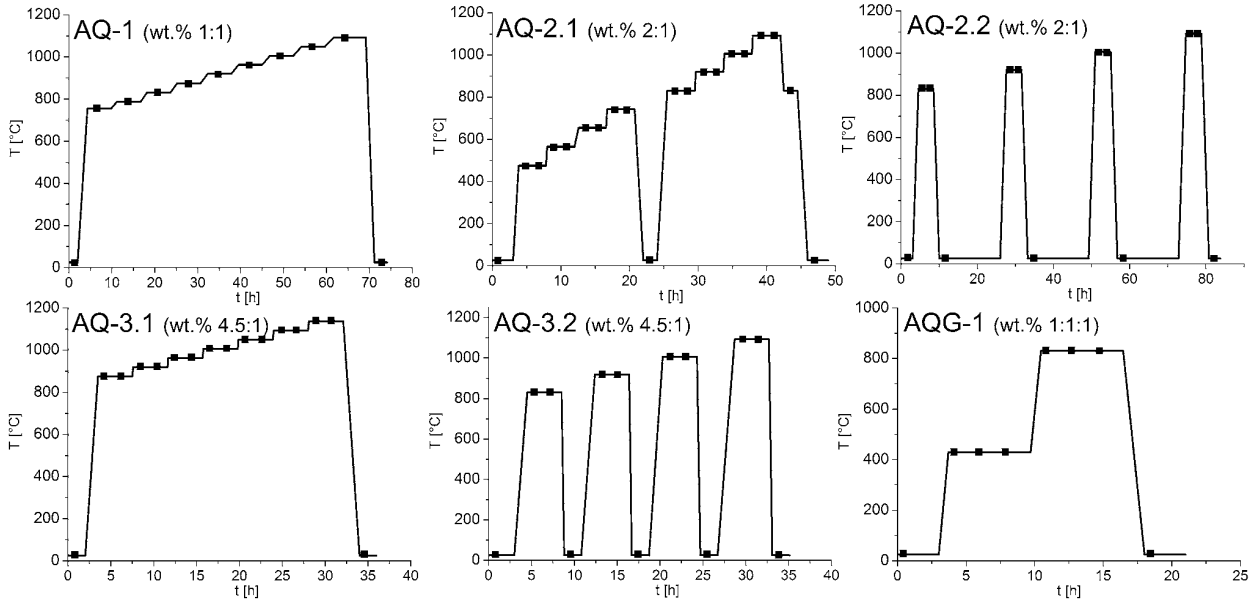

Fig. 1 Temperature histories of the in situ and the in situ/quench experiments. (In the in situ/quench experiments the sample was fired to the sintering temperatures and two hyperspectral Raman images were subsequently recorded. Afterwards the sample was quenched to RT before a last Raman image was recorded. In the in situ experiments, the green bodies were progressively fired to higher temperatures and Raman images were recorded in situ. Squares represent the start of each measurement.)

summarized in Table 1 and the temperature history is illustrated in Fig. 1. In general, at 815 °C lignite is reduced to ash. The first experiment was therefore carried out by firing the sample at 815 ± 5 °C for 2.5 h before a hyperspectral Raman image was recorded with a recording time of about 6.5 h. Afterwards the sample was fired to 850 ± 5 °C and stepwise (50 °C) to 1200 ± 5 °C and finally cooled down to RT. At each temperature step, a Raman image was taken with 2 × 1 s acquisition time for a single pixel of the image. The results of experiment AQ-1 demonstrated that such long single-point acquisition time are not necessary to obtain a sufficient image quality in this system. Therefore, the acquisition time was reduced to 0.5 s per point (pixel) for further experiments. To test whether mineral transformations already take place in the system below about 900 °C, a sample was fired between 500 ± 5 and 800 ± 5 °C in 100 °C-steps and then quenched to RT. Since the images taken in this temperature range revealed no significant mineral changes, further Raman images were recorded above 900 °C only. In the remaining course of experiment AQ-2.1 the sample was fired again to 900 ± 5 °C and further to 1200 ± 5 °C in 100 °C-steps (Fig. 1). At each temperature step a hyperspectral Raman image was recorded. The continuous cooling by 10 °C/min was interrupted at 900 ± 5 °C to record a Raman image. The image revealed no additional information to the images recorded at 1200 ± 5 °C or RT. Thus, the following experiments were quenched directly to RT before taking a hyperspectral Raman image.

As mentioned above, two types of experiments were carried out. During the first type of experiments (in situ/quench experiments), the green body was fired to high temperatures with a heating rate of 10 °C/min. Immediately after reaching the respective temperature, two in situ hyperspectral Raman images were taken in a row. Thus, the second image was recorded after a dwell time of 2 h. Afterwards the sample was quenched to RT with a cooling rate of 10 °C/min before a RT Raman image was recorded. Then, the sample was fired to the next temperature step until the maximum temperature had been reached (Fig. 1). The analysis of the quenched sample corresponds to a conventional sinter experiment during which the sample has to be quenched to RT before being analyzed. In the second type of experiments, the samples were fired to high temperature without quenching the sample. Two subsequent Raman images were taken at each temperature step before the sample was further heated to the next temperature (Fig. 1). After reaching the final temperature, the sample was cooled down to RT and a final Raman image was recorded.

2.3 Data treatment and analysis

In general, mineral phases are identified by the characteristic positions and relative intensities of their fundamental

Raman bands. With increasing temperature, the Raman bands of mineral phases usually shift to lower wavenumbers and their linewidth (full width of half-maximum) increases (e.g., Stange et al. 2018). Additionally, the black body radiation of the sample increases with increasing temperature and thereby progressively reduces the signal-to-noise ratio. The identification of minerals at high temperatures is complicated by the fact that reference Raman spectral databases, such as, e.g., the RRUFF database (Laetsch and Downs 2006), only contain RT spectra that usually differ significantly from their high-temperature (HT) counterparts. Therefore, we started to collect HT Raman spectra of relevant pure mineral phases, including, e.g., quartz, anhydrite, wollastonite, and pseudowollastonite, in order to identify mineral phases in multi-component systems but also for the quantitative phase determination (see below).

The data reduction and creation of hyperspectral false color Raman images was carried out using the LabSpec 6 program. The images show the 2-dimensional, micrometer-scale distribution of mineral phases at a given temperature. The dominant mineral phase in a given Raman spectrum was determined by the classical least-squares (CLS) fitting procedure. This mathematical procedure is based on the assumption that a multiphase spectrum is a simple mixture of spectra of each individual phase (Fig. 2). Mixed spectra are unavoidable due to the limitation in the lateral and, in particular, the depth resolution with respect to the grain sizes. At each point within the multidimensional spectral field, the CLS matching procedure finds a linear combination of reference spectra from the pure phases that best describe the respective raw spectrum. Our own temperature-depend Raman spectra, recorded under the same experimental conditions, were used as input spectra in the CLS fitting procedure to obtain the relative phase proportions, as described in more detail in Stange et al. (2018) and Hauke et al. (2019). This procedure, at least partly, takes into account differences in the Raman cross sections (Hauke et al. 2019). Eventually, the image is generated by coloring each pixel (point) relative to the proportion of individual components in the spectrum. As an example, Fig. 3 shows the HT Raman spectra of anhydrite, quartz, and wollastonite collected at 1090 ± 5 °C, which were used to analyze the image recorded at 1093 ± 5 °C. The false-colored hyperspectral Raman images are presented in the unmixed mode that displays the phase with the highest fractional intensity within a Raman spectrum with a color assigned to that phase (Stange et al. 2018; Hauke et al. 2019). The color shading of a pixel from bright to dark further renders the total fraction of that phase, with bright and dark coding reflecting higher and lower fractions, respectively.

In Fig. 2, creation of a false-color image with the classical least-squares (CLS) fitting method using high-temperature reference spectra of pure phases, collected under the same experimental conditions. This mathematical method is based on the assumption that a multiphase spectrum is a simple mixture of the spectra of each individual phase, here quartz and anhydrite. Quartz (red) is identifiable by its most intense Raman band near 464 cm^{-1} and anhydrite (blue) by the intense $\nu_1(SO_4)$ band near 1015 cm^{-1}.

In Fig. 3, High-temperature (1090 ± 5°) reference Raman spectra of wollastonite, anhydrite, and quartz which were used to generate the hyperspectral Raman image shown in the lower right corner (from exp. AQ-3.1). (Note that each mineral phase can clearly be identified by its characteristic Raman spectrum.)

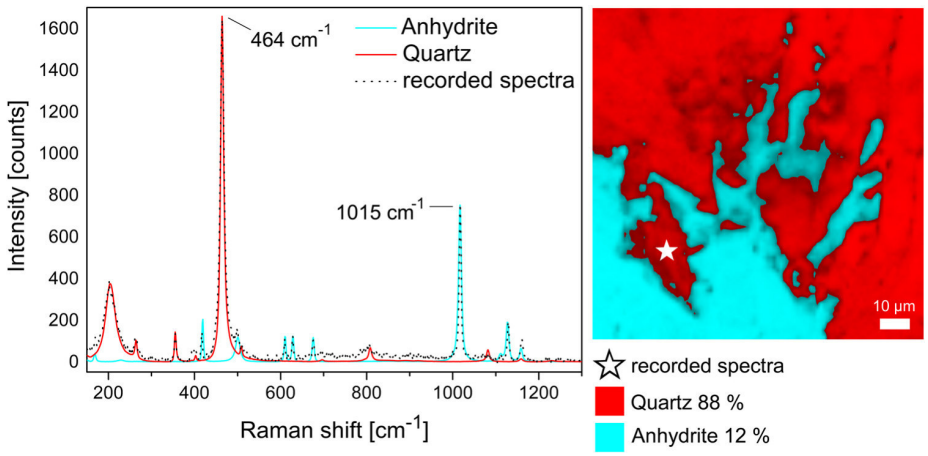

Fig. 2 A false-color image

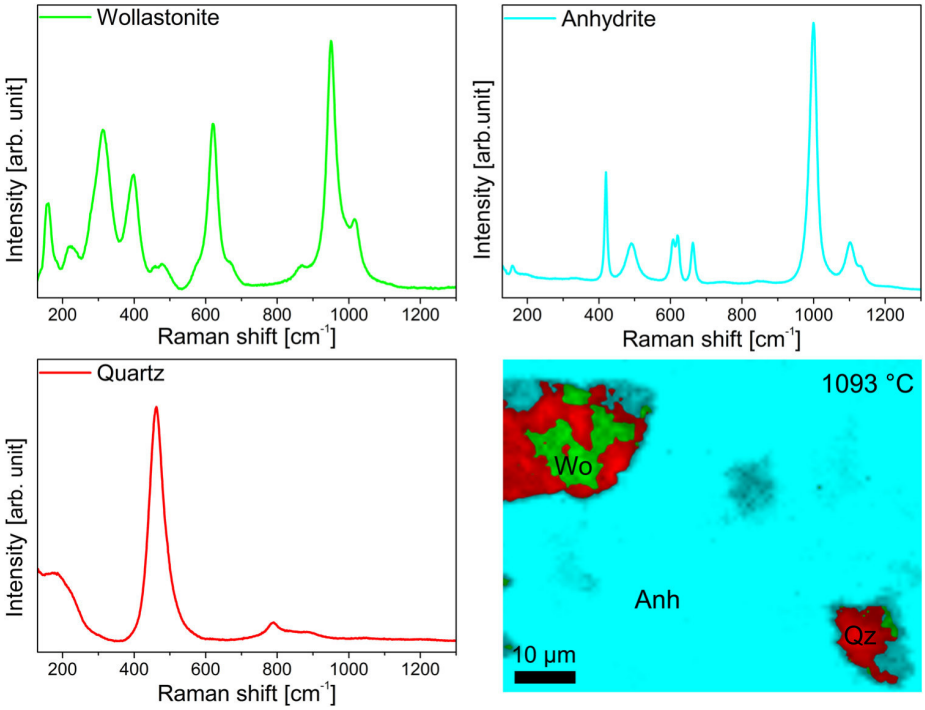

Fig. 3 High-temperature (1090 ± 5 °) reference Raman spectra of wollastonite, anhydrite, and quartz

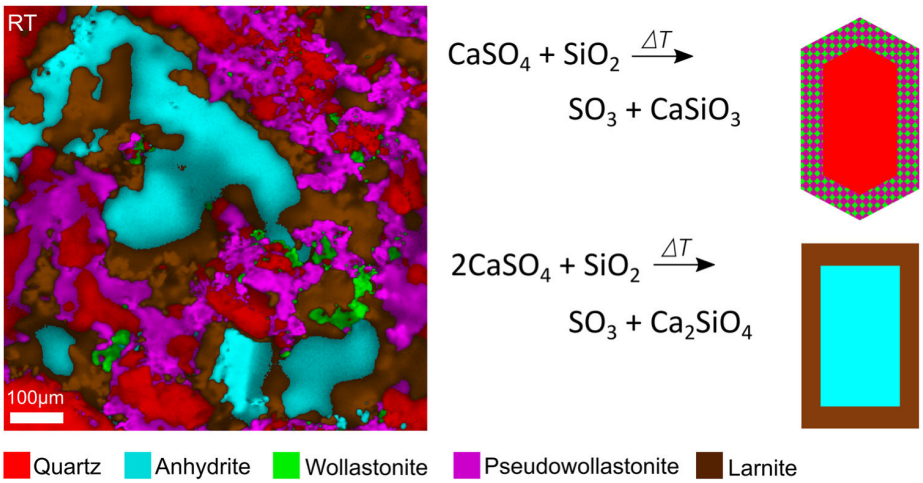

Fig. 4 Normalized false-color hyperspectral Raman images of the in situ experiment AQ-1

3 Results

3.1 In situ experiment AQ-1 (Anh + Qz, wt% 1:1)

Normalized false-color hyperspectral Raman images (not shown here) collected during experiment AQ-1 (Fig. 1a) displays no reaction between anhydrite and quartz within the imaged area up to a temperature of 1093 ± 5 °C. Surprisingly, only after the sample had been cooled down to RT after a total sintering time of 9 h at 1093 ± 5 °C, wollastonite, pseudowollastonite, and the dicalcium silicate larnite were identified as reaction products (Fig. 4). At RT, wollastonite and its high-temperature polymorph pseudowollastonite had formed rims around quartz grains, whereas larnite is located in contact to anhydrite or pseudowollastonite grains. It follows that the new phases must

have crystallized during cooling, since they could not be identified in situ at high temperatures.

In Fig. 4, after 9 h sintering at 1093 ± 5 °C the sample was quenched to RT. Wollastonite and pseudowollastonite crystallized around quartz grains and larnite could be identified as rims around anhydrite and near to pseudowollastonite grains. The two reactions leading to a monocalcium silicate rim around quartz and a dicalcium silicate rim around anhydrite are also given.

3.2 In situ experiment AQ-2.1 and in situ/quench experiment AQ-2.2 (Anh + Qz, wt% 2:1)

The solid-state reactions during experiments AQ-2.1 and AQ-2.2 (higher anhydrite content as AQ-1) were investigated by Raman spectroscopy at sintering-temperatures of up to 1093 ± 5 °C. In exp. AQ-2.1 the 100 µm × 100 µm-sized images were recorded at each temperature step before the sample was fired to the next temperature step (Fig. 1b). Unless otherwise described, there is no change in mineral content at lower temperatures and increasing dwell time. In experiment AQ-2.2 the sample was analyzed at each temperature step and after quenching before firing to the next temperature step (Fig. 1c). From Fig. 5 it is discernable that wollastonite started to crystallize at 919 ± 5 °C while the first image was recorded. With increasing reaction time, more and more wollastonite crystallized by mainly replacing anhydrite. After 2 h at 1093 ± 5 °C rims of wollastonite have formed along anhydrite-quartz interfaces. Furthermore, at this temperature, a new phase with an intense Raman band near 843 cm^{-1} was identified in direct contact to wollastonite. After quenching to RT, larnite could be identified at the same location. Obviously, the high temperature modification of dicalcium silicate α'_L-Ca_2SiO_4 must have formed at 1093 ± 5 °C (Fig. 5). The hyperspectral Raman images of the in situ/quench experiment (AQ-2.2) show that wollastonite crystallized at 919 ± 5 °C at grain boundaries between anhydrite and quartz (Fig. 5), as was already observed in experiment AQ-2.1. Surprisingly, after the second quenching cycle and firing to 1006 ± 5 °C pseudowollastonite crystallized in direct contact to wollastonite (Fig. 6), i.e., at a temperature that is about 120 °C below the wollastonite-pseudowollastonite transition temperature (Osborn and Schairer 1941). After stepwise heating/quenching of the sample to/from higher temperatures, pseudowollastonite continued to grow at the expense of anhydrite. Interestingly, during each cooling/quenching step most though not all pseudowollastonite grains, that were present at high temperatures, seem to be disappeared or were transformed to wollastonite.

In Fig. 5, Normalized false-color hyperspectral Raman images of the in situ experiment AQ-2.1, which were recorded at different temperatures and dwell times. The images display nucleation and isothermal growth of wollastonite at 919 ± 5 °C and the formation of α'_L-dicalcium silicate at 1093 ± 5 °C. During the cooling process, the α'_L-phase transformed to the β-phase (larnite) and remained metastable at RT. The noticeable changes in the texture between 25 ± 1 and 919 ± 5 °C result from volume changes due to mineral reactions or phase transitions, shrinkage and densification processes during firing.

In Fig. 6, at 919 ± 5 °C, wollastonite crystallized between a grain boundary of anhydrite and quartz. Pseudowollastonite could be identified at first after firing the sample to 1006 ± 5 °C and subsequent quenching. At a temperature of 1093 ± 5 °C the pseudowollastonite grains grew further and more and more wollastonite crystallized along anhydrite and quartz interfaces. Both monocalcium silicate polymorphs remained stable at RT.

3.3 In situ experiment AQ-3.1 and in situ/quench experiment AQ-3.2 (Anh + Qz, wt% 4.5:1)

Normalized false-color hyperspectral Raman images (100 µm × 100 µm) were recorded during experiment AQ-3.1 (in situ) and AQ-3.2 (in situ/quench). The anhydrite content of these samples is higher than that in AQ-2.1 and AQ-2.2. In experiment AQ-3.1, the sample was fired to 875 ± 5 °C with a heating rate of 10 °C min^{-1}. Afterwards, the sample was fired stepwise (~ 50 °C-steps) to 1137 ± 5 °C. Within the first image that was recorded at

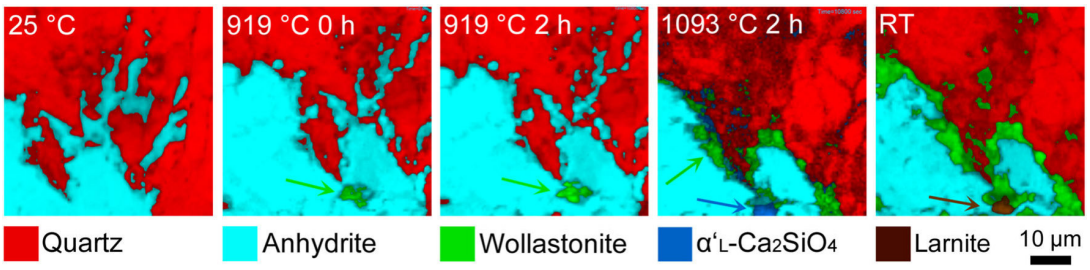

Fig. 5 Normalized false-color hyperspectral Raman images of the in situ experiment AQ-2.1

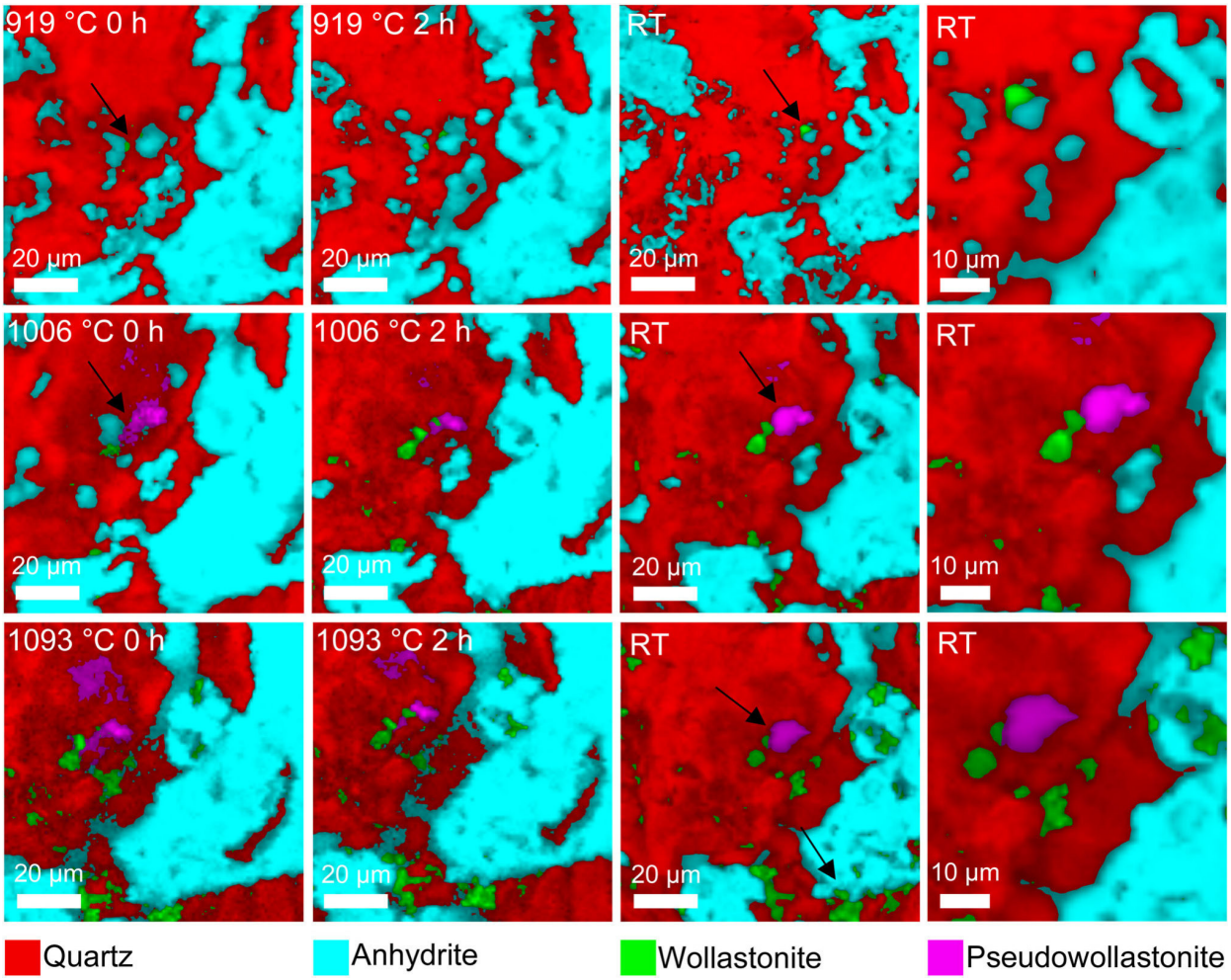

Fig. 6 Normalized false-color hyperspectral Raman images of the in situ/quench experiment AQ-2.2

971 ± 5 °C, a new but still unidentified silicate phase with the most intense Raman band near 750 cm^{-1} is located in contact to a quartz grain (Fig. 7). This phase disappeared at the expense of wollastonite during quenching to RT. Wollastonite could not be detected in situ before having fired the sample to 1006 ± 5 °C, which is nearly 100 °C above the formation temperature that was determined from the experiments with a lower anhydrite content (exp. AQ-2.1/2). At 1137 ± 5 °C, pseudowollastonite could be detected, which transformed to wollastonite during cooling to RT. The results of the in situ/quench experiment (AQ-3.2) confirm the observation that quartz is replaced by wollastonite at high temperatures. The time-series images (not shown here) revealed that wollastonite first formed near to a quartz grain after 2 h sintering at 1006 ± 5 °C. In the further course of the experiment at 1093 ± 5 °C, wollastonite increasingly crystallized at the expense of quartz (Fig. 3).

In Fig. 7, at 960 ± 5 °C, a new, not yet identified silicate phase crystallized, which disappeared after quenching the sample to RT. At 1006 ± 5 °C, wollastonite crystallized near quartz grains and seems to mainly replace anhydrite. At 1037 ± 5 °C, the high-temperature polymorph pseudowollastonite could be identified, which transformed to wollastonite during cooling to RT.

3.4 In situ experiment AQG-1 (Qz + Anh + Ge, wt%: 1:1:1)

To study the potential influence of Al on the sintering reactions in the quartz-anhydrite system, we added natural gehlenite grains to the precursor material. Gehlenite is also a common mineral phase in lignite ashes. The natural gehlenite grains were partly intergrown with grossular crystals, which is another Al source. The pressed sample was continuously fired from 25 ± 1 to 430 ± 5 °C and

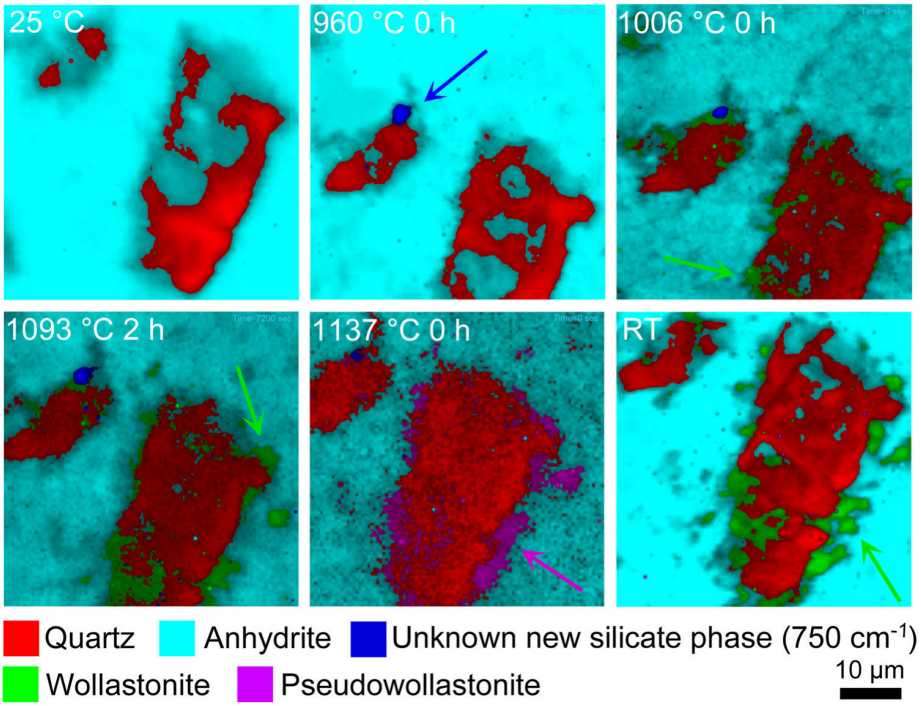

Fig. 7 Normalized false-color hyperspectral Raman images of the in situ experiment AQ-3.1

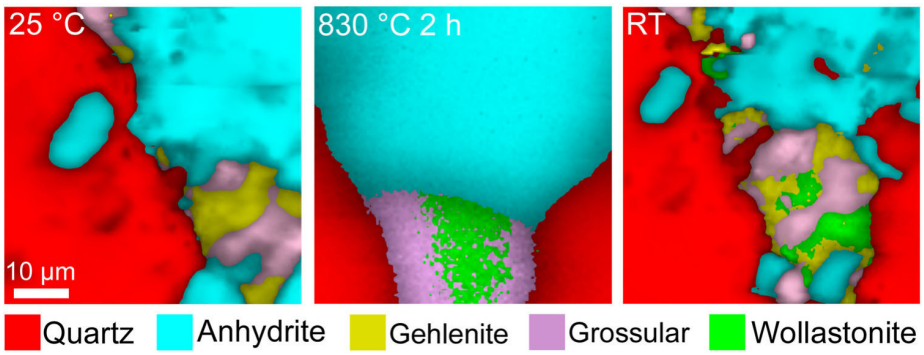

Fig. 8 Normalized false-color hyperspectral Raman images of the in situ experiment AQG-1. (Note that at 830 ± 5 °C wollastonite partly replaced gehlenite and grossular, the latter being an impurity in the natural gehlenite crystal used for the experiment.)

after having subsequently recorded three 100 µm × 100 µm-sized Raman images, the sample was fired further to 830 ± 5 °C (Fig. 1f). The first image was taken immediately after reaching the target temperature, whereas the second and third images were recorded after a dwell time of 2 and 4 h, respectively. The Raman images taken at temperatures below 430 °C did not reveal any textural or mineralogical changes. At 830 ± 5 °C and after a soaking time of about 2 h, gehlenite and grossular were partially replaced by wollastonite (Fig. 8). However, further sintering at this temperature did not cause a progress of the replacement reaction, i.e., a kind of textural equilibrium has been reached that, however, is not a chemical equilibrium.

4 Discussion

4.1 The decomposition of anhydrite

In the binary system quartz-anhydrite, no solid-state reactions or mineral transformations could be detected below about 920 °C within dwell times of 4–6.5 h. The only spectroscopically detectable transformation was the displacive phase transition from low to high quartz at 573 °C.

The reason for this is most likely that the decomposition of pure anhydrite to lime and sulfur oxide, represented by

$$CaSO_4 \overset{T\sim 1100-1400\,^{\circ}C}{\longrightarrow} CaO + SO_3, \quad (1)$$

does not start at temperatures below about 1200 °C (e.g., Hofman and Mostowitsch 1909). Other authors postulated that the β- to α-$CaSO_4$ transformation occurs at this temperature (Bensted and Varma 1971; Prieto-Taboada et al. 2014) and, based on DTA studies, suggested that the decomposition of pure anhydrite does not occur below 1400 °C (Bensted and Varma 1971; Mihara et al. 2007). However, in the present study the crystallization and the growth of wollastonite could be detected in all experiments at temperatures as low as about 920 °C. According to Gay (1965), the decomposition of anhydrite below 1100 °C is only possible within an open system. Other authors, in turn, suggested that the presence of silicate compounds may trigger the decomposition of anhydrite at lower temperatures than pure anhydrite (Mihara et al. 2007). Our results support this hypothesis. In experiments with a high proportion of quartz, wollastonite could be identified at about 920 °C, whereas in experiments with lesser quartz wollastonite first crystallized at about 1100 °C. Thus, the lower the fraction of quartz in the system, the higher the temperature at which wollastonite started to crystallize. It follows that the quartz content affects the decomposition of anhydrite and, in turn, the formation of calcium silicates as discussed in the following.

4.2 The formation of calcium silicates

It is well-known that wollastonite can be synthesized at about 1000 °C by a reaction between quartz and calcite, whereby CO_2 is released into the atmosphere and lime is formed as an intermediate product (e.g., Tschegg et al. 2009). The decomposition of anhydrite also produces lime, which is then available to react with quartz, forming a reaction rim of wollastonite around quartz grains (AQ-1, Fig. 4; AQ-2.1, Fig. 5) or replaced them (AQ-3.1, Fig. 7; AQ-3.2). This reaction can be represented by:

$$CaO + SiO_2 \overset{T\sim 1000\,^{\circ}C}{\longrightarrow} CaSiO_3 \quad (2)$$

At 1125 °C, wollastonite is expected to transform to pseudowollastonite (Osborn and Schairer 1941). In experiment AQ-3.1 the sample was heated to 1137 ± 5 °C and pseudowollastonite bands could indeed be detected in the Raman spectra within the imaged area (volume). However, after quenching to RT, pseudowollastonite transformed to wollastonite. On the other hand, after the second quenching step and having fired the sample to 1006 ± 5 °C, pseudowollastonite could already be identified in direct contact to wollastonite (AQ-2.2, Fig. 6), i.e., significantly below its stability temperature. This is at first surprising, but in agreement with observations made by Stange et al. (2018). These authors also observed the formation of pseudowollastonite already 290 °C below the phase transition temperature during sintering of a kaolin-based green body. After quenching to RT, most pseudowollastonite grains transformed to wollastonite, i.e., only a few small crystals remained metastable at RT. This is in contrast to results from experiment AQ-1. Here, both polymorphs were found as rims around quartz grains after the sample was quenched from 1093 ± 5 °C to RT (Fig. 4).

Within the ternary system anhydrite-quartz-gehlenite (exp. AQG-1), wollastonite was already detected at temperatures below 900 °C. The in situ Raman images recorded at 830 ± 5 °C clearly revealed that gehlenite and grossular were both partly replaced by wollastonite (Fig. 8). It follows that wollastonite formed by a different reaction pathway involving the decomposition of gehlenite, possibly according to following reaction:

$$Ca_2Al(AlSi)O_7 \overset{T\sim 830\,^{\circ}C}{\longrightarrow} CaSiO_3 + CaAl_2O_4 \quad (3)$$

Such reaction would produce a calcium spinel ($CaAl_2O_4$), which, however, has not been detected in our experiments. Unfortunately, spinel is difficult to identify by Raman spectroscopy (Shoval et al. 2011), particular at high temperatures, and we can thus not fully rule out that a calcium spinel formed during the reaction. Alternatively, following decomposition reaction could be possible:

$$Ca_2Al(AlSi)O_7 \overset{T\sim 830\,^{\circ}C}{\longrightarrow} CaSiO_3 + CaO + Al_2O_3 \quad (4)$$

However, thermodynamic calculations using FactSage 7.2 revealed that the free enthalpy of this reaction at 830 °C is about 40 kJ larger than for reaction (3). Thermodynamically, this reaction is thus less favored. In any case, whatever the details of the solid–solid replacement reaction are, a direct formation of wollastonite by the decomposition of gehlenite has so far only been described by Tschegg et al. (2009) and recently observed in situ during sintering of a kaolin-based green body (Stange et al. 2018).

At high quartz content and sintering temperatures of 1093 ± 5 °C, dicalcium silicate was detected (AQ-2.1, Fig. 5). Like wollastonite, dicalcium silicate forms by a reaction between quartz and lime (e.g., Mitsuda et al. 1985; Singh 2006):

$$2CaO + SiO_2 \overset{T\sim 930-1020\,^{\circ}C}{\longrightarrow} Ca_2SiO_4 \quad (5)$$

In experiment AQ-2.1, the high-temperature phase α'_L-Ca_2SiO_4 could be identified. From the time- and temperature-resolved images (Fig. 5), it is apparent that the formation of α'_L-Ca_2SiO_4 is related to the reaction between wollastonite and lime:

$$CaSiO_3 + CaO \overset{T\sim 1100\,^{\circ}C}{\longrightarrow} Ca_2SiO_4 \quad (6)$$

At RT, calcio-olivine is the stable Ca_2SiO_4 polymorph (Fix et al. 1969; Sokol et al. 2015). However, Ca_2SiO_4 formed at 1093 ± 5 °C could be identified as larnite after cooling down to RT by its main fundamental Raman band near 858 cm^{-1} (Remy et al. 1997; Reynard et al. 1997). Although some authors (Fix et al. 1969; Sokol et al. 2015) claimed that β-Ca_2SiO_4 only forms during the cooling process of α'_L-Ca_2SiO_4 and transforms to γ-Ca_2SiO_4 (calcio-olivine) during cooling to RT, obviously larnite remained metastable after quenching the sample from about 1100 °C to RT. The same conclusion can be drawn from the RT data of AQ-1. The Raman images show that larnite formed as reaction rim around anhydrite grains in direct contact to wollastonite, suggesting that larnite formed by reaction (6). On the other hand, rims of dicalcium silicate appear to have reacted with the adjacent quartz to wollastonite (Fig. 5). Stange et al. (2018) also observed wollastonite rims around larnite grains in a quench experiment with a calcite- and quartz-bearing kaolin green body. They referred to a study of Ptácek and co-workers (Ptáček et al. 2013), who suggested that dicalcium silicate reacts with free SiO_2 to wollastonite, which then converts to pseudowollastonite at temperatures above 1125 °C (Ptáček et al. 2013):

$$Ca_2SiO_4 + SiO_2 \overset{T\sim 1025-1050\,^{\circ}C}{\longrightarrow} 2\beta\text{-}CaSiO_3 \overset{T\sim 1125\,^{\circ}C}{\longrightarrow} 2\alpha\text{-}CaSiO_3 \quad (7)$$

It follows that wollastonite cannot only form by a reaction between quartz and lime, but could also be a breakdown product of dicalcium silicate or of gehlenite if Al is present in the system. Which of the reactions is predominant in a given system seems to depend on the local chemistry. The formation of dicalcium silicate at high temperatures, for instance, is more strongly bound to anhydrite as it provides the required CaO (Rashid et al. 2014).

4.3 Quenching effects

To study the influence of quenching on the mineral paragenesis, two in situ/quench experiments with different quartz-anhydrite ratio were performed (AQ-2.2 and AQ-3.2). The in situ/quench experiment with an anhydrite-quartz weight ratio of 2:1 (AQ-2.2) showed mineral reactions other than the corresponding experiment without interim quenching cycles (AQ-2.1). During the in situ experiment (AQ-2.1) α'_L-Ca_2SiO_4 crystallized at the expense of wollastonite and transformed to larnite at RT. However, the Raman images collected during the in situ/quench experiment (AQ-2.2) do not reveal the formation of dicalcium silicate phases, indicating that a long sintering period is needed for the formation of dicalcium silicates to supply more CaO by the decomposition of anhydrite. In both experiments, the onset temperature for the first appearance of wollastonite was about 920 °C. However, in the in situ/quench experiment AQ-2.2 the crystallization of pseudowollastonite could be detected within the imaged area. Here, it was first observed after the second quenching step and after having heated the sample to 1006 ± 5 °C. Pseudowollastonite clearly grew further during the course of the heating/quenching experiment (Fig. 6), but it could not be identified during the in situ experiment AQ-2.1 (Fig. 5). It is possible that quenching triggers the formation of pseudowollastonite that grew to grain sizes larger than 10 µm in the heating/quenching experiment. Quenching seems to considerably affect the formation of pseudowollastonite in samples with an anhydrite-quartz composition of 2:1 (wt%), but had significantly less effects in the experiments with a higher anhydrite-to-quartz ratio of 4.5:1 (AQ-3.1/2). Noticeable here is that more wollastonite crystallized during the in situ run within the images area (volume). However, due to the small analyzed volume (100 µm × 100 µm × ~ 15 µm) that cannot unconditionally be considered as being statistically representative as it contains only a relative small number of particles, any quantitative comparison of the phase composition obtained from different experiments should be rated with care.

5 Conclusion

First high-temperature, in situ Raman experiments with synthetic mixtures of natural anhydrite, quartz, and gehlenite gave new insights into solid-state calcium silicate mineral reactions:

(1) The thermal decomposition of anhydrite to CaO and SO_3 was found to be significantly influenced by the quartz content of the sample. In those experiments, where more quartz was available, anhydrite decomposed at lower temperatures than in experiments with lesser quartz content.
(2) Wollastonite was formed by the reaction between quartz and lime at 920 or 1000 °C depending on the quartz content. In the gehlenite bearing system, wollastonite was found to replace gehlenite at temperatures of > 830 °C. Pseudowollastonite was identified already at 1006 ± 5 °C. At about 1100 °C the crystallization of wollastonite to α'_L-Ca_2SiO_4 was observed. The formation of wollastonite by the reaction of dicalcium silicate with quartz was observed locally after cooling to RT. Accordingly,

three wollastonite-forming reactions could be identified in this study. During the cooling process, α'_L-Ca_2SiO_4 crystallized to β-Ca_2SiO_4 (larnite) and remained metastable at RT.

(3) Quenching and heating periods have a significant effect on the final sintering products.

In general, most high-temperature analyses are studied after quenching the sample to RT. However, valuable information may be lost, since quenching may change the mineralogy and new samples have to be used for each temperature–time step, making it particularly difficult to follow textural changes. Raman spectroscopy is currently the only analytical method to visualize mineral reactions in situ and two dimensions during heating or cooling with a micrometer-scale resolution. This allows the visualization of reactions among individual grains and along grain boundaries. Thus, the mechanisms of solid-state reactions can be investigated with high spatial and temporal resolution and with a high temperature accuracy (± 5 °C). Such spatially resolved in situ studies are essential to refine current thermodynamic and kinetics models that are used to predict HT phase paragenesis or to reconstruct the temperature–time histories of naturally or technically sintered materials, e.g. in brown coal blocks. In this way, the mineral paragenesis of sintering crusts in brown coal blocks can be used as temperature indicator to unravel the actual combustion temperature of lignite. With reference to the available results, the use of quartz-rich coal leads to a premature decomposition of anhydrite and the formation of calcium silicates. It is apparent from our results that realistic modelling of HT sintering reactions has to consider the full energy landscape of a system that also includes metastable energy states.

Acknowledgements Many thanks go to T. Schulz for the technical support with the heating stage. We further would like to thank A. Zacke and D. Vlcék of the Mineralogical Museum, University Bonn, for providing the minerals. Financial support by the RWE Power AG is gratefully acknowledged. This work was financially supported by the RWE Power AG, Kraftwerk Niederaußem, Bergheim, Germany.

References

Bensted J, Varma SP (1971) Infrared spectroscopic studies of calcium sulphate heated to high temperatures. Z Naturforsch 26b:690–693

Fix W, Heymann H, Heinke R (1969) Subsolidous relations in the system $2CaO{\cdot}SiO_2$–$3CaO{\cdot}P_2O_5$. J Am Ceram Soc 52:346–347

Gay P (1965) Some crystallographic studies in the system $CaSO_4$–$CaSO_4{\cdot}2H_20$ I. The polymorphism of anhydrous $CaSO_4$. Mineral Mag 270:347–353

Hauke K, Kehren J, Böhme N, Zimmer S, Geisler T (2019) In situ hyperspectral Raman imaging: a new method to investigate sintering processes of ceramic material at high temperature. Appl Sci 9:1–23. https://doi.org/10.3390/app9071310

Hofman HO, Mostowitsch W (1909) The behavior of calcium sulfate at elevated temperatures with some fluxes. Trans Am Inst Min Metall Eng 32:628–653

Kostakis G (2011) Mineralogical composition of boiler fouling and slagging deposits and their relation to fly ashes: the case of Kardia power plant. J Hazard Mater 185:1012–1018. https://doi.org/10.1016/j.jhazmat.2010.10.006

Laetsch T, Downs R (2006) Software for identification and refinement of cell parameters from powder diffraction data of minerals using the RRUFF project and American Mineralogist crystal structure databases. Abstracts from 19th general meeting of the International Mineralogical Association in Kobe, Japan

Li J, Zhu M, Zhang Z, Zhang K, Shen G, Zhang D (2016) The mineralogy, morphology and sintering characteristics of ash deposits on a probe at different temperatures during combustion of blends of Zhundong lignite and a bituminous coal in a drop tube furnace. Fuel Process Technol 149:176–186. https://doi.org/10.1016/j.fuproc.2016.04.021

Li J, Zhu M, Zhang Z, Zhang K, Shen G, Zhang D (2017) Stratification and chemistry evolution of ash deposits during combustion of Zhundong lignite in a drop tube furnace. Energy Procedia 105:4216–4221. https://doi.org/10.1016/j.egypro.2017.03.904

Mihara N, Kuchar D, Kojima Y, Matsuda H (2007) Reductive decomposition of waste gypsum with SiO_2, Al_2O_3, and Fe_2O_3 additives. J Mater Cycles Waste Manag 1:21–26

Mitsuda T, Asami J, Matsubara Y, Toraya H (1985) Hydrothermal formation of γ-dicalcium silicate from lime-silica mixt. Cem Concr Res 15:613–621

Mohammadi H, Hafezi M, Nezafati N, Heasarki S, Nadernezhad A, Ghazanfari SMH (2014) Bioinorganics in bioactive calcium silicate ceramics for bone tissue repair: bioactivity and biological properties. J Ceram Sci Technol 5:1–12. https://doi.org/10.4416/JCST2013-00027

Nankervis JC, Furlong RB (1980) Phase changes in mineral matter of North Dakota lignites caused by heating to 1200°C. Fuel 59:425–430. https://doi.org/10.1016/0016-2361(80)90196-9

Osborn EF, Schairer JF (1941) The ternary system pseudowollastonite–akermanite–gehlenite. Am J Sci 239:715–763

Prieto-Taboada N, Gómez-Laserna O, Martínez-Arkarazo I, Olazabal MÁ, Madariaga JM (2014) Raman Spectra of the different phases in the $CaSO_4$–H_2O system. Anal Chem 86:10131–10137. https://doi.org/10.1021/ac501932f

Ptáček P, Opravil T, Šoukal F, Havlica J, Holešinský R (2013) Kinetics and mechanism of formation of gehlenite, Al–Si spinel and anorthite from the mixture of kaolinite and calcite. Solid State Sci 26:53–58. https://doi.org/10.1016/j.solidstatesciences.2013.09.014

Rashid AR, Shamsudin R, Hamid MAA, Jalar A (2014) Low temperature production of wollastonite from limestone and silica sand through solid-state reaction. J Asian Ceram Soc 2:77–81. https://doi.org/10.1016/j.jascer.2014.01.010

Remy C, Reynard B, Madon M (1997) Raman spectroscopic investigations of dicalcium silicate: polymorphs and high-temperature phase transformations. J Am Ceram Soc 80:413–423. https://doi.org/10.1111/j.1151-2916.1997.tb02846.x

Reynard B, Remy C, Takir F (1997) High-pressure Raman spectroscopic study of Mn_2GeO_4, Ca_2GeO_4, Ca_2SiO_4, and $CaMgGeO_4$ olivines. Phys Chem Miner 24:77–84. https://doi.org/10.1007/s002690050019

Shoval S, Boudeulle M, Panczer G (2011) Identification of the thermal phases in firing of kaolinite to mullite by using micro-Raman spectroscopy and curve-fitting. Opt Mater 34:404–409. https://doi.org/10.1016/j.optmat.2011.08.031

Singh NB (2006) Hydrothermal synthesis of β-dicalcium silicate (β-Ca_2SiO_4). Prog Cryst Growth Charact Mater 52:77–83. https://doi.org/10.1016/j.pcrysgrow.2006.03.011

Sokol EV, Seryotkin YV, Kokh SN, Vapnik Y, Nigmatulina EN, Goryainov SV (2015) Flamite, (Ca, Na, K)2(Si, P)O4, a new mineral from ultrahightemperature combustion metamorphic rocks, Hatrurim Basin, Negev Desert, Israel. Mineral Mag 79:583–596. https://doi.org/10.1180/minmag.2015.079.3.05

Stange K, Lenting C, Geisler T (2018) Insights into the evolution of carbonate-bearing kaolin during sintering revealed by in situ hyperspectral Raman imaging. J Am Ceram Soc 101:897–910. https://doi.org/10.1111/jace.15209

Tschegg C, Ntaflos T, Hein I (2009) Thermally triggered two-stage reaction of carbonates and clay during ceramic firing—a case study on Bronze Age Cypriot ceramics. Appl Clay Sci 43:69–78. https://doi.org/10.1016/j.clay.2008.07.029

Vuthaluru HB, Zhang DK (2001) Effect of Ca- and Mg-bearing minerals on particle agglomeration defluidization during fluidized-bed combustion of a South Australian lignite. Fuel Process Technol 69:13–27. https://doi.org/10.1016/S0378-3820(00)00129-6

EPILOGUE and ADDITIONAL STUDIES

The presented high-temperature, in situ and in situ/quench Raman experiments with synthetic mixtures of anhydrite and quartz provide new insights into solid-state calcium silicate mineral reactions. The most important result is that the quartz content was found to play a significant role in the formation of calcium silicates. The higher the quartz content, the lower the decomposition temperature of the anhydrite (~920 °C) at which the formation of wollastonite occurs simultaneously by the reaction between quartz and lime. The formation of pseudowollastonite was identified within an in situ/quench experiment already at ~1005 °C, i.e., about 120 °C below the wollastonite-pseudowollastonite transition temperature [49], suggesting that quenching may trigger the formation of pseudowollastonite and, therefore, quenching and heating periods have a significant effect on the final sintered products. At ~1100 °C the crystallization of wollastonite to α'_L-Ca_2SiO_4 was observed, which transformed to β-Ca_2SiO_4 (larnite) during cooling and remained metastable at RT. Additionally, two further wollastonite-forming reactions could be identified in this study. The formation of wollastonite by the reaction of dicalcium silicate with quartz was observed locally after cooling to RT. Moreover, one first experiment was carried out with additional gehlenite, where wollastonite was found to replace gehlenite at temperatures of < 830 °C.

As a supplement to the presented publication *"In situ Raman imaging of high-temperature solid-state reactions in the $CaSO_4$–SiO_2 system"* [48], a second experiment with an anhydrite-, quartz-, and gehlenite-bearing green body (wt.-% 1:1:1) was performed to study the solid-state reactions during heating (10 °C/min) between ~655 and ~1100 °C in ~50 °C-steps and after cooling (10 °C/min) to RT. Figure 11 shows the hyperspectral Raman images of the experiment AQG-2, which were recorded after a dwell time of two hours. Interestingly, in regions with a high quartz content, anhydrite began to partially decompose already at 655 ± 5 °C. SO_3 and CaO were released, leaving CaO available for the formation of new mono- or dicalcium silicate by the reaction with quartz. In contrast to the experiments carried out with a quartz-anhydrite ratio 2:1 (wt.-%), a higher CaO content provided by the decomposition of anhydrite preferentially led to the formation of the high-temperature polymorph α'_L-Ca_2SiO_4. Moreover, the high-temperature modification pseudowollastonite crystallized contemporaneously to wollastonite in contact with quartz and α'_L-Ca_2SiO_4, which is in good agreement with previous observations [26]. Between 699 and 919 ± 5 °C, the fraction of dicalcium silicate near quartz continued to increase, especially in contact with the large quartz grain in the upper part of the imaged area, while CaO decreased, i.e., was replaced by α'_L-Ca_2SiO_4. In the same temperature range, only some new wollastonite grains grew at interfaces between quartz and lime. It follows that the formation of calcium silicate strongly depends on the local chemistry.

At a higher temperature (~830 °C), pseudowollastonite was clearly identified near gehlenite. With increasing temperature and dwell time, more pseudowollastonite crystallized at the expense of gehlenite and quartz. This result agrees with observations made by Stange et al. [26], who identified pseudowollastonite in contact with gehlenite, wollastonite, and quartz during sintering of a kaolin-based green body ~290 °C below the expected critical temperature for the wollastonite-pseudowollastonite transition (~1125 °C [49]). Upon quenching to RT, the pseudowollastonite almost completely transformed to wollastonite in this experiment.

Between 919 and 963 ± 5 °C, more gehlenite becomes visible at the sample surface due to the disappearance of CaO. Obviously, however, enough CaO remained in the matrix, which facilitated the formation of new anhydrite during quenching to RT by the reaction with SO_3 from the captured atmosphere. Alternatively, the CaO was supplied by the decomposition of gehlenite. At the same time, new wollastonite nuclei were formed in the gehlenite matrix. At 963 ± 5 °C, the transformation of α'_L-Ca_2SiO_4 to wollastonite occurred by replacing the large quartz grain, which was previously only

observed after quenching (in situ exp. AQ-1) and described by the reaction between dicalcium silicate and free quartz [26,50]. Although the imaged area shifted during the measurement process, the continued transformation could be followed until the maximum sintering temperature (1093 ± 5 °C) was reached (images are not shown here). At RT, wollastonite was identified as predominant mineral phase in the gehlenite matrix, previously formed at high temperatures by all three formation reaction pathways reported in the presented publication [48].

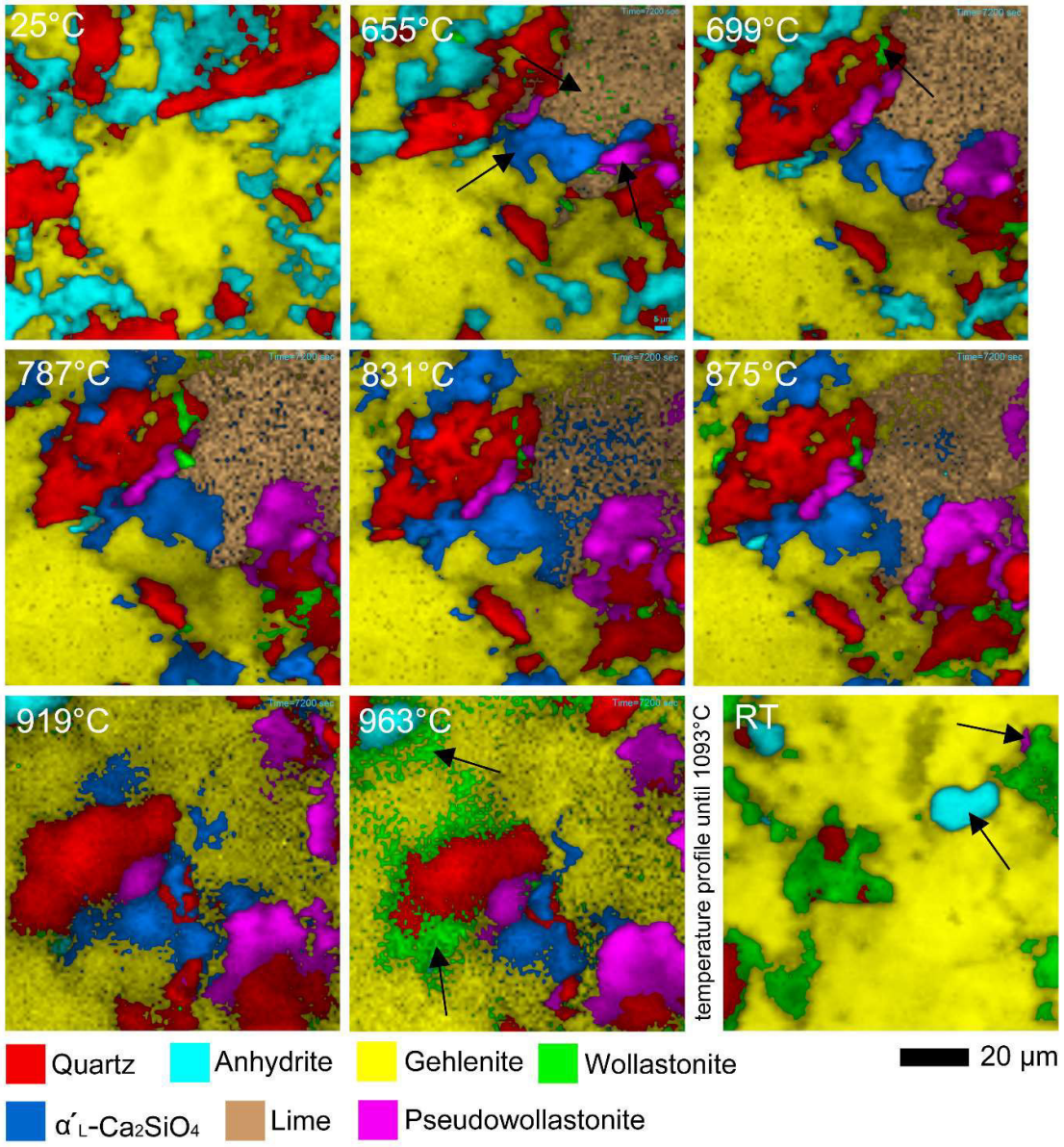

Figure 11: Normalized false-color hyperspectral Raman images of the mineral distribution of a 100 x 100 µm² surface area of a green body composed of gehlenite, anhydrite, and quartz at different sintering temperatures (in situ exp. AQG-2). The black arrows point to the location of the predominant mineral reactions that can be derived from the images. At 655 °C, anhydrite started to decompose and CaO was released. Depending on the local CaO supply, pseudo-/wollastonite or α'$_L$-Ca_2SiO_4 was formed by the reaction between CaO and quartz. Note that two additional formation reactions of wollastonite were identified. At 963 °C, α'$_L$-Ca_2SiO_4 transformed to wollastonite by the reaction with quartz, while at the same temperature step wollastonite was identified within the gehlenite matrix. During cooling, pseudowollastonite transformed to wollastonite but partially remained stable at RT.

3 In Situ Hyperspectral Raman Imaging of Ternesite Formation and Decomposition at High Temperatures

PREFACE and ADDITIONAL STUDIES

Based on the previous analyses, in the second study, CaO (lime) was added to the $CaSO_4$-SiO_2 system. The aim was to detect differences in the reaction pathways of the previously observed calcium silicate reactions when free CaO is available at the beginning of the sintering experiments. In addition, the study of the formation of ternesite ($Ca_5(SiO_4)_2SO_4$) was the main focus of the second study. Like the calcium silicates described in the first study, ternesite also forms sinter deposits in industrial furnaces [51]. Figure 12 shows a sinter deposit found on a heat transfer surface in a coal power plant within the transition zone from the silicate slagging zone of the combustion chamber to the sulfate sintering zone of the bundle heating surfaces.

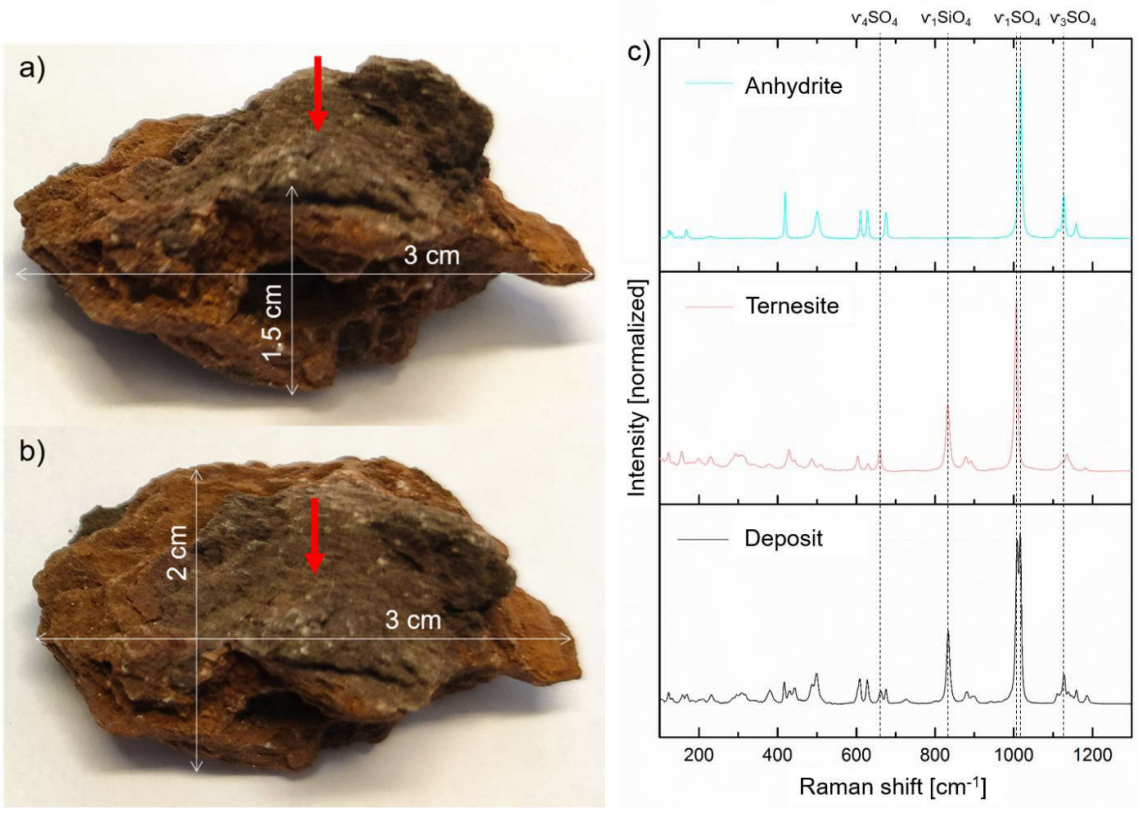

Figure 12: (a) Front view and (b) top view of the same fragment which was deposited on a heat transfer surface of a brown coal power plant. The red arrows mark the analytical point of the Raman study (laser power: 0.4 W, acq. time: 50 s) presented in (c). The Raman spectrum identifies anhydrite and ternesite by the characteristic stretching and bending modes of the SO_4 and SiO_4 tetrahedra, respectively.

The deposit (3 cm x 2 cm x 1.5 cm) consists of a brownish and a black layer. It appears that the brownish layer was formed first and the black material that was examined with Raman spectroscopy was deposited afterwards. The red arrows mark the location of the measurement. A quantitative XRD analysis of the powdered total material revealed a composition of about 26 vol.-% anhydrite, 25 vol.-% ternesite, 15 vol.-% amorphous fraction, and 30 vol.-% Fe/Mg compounds. The Raman spectroscopic analysis identified ternesite and anhydrite in the black material due to the characteristic stretching and bending modes of the SO_4 and SiO_4 tetrahedra, respectively (Figure 12c). In order to study the deposit in detail, a 30 x 100 μm^2 surface area near the location of the single measurement was analyzed by hyperspectral Raman imaging. Figure 13 shows the distribution patterns of ternesite and anhydrite within the measured area, whereby a blue and red color symbolizes a low and high content, respectively. The corresponding false-color Raman image shows that the ternesite grains are surrounded by an anhydrite matrix, indicating that the formation of ternesite was accompanied by the onset of anhydrite decomposition. In this way, ternesite traps sulfur oxides that are released, for example, during the decomposition of anhydrite during the combustion process of lignite.

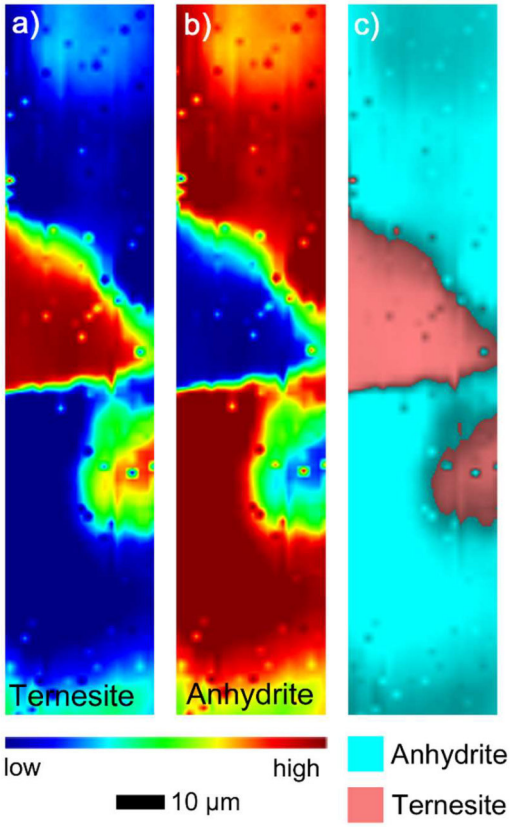

Figure 13: Distribution pattern of (a) ternesite and (b) anhydrite within a 30 x 100 µm² surface area of the deposit. Blue color symbolizes a low content and red color symbolizes a high content. (c) The corresponding normalized false-color hyperspectral Raman image.

Another environmental aspect is that ternesite plays a key role in a new innovative, low-carbon clinker technology [13]. Due to its lower firing temperature, the CO_2 emissions of the belite calciumsulfo-aluminate ternesite (BCT) clinker can be reduced compared to those of conventional clinker production. Thus, knowledge of the high-temperature properties of ternesite is important to industry in several ways. A detailed understanding of the thermodynamics and kinetics of HT solid-state and melting reactions within the $CaO\text{-}SiO_2\text{-}CaSO_4$ system as well as the HT processes of pure ternesite is essential to fully exploit the technical advantages of ternesite. Using in situ Raman spectroscopy, the thermal behavior of both the pure and the multi-phase system was investigated and presented in the following publication.

The following publication is reprinted from "Böhme N, Hauke K, Neuroth M, Geisler T. In Situ Hyperspectral Raman Imaging of Ternesite Formation and Decomposition at High Temperatures. *Minerals* **2020,** 10, 287" [52].

(Editor's choice article)

Author contributions:

The planning of the experiments, the procurement of the sample material, and all Raman measurements were performed by Nadine Böhme. Data processing and analysis were performed by Nadine Böhme, Kerstin Hauke, and Thorsten Geisler. In addition, literature research and the preparation of the original draft were done by Nadine Böhme with the assistance of Kerstin Hauke. Manuela Neuroth provided information on high-temperature mineral reactions during coal combustion. Thorsten Geisler commented and proofread the manuscript, while all authors contributed to the final version of the manuscript. All co-authors agree to the use of the publications for this dissertation and to the identification of the doctoral student's contribution.

minerals

MDPI

Article

In Situ Hyperspectral Raman Imaging of Ternesite Formation and Decomposition at High Temperatures

Nadine Böhme [1,*], Kerstin Hauke [1], Manuela Neuroth [2] and Thorsten Geisler [1]

[1] Institut für Geowissenschaften, Universität Bonn, 53115 Bonn, Germany; kerstinhauke@uni-bonn.de (K.H.); tgeisler@uni-bonn.de (T.G.)

[2] RWE Power AG, Research and Development, Kraftwerk Niederaußem, 50129 Bergheim, Germany; m.neuroth@rwe.com

* Correspondence: nadine.boehme@uni-bonn.de

Received: 8 February 2020; Accepted: 19 March 2020; Published: 21 March 2020

Abstract: Knowledge of the high-temperature properties of ternesite ($Ca_5(SiO_4)_2SO_4$) is becoming increasingly interesting for industry in different ways. On the one hand, the high-temperature product has recently been observed to have cementitious properties. Therefore, its formation and hydration characteristics have become an important field of research in the cement industry. On the other hand, it forms as sinter deposits in industrial kilns, where it can create serious problems during kiln operation. Here, we present two highlights of in situ Raman spectroscopic experiments that were designed to study the high-temperature stability of ternesite. First, the spectra of a natural ternesite crystal were recorded from 25 to 1230 °C, which revealed a phase transformation of ternesite to the high-temperature polymorph of dicalcium silicate (α'_L-Ca_2SiO_4), while the sulfur is degassed. With a heating rate of 10 °C/h, the transformation started at about 730 °C and was completed at 1120 °C. Using in situ hyperspectral Raman imaging with a micrometer-scale spatial resolution, we were able to monitor the solid-state reactions and, in particular, the formation properties of ternesite in the model system CaO-SiO_2-$CaSO_4$. In these multi-phase experiments, ternesite was found to be stable between 930 to 1020–1100 °C. Both ternesite and α'_L-Ca_2SiO_4 were found to co-exist at high temperatures. Furthermore, the results of the experiments indicate that whether or not ternesite or dicalcium silicate crystallizes during quenching to room temperature depends on the reaction progress and possibly on the gas fugacity and composition in the furnace.

Keywords: ternesite; dicalcium silicate; calcium sulfate; high-temperature; in situ; Raman imaging

1. Introduction

Ternesite ($Ca_5(SiO_4)_2SO_4$) has only been described so far from three localities worldwide (Mayen, Germany [1]; Negev Desert, Israel; and Judean Mts, Palestine [2]). It is isotypic to silicocarnotite ($Ca_5(PO_4)_2SiO_4$) [2] and a number of other compounds, where Cd and Ge substituted Ca and Si, respectively [1]. Thus, the ternesite structure is able to accommodate various chemical partners and may be stable under a wide range of thermal conditions [3]. The high-temperature (HT) behavior of ternesite has gained increasing interest in industry over the last few years. Ternesite has been identified as deposits in cement rotary kilns [4,5] as well as on heat transfer surfaces in brown coal power plants within the transition zone from the silicate slagging zone of the combustion chamber to the sulfate sintering zone of the bundle heating surfaces [6]. Here, the formation temperatures seem to correspond to those estimated for natural ternesite that occurs in metamorphosed volcanic rocks, with estimated formation temperatures between 1000 to 1300 °C [1,7]. In natural and synthetic occurrences, ternesite is commonly associated with dicalcium silicate (larnite or belite, respectively).

In recent work, a new innovative low-carbon-emission clinker technology has been described in which ternesite plays a key role [3,8–12]. The so-called belite calciumsulfoaluminate ternesite (BCT) technology combines the early age strength of calcium sulfoaluminate cements with the durability of belite-bearing cements. In this system, ternesite bridges the reactivity gap between the rapid aluminate reaction and the late strength development of belite. Due to its lower firing temperature, the CO_2 emissions of the BCT clinker can be reduced compared to those of conventional clinker production. Yet, another environmental aspect during the combustion of brown coal is that ternesite fixes sulfur oxides during coal combustion process that is released, for instance, by the decomposition of anhydrite (~1200 °C [13]), which occurs already at temperatures as low as about 920 °C if other mineral phases are present [14,15].

It follows that a detailed understanding of the thermodynamics and kinetics of HT solid-state and melting reactions within the CaO-SiO_2-$CaSO_4$ system is essential in order to fully exploit the technical advantages of ternesite. In particular, ternesite can serve as a temperature indicator once its thermal stability field is known, which can help kiln operators to optimize the combustion temperatures. In the present study, samples of calcium oxide, quartz, and anhydrite were fired to about 1100 °C and the reactions were monitored in situ by confocal hyperspectral Raman imaging, which allowed monitoring of the HT solid–solid reactions at the micrometer scale without the need to quench the sample to room temperature (RT) before analyzing it [15–17]. However, before performing the multiphase sinter experiments, we studied the thermal behavior of a natural ternesite crystal between RT and 1230 °C in 10 °C-steps by Raman spectroscopy. The results of this experiment are also used to provide HT reference Raman spectra that are necessary for hyperspectral Raman image generation.

2. Materials and Methods

2.1. Characterization of the Starting Materials and Sample Preparation

To study the temperature behavior of ternesite by Raman spectroscopy, a natural blue crystal aggregate from Mayen, Germany, was used. The sample was prepared to a cylinder with a diameter of 3 mm and a height of <1 mm to minimize the temperature gradient between sample surface and thermocouple. The chemical composition of the sample was determined by electron microprobe on a polished section using a JEOL 8200 Superprobe (JEOL, Ltd., Tokyo, Japan) at the Institute of Geosciences of the University of Bonn, Bonn, Germany. The acceleration voltage and beam current were set to 15 keV and 15 nA, respectively. The Kα-lines of Ca, Si, and S were measured along with the background at both sides of the peaks for 10 s. Wavelength- and energy-dispersive X-ray scans revealed that the ternesite does not contain any other elements in significant amounts (>100 ppm). The average composition of 88 individual spot analyses (Table 1) agrees very well with results from previous work [1].

Table 1. Summary of 88 electron microprobe analyses of the ternesite sample used in this study compared with results of Irran et al. [1].

Oxides	Range [1] (wt.%)	Average [1] (wt.%)	Range [This Study] (wt.%)	Average [This Study] (wt.%)
CaO	57.32–60.35	58.90 ± 0.83	57.69–59.21	58.50 ± 0.28
SiO_2	23.05–27.23	25.22 ± 1.28	24.57–25.79	25.13 ± 0.28
SO_3	13.80–18.04	16.34 ± 1.25	15.21–17.02	16.27 ± 0.34

The sinter experiments were carried out with small green bodies that were produced by compacting 40 mg of powdered precursor material into cylinders (3 mm × 2.7 mm) at a pressure of 10 kPa to produce a flat surface. The cylinders were prepared from natural crystals of anhydrite (Tirol, Austria), quartz (origin unknown), and CaO powder (©Merck, Darmstadt, Germany). Before firing, all cylinders were checked for the occurrence of initial calcium silicates/sulfates and potential contaminations

by ultra-fast Raman imaging (see Section 2.2) and XRD measurements using a Bruker D4 powder diffractometer (Bruker, Madison, WI, USA) at the RWE Power AG, Niederaußem, Germany. Although the CaO was stored in a furnace at 100 °C before usage, a few calcite grains could be detected, which, however, decomposed to CaO during the experiments.

2.2. Experimental Details

To study the formation temperature of ternesite in the CaO-SiO_2-$CaSO_4$ system, an isochronal single crystal heating and three sintering experiments were carried out to temperatures of up to 1104 ± 5 °C (Table 2). A LINKAM TS 1500 heating stage (volume size ~20 mm^2) was used for the experiments that was mounted onto the automated *x*-*y*-*z* stage below the microscope objective of the Raman microscope. Due to the height and the volume of the sample cylinder, a strong temperature gradient unavoidably occurs within the furnace. This gradient was empirically determined by a procedure that is described in detail by Stange and co-workers [17].

Table 2. Experimental conditions.

Exp.	Anh:Qtz:CaO (mol ratio)	Type of Experiment	T_{range} (°C)	T_{steps} (°C)	T_{rate} (°C/min)	Acquisition Time (s)	Recording Time (h)
Ternesite		in situ	30–1230	10	10 ↗↘	100 s	–
AQC-1.1	1:2:4	in situ	927–1104	~50	10 ↗↘	0.5	2 × 2 (4) *
AQC-1.2	1:2:4	in situ	659–1104	~50	10 ↗↘	0.5	2 × 2 (4) *
AQC-2	1:2:4	in situ/quench	838–1104	~50	10 ↗↘	0.5	2 × 2 (4) *

* During a dwell time of 4 h, two Raman images with a recording time of about 2 h were recorded.

Two types of experiments were performed in air atmosphere (Table 2). During the first type of in situ experiments (AQC-1.1/2), the samples were fired to a high temperature with a heating rate of 10 °C/min. Immediately after reaching the respective temperature, two in situ hyperspectral Raman images were taken in succession. Thus, the second image was recorded after a dwell time of two hours. Then, the sample was fired and measured in 50 °C steps until the maximum temperature had been reached. After recording the last image at the maximum temperature, the sample was cooled down to RT with a cooling rate of 10 °C/min and a final Raman image was recorded at RT. In the second type of in situ experiments (AQC-2), the effect of quenching was studied. After recording a Raman image at the firing temperature, the sample was cooled to RT with a cooling rate of 10 °C/min. At RT, a'Raman image was then recorded, before firing the sample to the next temperature step. We note that the images taken at RT form the basis for the interpretation of conventional sintering experiments, in which the sample has to be quenched before it can be analyzed.

2.3. Raman Spectroscopy

All Raman measurements were carried out using a Horiba Scientific HR800 Raman spectrometer (Horiba Scientific, Kyōto, Japan) at the Institute of Geosciences of the University of Bonn, Born, Germany. The instrument is equipped with a 2W Nd:YAG laser (λ= 532.09 nm), an electron-multiplier charge-coupled device (CCD) detector, and an Olympus BX41 microscope. A 50x long-working distance objective with a numerical aperture (NA) of 0.5, a grating with 600 grooves/mm, and a 100-µm spectrometer entrance slit were used for all measurements. The spectral resolution of all measurements was ~3.5 cm^{-1}, as given by the width of the intense Ne line at 1707.06 cm^{-1}. To correct for any spectrometer shift during long-time measurements, the intense Ne line was continuously monitored as "internal" frequency standard in all spectra [14,17,18]. An edge-filter was used to remove the Rayleigh signal. Single crystal spectra were acquired for 100 s. In situ hyperspectral Raman images were recorded from an area of 100 × 100 $µm^2$ with a 1-µm step size (100 × 100 $µm^2$ = 10,000 pixel per image) in *x* and *y* direction. At each step, a Raman spectrum was recorded for 0.5 s. Due to temperature- or reaction related shrinkage- or expansion effects, the sampling area can strongly shift during cooling. Therefore, at HT, 100 × 100-$µm^2$-sized images were

taken, and, at RT, larger 140 × 140-µm^2-sized images were taken, so that the same area could be investigated at all temperature steps. The focus was reset before each image was taken in order to compensate for these effects using the autofocus function of the instrument. This procedure is based on the depth profiling of the intensity of a spectral range and determines the focus through the highest signal-to-noise ratio.

The best achievable the lateral and axial (depth) resolution of the Raman measurements with the focus at the sample surface is usually estimated from the theoretical diffraction limit given by $d_l \approx 1.22\lambda/NA$ and $d_a \approx 4\lambda/NA^2$, yielding 1.3 and 8.5 µm in our case, respectively. However, the real lateral and axial resolution may rather be in the order of $d_l \approx 2$ µm and $d_a \approx 15$ µm, respectively [16,17]. The confocal hole was set to 300 µm, which has to be empirically proven to provide the best compromise between depth resolution and the signal-to-noise ratio for our instrument [16]. It is important to note that the axial resolution at the surface also depends on the absorption properties of the material investigated. In previous work, a Raman intensity loss of 20% to 40% was observed within the first ten micrometers, whereas within the first 20 µm, which is a typical grain diameter, already about half of the intensity of the Raman bands is lost [16].

2.3.1. High-Temperature Raman Spectroscopy of Ternesite

The natural ternesite sample was fired from 30 to 1230 ± 5 °C in 10 °C-steps. At each temperature step, a spectrum was recorded from the same spot in the wavenumber range of 100–1730 cm^{-1} (Table 2). For quantitative analysis, the Raman spectra were least-squares fitted using an appropriate number of Gauss-Lorentz functions along with (i) a 5th order polynomial background function in the frequency range from 100 to 1230 cm^{-1} for the ternesite RT spectrum and (ii) a cubic function in the frequency range from 700 to 1200 cm^{-1} for spectra taken above RT. The wavenumber and temperature ranges were chosen, because they comprise the main Raman bands of ternesite that are of interest here. Again, the Ne emission band at 1707.06 cm^{-1} was fitted using a Gauss function to correct for any spectrometer shift that, if not corrected, would induce a systematic error and thus the accuracy of the results. The reported Raman frequencies are usually precise within ±0.2 to ±0.5 cm^{-1}, but for weak and broad bands, particularly those measured at high temperatures, we estimated a precision in the order of ±1 to ±2 cm^{-1}. Fitting was performed with the LabSpec 6.4.4.15 (Horiba Scientific, Kyōto, Japan) program that comes with the instrument.

2.3.2. Hyperspectral Raman Imaging

The data reduction and generation of hyperspectral false-color Raman images is based on the classic least-squares (CLS) fitting procedure, as described in detail elsewhere [15–17], and was performed with the LabSpec software. In general, mineral phases are identified by the characteristic positions and relative intensities of their fundamental Raman bands. With an increasing temperature, the Raman bands of mineral phases usually shift to lower wavenumbers and their linewidth (full width of half-maximum) increases [15]. Both are usually, though not always, a feature of every vibrational mode of a mineral phase. Additionally, the black body radiation of the samples increases with an increasing temperature and reduces the signal-to-noise ratio. The identification of minerals at high temperatures is further complicated by the fact that reference Raman spectral databases, such as, e.g., the RRUFF database [18], only contain RT spectra that usually differ significantly from their HT counterparts. Therefore, the HT Raman spectra of relevant mineral phases, including quartz, anhydrite, larnite, and ternesite, were collected to build an in-house data base for the identification of mineral phases in multi-component systems at high temperatures and as reference spectra to be used as input data for the CLS fit. The semi-quantitative mineral fractions of an imaged area were calculated by averaging the CLS fractions of all 10,000 spectra. We note that the accuracy of the absolute mineral fractions is influenced by (i) crystal orientation, (ii) grain size, (iii) the temperature dependence of band position and linewidth, and (iv) the relative Raman scattering cross-sections of the mineral phases. Moreover, it has to be noted that we analyzed a relatively small area at the surface that is not necessarily representative for the whole green body. However, hyperspectral Raman imaging delivers in situ information about the formation and decomposition of

distinct phases and their textural relationship without the necessity of quenching the sample to RT. Moreover, Raman images can be taken during heating and cooling with a high-temperature, time, and spatial resolution [16].

3. Results

3.1. Room Temperature (RT) Raman Spectrum

Ternesite crystallizes in the space group *Pnma* (D^{16}_{2h}), i.e., no. 62 [1]. A group theoretical analysis yields the following irreducible representation for optical modes in the ternesite structure:

$$\Gamma_{optic} = 32A_g + 28A_u + 28B_{1g} + 31B_{1u} + 32B_{2g} + 27B_{2u} + 28B_{3g} + 31B_{3u} \quad (1)$$

From these, the A_g, B_{1g}, B_{2g}, und B_{3g} modes are Raman active, i.e., 120 Raman bands are expected. The two equivalent SiO_4 and SO_4 tetrahedra have C_1 and C_s symmetry in the unit cell of the ternesite structure, which has four formula units [1]. We therefore expect 20 internal bending and 16 internal stretching bands, so that 48 lattice vibrations remain. Figure 1a shows the Raman spectrum of the natural ternesite sample recorded at RT before firing from 100 to 1230 cm^{-1}. In addition, we included the fitted functions in the diagram as well as an RT Raman reference spectrum of ternesite from the same location as our sample, which is published in the RRUFF™ mineral database [18]. We note that both spectra match very well. The only obvious differences are different relative band intensities. This, however, merely reflects a different crystal orientation with respect to the laser polarization, particularly affecting highly polarized bands, such as the $v_3(SO_4)$ band at 1182 cm^{-1}. A least-squares fit of 51 Raman bands and a 5th order polynomial background to the data in the frequency range of 100 to 1230 cm^{-1} yielded a satisfactory agreement between the measured and fitted sum spectrum (reduced $X^2 = 0.065$), leaving at least 69 Raman bands undetected (Figure 1). These may either be hidden as part of broader bands due to limitations in the spectral resolution or too weak to be detected with the chosen analytical parameters. All bands are numbered for ease of reference and their frequencies and widths are listed in Table 3.

Within the frequency range 100–250 cm^{-1}, 13 of the expected 48 lattice modes can be identified (Figure 1b). These modes are assigned to rotational and translational lattice modes, which involve the vibration of the Ca ions against the rigid, i.e., strongly covalently bound SiO_4 and SO_4 units and which are therefore well-split in energy from the internal vibrations of the SiO_4 and SO_4 tetrahedra. Their internal bending modes are located in the frequency range between 250 and 700 cm^{-1} (Figure 1c). The group of bands in the 250–460 cm^{-1} range may be attributed to the v_2 bending modes of the SO_4 and SiO_4 tetrahedra [19,20]. The bands near 428 (no. 21) and 442 cm^{-1} (no. 22) can be assigned to the internal $v_2(SO_4)$ vibration because they clearly disappear at temperatures of >730 °C when the decomposition of ternesite starts (Figure 2). The band at 531 cm^{-1} (no. 27) and possibly the band at 510 cm^{-1} (no. 26) can be assigned to the anti-symmetric $v_4(SiO_4)$ bending modes due to the fact that bending modes of the SiO_4 groups are expected near these frequencies [20]. The three bands between 600 and 660 cm^{-1} (no. 31–33) are certainly due to internal $v_4(SO_4)$ bending vibrations, because this is the typical frequency range of these vibrations in sulfate crystals [21] and they also clearly disappear at temperatures of >730 °C (Figure 2). The bands at frequencies higher than 700 cm^{-1} are assigned to the internal symmetric and anti-symmetric stretching vibrations of both tetrahedral units (Figure 1d). The three bands are located at 878, 891, and 897 cm^{-1} (no. 39–41) and those at frequencies larger than 1100 cm^{-1} (no. 48–51) can be assigned to the v_3 stretching modes of the SiO_4 and SO_4 tetrahedra, respectively. The most intense Raman bands are located at 1006 cm^{-1} (no. 45 + 46) and the second most intense band near 832 cm^{-1} (no. 37), which can be unequivocally assigned to the symmetric $v_1(SO_4)$ and $v_1(SiO_4)$ modes, respectively (Figure 1c). Note that the $v_1(SO_4)$ is slightly asymmetric towards the lower frequency side which is reflected by the fact that we needed a second function, centered at 1001 cm^{-1}, to satisfactorily fit the band profile in this frequency range (Figure 1d).

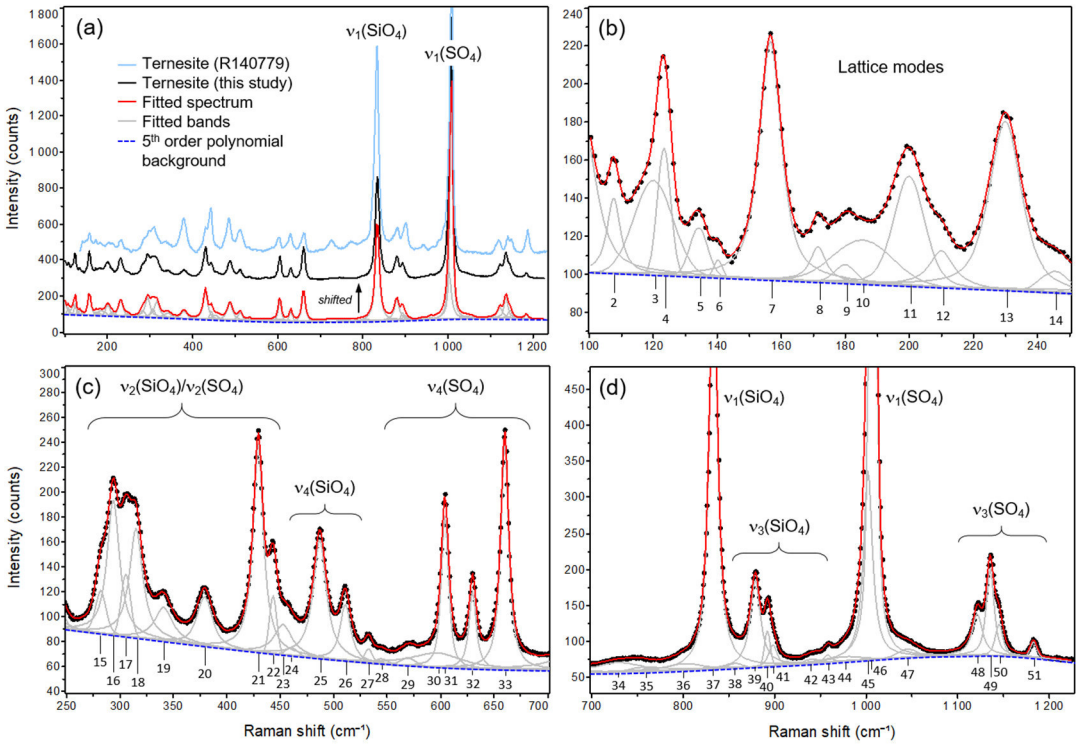

Figure 1. (**a**) Room-temperature (RT) Raman spectrum of the natural ternesite sample in the frequency range between 100 and 1230 cm^{-1} in comparison with a ternesite reference RT spectrum from the RRUFF^{TM} spectral data base [18]. The fitted spectrum, the deconvoluted bands, and the simultaneously fitted 5th order polynomial background are also shown but shifted from the measured spectrum along the y axis for clarity. (**b**–**d**) Cutouts from the spectrum shown in (**a**) in the frequency ranges of (**b**) the lattice vibrations between 100 and 250 cm^{-1}, (**c**) the internal bending modes of SO_4/SiO_4 groups between 250 and 700 cm^{-1}, and (**d**) the internal stretching modes between 700 and 1230 cm^{-1}, respectively. The bands are labelled with ascending numbers, which are used in Table 3 for easy assignment.

Table 3. Frequencies (Raman shift), widths, given as the full width at half maximum (FWHM), and the relative intensities of 51 observed Raman bands of ternesite at room temperature and the proposed mode assignment.

No.	Raman Shift (cm^{-1})	FWHM (cm^{-1})	Relative Intensity *	Remarks	Herzberg Numbering	Approximate Type of Mode
1	95.4	11.1	vw	outside measured frequency range, but used in the fitting process		
2	106.6	5.0	vw			
3	119.0	14.3	vw			
4	122.3	4.9	w			
5	133.1	6.6	vw			
6	139.2	3.2	vw			Lattice vibrations
7	155.5	8.2	s			
8	170.5	5.8	vw			
9	179.0	7.7	vw			
10	184.4	21.9	vw			
11	198.9	11.4	w			
12	209.0	9.2	vw			
13	229.0	12.0	s			
14	244.5	11.1	vw			

Table 3. *Cont.*

No.	Raman Shift (cm^{-1})	FWHM (cm^{-1})	Relative Intensity *	Remarks	Herzberg Numbering	Approximate Type of Mode
15	280.9	11.6	w			
16	292.6	13.8	s			
17	304.4	10.4	w		$v_2(SO_4)$ or $v_2(SiO_4)$	O–S–O or O–Si–O symmetric bending
18	313.9	14.8	s			
19	339.8	20.1	vw			
20	378.1	17.1	w			
21	428.2	11.4	s		$v_2(SO_4)$	O–S–O symmetric bending
22	442.1	8.0	w			
23	451.5	20.1	w		$v_2(SO_4)$ or $v_2(SiO_4)$	O–S–O or O–Si–O symmetric bending
24	459.6	13.6	vw			
25	485.8	14.7	s			
26	509.7	11.9	w		$v_4(SiO_4)$	O–Si–O anti-symmetric bending
27	531.4	8.2	w			
28	543.6	15.1	vw			
29	568.5	15.6	vw			?
30	595.8	62.5	vw	very broad		
31	602.8	8.3	s		$v_4(SO_4)$	O–S–O anti-symmetric bending
32	628.7	8.0	w			
33	658.8	8.8	s			
34	728.4	62.2	vw	very broad		?
35	752.7	29.1	vw	772 cm^{-1} in RRUFF spectrum		
36	799.8	47.0	w			
37	832.0	10.9	vs		$v_1(SiO_4)$	Si–O symmetric stretching
38	855.3	17.0	vw			
39	877.8	13.3	s		$v_3(SiO_4)$	Si–O anti-symmetric stretching
40	891.0	7.2	w			
41	896.9	10.8	w			
42	940.1	17.5	w			
43	956.9	8.7	w			?
44	975.5	42.7	vw	broad		
45	1000.9	11.6	s	hidden	$v_1(SO_4)$	S–O symmetric stretching
46	1006.0	7.7	vs			
47	1043.9	25.0	w			?
48	1120.2	13.3	s		$v_3(SO_4)$	S–O anti-symmetric stretching
49	1134.3	10.1	s			
50	1144.0	10.0	w			
51	1181.8	8.8	w			

Based on intensity maximum: vs: very strong; s: strong, w: weak; vw: very weak.

3.2. High-Temperature (HT) Raman Spectra of Ternesite

In the following, we will focus our analysis on the temperature behavior of the most intense v_1 bands of the SiO_4 and SO_4 units. These Raman bands are of particular importance, as they act as fingerprint bands for the identification of ternesite and can be used to quantitatively follow the decomposition of ternesite to dicalcium silicate and sulfur at high temperatures by Raman spectroscopy. When heated to temperatures below about 800 °C, all observable bands become broader and generally shift to lower frequencies (Figure 2). By plotting the fitted frequencies of the v_1 bands as a function of temperature, it is evident that the $v_1(SO_4)$ band exhibits a stronger shift with an increasing temperature, $\delta\nu/\delta T$, than the $v_1(SiO_4)$ band, reflecting a different temperature dependence of both modes (Figure 3a). However, the most pronounced feature of the temperature dependence of the frequency of both modes is that it is wavy over the entire temperature interval, whereby the amplitudes of the fluctuations

significantly exceed the experimental errors (Figure 3a). However, at low temperatures, i.e., between RT and 160 °C, the data can in both cases be very well described by a linear function ($r^2 > 0.9995$). At about 160 °C, however, both modes ceased to shift to lower frequencies until about 250 °C. At about 890 °C, the $v_1(SO_4)$ frequency shows another local minimum before the frequencies shift to a higher value until 930 °C. However, at this stage, the error in the $v_1(SO_4)$ frequency strongly increases, which is reflected by a high scatter, because the band becomes very weak. The temperature dependence of the $v_1(SiO_4)$ frequency is characterized by a local minimum close to 780 °C, from which the frequency rose continuously with slight fluctuations until 1120 °C. At higher temperatures, the frequency decreases again until the maximum sintering temperature is finally reached.

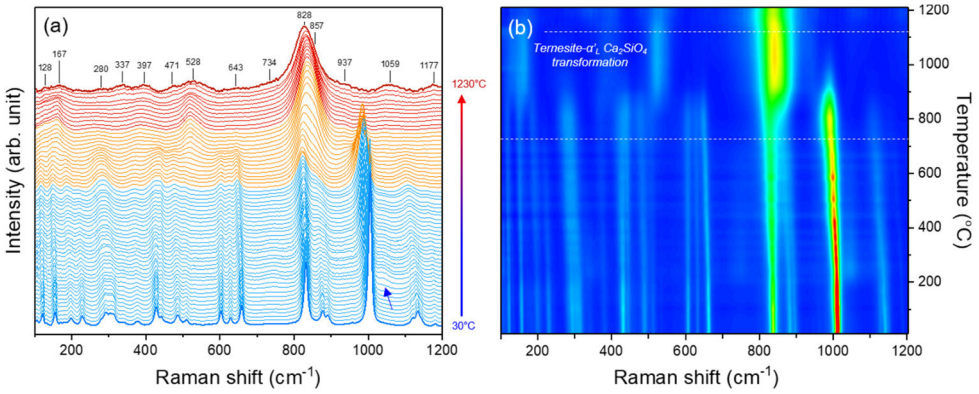

Figure 2. (**a**) Stacked Raman spectra (20 °C-steps) of the ternesite recorded between 25 and 1230 ± 5 °C. From 730 ± 5 °C, the ternesite transformed to α'_L-Ca_2SiO_4 and sulfur (orange spectra). Above 1120 ± 5 °C, only bands of α'_L-Ca_2SiO_4 can be identified (red spectra). At 1230 °C, only 14 Raman modes can be identified between 100 and 1230 cm^{-1} and their frequencies are indicated. Note that the spectra are shown after background correction. The blue arrow points to a sudden intensity increase in the weak band at 1044 cm^{-1} (no. 47) at 170 °C. (**b**) The color-coded Raman intensity as a function of the Raman shift and temperature (red and blue colors represent high and low intensities, respectively). Dashed lines mark the temperature range in which ternesite transformed to α'_L-Ca_2SiO_4 in our experiment.

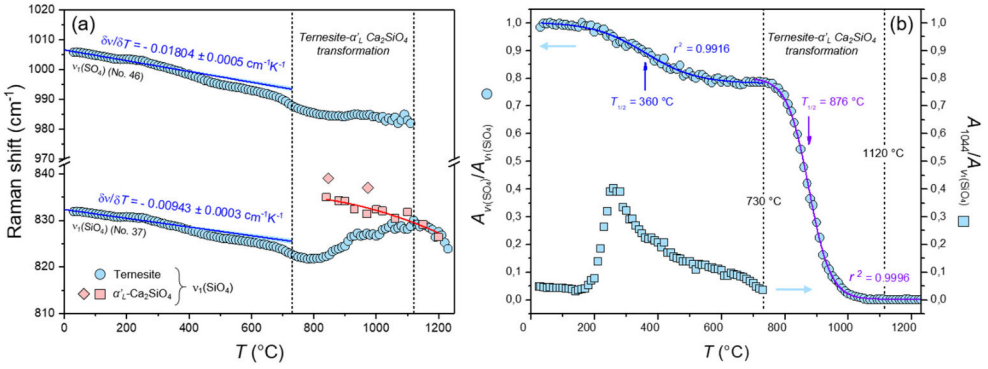

Figure 3. (**a**) The frequency of the $v_1(SO_4)$ and $v_1(SiO_4)$ bands of ternesite as a function of temperature. Stippled lines mark the onset and end of the ternesite-to-dicalcium silicate phase transition between about 730 to 1120 °C, respectively. The published high-temperature (HT) Raman frequencies of α'_L-Ca_2SiO_4 [20] and own preliminary and unpublished HT data along with a quadratic fit (red curve) are also shown. Blue lines represent linear least-squares fits to the data below 160 °C (n = 14). (**b**) The temperature dependence of the integrated intensity ratios $A_{v1(SO4)}/A_{v1(SiO4)}$ (blue circles, left axis) and $A_{1044}/A_{v1(SiO4)}$ (blue squares, right axis) between both v_1 bands, normalized between 0 and 1, and between the weak band near 1044 cm^{-1} and the $v_1(SO_4)$ band, respectively. The blue and purple curve represent least-squares fit of a sigmoidal Boltzmann function to the data between RT and 730 °C and between 700 and 1230 °C, respectively. See text for more details.

From Figure 2, it is further evident that the sulfate-related vibrational modes disappear between about 750 and 1000 °C (orange spectra in Figure 2a), even the very strong $v_1(SO_4)$ band (Figure 2b). In this temperature interval, the overall number of observable Raman bands is largely reduced from 51 to 14 (red spectra in Figure 2a), reflecting a change in the crystal symmetry and, in particular, of the chemistry (loss of sulfur). A group theoretical analysis based on an orthorhombic structure of the HT polymorph of dicalcium silicate (α'_L-Ca_2SiO_4) revealed 48 Raman active modes [20]. Note, however, that due to the low intensity and large broadening of the bands at HT, the number and positions of the bands were difficult to define. In any case, ternesite evidently decomposed to α'_L-Ca_2SiO_4, CaO, and $SO_3\uparrow$. The formation of α'_L-Ca_2SiO_4 is evidenced by the observation that the frequency of the $v_1(SiO_4)$ band of ternesite merges at about 1120 °C with the HT frequencies observed for pure α'_L-Ca_2SiO_4. Our values for the $v_1(SO_4)$ band of the α'_L-Ca_2SiO_4 plot are at lower wave numbers at a given temperature than two values from the literature [20] (Figure 3a). The literature data represent the maximum of the overall $v_1(SO_4)$ band profile that, however, is composed of at least two bands, i.e., the $v_1(SO_4)$ and a $v_3(SO_4)$ band, which both were considered in the fitting procedure.

The formation of lime could not be observed, because lime has no first-order Raman spectrum and its weak second-order spectrum, used for the CLS fitting method (see Section 2.3.2), is strongly overlaid by the much more intense Raman signals of ternesite and dicalcium silicate. In any case, it is safe to state that, at 730 °C, the SO_4 tetrahedra started to detach from the ternesite structure, and, at 1120 °C, the transformation from ternesite to dicalcium silicate and sulfur is essentially completed, as the $v_1(SO_4)$ band could not be detected in the spectra anymore.

It is noteworthy that at a temperature of about 170 °C, the intensity of the weak SO_4-related stretching band near 1044 cm^{-1} (no. 47) begun to significantly increase (blue arrow in Figure 2a) until about 260 °C from where it almost exponentially decreased until ternesite started to decompose at 730 °C (Figure 3b). In Figure 3b, we have also plotted the integrated intensity ratio between both v_1 bands, $R_{v1} = A_{v1(SO4)}/A_{v1(SiO4)}$, normalized between 0 and 1, as a function of temperature. This plot is intriguing because it is clearly characterized by two sigmoidal segments that each can be well fitted ($r^2 > 0.991$) with a sigmoidal Boltzmann function of the form $R_{v1} = R_2 + (R_1 - R_2)/(1 + \exp((T - T_{1/2})/\alpha))$, where R_1 and R_2 are the equilibrium values of the ratio before and after the transition, respectively, $T_{1/2}$ is the inflection point of the curve, i.e., the temperature at which R_{v1} has changed by 50%, and α is a coefficient that describes the behavior of the slope of the process during the transition. From the fit, we obtain the characteristic half-life temperatures at which 50% of the ternesite is transformed into α'_L-Ca_2SiO_4 of $T_{1/2}$ = 360 ± 4 °C and 876 ± 2 °C for the first stage below 730 °C and the second stage, respectively. The wavy temperature dependence of the v_1 frequencies is in agreement with the occurrence of major structural changes even at temperatures far below the actual ternesite decomposition temperature, as such, a behavior cannot be explained by thermally induced mode anharmonicity alone.

3.3. In Situ Experiments AQC-1.1 and AQC-1.2

In the experiment AQC-1.1, the green body was first fired to 927 ± 5 °C with a heating rate of 10 °C/min. Afterwards, the sample was fired stepwise (~50 °C-steps) to 1104 ± 5 °C. At 927 ± 5 °C, the HT polymorph of dicalcium silicate, i.e., α'_L-Ca_2SiO_4, already formed at interfaces between lime, anhydrite, and quartz (Figure 4). However, from Figure 4 it is also evident that α'_L-Ca_2SiO_4 did not only crystallize at the interfaces between these three phases, but also as small grains within the CaO matrix. In this case, SiO_2 was likely supplied by small quartz particles below the image plane. At this temperature, ternesite was also identified by its dominant Raman band at 983 cm^{-1}. It initially replaced isolated α'_L-Ca_2SiO_4 grains (Figure 4), but with increasing time also started to replace the large quartz grain in the upper left of the imaged area. As the temperature increased, this large quartz grain was replaced more and more by ternesite, whereby either reaction rims were formed around larger quartz grains or smaller quartz grains were completely replaced pseudomorphically. In particular, the time series images at 971 ± 5 °C show the time-dependent replacement of this quartz grain by ternesite, in which only a quartz

relic remained in the middle of the grain until the end of the experiment. Noticeably, at 1016 ± 5 °C, dicalcium silicate (α'_L-Ca_2SiO_4) formed new reaction rims around ternesite, producing a layered texture with quartz in the center, ternesite in the middle, and α'_L-Ca_2SiO_4 in the outer layer. At a temperature of 1060 ± 5 °C, the quartz-ternesite replacement proceeded, while new anhydrite had formed (Figures 4 and 5a). This indicates that there must have been a high sulfur fugacity in the furnace. At the maximum firing temperature of 1104 ± 5 °C, the Raman images show a heterogeneous transformation of the large grain of ternesite, still comprising a quartz relic in its center, into dicalcium silicate, which leads to a spotty appearance (Figure 4). On cooling to RT, this α'_L-Ca_2SiO_4 grain completely transformed to β-Ca_2SiO_4 (larnite), unambiguously identified by its main fundamental Raman band near 858 cm^{-1} [15,20,22], while smaller dicalcium silicate grains recrystallized to ternesite.

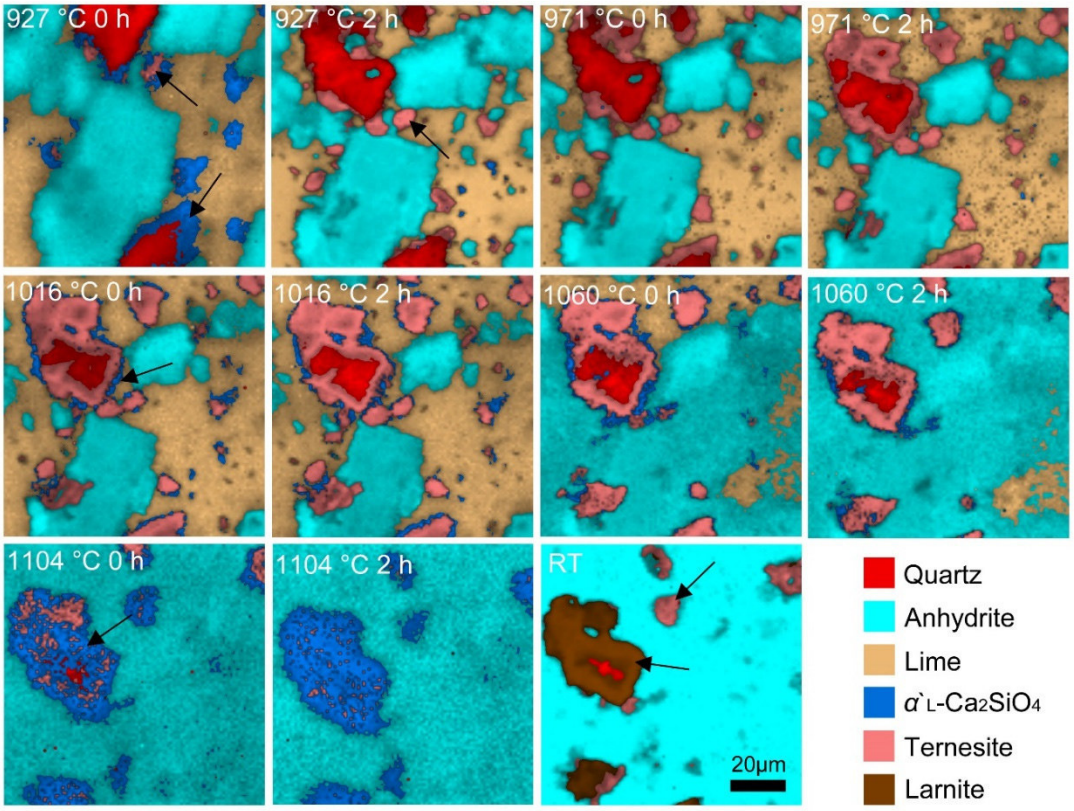

Figure 4. False-colored hyperspectral Raman images of the mineral distribution of a 100 × 100-µm^2 surface area of a green body made of CaO, anhydrite, and quartz at different temperatures and two dwell times (experiment AQC−1.1). The specified dwell time indicates the time that has elapsed after reaching the reaction temperature. The black arrows hint to new formed mineral phases. Note that the decomposition of ternesite started at 1016 ± 5 °C and continued to 1104 ± 5 °C (see arrows). During the cooling process, the α'_L-phase transformed to the β-phase (larnite) and also partially remained metastable at RT (see arrows).

Before starting the AQC-1.2 experiment, a SiO_2-$CaCO_3$ sample was fired for five hours at 1200 ± 5 °C to remove sulfur contamination from the furnace by the formation of ternesite during the experiment. Hyperspectral Raman images collected during experiment AQC-1.2 between 659 and 882 ± 5 °C (not shown here) did not reveal the formation of ternesite within the imaged area, but dicalcium silicate could already be observed at 695 ± 5 °C. Its fraction within the imaged area (or better volume) increased steadily with temperature and time over the entire temperature range of this experiment, while, simultaneously, the fractions of CaO supplying minerals and quartz decreased (Figure 5b). Wollastonite was detected locally in contact with a quartz grain from 1016 ± 5 °C.

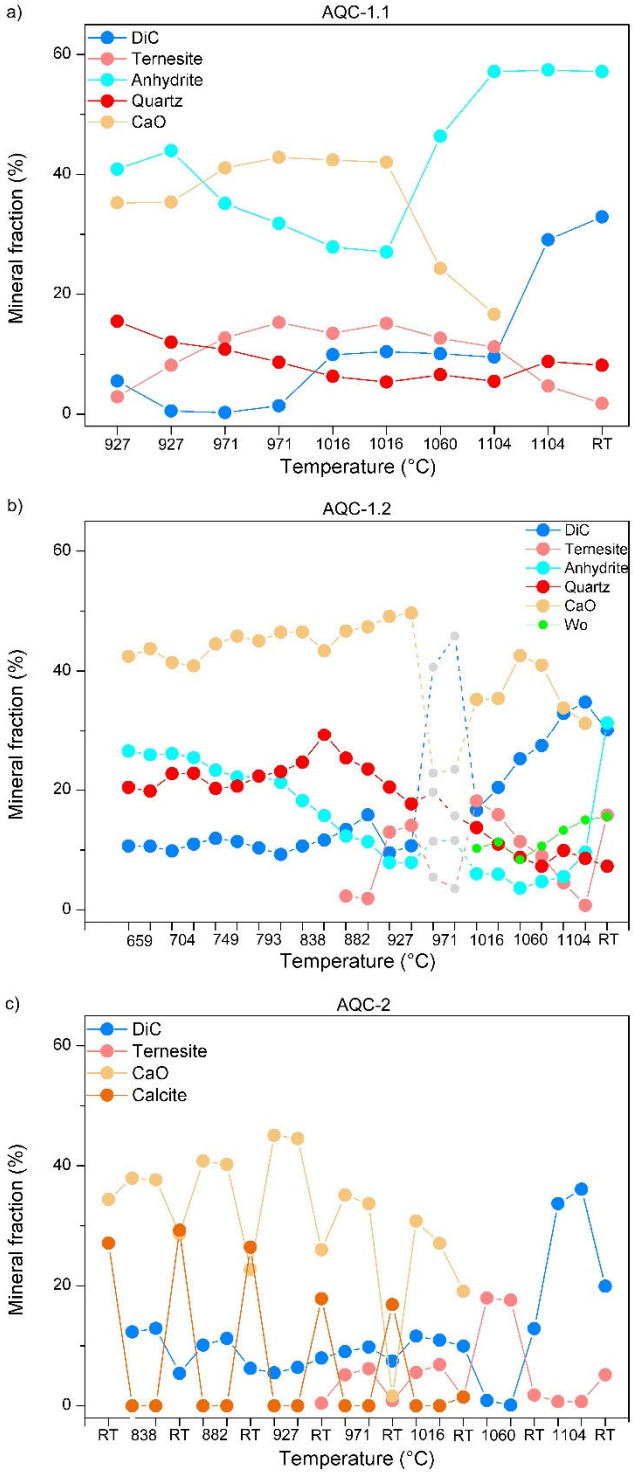

Figure 5. The evolution of the mineral fractions (DiC = dicalcium silicate, ternesite, quartz, anhydrite, CaO, calcite, and Wo = wollastonite) within the imaged volume as a function of temperature and time. (**a**) Experiment AQC-1.1, (**b**) experiment AQC-1.2 (light grey circles correspond to a failed measurement, where the focus was lost), and (**c**) experiment AQC-2 (contents of anhydrite and quartz are not shown here).

Within the imaged area, ternesite was first identified at 882 ± 5 °C (Figure 6) as a replacement product of α'_L-Ca_2SiO_4 that reacted with anhydrite, as observed in experiment AQC-1.1. During heating to 1016 ± 5 °C, more dicalcium silicate crystals were transformed to ternesite and grew together, forming

a larger aggregate that is outlined by a stippled white line in Figure 6. During further heating, this grain and other smaller grains re-transformed to α'_L-Ca_2SiO_4 and sulfur. The transition temperature for the reverse reaction is between 1016 and 1060 ± 5 °C (Figure 5b). After heating to 1060 ± 5 °C, the recrystallization was already well advanced compared to the reaction progress observed in experiment AQC-1.1 (cf. Figure 4). Again, the recrystallization process produced a spotty intergrowth texture. At the maximum temperature of 1104 ± 5 °C, only some relics of ternesite remained inside the outlined area. Interestingly, during quenching to RT, ternesite recrystallized at the edge of the large dicalcium silicate grains, now transformed to its β-polymorph larnite, or within the newly formed anhydrite matrix, but not within the outlined area that now is a large larnite aggregate.

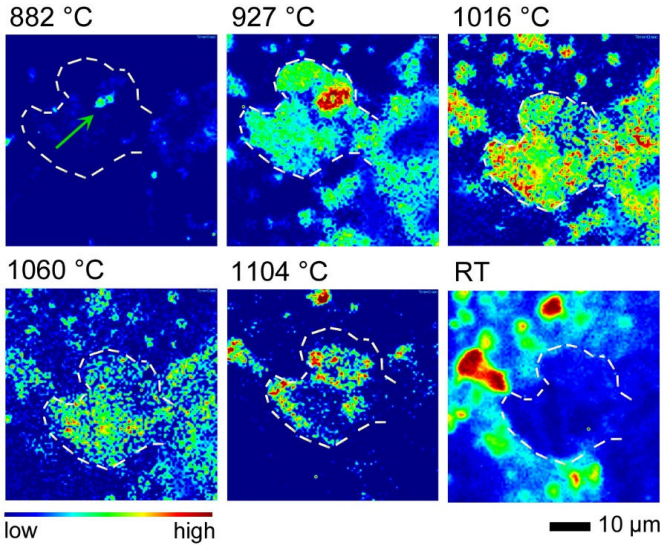

Figure 6. Normalized false-color Raman images of the ternesite fraction from the in situ experiment AQC-1.2, each recorded at the beginning of each temperature step. At 882 ± 5 °C, ternesite could already be identified (green arrow). With increasing temperature, more and more ternesite replaced dicalcium silicate and after exceeding 1060 ± 5 °C recrystallized to dicalcium silicate.

3.4. In Situ/Quench Experiment AQC-2

The experiment AQC-2 was carried out using the same precursor materials as in experiments AQC-1.1 and AQC-1.2. In Figure 7, we show the hyperspectral false-color Raman images that were taken during firing at any high temperature and quenching step, as well as notes to the predominant reactions that can be derived from each in situ image. During firing to the first temperature step of 838 ± 5 °C, calcite decomposed to CaO and CO_2 but recrystallized during the following quenching steps. This demonstrated that, in addition to a high sulfur fugacity, there also must have been a high CO_2 fugacity in the furnace. However, in the course of the sintering experiment, less and less CaO was formed at high temperatures and therefore less and less calcite could be identified at RT (Figure 5c). At 838 ± 5 °C, dicalcium silicate (α'_L-Ca_2SiO_4) was detected, which transformed to larnite during cooling. Moreover, some isolated calcio-olivine (γ-Ca_2SiO_4) crystals were identified by their Raman band near 813 cm^{-1} [20], which were located near a large quartz grain (Figure 7).

From 927 ± 5 °C, ternesite could be identified in various spectra throughout the imaged area. However, the nucleation and growth of ternesite inside dicalcium silicate grains became first visible within the hyperspectral Raman images at 971 ± 5 °C. After stepwise heating/quenching of the green body to/from higher temperatures, ternesite continuously grew at the expense of α'_L-Ca_2SiO_4 until 1060 ± 5 °C (Figure 5c). Interestingly, during each quenching step, many ternesite grains that were present at high temperatures appeared to be transformed into larnite. During heating to 1104 ± 5 °C and quenching to RT, dicalcium silicate crystallized at the expense of ternesite, although some small grains of ternesite remained at RT (Figure 8). From Figure 5c, it can be deduced that, in our experiments,

ternesite was stable within an in situ temperature range between 927 and 1060 ± 5 °C. On the other hand, if only the results of the quenched sample (ex situ) are considered, it could be concluded that the upper stability limit for ternesite was 1104 ± 5 °C.

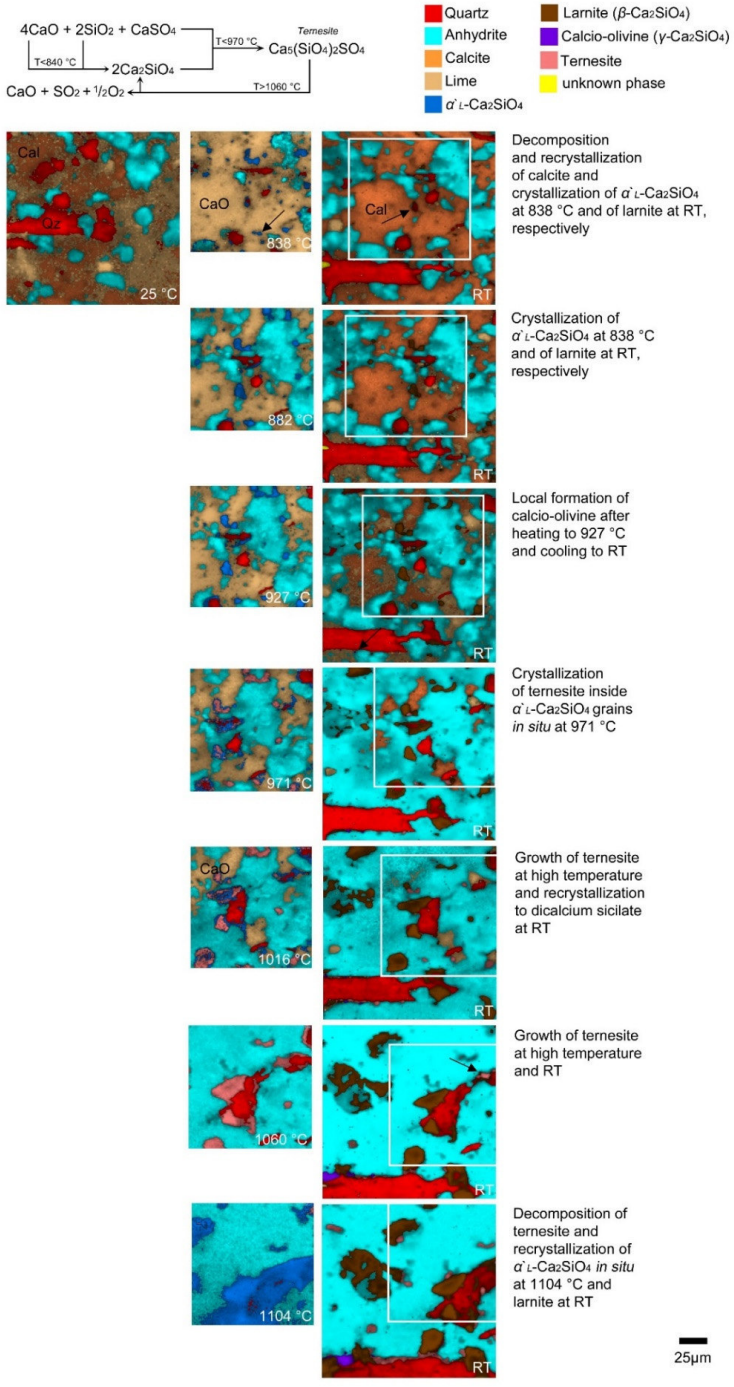

Figure 7. False-colored hyperspectral Raman images of the mineral distribution of a 100 × 100-µm^2 surface area of a green body made of CaO, anhydrite, and quartz at different sintering temperatures (in situ/quench experiment AQC-2) with information on the predominant reactions that can be derived from the images. Note that a larger area was measured at RT. The white frame marks the corresponding area at HT. The imaged area varies slightly due to the shrinkage and expansion of the sample. The black arrows in the image taken at 838 °C and at RT (upper right) point to small crystals of larnite or its high-temperature polymorph, respectively.

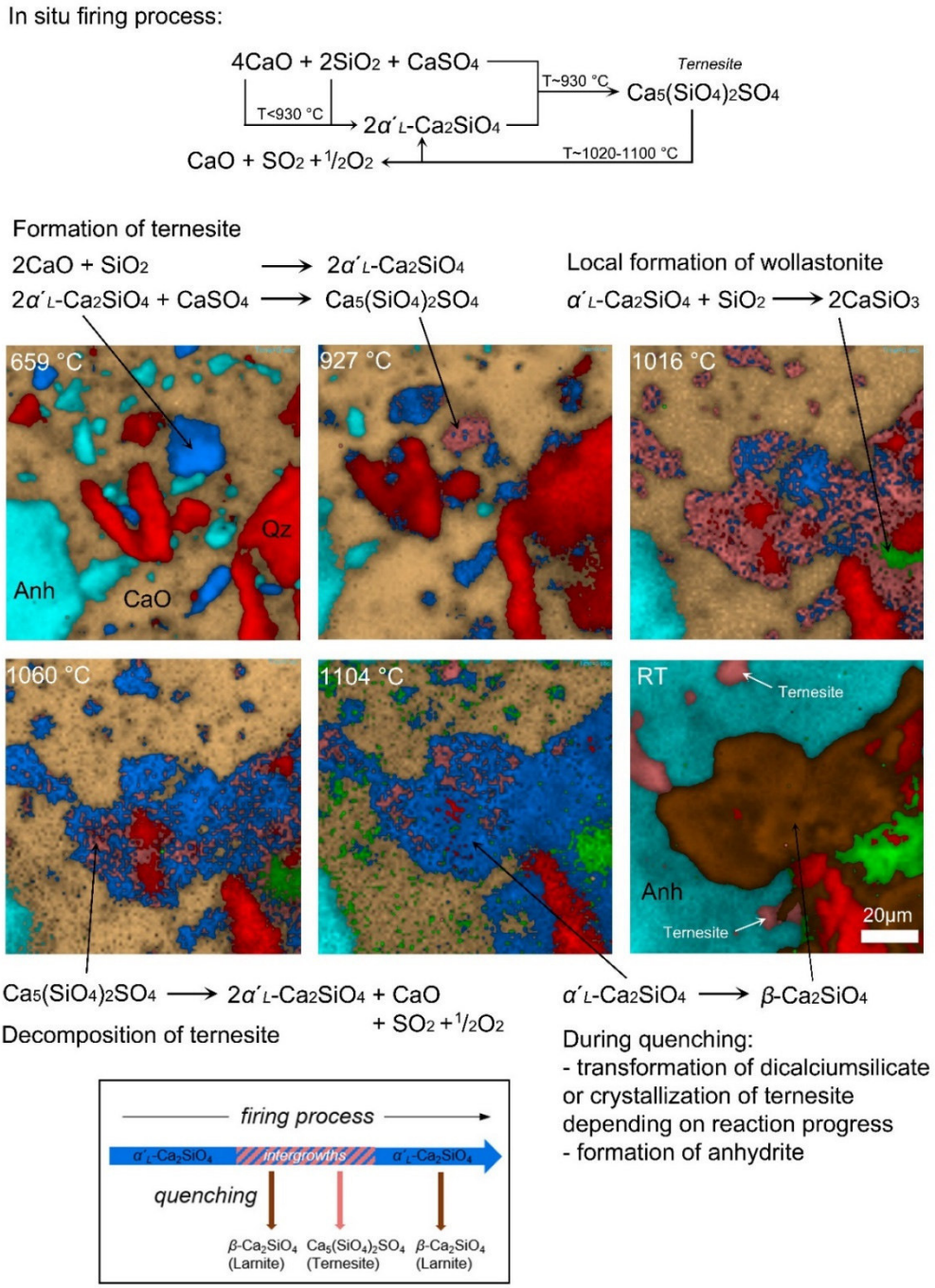

Figure 8. Graphical summary of the main results of the sintering experiments.

4. Discussion

4.1. The Formation of Calcium Silicates

Within the ternary system $CaSO_4$-SiO_2-CaO, dicalcium silicate has previously been observed at temperatures even below about 660 °C. It mainly forms by a reaction between quartz and lime [22–24]:

$$2CaO + SiO_2 \overset{T < 670\ ^\circ C}{\rightarrow} Ca_2SiO_4 \quad (2)$$

The formation temperature is much lower than in other experiments, which were performed with anhydrite as a CaO source only [15]. The addition of free CaO (lime) enables the dicalcium silicate

formation at lower temperatures because calcium is directly available. However, in this study, the first image was taken at about 660 °C (experiment AQC-1.2). The time- and temperature-series Raman images reveal that α'_L-Ca_2SiO_4 crystallized at the interface between quartz and lime or anhydrite and was formed as a rim around large quartz grains in some cases (exp. AQC 1.1, Figure 4). Hauke and co-workers [16] observed in a sintering experiment with quartz and lime that such rims of dicalcium silicate represent a barrier between the reactants. The further crystallization of α'_L-Ca_2SiO_4 thus had to proceed by diffusion of Ca^{2+} ions through this barrier layer [16,25]. The observed nucleation of small α'_L-Ca_2SiO_4 grains within the CaO matrix can be explained by small quartz particles embedded in the matrix, which are more reactive than the larger ones due to their larger surface area [16]. Such grain size effects are also important with regard to technical applications. Depending on the homogeneity or inhomogeneity of the starting materials, more or less precursor material is converted to the target substance or leads to fouling in kilns [26,27]. At temperatures >700 °C, dicalcium silicate occurs as α'_L-Ca_2SiO_4, which reversibly transforms to β-Ca_2SiO_4 during quenching [20].

In experiment AQC 1.2, wollastonite could be identified at about 1020 °C near to a quartz grain. On the one hand, it is well known that wollastonite can be formed by a reaction between quartz and lime [28]. In sinter experiments with anhydrite and quartz, wollastonite already crystallized at temperatures of about 920 °C [15]. The thermal decomposition of anhydrite to CaO and SO_3 was found to be significantly influenced by the quartz content of the sample. In those experiments, where more quartz was available, anhydrite decomposed at lower temperatures than in experiments with lesser quartz content. With an increasing temperature and reaction time, α'_L-Ca_2SiO_4 could be identified in the expense of wollastonite [15]. On the other hand, the hyperspectral Raman images of experiment AQC-1.2 reveal that wollastonite could also be a breakdown product of dicalcium silicate and free SiO_2 [15,17,29]:

$$Ca_2SiO_4 + SiO_2 \overset{T \sim 1020–1050\ ^\circ C}{\rightarrow} 2CaSiO_3 \quad (3)$$

The previous formation of dicalcium silicate is bound to a high CaO content [30] that is supplied by the decomposition of anhydrite. Which of the reactions proceeds seems to strongly depend on the local chemistry.

4.2. The Formation and Decomposition of Ternesite

In all experiments, ternesite could be identified at temperatures of about 930 °C. From the time- and temperature-resolved images (Figures 4, 6 and 7), it is apparent that the formation of $Ca_5(SiO_4)_2SO_4$ is related to the reaction between dicalcium silicate and anhydrite:

$$2Ca_2SiO_4 + CaSO_4 \overset{T \sim 930\ ^\circ C}{\rightarrow} Ca_5(SiO_4)_2SO_4 \quad (4)$$

Gutt and Smith [7] were the first to produce ternesite by heating samples consisting of calcite, quartz, and anhydrite. Other authors who synthesized ternesite, firstly produced dicalcium silicate or belite, respectively [3,31]. These authors proposed that ternesite is formed in a two-step reaction process with dicalcium silicate as an intermediate state, even if quartz, lime, and anhydrite are present. The formation of ternesite by wollastonite as Si and Ca source is also possible, but requires a higher activation energy [32]. Whereas α'_L-Ca_2SiO_4 was observed to replace quartz grains, producing reaction rims, ternesite started to nucleate in the interior of dicalcium silicate grains and from here it continued to grow outwards. The $CaSO_4$ required for the formation of ternesite likely originates from small anhydrite grains that, although invisible in the image, were detected in the respective Raman spectra.

In previous work, the stability temperature of ternesite was estimated to be in the range between 1000 and 1300 °C [1,3,7,32]. The highest ternesite content was reached at temperatures between 1100 and 1200 °C due to the residence time at a high temperature [32]. Depending on whether the system was open or closed, ternesite decomposed at 1150 or 1300 °C, respectively [3,7]. Note that within this temperature regime, the decomposition of a single, isolated ternesite crystal was already completed (Figures 2 and 3). The upper limit also depends on the gas fugacity. At a low oxygen partial pressure,

like in kilns, the stabilization of ternesite at higher temperatures could be achieved by an increased SO_2 partial pressure. In air, a low SO_2 pressure is required at high temperatures [3]. Other experiments show an improved thermal stability of ternesite with increased oxygen concentration [32]. However, all samples were analyzed after they were quenched to RT. The Raman images collected during the in situ/quench experiment (AQC-2), however, clearly reveal that important information can be lost if samples are only analyzed after quenching to RT. For instance, the in situ Raman images show the ternesite formation at 927 ± 5 °C, but at RT no ternesite could be identified (Figure 7). At the next temperature step (971 ± 5 °C) and after quenching again ternesite was detected. After the last firing step, ternesite was found separately located near to larnite. Obviously, ternesite also crystallized during cooling to RT, because at about 1100 °C α'_L-Ca_2SiO_4 was identified in situ at the same place. During the in situ experiments, dicalcium silicate was observed already at a sintering temperature of about 1000 °C, indicating that quenching stabilizes ternesite or a long sintering period is needed for the breakdown of ternesite according to:

$$Ca_5(SiO_4)_2SO_4 \overset{T \sim 1020\ ^\circ C}{\rightarrow} 2Ca_2SiO_4 + CaO + SO_2 + 1/2O_2 \quad (5)$$

4.3. The Ternesite–Dicalcium Silicate Co-Existence

Ternesite and the Ca_2SiO_4 polymorphs could be clearly identified in all experiments. It appears that both ternesite and α'_L-Ca_2SiO_4 can co-exist at HT over a broad temperature range and that it depends on reaction progress and likely the sulfur fugacity in the furnace whether ternesite or β-Ca_2SiO_4 crystallizes during cooling. The HT study of a single ternesite crystal reveals significant spectral changes. The position, width, and intensity of the main Raman bands changed significantly with increasing temperature (Figures 2 and 3). As expected, the most dramatic changes occurred in the temperature regime between 730 and 1120 °C, where the ternesite structure broke down (Equation (4)). Due to collapsed tetrahedra, the SiO_4 groups move closer to the Ca^{2+} ions and the bond spacing is shortened. The spotty appearance of partly transformed ternesite crystals observed in the multi-component sintering experiments suggests that the transformation process started by the formation of α'_L-Ca_2SiO_4 nuclei within ternesite that grew further until the entire ternesite host is replaced by dicalcium silicate. The observation of a clear sigmoidal change in the $R_{\nu 1}$ intensity ratio as a function of temperature (Figure 3b) supports such a process, where the initial slow rate can be attributed to the time required for forming a significant number of α'_L-Ca_2SiO_4 nuclei. During the intermediate period, the transformation is rapid, since the nuclei grow into particles and consume the ternesite phase while α'_L-Ca_2SiO_4 nuclei continue to form in the remaining ternesite phase. Once the transformation comes near to completion, there is little untransformed ternesite for the nuclei to form in and to grow so the formation of new α'_L-Ca_2SiO_4 domains becomes slow. Furthermore, the already existing α'_L-Ca_2SiO_4 domains begin to touch each other, forming a boundary where growth may stop or the reaction becomes diffusion-controlled. By performing a series of isothermal or isochronal ternesite heating experiments with different heating rates, the activation energy of the process and the nature of the transformation can potentially be determined [33], which is a challenge for the future. The most intriguing observation from our single crystal heating study, however, is that significant spectral changes were observed already at temperatures as low as 170 °C, which cannot be explained by thermally induced anharmonicity and thus must reflect structural rearrangements that precede the decomposition of ternesite to α'_L-Ca_2SiO_4.

5. Summary and Conclusion

The main results and conclusions are summarized in a graphical summary in Figure 8. During the firing of CaO-SiO_2-$CaSO_4$ green bodies, α'_L-Ca_2SiO_4 was found to crystallize first and then to transform to ternesite at about 930 °C. A longer dwell time led to an earlier formation of ternesite (c.f. Figure 7, 882 ± 5 °C). In the multi-phase experiments, ternesite decomposed to dicalcium silicate, lime, and sulfur oxide within the temperature range between 1020 and 1100 °C. During quenching to

RT, α'_L-Ca_2SiO_4 transformed to β-Ca_2SiO_4 (larnite) or recrystallized to ternesite, whereby it evidently depends on the reaction progress whether ternesite or larnite was identified after quenching to RT.

In addition, a natural ternesite crystal was heated to 1230 °C in 10 °C-steps and analyzed by HT Raman spectroscopy. This experiment already revealed structural changes in ternesite during firing at temperatures as low as 170 °C and a phase transformation to α'_L-Ca_2SiO_4 between 730 and 1120 °C. Within this temperature range, both the ternesite and dicalcium silicate domains co-exist. These results basically confirm the upper stability limit of ternesite determined by the multi-phase sintering experiments and remarkably demonstrate the power of in situ Raman imaging to study high-temperature solid-state reactions in multi-component systems.

Author Contributions: Conceptualization, N.B. and T.G.; Methodology, N.B., K.H. and T.G.; Software, N.B.; Validation, N.B, K.H. and T.G.; Formal Analysis, N.B. and K.H.; Investigation, N.B.; Resources, N.B.; Data Curation, N.B.; Writing–Original Draft Preparation, N.B. and K.H.; Writing–Review & Editing, T.G.; Visualization, N.B.; Supervision, T.G.; Project Administration, T.G. and M.N.; Funding Acquisition, T.G. All authors have read and agreed to the published version of the manuscript.

Funding: This research was financially supported by the RWE Power AG, Kraftwerk Niederaußem, Bergheim, Germany. K.H. is funded by the Deutsche Forschungsgemeinschaft (DFG, grant number GE1094/22-1).

Acknowledgments: Many thanks go to B. Ternes for providing the natural ternesite sample.

Conflicts of Interest: The authors declare no conflict of interest.

References

1. Irran, E.; Tillmanns, E.; Hentschel, G. Ternesite, $Ca_5(SiO_4)_2SO_4$, a new mineral from the Ettringer Bellerberg/Eifel, Germany. *Miner. Pet.* **1997**, *60*, 121–132. [CrossRef]
2. Galuskin, E.; Galuskina, I.; Gfeller, F.; Krüger, B.; Kusz, J.; Vapnik, Y.; Dulski, M.; Dzierżanowski, P. Silicocarnotite, $Ca_5[(SiO_4)(PO_4)](PO_4)$, a new old mineral from the Negev Desert, Israel, and the ternesite–silicocarnotite solid solution: Indicators of high-temperature alteration of pyrometamorphic rocks of the Hatrurim Complex, Southern Levant. *Eur. J. Miner.* **2016**, *28*, 105–123. [CrossRef]
3. Hanein, T.; Galan, I.; Glasser, F.P.; Skalamprinos, S.; Elhoweris, A.; Imbabi, M.S.; Bannerman, M.N. Stability of ternesite and the production at scale of ternesite-based clinkers. *Cem. Concr. Res.* **2017**, *98*, 91–100. [CrossRef]
4. Brotherton, P.D.; Epstein, J.M.; Pryce, M.W.; White, A.H. Crystal Structure of "Calcium Sulphosilicate", $Ca_5(SiO_4)_2SO_4$. *Aust. J. Chem.* **1974**, *27*, 657–660. [CrossRef]
5. Pryce, M.W. Calcium sulphosilicate in lime-kiln wall coating. *Miner. Mag.* **1972**, *38*, 968–971. [CrossRef]
6. Neuroth, M. *Internal Report of RWE, KW Neurath*, Unpublished work. 2017.
7. Gutt, W.; Smith, M.A. A new calcium silicosulphate. *Nature* **1966**, *210*, 408–409. [CrossRef]
8. Dienemann, W.; Schmitt, D.; Bullerjahn, F.; Haha, M. Ben Belite-Calciumsulfoaluminate-Ternesite (BCT)—A new low-carbon clinker technology. *Cem. Int.* **2013**, *11*, 100–109.
9. Bullerjahn, F.; Schmitt, D.; Haha, M. Ben Cement and Concrete Research Effect of raw mix design and of clinkering process on the formation and mineralogical composition of (ternesite) belite calcium sulphoaluminate ferrite clinker. *Cem. Concr. Res.* **2014**, *59*, 87–95. [CrossRef]
10. Shen, Y.; Qian, J.; Huang, Y.; Yang, D. Synthesis of belite sulfoaluminate-ternesite cements with phosphogypsum. *Cem. Concr. Compos.* **2015**, *63*, 67–75. [CrossRef]
11. Galan, I.; Elhoweris, A.; Hanein, T.; Bannerman, M.N.; Glasser, F.P. Advances in clinkering technology of calcium sulfoaluminate cement. *Adv. Cem. Res.* **2017**, 1–13. [CrossRef]
12. Hanein, T.; Elhoweris, A.; Khare, S.; Skalamprinos, S.; Jen, G.; Whittaker, M.; Imbabi, M.S.; Glasser, F.P.; Galan, I.; Bannerman, M.N. Production of belite calcium sulfoaluminate cement using sulfur as a fuel and as a source of clinker sulfur trioxide: Pilot kiln trial. *Adv. Cem. Res.* **2016**, *28*, 643–653. [CrossRef]
13. Hofman, H.; Mostowitsch, W. The behavior of calcium sulfate at elevated temperatures with some fluxes. *Trans. Am. Inst. Min. Metall. Eng.* **1909**, *32*, 628–653.
14. Mihara, N.; Kuchar, D.; Kojima, Y.; Matsuda, H. Reductive decomposition of waste gypsum with SiO_2, Al_2O_3, and Fe_2O_3 additives. *J. Mater. Cycles Waste Manag.* **2007**, *9*, 21–26. [CrossRef]
15. Böhme, N.; Hauke, K.; Neuroth, M.; Geisler, T. In situ Raman imaging of high-temperature solid-state reactions in the $CaSO_4$–SiO_2 system. *Int. J. Coal Sci. Technol.* **2019**, *6*, 247–259. [CrossRef]

16. Hauke, K.; Kehren, J.; Böhme, N.; Zimmer, S.; Geisler, T. In situ Hyperspectral Raman Imaging: A new Method to investigate Sintering Processes of Ceramic Material at High Temperature. *Appl. Sci.* **2019**, *9*, 1310. [CrossRef]
17. Stange, K.; Lenting, C.; Geisler, T. Insights into the evolution of carbonate-bearing kaolin during sintering revealed by in situ hyperspectral Raman imaging. *J. Am. Ceram. Soc.* **2018**, *101*, 897–910. [CrossRef]
18. Lafuente, B.; Downs, R.T.; Yang, H.; Stone, N. The power of databases: The RRUFF project. In *Highlights in Mineralogical Crystallography*; Armbruster, T., Danisi, R.M., Eds.; De Gruyter: Berlin, Germany, 2015; pp. 1–30.
19. Yuan, X.; Mayanovic, R.A.; Zheng, H. Determination of pressure from measured Raman frequency shifts of anhydrite and its application in fluid inclusions and HDAC experiments. *Geochim. Cosmochim. Acta* **2016**, *194*, 253–265. [CrossRef]
20. Remy, C.; Reynard, B.; Madon, M. Raman Spectroscopic Investigations of Dicalcium Silicate: Polymorphs and High-Temperature Phase Transformations. *J. Am. Ceram. Soc.* **1997**, *80*, 413–423. [CrossRef]
21. Ben Mabrouk, K.; Kauffmann, T.H.; Aroui, H.; Raman, M.D.F. Raman study of cation effect on sulfate vibration modes in solid state and in aqueous solutions. *J. Raman Spectrosc.* **2018**, *44*, 1603–1608. [CrossRef]
22. Reynard, B.; Remy, C.; Takir, F. High-pressure Raman spectroscopic study of Mn_2GeO_4, Ca_2GeO_4, Ca_2SiO_4, and $CaMgGeO_4$ olivines. *Phys. Chem. Miner.* **1997**, *24*, 77–84. [CrossRef]
23. Mitsuda, T.; Asami, J.; Matsubara, Y.; Toraya, H. Hydrothermal formation of γ-dicalcium silicate from lime-silica mixt.pdf. *Cem. Concr. Res.* **1985**, *15*, 613–621. [CrossRef]
24. Singh, N.B. Hydrothermal synthesis of β-dicalcium silicate (β-Ca_2SiO_4). *Prog. Cryst. Growth Charact. Mater.* **2006**, *52*, 77–83. [CrossRef]
25. Fierens, P.; Picquet, P. Kinetic Studies of the Thermal Synthesis of Calcium Silicates above 1400 °C: I, Dynamic Thermal Synthesis of Ca_2SiO_4. *J. Am. Ceram. Soc.* **1975**, *58*, 50–51. [CrossRef]
26. Kostakis, G. Mineralogical composition of boiler fouling and slagging deposits and their relation to fly ashes: The case of Kardia power plant. *J. Hazard. Mater.* **2011**, *185*, 1012–1018. [CrossRef]
27. Li, J.; Zhu, M.; Zhang, Z.; Zhang, K.; Shen, G.; Zhang, D. The mineralogy, morphology and sintering characteristics of ash deposits on a probe at different temperatures during combustion of blends of Zhundong lignite and a bituminous coal in a drop tube furnace. *Fuel Process. Technol.* **2016**, *149*, 176–186. [CrossRef]
28. Tschegg, C.; Ntaflos, T.; Hein, I. Thermally triggered two-stage reaction of carbonates and clay during ceramic firing-A case study on Bronze Age Cypriot ceramics. *Appl. Clay Sci.* **2009**, *43*, 69–78. [CrossRef]
29. Ptáček, P.; Opravil, T.; Šoukal, F.; Havlica, J.; Holešinský, R. Kinetics and mechanism of formation of gehlenite, Al-Si spinel and anorthite from the mixture of kaolinite and calcite. *Solid State Sci.* **2013**, *26*, 53–58. [CrossRef]
30. Rashid, A.R.; Shamsudin, R.; Abdul Hamid, M.A.; Jalar, A. Low temperature production of wollastonite from limestone and silica sand through solid-state reaction. *J. Asian Ceram. Soc.* **2014**, *2*, 77–81. [CrossRef]
31. Choi, G.; Glasser, F.P.; Skalny, C.J. The sulphur cycle in cement kilns: Vapour pressures and solid-phase stability of the sulphate phases. *Cem. Concr. Res.* **1988**, *18*, 367–374. [CrossRef]
32. Scholten, T. Reaktionskinetik von sulfatischen Klinkerphasen in Zementen mit verminderter CO_2-Last. Ph.D. Dissertation, Technische Universität Clausthal, Clausthal-Zellerfeld, Germany, 2017.
33. Rheingans, B.F. Analysis of the kinetics of phase transformations. *J. Mater. Sci.* **1992**, *27*, 3977–3987.

EPILOGUE

The second study reports the results of sintering experiments with green bodies that contained anhydrite, quartz, and lime. In these multi-phase experiments, the additional free CaO (lime) in contact with quartz resulted in preferential formation of dicalcium silicate rather than of wollastonite when compared to the first study where Ca was only provided by the decomposition of anhydrite.

It was found that the formation of ternesite occurs at about 930 °C due to the reaction between α'_L-Ca_2SiO_4 and anhydrite. A longer dwell time led to an earlier formation of ternesite, which transformed to dicalcium silicate, lime, and sulfur oxide within the temperature range between 1020 and 1100 °C. Therefore, a small stability field of about 90–170 °C for ternesite was determined from the in situ multi-phase experiments. During quenching to RT, α'_L-Ca_2SiO_4 transformed to β-Ca_2SiO_4 (larnite) or recrystallized to ternesite, although it obviously depended on the reaction progress whether larnite or ternesite was observed at RT. Furthermore, the upper stability limit of ternesite determined by the sintering experiments was confirmed by a heating study of a natural ternesite crystal, which revealed a phase transformation to α'_L-Ca_2SiO_4 between 730 and 1120 °C. Within this temperature range, both ternesite and dicalcium silicate domains co-exist.

4 High-temperature phase transformations of hydroxylapatite and the formation of silicocarnotite in the hydroxylapatite - quartz - lime system studied in situ and in operando by Raman spectroscopy

PREFACE

The third study focuses on the formation of silica-/calcium phosphates, thus the sulfate component was replaced by a phosphate-containing material compared to the previous studies. The minerals of the model system $Ca_{10}(PO_4)_6(OH)_2$-SiO_2-CaO are of great technical interest as they play an important role in medical applications due to their excellent biocompatibility. Both hydroxylapatite ($Ca_{10}(PO_4)_6(OH)_2$, HAp) and β-tricalcium phosphate (β-$Ca_3(PO_4)_2$, β-TCP) are well-known mineral phases for bone substitution [e.g., 17]. The detailed information on the properties, synthesis, and applications of calcium phosphate materials has been reviewed by Dorozhkin [53,54]. Recently, however, promising studies with silicon-substituted calcium phosphates yielding silicocarnotite ($Ca_5(PO_4)_2SiO_4$) have shown that silicon is an essential trace element for bone mineralization and can enhance the bioactivity of calcium phosphate materials [18–23]. Moreover, the studied minerals are also identified as sinter deposits in industrial kilns. In particular, HAp and silicocarnotite are found in sewage sludge ashes, which are of increasing interest due to the debate on the combustion of alternative fuels instead of coal. Silicocarnotite can also be identified in basic slags produced in metallurgical processes [55,56]. A detailed knowledge of the thermodynamics and kinetics of the HT reactions in the $Ca_{10}(PO_4)_6(OH)_2$-SiO_2-CaO system is thus of great importance for the various fields of the high-temperature industry.

In the present study, the individual thermal behavior of HAp and TCP between RT and 1300 °C in 10 °C-steps and a natural silicocarnotite crystal between RT and 1200 °C in 50 °C-steps was investigated by Raman spectroscopy. The results of these experiments were important to identify the different phosphate phases at high temperatures, i.e., the Raman spectra provide HT reference spectra that are needed for hyperspectral Raman imaging. Furthermore, samples containing HAp, quartz, and CaO were fired to about 1200 °C and the mineral reactions, in particular the formation of silicocarnotite, were studied by in situ hyperspectral Raman imaging.

The following manuscript "Böhme N, Hauke K, Dohrn M, Neuroth M, Geisler T. High-temperature phase transformations of hydroxylapatite and the formation of silicocarnotite in the hydroxylapatite - quartz - lime system studied in situ and in operando by Raman spectroscopy. *J Mater Sci* **2022**. Submitted [57]" is currently under review.

Author contributions:

Nadine Böhme planned the experiments and procured the sample material. The sample preparation and all Raman measurements were also performed by Nadine Böhme. Matthias Dohrn performed and evaluated the DTA/TG analyses. In addition, literature research and the preparation of the original draft were done by Nadine Böhme with the assistance of Kerstin Hauke. Manuela Neuroth provided information on the combustion process of biomasses. Thorsten Geisler commented and proofread the manuscript, while all authors contributed to the final version of the manuscript. All co-authors agree to the use of the publications for this dissertation and to the identification of the doctoral student's contribution.

Abstract: Silica-/calcium phosphate ceramics are of high interest in various aspects. On the one hand, they play an important role in medical applications due to their excellent biocompatibility. Therefore, detailed knowledge of the formation and stability properties of the high-temperature products ensures production under controlled conditions. On the other hand, they were identified as sinter deposits in industrial kilns, where it can indicate problems caused by too high combustion temperatures during the thermal combustion processes. Here, we report the results of two Raman heating studies to ~1300 °C in 10 °C-steps with nanocrystalline hydroxylapatite (HAp) and tricalcium phosphate (TCP), and a Raman heating study of natural silicocarnotite (to ~1200 °C, 50 °C-steps). The Raman experiments were complemented with thermal analyses. The Raman spectra of nanocrystalline HAp recorded at high temperatures revealed the stepwise loss of adsorbed water and surface-bound OH groups until ~570 °C. Significant loss of structural OH started at ~770 °C and was completed at ~850 °C, when HAp transformed to β-TCP. Between ~1220 and ~1270 °C, β-TCP was found to transform to α-TCP. The room temperature Raman spectrum of silicocarnotite is characterized by an intense $v_1(PO_4)$ band at 951 ± 1 cm^{-1} that shifts to ~930 cm^{-1} at ~1200 °C. Using hyperspectral Raman imaging with a micrometer-scale spatial resolution, we were able to monitor in operando and in situ the solid-state reactions in the model system $Ca_{10}(PO_4)_6(OH)_2$-SiO_2-CaO, in particular, the formation of silicocarnotite. In these multi-phase experiments, silicocarnotite was identified at ~1150 °C. The results demonstrate that silicocarnotite can form from by a reaction between β-TCP and α'_L-Ca_2SiO_4, but also between β-TCP and $CaSiO_3$ with additional formation of quartz.

Keywords: calcium phosphate ceramics, silicocarnotite, hydroxlyapatite, tricalcium phosphate, high-temperature, sintering reactions, in situ, Raman imaging

1 Introduction

Since the first experiment with implanted tricalcium phosphate (TCP) into animals was performed in 1920 to test its ability as a bone substitute [1], numerous studies on calcium phosphate materials have been published. This reflects the fact that calcium phosphate phases play an important role in ceramics for biomedical application due to their excellent biocompatibility, bioactivity, and osteoconductive properties [e.g., 2–11]. Furthermore, silica-/calcium phosphates have been identified in sinter residues from thermal combustion processes. As part of the debate about coal combustion, significant attention is currently being paid to alternative fuels like biomasses and sewage sludge. Several studies demonstrate the presence of calcium phosphates in biomass ashes/deposits [12] from olive pit [13–15], manure [16], agricultural and forest residues [17], and from bone material [18]. Recently, hydroxlyapatite ($Ca_{10}(PO_4)_6(OH)_2$, HAp) was found to be the most frequent mineral phase in sewage sludge ashes [19–21].

Meanwhile, HAp is the best-known calcium phosphate based bioceramic, because its chemical compound and crystalline structure are similar to the inorganic part of bone composition [6,22–24]. However, studies have indicated a better bioresorption of β-tricalcium phosphate (β-$Ca_3(PO_4)_2$, β-TCP) due to its greater solubility than HAp in physiological environments [2,9]. Both, HAp and TCP based materials can be prepared by several methods (e.g., precipitation, sol-gel, hydrothermal, solid-state reaction [25], and surfactant template method [26,27]). The phase transformation of HAp to β-TCP was observed by the gradually release of OH^- ions at about 1000 °C [28,29] or even above 1200 °C [30]. Other authors reported a transition temperature range between 700 and 900 °C [31]. At about 1125 °C, the metastable β-phase transforms to the first high-temperature α-phase of $Ca_3(PO_4)_2$ [32,33] and at about 1450 °C to the α'-$Ca_3(PO_4)_2$ polymorph [32–35]. The high-temperature (HT) phase equilibria of TCP minerals were first investigated in 1959 by Nurse and co-workers [32] within the subsystem $Ca_3(PO_4)_2$-Ca_2SiO_4. Recently, highly promising studies with silicon-substituted calcium phosphates have shown that silicon is an essential trace element for bone mineralization and can improve the bioactivity

of calcium phosphate materials [36–41]. The wide range of CaO, SiO_2, and P_2O_5 solid solutions varies with temperature and makes silicocarnotite ($Ca_5(PO_4)_2SiO_4$) [32,34,42–45] an excellent ceramic with great potential for medical applications [41,45–48], which creates interest in knowledge about its synthesis conditions [35,46,49,50].

Although silicocarnotite was found in basic slags rich in phosphorus centuries ago [51,52], the natural silicocarnotite, however, was first identified and described by Galuskin and co-authors in 2015 [53]. The minerals of the silicocarnotite-ternesite solid solution series occur in larnite and gehlenite rocks of the Hatrurim Complex (Israel/Palestine). Both in nature and laboratory, silicocarnotite is commonly associated with dicalcium silicate (larnite, Ca_2SiO_4, or C_2S). The synthetic formation of silicocarnotite is described as cooling product of the so-called R phase, which is assumed to represent a solid solution between α'-$Ca_3(PO_4)_2$ and α-Ca_2SiO_4. An upper stability limit of about 1450 °C has been found for silicocarnotite [33–35]. Obviously, the HT behavior of silica-/calcium phosphates has attracted increasing interest due to its potential for technical and medical applications. Moreover, HAp, TCP, and silicocarnotite can serve as temperature indicators once their thermal stability fields are known, which could help kiln operators to optimize the combustion temperatures. Furthermore, this knowledge is important to ensure that the phosphate bioceramics are synthesized under optimal conditions. It follows that a detailed knowledge of the thermodynamics and kinetics of the HT reactions in the system $Ca_{10}(PO_4)_6(OH)_2$-SiO_2-CaO is essential in order to better understand the high-temperature behavior of silica-/calcium phosphates.

In the present study, samples of calcium oxide, quartz, and HAp were fired to about 1200 °C and the reactions were monitored in situ by confocal hyperspectral Raman imaging. The Raman spectrometer system with integrated heating stage allows to visualize mineral reactions and textures even at high temperatures with a spatial resolution of a few micrometers and without the need to quench the sample to room temperature (RT) before analyzing it [54–57]. Therefore, solid-state reactions can be studied in operando, i.e., while they are running. However, before performing the multi-phase sinter experiments, we studied the individual thermal behavior of HAp and TCP between RT and 1350 °C in 10 °C-steps and of a natural silicocarnotite crystal between RT and 1200 °C in 50 °C-steps, respectively, by Raman spectroscopy. The results of these experiments were, inter alia, essential to identify the different phosphate phases at high temperatures, i.e., the Raman measurements provide HT reference spectra that are needed for hyperspectral Raman imaging.

2 Materials and methods

2.1 Samples and sample preparation

To study the temperature behavior of silicocarnotite by Raman spectroscopy, natural silicocarnotite grains of the holotype specimen YV-415 within a silicocarnotite-bearing gehlenite from Har Parsa, Negev, were used [53]. The sample contains 1.85 ± 0.15 wt.-% SO_3 as major impurity [51]. The polished sample, provided by the Museum of Natural History in Bern, was prepared to a sample with a diameter of 5 mm and a height of < 1 mm to minimize the temperature gradient between sample surface and thermocouple. The isochronal heating experiments with nanocrystalline HAp and TCP (©VWR, Darmstadt, Germany) were carried out with a small green body that was produced by compacting powdered precursor material into a cylinder (3 mm x 1 mm) at a pressure of 10 kPa to produce a flat surface.

The sinter experiments were carried out with cylindrical green bodies (3 mm x 1.5 mm) that were produced by compacting 20 mg of powdered precursor material. The samples were prepared from natural crystals of quartz (origin unknown), nanocrystalline HAp powder (©VWR, Darmstadt, Germany) and CaO powder (©Merck, Darmstadt, Germany). Before firing, the materials were checked

for the occurrence of potential contaminations by ultra-fast Raman imaging and XRD measurements using a Bruker D4 powder diffractometer (Bruker, Madison, USA) at the RWE Power AG, Niederaußem, Germany. The crystallite size of HAp was estimated to be about 25 nm based on the broadening of X-ray diffraction peaks obtained with the TOPAS (Bruker) software using the Scherrer formula.

Although the CaO was stored in a furnace at 100 °C before usage, a few calcite grains could be detected, which, however, decomposed to CaO during the experiments. Because β-TCP is not stable at RT, conventional powder consists of HAp. Also traces of monetite, $Ca(PO_3OH)$, were identified in the precursor material [58].

2.2 Experimental details

To study (i) the formation temperature of silicocarnotite, (ii) the decomposition mechanism(s) of HAp to TCP and potential other products, and (iii) the phase transformation of β-TCP to α-TCP, heating experiments of pure materials and four sintering experiments in the $Ca_{10}(PO_4)_6(OH)_2$-SiO_2-CaO system were carried out at temperatures of up to 1190 ± 5 °C (Table 1). The experiments were performed using a LINKAM TS 1500 heating stage (Linkam Scientific Instruments, Surrey, UK) that was mounted onto the automated x-y-z stage below the microscope objective of the Raman microscope. Due to the height and the volume of the sample cylinder, a strong temperature gradient unavoidably occurs within the furnace. This gradient was empirically determined by a procedure that is described in detail by Stange and co-workers [54].

Two types of sinter experiments with two different mixtures of HAp, quartz, and lime were performed (Table 1). In the in situ experiments TQC-1 and TQC-2, the samples were fired to high temperature with a heating rate of 10 °C/min. Immediately, after reaching the respective temperature, two in situ Raman images were subsequently taken. Then, the sample was fired and measured in 50 °C-steps until the maximum temperature was reached. After recording the last image at the maximum temperature, the sample was cooled down to RT with a cooling rate of 10 °C/min and a last Raman image was recorded. In experiment TQC-3 the effect of quenching was studied. After recording a Raman image at the firing temperature, the sample was cooled to RT with a cooling rate of 10°C/min. At RT, a Raman image was recorded before firing the sample to the next temperature step. We note that the images acquired at RT form the basis for the interpretation of conventional sintering experiments, in which the sample has to be quenched at RT before analysis.

Table 1: Experimental conditions.

Exp.	**HAp:Qz:CaO** [wt.-%]	**Type of experiment**	**T_{range}** [°C]	**T_{step}** [°C]	**T_{rate}** [°C/min]	**Acquisition time** [s]	**Recording time** [h]
Silicocarnotite		Heating study	30–1200	50	10 ↗↘	100	-
Hydroxylapatite (HAp)		Heating study	30–1350	10	10 ↗↘	100	-
Tricalcium phosphate (TCP)		Heating study	30–1350	10	10 ↗↘	100	-
TQC-1	4:2:1	In situ	820–1190	50	10 ↗↘	0.5 (SWIFT)	2 x 2 (4)*
TQC-2	1:1:1	In situ	960–1190	50	10 ↗↘	0.5 (SWIFT)	2 x 2 (4)*
TQC-3	1:1:1	In situ/quench	960–1190	50	10 ↗↘	0.5 (SWIFT)	2 x 2 (4)*

*During a dwell time of 4 h, two Raman images with a recording time of about 2 h were recorded.

2.3 Raman spectroscopy

The Raman measurements were carried out using two different Raman spectrometers (Horiba Scientific HR800/HR800 Evolution, Kyōto, Japan) both equipped with an electron-multiplier charge-coupled device (CCD) detector, an Olympus BX41 microscope, and a 2W Nd:YVO_4 (λ = 532.11 nm) and a Nd:YAG (λ = 532.09 nm) laser, respectively. A 50x long-working distance objective with a numerical

aperture (*NA*) of 0.5, a grating with 600 grooves/mm, and a 100 µm spectrometer entrance slit was used for all measurements. With this setting, the spectral resolution of all measurements was 3.5 cm^{-1}, as given by the width of a Ne line at 1707.36 cm^{-1} and 1707.06 cm^{-1}, respectively. To correct for any spectrometer shift during long-time measurements, the intense Ne line was continuously monitored as ''internal'' frequency standard in all spectra [54,59,60]. The linearity of the spectrometer was regularly calibrated using the Rayleigh line and the fundamental band of a silicon standard at 570.7 cm^{-1}. During the heating studies, single crystal spectra were acquired for 100 s at each temperature step. For the sinter experiments, in situ hyperspectral Raman images were recorded from an area of 100 x 100 μm^2 with a 1 µm step size (100 x 100 μm^2 = 10,000 pixel per image) in *x* and *y* direction. At each step, a Raman spectrum was recorded for 0.5 s. Due to temperature- and reaction-related shrinkage or expansion effects, the sampling area can strongly shift during cooling and heating. Therefore, at HT 100 x 100 μm^2-sized and at RT, 160 x 160 μm^2-sized images were taken so that the same area could be analyzed at all temperature steps. The focus was reset before each image was taken in order to compensate for these effects using the autofocus function of the instrument that is based on a high precision piezo translator and feedback signal to automatically track and optimize the laser focus on the sample to achieve the optimal Raman signal-to-noise ratio. The best achievable lateral and axial (depth) resolution of the Raman measurements with the focus at the sample surface is usually estimated from the theoretical diffraction limit given by $d_l \approx 1.22\lambda/NA$ and $d_a \approx 4\lambda/NA^2$, yielding 1.3 and 8.5 µm in our case, respectively. However, the real lateral and axial resolution may rather be in the order of $d_l \approx 2$ µm and $d_a \approx 15$ µm, respectively [54,57]. It is important to note that the axial resolution at the surface also depends on the absorption properties of the material investigated. Generally, for the phases of interest, about 50 % of the Raman intensity is lost within the first 10 to 20 µm [57].

2.3.1 Hyperspectral Raman imaging

The data reduction and generation of hyperspectral false-color Raman images is based on the classic least-squares (CLS) fitting procedure [54,55,57]. In general, mineral phases are identified by the characteristic positions and relative intensities of their fundamental Raman bands. With an increasing temperature, the Raman bands of mineral phases usually shift individually to lower wavenumbers and their linewidth (full width of half-maximum) increases. Additionally, the black body radiation of the samples increases during firing and reduces the signal-to-noise ratio. The identification of minerals at high temperatures is further complicated by the fact that reference Raman spectral databases, such as, e.g., the RRUFF database [60], only contain RT spectra that usually differ significantly from their high-temperature (HT) counterparts. Therefore, the HT Raman spectra of relevant mineral phases were collected to build an in-house data base for the identification of mineral phases in multi-component systems at high temperatures and as reference spectra to be used as input data for the CLS analysis. The semi-quantitative mineral fractions of an imaged area were calculated by averaging the CLS fractions of all 10,000 spectra.

We note that the accuracy of the absolute mineral fractions is influenced by (i) crystal orientation, (ii) grain size, (iii) the temperature dependence of band position and linewidth, and (iv) the relative Raman scattering cross-sections of the mineral phases. Moreover, it has to be noted that we analyzed a relatively small area at the surface that is not necessarily representative for the entire green body. However, hyperspectral Raman imaging delivers 2-dimensional in situ information about the formation and decomposition of distinct phases and their textural relationship without the necessity of quenching the sample to RT. Moreover, Raman images can be taken during heating and cooling with a high-temperature, time, and spatial resolution. Note that all images created by our working group are shown in consistent colors.

2.3.2 Heating experiments

The green body of compacted HAp powder was fired from 30 to 1350 ± 5 °C in 10 °C-steps. At each temperature step, a spectrum was recorded from the same spot in the wavenumber range of 100–4000 cm^{-1}. A slight shift due to specimen expansion is possible, but not relevant since the material is homogeneous. After cooling down to RT, the same sample was fired from 30 to 1350 ± 5 °C in 10 °C-steps in order to record HT Raman spectra of TCP between 100 and 1730 cm^{-1}. The natural silicocarnotite sample was fired from 30 to 100 ± 5 °C and further until 1200 ± 5 °C in 50 °C-steps. Due to very small size of the silicocarnotite grains (< 5 µm) within the gehlenite matrix, an automated measurement at the same spot was not reliably possible and the analysis was performed manually at different spots.

For quantitative analysis, the RT Raman spectra of silicocarnotite, HAp, and TCP were least-squares fitted using an appropriate number of Gauss-Lorentz functions along with a cubic background function in the frequency range from 100 to 1200 cm^{-1}. Spectra of HAp and TCP taken above 30 °C were fitted between 850 and 1200 cm^{-1} and additionally between 3400 and 4000 cm^{-1} in the case of HAp. A 5^{th} order polynomial background function in the wavenumber range from 700 to 1200 cm^{-1} was used to correct the spectra of silicocarnotite taken above 30 °C. Before any fitting, the spectra were corrected for any spectrometer shift during long-time measurements using the Ne emission line at 1707.36 cm^{-1} and 1707.06 cm^{-1}, respectively, that was fitted using a Gauss function. The reported Raman frequencies are usually precise within ± 0.02 to ± 0.2 cm^{-1}, but for weak and broad bands, particular those measured at high-temperatures, we estimated a precision in the order of ± 0.3 to ± 1.2 cm^{-1} from multiple measurements. Spectrum fitting was performed using the LabSpec 6.4.4.15 (Horiba Scientific, Kyōto, Japan) software.

2.4 Thermogravimetric and differential thermal analysis (TG/DTA)

Two thermogravimetric and differential thermal analysis (TG/DTA) were carried out using a NETZSCH STA-449F3 system coupled with a 403 Aëolos Quadro quadrupole mass spectrometer (NETZSCH, Selb, Germany) at the RWE Power AG, Niederaußem, Germany. The measurements of the HAp sample were performed at a constant heating/cooling rate of 10 °C/min using an open corundum crucible in air. The scanning temperature range was from RT to 1350 °C (HAp) and to 1500 °C (β-TCP). The temperature measurement is typically accurate within ± 1 °C at low temperatures and accurate with ± 5 °C at high temperatures (> 1000 °C). Both measurements were performed one after the other. The TG curve during the first firing experiment shows the loss of OH^- ions, while the DTA results determine the formation and phase transformation temperatures, here in particular the HAp to β-TCP, β-TCP to α-TCP, and α-TCP to α'-TCP transitions.

3 Results

3.1 Room temperature (RT) Raman spectrum of silicocarnotite

Silicocarnotite ($Ca_5(PO_4)_2SiO_4$) and ternesite ($Ca_5(SiO_4)_2SO_4$) represent the phosphate- and sulfate-containing end member of a solid solution series. Both minerals are isotypic and crystallize in the space group *Pnma* (D^{16}_{2h}), i.e., no. 62 [42]. A group theoretical analysis yields the following irreducible representation for optical modes in the silicocarnotite structure:

$$\Gamma_{optic} = 35A_g + 31A_u + 31B_{1g} + 34B_{1u} + 35B_{2g} + 30B_{2u} + 31B_{3g} + 34B_{3u} \quad (1)$$

From these, the A_g, B_{1g}, B_{2g}, and B_{3g} modes are Raman active, i.e., 132 (8d: 108, 4c: 24) Raman bands are expected. There exist two types of PO_4 and SiO_4 tetrahedra on the mirror plane (MO_4) and those

in general positions (GO_4). Both tetrahedra types are connected with Ca^{2+} ions, which are coordinated by three oxygen atoms in the case of MO_4 and by four oxygen atoms in the case of GO_4 [42,53].

Figure 1 shows a Raman spectrum of the natural silicocarnotite sample recorded at RT. A least-squares fit of 49 Raman bands and a 3rd order polynomial background to the data in the frequency range of 100 to 1200 cm^{-1} yielded a good agreement between the measured and fitted sum spectrum (reduced $X^2 = 0.2$). 83 Raman bands remain undetected may be caused by hidden bands as part of broader bands due to limitations in the spectral resolution or too weak to be detected with the chosen analytical parameters.

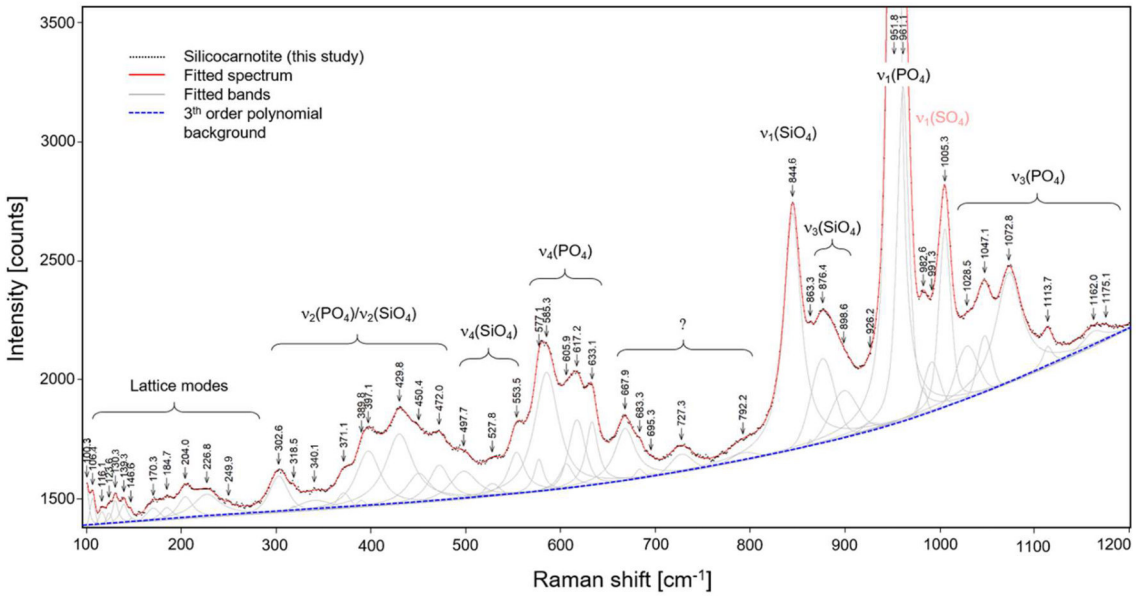

Figure 1: Room-temperature (RT) Raman spectrum of the natural silicocarnotite sample in the frequency range between 100 and 1200 cm^{-1}. The fitted spectrum, the deconvoluted bands, and the simultaneously fitted 3rd order polynomial background are also shown. The bands are assigned to the lattice vibrations and the internal bending and stretching modes of the PO_4 and SiO_4 tetrahedra.

Between 100 and 280 cm^{-1}, 12 of 21 lattice modes of Ca^{2+} rotational and translational modes can be identified. The group of bands between 300 and 500 cm^{-1} can be attributed to the $v_2(PO_4)$ and $v_2(SiO_4)$ bending modes [53,56,61–63]. The weak bands located at 498, 528, and 534 cm^{-1} may be assigned to the anti-symmetric $v_4(SiO_4)$ bending modes, as the $v_4(SiO_4)$ modes in the ternesite structure vibrate with similar frequencies [56]. The bands at frequencies higher than 800 cm^{-1} can be assigned to the internal symmetric and anti-symmetric stretching vibrations of both tetrahedral units. The bands at 876 and 899 cm^{-1} and those at frequencies larger than 1025 cm^{-1} correspond to the v_3 stretching modes of the SiO_4 and PO_4 tetrahedra, respectively [56,61,63–65]. The most intense Raman band is located at 952 cm^{-1} and the second most intense band near 845 cm^{-1}, which can be unequivocally assigned to the symmetric $v_1(PO_4)$ and $v_1(SiO_4)$ modes, respectively. As the sample is of natural origin and of the ternesite-silicocarnotite solid solution series, the $v_1(SO_4)$ mode can be additionally identified at 1005 cm^{-1} [53,56]. Note that the $v_1(PO_4)$ band is slightly asymmetric towards the higher frequency side. This is reflected by the fact that a second function, centered at 961 cm^{-1}, is needed to satisfactorily fit the band profile in this frequency range. In addition, it should be mentioned that the $v_1(PO_4)$ band was identified within a frequency range from 950 to 952 cm^{-1} measured at different localities on the analyzed grain, yielding an average $v_1(PO_4)$ frequency of 951 ± 1 cm^{-1}.

3.2 High-Temperature (HT) Raman spectra of silicocarnotite

Here, we present the first in situ, high-temperature (HT) Raman spectra from natural silicocarnotite crystals. In the following, we will focus on the analysis of the temperature behavior of the most intense v_1 bands of the SiO_4 and PO_4 units. These Raman bands are of great interest, as they can be used as fingerprint bands for the identification of silicocarnotite at RT, but also at high temperatures. Figure 2a presents a stacked plot of 21 Raman spectra, which were recorded between 30 and 1200 ± 1 °C in approximately 50 °C-steps.

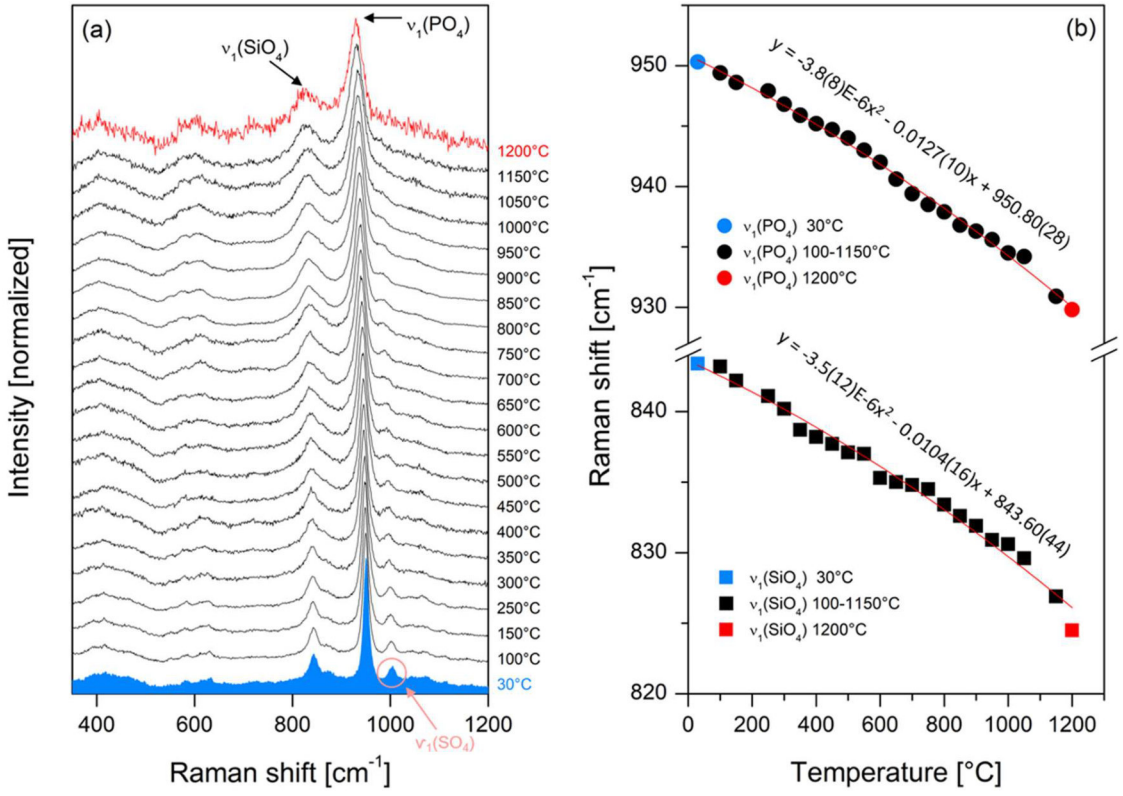

Figure 2: (a) Stacked Raman spectra (approx. 50 °C-steps) of the silicocarnotite sample recorded between 30 and 1200 ± 1 °C. (b) High-temperature (HT) frequencies of the $v_1(PO_4)$ and $v_1(SiO_4)$ bands each along with a quadratic fit (red curves, $r^2 > 0.98$).

During firing, all observable bands, including the $v_1(SiO_4)$ and $v_1(PO_4)$ bands, become broader and generally shift to lower frequencies. The FWHM values for both v_1 modes increase with increasing temperature and are listed in Table A1 in the Appendix. All identified bands remain detectable during the entire heating process, with the exception of the $v_1(SO_4)$ band that disappears between 1000 and 1050 °C. The ratio between the intensity of the $v_1(PO_4)$ band and the intensity of the $v_1(SO_4)$ band is 10:1 at RT and tends to zero at about 1050 °C (see Table A1). By plotting the fitted band positions of $v_1(PO_4)$ and $v_1(SiO_4)$ as a function of temperature, a different temperature dependence of the two modes becomes evident, as the $v_1(PO_4)$ mode shows a slightly larger frequency shift with increasing temperature than the $v_1(SiO_4)$ band (Figure 2b). From 30 to 1200 ± 1 °C, the $v_1(PO_4)$ and $v_1(SiO_4)$ bands shifted about 20 wavenumbers in respect to an experimental error of ± 0.02 and ± 0.3 cm^{-1} at RT and at 1200 °C, respectively, for the $v_1(PO_4)$ band and an experimental error of ± 0.3 and ± 1.2 cm^{-1} at RT and at 1200 °C, respectively, for the $v_1(SiO_4)$ mode. Interestingly, the ratio of the v_1 band intensities did not significantly change with increasing temperature ($A_{v1(PO4)}/A_{v1(SiO4)} \approx 4.8$), reflecting a particular temperature stability of silicocarnotite.

3.3 HT Raman spectroscopy of hydroxylapatite (HAp) and tricalcium phosphate (TCP)

The thermal decomposition of HAp can principally be followed by the release of structural hydroxyl groups that vibrate with a characteristic frequency of 3572 cm^{-1} at RT [61,64]. However, at RT, this band is hardly detectable in the Raman spectrum of the pressed nanocrystalline HAp tablet prepared for the heating study, as it is overlain by an intense and broad OH bands between 3520 and 4000 cm^{-1} (Figure 3a). We note here that these bands were not observed in spectra from the loose HAp powder. The $\nu(OH)_{HAp}$ band is first observable at temperature above 600 °C (Figure 3b). At RT, another broad intense OH band occurs near 3850 cm^{-1} that has two shoulders near 3800 cm^{-1} and 3890 cm^{-1}. Two further OH bands are detectable near 3960 cm^{-1} and 3980 cm^{-1}. All seven identifiable bands are labelled 1 to 7 from low to high frequency in Figure 3. The temperature behavior of the intensity of the different OH bands is shown in Figure 3c. The high frequency bands nos. 6 and 7 are the first OH bands that completely disappear during heating already at 120 °C. At about 200 °C, the OH band no. 5 disappears. The integrated intensity of OH bands nos. 2 and 4 gradually decrease between 100 and 400 °C and at 450 °C these bands also disappear. The OH band no. 3 can be detected until 570 °C. At about the same temperature, the characteristic $\nu(OH)_{HAp}$ band can be clearly identified near 3555 cm^{-1} (Figure 3b). From Figures 3b and 3c, it is further evident that the integrated intensity of $\nu(OH)_{HAp}$ is almost constant in the temperature range between 600 and 750 °C, but rapidly decreases at about 770 °C. At 810 ± 1 °C, the $\nu(OH)_{HAp}$ band cannot be detected in the spectra anymore.

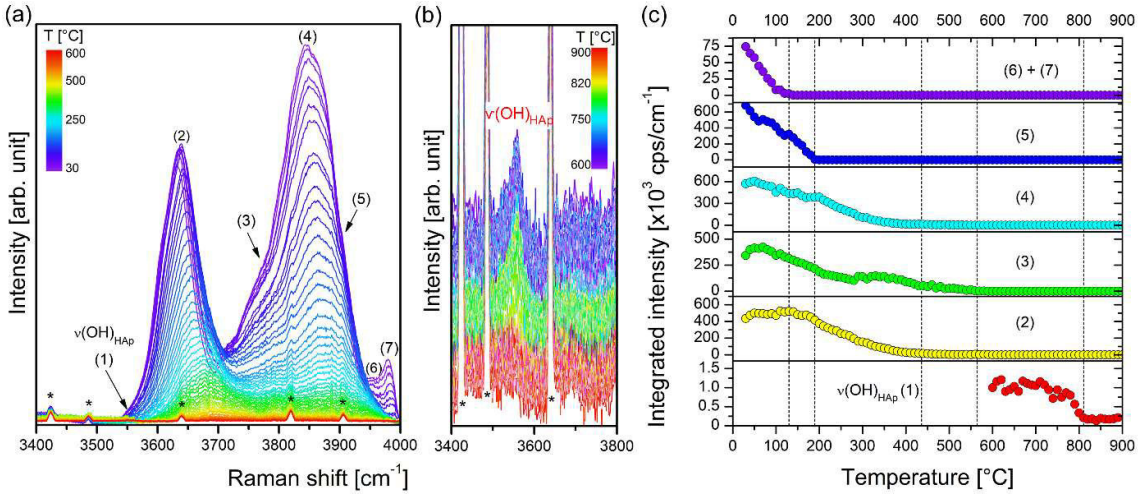

Figure 3: Stacked Raman spectra (10 °C-steps) of the hydroxylapatite (HAp) sample recorded between (a) 30 and 600 °C and (b) 600 and 900 °C with identified $\nu(OH)_{HAp}$ band and OH bands generated by surface-bound water. The black stars mark spikes caused by the long measuring time at high temperatures. (c) The temperature dependence of the integrated intensities of the identified OH bands. The $\nu(OH)_{HAp}$ band disappears at about 810 °C.

In the following, an analysis on the temperature behavior of the Raman bands of the PO_4 groups within the HAp and the TCP structures is presented. The most intense Raman band reflects the fully symmetric stretching motions of the PO_4 units of HAp. The other internal PO_4 modes are much weaker, but can also be used to quantitatively follow the decomposition of HAp to β-TCP and other calcium phosphates by Raman spectroscopy. The internal stretching and bending modes of the PO_4 tetrahedra can be identified within the frequency range between 300 to 1200 cm^{-1} (Figure 4). The groups of bands with the intense bands between 430 and 590 cm^{-1} at RT can be assigned to the internal $\nu_2(PO_4)$ and $\nu_4(PO_4)$ bending vibrations, respectively. The most intense band is due to the symmetric stretching mode $\nu_1(PO_4)$ and is located at 961 cm^{-1} at RT. The bands between 1000 and 1100 cm^{-1} can be assigned to the anti-symmetric stretching modes of PO_4 tetrahedra [61,64,66,67].

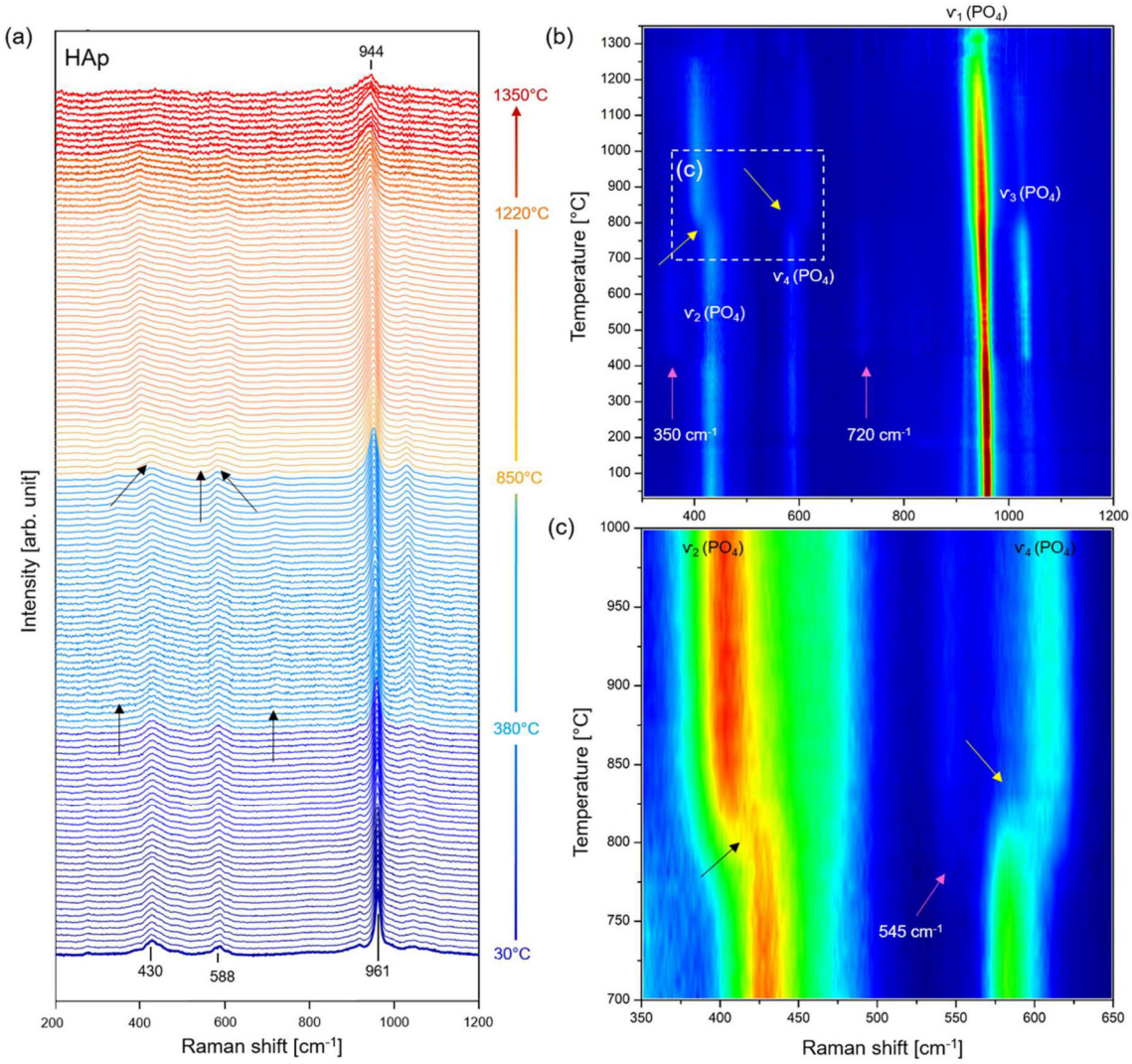

Figure 4. (a) Stacked Raman spectra (10 °C-steps) of nanocrystalline HAp recorded between 30 and 1350 ± 1 °C. Spectral changes during firing are highlighted by different colors and marked by black arrows marking the same spectral changes as the arrows in b and c. (b, c) The color-coded Raman intensity as a function of the Raman shift and temperature (red and blue colors represent high and low intensities, respectively). (b) Within the frequency range 300–1200 cm^{-1}, all PO_4 Raman modes can be identified. The most intense band $\nu_1(PO_4)$ is located at 961 cm^{-1} at RT. The yellow arrows point to a dramatic shift of ν_2 and $\nu_4(PO_4)$ bands between 770 and 850 °C. At about 400 °C, two new bands (350 cm^{-1}, 720 cm^{-1}) occur (pink arrows). (c) Zoomed part of the spectrum showing the bending vibrations between 700 and 1000 °C. At about 770 °C, a new band at 545 cm^{-1} occurs (pink arrow). See text for more details.

Plotting the fitted frequencies of the $\nu_1(PO_4)$ band as a function of temperature, a stepwise structural alteration of nanocrystalline HAp becomes evident from three local minima or short-term shifts to higher frequencies, indicating a slight shortening of the P–O bonds (Figure 5). The first local minimum at 200 °C maybe marks the loss of adsorbed water bound to the nanocrystalline HAp crystallites. When the temperature reaches 380 °C, the $\nu_1(PO_4)$ frequency shows a second minimum that correlates roughly with a marked intensity decrease of OH band (3) (Figure 3) and may be related to the loss of surface-bound hydroxyl groups [23,68]. Note that nanocrystallites are dominated by relaxed surface bonds, which has an impact on the vibrational properties, as, for instant, on the average P–O bond length and thus on the average frequency of the P–O vibrations. Between about 400 and 770 °C, the $\nu_1(PO_4)$ band shifts to lower frequencies with a third local minimum at about 570 °C that possibly represents another stage of loss of OH modes at the surface (Figure 5). Additionally, the $\nu_1(PO_4)$ and the $\nu_2(PO_4)$ bands narrow and, notably, the intensity of the $\nu_1(PO_4)$ band decrease within this

temperature interval, while the polarizability, i.e., the Raman intensity of the $v_3(PO_4)$ band increases (Figure 4b). The overall number of observable Raman bands increases, reflecting a change in the crystal symmetry and the loss of hydroxyl groups. At about 400 °C, a new band is observed at about 720 cm^{-1} (HT) and another second weak band appears near 350 cm^{-1} that we assign to the pyrophosphate β-$Ca_2P_2O_7$ (Ca/P < 1.5) [69–72].

At 770 °C, a very weak new band is observed at 545 cm^{-1} (HT) which increases in intensity at about 850 °C, indicating the formation of β-TCP [67]. A group theoretical analysis based on a rhombohedral structure (*R3c*) of the β-polymorph of TCP reveals 136 Raman active modes [73] which compares with 62 Raman active modes predicted for HAp ($P6_3/m$) [74,75]. Thus, more bands are expected with increasing temperature. However, due to the low intensity and large broadening of the bands at HT, the number and positions of the bands are difficult to determine. In general, also the identification of other calcium phosphates such as β-$Ca_2P_2O_7$, is very difficult as long as HT reference spectra are missing.

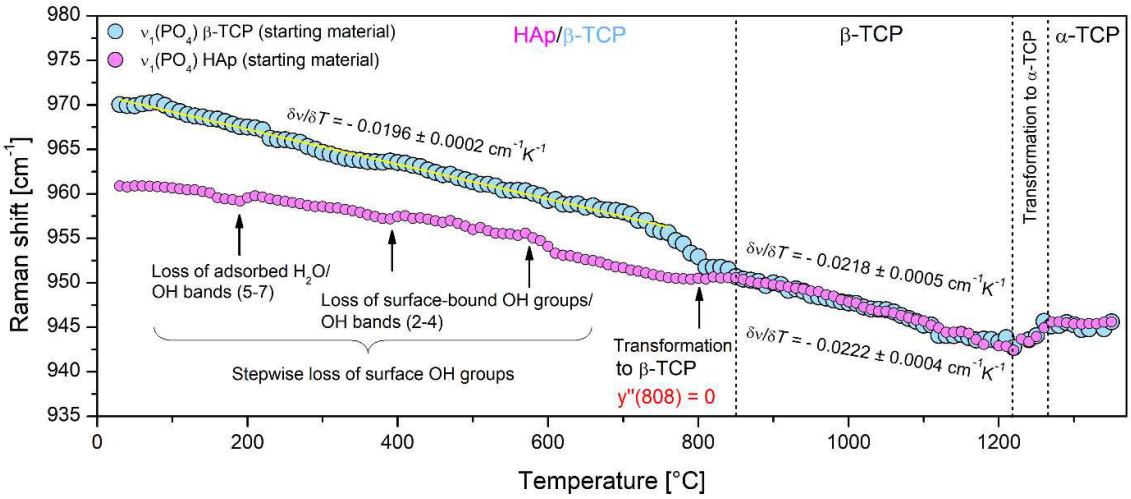

Figure 5: The frequencies of the $v_1(PO_4)$ bands of nanocrystalline HAp (pink) and tricalcium phosphate (TCP) (blue) as a function of temperature. Stippled lines mark the HAp to β-TCP and the β-TCP to α-TCP phase transformation, respectively.

Between 770 and 850 °C, the positions of the bending modes change significantly (Figure 4c). At about 810 °C, the $v_2(PO_4)$ and $v_4(PO_4)$ frequencies shift abruptly to lower and higher wavenumbers, respectively, while the PO_4 stretching mode frequency shift to a higher value. The inflection point of $v_1(PO_4)$ frequencies in the 700–900 °C range was determined at 808 °C. In addition, the intensity of the $v_2(PO_4)$ band increases with temperature increase and the intensities of the anti-symmetric modes decrease. Obviously, HAp decomposed to β-TCP, H_2O, and as an intermediate product to β-$Ca_2P_2O_7$.

The formation of β-TCP is further evidenced by the observation that the frequency of the $v_1(PO_4)$ band of HAp merges at about 850 °C with the HT $v_1(PO_4)$ frequencies observed for β-TCP (Figure 7). Figure 6 shows all Raman spectra of β-TCP in the frequency range of 200–1200 cm^{-1} recorded between 30 and 1260 ± 1 °C. At RT, there are two distinct bands at 948 and 969 cm^{-1} and one shoulder at about 961 cm^{-1}, respectively, corresponding to $v_1(PO_4)$ vibrations of β-TCP [65,67,72,76], resulting from three nonequivalent PO_4 units in the unit cell [73]. Interestingly, the weak band at 918 cm^{-1}, that is also assigned to a $v_1(PO_4)$ mode, does not shift significantly (± 2 cm^{-1}) until 1350 °C. The weak band located at 1089 cm^{-1} within the RT spectrum of β-TCP (Figure 6) was not observed during the heating study of HAp. However, it can be clearly attributed to the $v_3(PO_4)$ modes of β-TCP [67].

When β-TCP is fired from RT to temperatures below about 770 °C, all observable bands become broader and generally shift to lower frequencies. The evolution of the frequency of the most intense

$v_1(PO_4)$ band as a function of temperature can be approximately described by a linear function until 770 °C ($r^2 > 0.99$). Here, the v_1 band shifts visibly to lower values and remains constant between about 800 und 830 °C (Figure 5). From Figure 6, it is evident that the two intense $v_1(PO_4)$ bands of β-TCP merge at about 850 °C indicating a degeneration of $v_1(PO_4)$ modes. Furthermore, both 850 °C spectra of HAp and β-TCP as starting material show almost the same positions of PO_4 modes and in each case the symmetric bending vibrations result in a stronger polarizability, i.e., higher Raman intensity, than the respective anti-symmetric bending vibrations (Figure 7c). Above about 850 °C, both $v_1(PO_4)$ bands exhibit the same shift ($\delta v/\delta T$ = -0.02) with increasing temperature (Figure 5). At about 1220 °C, the $v_1(PO_4)$ bands show a local minimum before the frequencies shift to a higher value of 945 cm^{-1} until 1260 °C (Figures 5 and 6). In this temperature range, the β-polymorph of TCP reconstructively transformed to the α-TCP polymorph. At higher temperatures, both modes cease to shift to higher frequencies until the maximum sintering temperature is finally reached.

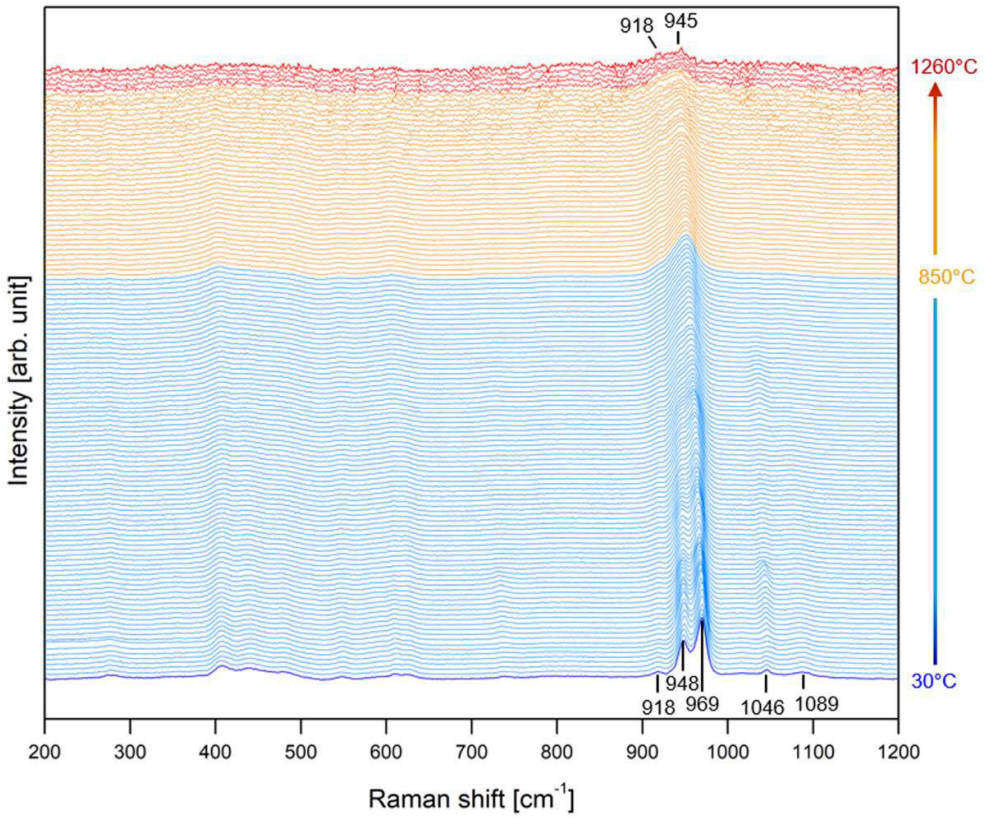

Figure 6: Stacked Raman spectra (10 °C-steps) from the β-TCP sample recorded between 30 and 1260 ± 1 °C. The characteristic $v_1(PO_4)$ modes are located at 948 and 969 cm^{-1}, respectively. Above 850 ± 1 °C, the two $v_1(PO_4)$ bands merge into a single band (yellow spectra). Between 1220 and 1260 ± 1 °C, β-TCP transformed to α-TCP (red spectra) in our experiment.

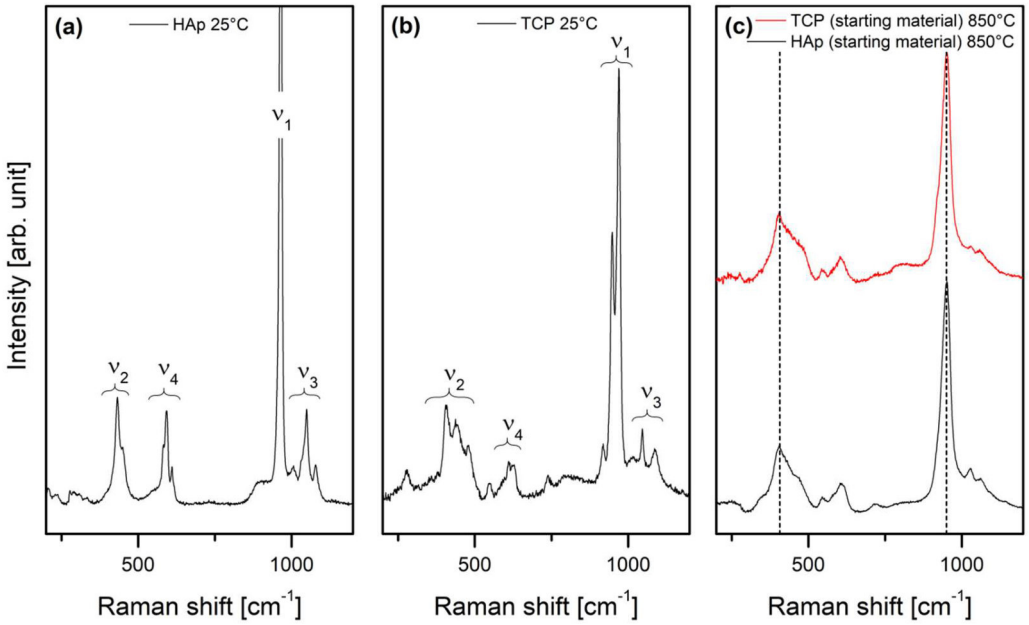

Figure 7: Room-temperature (RT) Raman spectra of (a) HAp and (b) TCP with identified vibrational modes of the PO_4 groups.(c) Comparison of Raman spectra of HAp and TCP recorded at 850 ± 1 °C.

3.4 Results of the thermal analyses of HAp and TCP

Figure 8a shows the thermogravimetric measurement of the nanocrystalline HAp powder up to 1350 °C. In Table 2, we link the thermal analyses results with those from high-temperature Raman spectroscopy. The TG curve from HAp reveals a first mass loss step in the temperature range between about 100 and 200 °C (green curve) that can be explained by the loss of adsorbed water, reflected by the disappearance of Raman bands (6) and (7). A second mass loss is observed between 200 and 380 °C. Above about 380 °C, the weight decreases rapidly until 480 °C and results in the largest mass loss of ~3.1 wt.-% (mass loss step 3), possibly due to the loss of further surface-bound water. After this temperature, the mass decreases slowly (mass loss steps 4 to 6) with another step near 750 °C (mass loss step 5). Beyond 1050 °C, the sample weight remains stable at ~93.7 % of the original weight. Figure 8a additionally shows a quadrupole mass spectrometric measurement of the molecular mass 18, corresponding to molecular water, as a function of temperature (orange curve). These data show two broad and less intense peaks at about 115 and 770 ± 1 °C and one intense peak near 450 ± 1 °C, which correlate well with the events observed in the TG curve.

The DTA curves of HAp and β-TPC are shown in Figure 8b. Between RT and about 460 °C the DTA heating curve of HAp is characterized by a broad and intense endothermic signal that can be assigned to the loss of adsorbed water and surface OH groups, also observed by Raman spectroscopy. Between 700 and 800 °C, small endothermic signals possibly can be attributed to the stepwise loss of structural OH^- ions as HAp transforms to β-TCP. The endothermic peak observed at 1300 (onset: 1277) ± 5 °C can be assigned to the β- to α-TCP transition, whereas the exothermic peak at 1080 ± 5 °C observed during cooling is associated with its reverse reaction. Both the endothermic and the exothermic peak, resulting from the β- ↔ α-TCP transition, have a similar peak area (~1535 versus ~1640 µVs, respectively). A second experiment was performed until 1500 °C, but revealed no further mass loss (data not shown here). The DTA curve of β-TCP shows two endothermic peaks at 1300 ± 5 °C (onset at 1287) and at 1480 (onset at 1454) ± 5 °C. The first peak reflects the β- to α-TCP polymorphic phase transformation and the second relates to the α- to α'-TCP transition. During cooling, an exothermic peak at 1450 (onset at 1444) ± 5 °C is observed, reflecting the reverse α'- to α-TCP transformation. The

two small exothermic signals at 1270 and 1080 ± 5 °C can be attributed to the transformation of the α-phase to β-TCP.

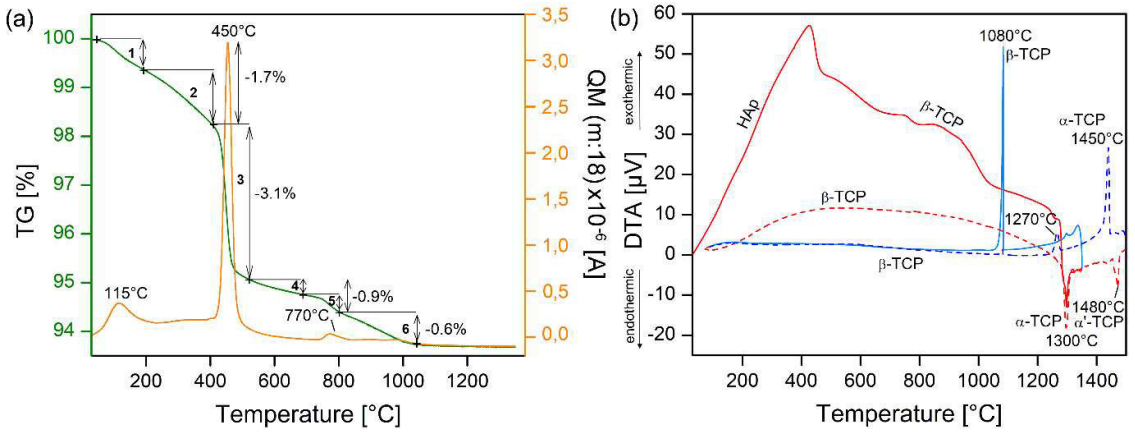

Figure 8: (a) Thermogravimetric (TG) and quadrupole mass (QM) measurements of mass 18 (H_2O) of nanocrystalline HAp powder. The strong weight loss (-3.1 %) at about 450 ± 1 °C corresponds to the loss of surface-bound water. (b) Differential thermal analysis (DTA) of HAp (solid lines) and β-TCP powder (dashed lines), respectively.

Table 2: Summary of in situ Raman spectroscopic and TG/QM/DTA results of pure HAp and β-TCP and interpretation of the observed features.

T [°C]	**Raman HT study** 100 - 1200 cm^{-1}	3000 - 4000 cm^{-1}	**TG/QM** (m:18)	**DTA**	**Interpretation**
115-120	$\delta\nu_1(PO_4)_{HAp}/\delta T$: 1. step	OH bands (6) and (7) were not detected anymore	First mass loss / peak at 115 °C		Loss of adsorbed molecular water
200		OH band (5) was not detected anymore	-	-	Loss of surface-bound hydroxyl groups → at 450 °C: Formation of pyrophosphates possibly as surface layers around nanocrystallites
380	$\delta\nu_1(PO_4)_{HAp}/\delta T$: 2. step	-	-	-	
450	New bands appeared near 350 and 770 cm^{-1}	OH bands (2) and (4) were not detected anymore	3.1 % mass loss / peak at 450 °C	Endothermic peak at 460 °C	
570	$\delta\nu_1(PO_4)_{HAp}/\delta T$: 3. step	OH band (3) was not detected anymore	-	-	
770	Shift of $\nu_1(PO_4)$ to higher frequency New band appeared near 545 cm^{-1}	The intensity of the OH band (1) begun to dramatically decrease	Mass loss / peak at 770 °C	Endothermic signals	Dramatic increase of HAp decomposition
810 850	Inflection point of the polynomial fit Bands near 350 and 770 cm^{-1} were not detected anymore	The OH band (1) was not detected anymore	-		Formation of β-TCP
1260-1280	Sudden shift of $\nu_1(PO_4)$ to higher frequency	-	-	Endothermic peak onset at 1280	β-TCP to α-TCP transformation during heating, *T* depends on the heating rate
1080	-	-	-	Sharp exothermic peak	α-TCP to β-TCP transformation during cooling, *T* depends on the cooling rate
~1450	-	-	-	Exo-/endo-thermic peak onsets at 1450	α -TCP to α'-TCP and α'-TCP to α -TCP transformation

3.5 Multi-phase in situ experiments (TQC-1 and TQC-2)

In the first experiment TQC-1, the green body containing HAp, quartz, and CaO in a weight ratio 4:2:1 was fired to 820 ± 5 °C with a heating rate of 10 °C/min and then stepwise (~50 °C-steps) to 1190 ± 5 °C. Figure 9a shows extracts of four false-colored hyperspectral Raman images taken at different temperatures and dwell times. It is clearly discernible that nanocrystalline HAp transforms unevenly (c.f., Chapter 3.3). At 820 ± 5 °C, the nanocrystalline HAp grains transformed to β-TCP only in the upper part of the imaged area. The temperature-dependent change of bending mode positions described above marks this transformation. In Figure 9b, two spectra of the image taken at 820 ± 5 °C after a dwell time of two hours are shown in a frequency range from 300 to 750 cm^{-1}. The spectrum 1 identifies HAp, however, it does not differ significantly from spectra recorded at lower temperatures, e.g., 700 ± 1 °C. The spectrum 2 can be compared to those taken at 820 ± 1 °C during the heating study of HAp and β-TCP, respectively. The bands at about 350 and 720 cm^{-1} (HT) can be assigned to pyrophosphates [69–72] formed by the decomposition of HAp. Within the imaged area, pyrophosphate is only visible at 820 ± 5 °C immediately after the temperature is reached. Upon further heating, the pyrophosphate concentration decreased as shown by single-phase images in Figure 9c. After two hours at 870 ± 5 °C, the bands identifying pyrophosphate are no longer detectable in the spectra. Whereas, more and more β-TCP can be identified. It is possible that additional β-TCP was formed by the reaction between pyrophosphate and small lime particles located below the image plane.

At 910 ± 5 °C, the spectra of HAp and β-TCP become increasingly similar and the colors in the Raman image appear blurred. Between 910 and 1190 ± 5 °C HAp completely transformed to β-TCP, but no other phases newly crystallized within the imaged area. However, after cooling down to RT, wollastonite was found outside the investigated area, formed by a reaction between lime and quartz.

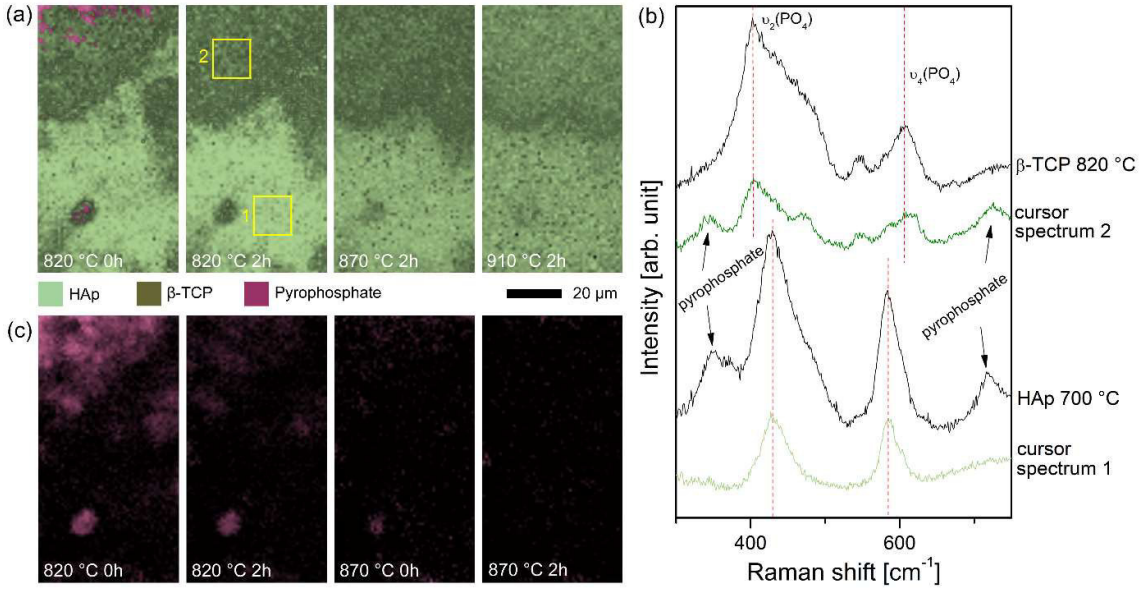

Figure 9: (a) Cutouts of false-colored hyperspectral Raman images of experiment TQC-1. Within the yellow boxes two spectra were taken, which are shown in (b) and compared to a HAp spectrum recorded at 700 ± 1 °C and a β-TCP spectrum recorded at 820 ± 1 °C, respectively. Note that the imaged areas represent many of nanocrystals and the crystallization seam is due to the transformation of HAp to β-TCP. (c) Single-phase Raman images of pyrophosphate identified at the first heating step at 820 ± 5 °C and formed by the decomposition of HAp. With increasing dwell time and temperature, the concentration of pyrophosphate decreased.

A proportional weight ratio of the phases of the green body was chosen for the in situ experiment TQC-2. False-color hyperspectral Raman images of an area 100 x 100 $µm^2$ were recorded in situ during stepwise high-temperature sintering (~50 °C-steps) to 1190 ± 5 °C (Figure 10). Two images were taken

in succession at each temperature. However, only representative images are shown here. At 960 ± 5 °C, all calcite was already decomposed to CaO and CO_2, as expected [57]. As in experiment TQC-1, the nanocrystalline HAp partially transformed to β-TCP and possibly to pyrophosphate, indicated by newly identified but very weak bands at about 350 and 720 cm^{-1} [69–72]. Moreover, the HT polymorph of dicalcium silicate (α'_L-Ca_2SiO_4) crystallized at interfaces between quartz and lime and as small grains within the HAp matrix. α'_L-Ca_2SiO_4 likely formed by the reaction with small SiO_2/CaO particles located below the focal image plane. Between 960 and 1050 ± 5 °C, more and more α'_L-Ca_2SiO_4 replaced larger quartz grains (marked in Figure 10). Furthermore, more β-TCP has formed from HAp. After the temperature was increased to 1100 ± 5 °C, the α'_L-Ca_2SiO_4 grains grew together and quartz was observed only as relics in the center of some grains. The time series images at 1150 ± 5 °C show the time-dependent formation of silicocarnotite, which could be identified after a dwell time of two hours in various spectra throughout the image area by its characteristic fundamental Raman bands near 930 and 828 cm^{-1} (spectrum 1 in Figures 10 and 11). These small silicocarnotite grains are located near dicalcium silicate grains within the HAp/β-TCP matrix. After firing to the maximum temperature of 1190 ± 5 °C, more silicocarnotite grains could be identified and HAp completely transformed to β-TCP within the recorded area.

Surprisingly, however, after cooling to RT, HAp could still be identified in the left half of the RT image in Figure 10. However, β-TCP is the main phosphate phase, identified by its intense double band near 948 and 969 cm^{-1} [65,67,72,76], while α'_L-Ca_2SiO_4 within the imaged area completely transformed to β-Ca_2SiO_4 (larnite) [55,56,62,77] during cooling. In particular, silicocarnotite could be identified in contact with dicalcium silicate at the same location within the β-TCP matrix where it was also detected at HT (spectrum 2 in Figures 10 and 11). Furthermore, silicocarnotite formed a distinct reaction rim around a large quartz grain that was preserved in the lower right of the imaged area. Notably, at RT, also wollastonite could be identified, usually in contact to silicocarnotite and larger quartz grains.

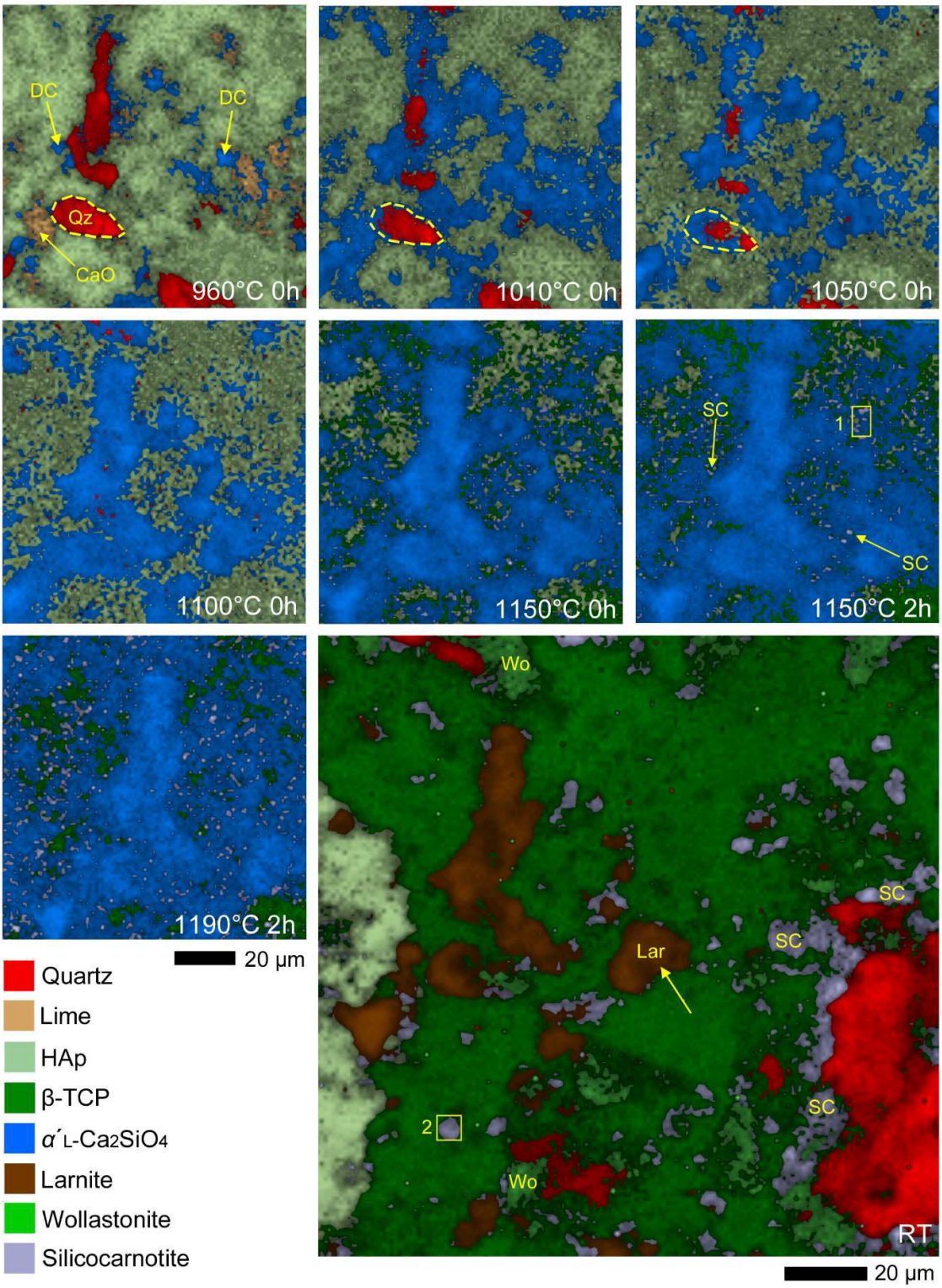

Figure 10: False-colored hyperspectral Raman images of the mineral distribution of a 100 x 100 µm² surface area of a green body containing HAp, CaO, and quartz at different temperatures and two dwell times (experiment TQC-2). The yellow arrows mark the new formed mineral phases dicalcium silicate (DC), and silicocarnotite (SC). Note that the formation of silicocarnotite started at 1150 ± 5 °C. During the cooling process, the α'L-phase of dicalcium silicate transformed to the ß-phase (larnite). Within the yellow boxes two average spectra were extracted (Figure 11).

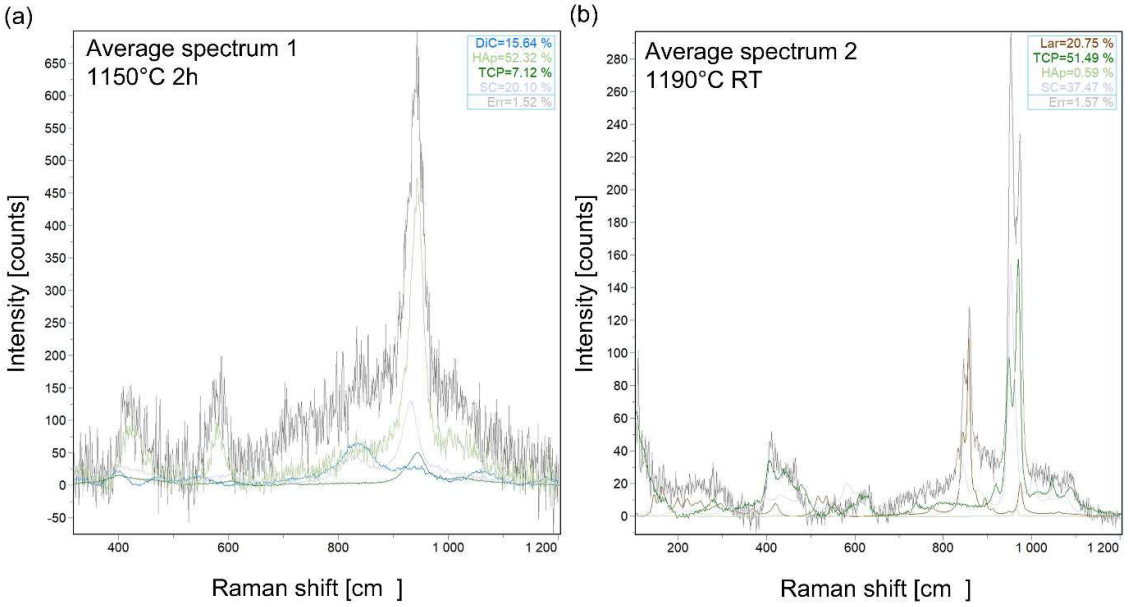

Figure 11: Average spectrum of (a) small silicocarnotite grains within the HAp matrix at 1150 ± 5 °C and of (b) a larger silicocarnotite grain within the β-TCP matrix at RT after cooling down from 1190 ± 5 °C.

3.6 In Situ/quench experiment TQC-3

The experiment TQC-3 was performed using the same precursor materials as in experiments TQC-1 and TQC-2 and the same weight ratio chosen for experiment TQC-2 to study the effect of quenching on phase assemblage. After recording a 100 x 100 µm^2-sized Raman image at the firing temperature, the sample was cooled to RT with a cooling rate of 10°C/min. At RT, a 160 x 160 µm^2-sized Raman image was recorded before firing the sample to the next temperature step. Due to the shrinkage and expansion of the sample the imaged area varies slightly. Unfortunately, not all mineral reactions observed at RT could also be identified at HT.

Figure 12 shows a direct comparison of the false-color hyperspectral Raman images recorded during the high-temperature firing and the quenching steps. During firing to the first temperature step of 960 ± 5 °C, calcite was already decomposed to lime but partially recrystallized during the following quenching step due to a high CO_2 fugacity in the furnace [56]. During the next firing steps, however, no more CaO was available anymore and therefore no calcite could form during quenching to RT. At 960 ± 5 °C, dicalcium silicate (α'_L-Ca_2SiO_4) was first detected, but transformed to larnite during cooling. Moreover, it is evident that during the first heating step HAp only partially decomposed to β-TCP and possibly other pyrophosphates, the formation of which is suggested by the observation of a weak Raman band near 720 cm^{-1} indicative for pyrophosphates [69–72]. In the course of the sintering experiment, the decomposition of HAp advanced and more and more α'_L-Ca_2SiO_4/larnite grew in the expense of quartz.

After heating to 1050 ± 5 °C and cooling down to RT, silicocarnotite and wollastonite were detected in contact with a large quartz grain located in the lower left of the image. About 8 vol.-% silicocarnotite can be clearly identified within the 5 x 5 µm^2 area marked by a yellow box in Figure 12. During the next firing/quenching step (1100 ± 5 °C) wollastonite grew at the expense of quartz, but on further firing/quenching (1150 ± 5 °C) the wollastonite content decreased while the silicocarnotite content increased as rim around the quartz grain. Interestingly, the quartz concentration seems to have remained stable and the wollastonite increased again during the last quenching from 1190 ± 5 °C.

From 1100 ± 5 °C, small silicocarnotite nuclei, surrounded by HAp/β-TCP matrix, could also be identified in various HT spectra throughout the imaged area. However, it has to be noted that due to the similarity of the spectra of silicocarnotite and β-TCP at HT, it is difficult to distinguish between these phases, in particular, if one of them occurs in low concentrations. Nevertheless, the large difference between the HT and RT silicocarnotite concentrations within the imaged area indicates that the main growth of silicocarnotite grains inside the HAp/β-TCP matrix near to larnite grains must have occurred during cooling down to RT. During firing to the next temperature steps at 1150 and 1190 ± 5 °C and quenching to RT, respectively, the formation of β-TCP from nanocrystalline HAp was advanced, which should have been already completed considering the heating study with HAp. At 1190 ± 5 °C, silicocarnotite grains became visible at HT und grew further during cooling to RT. At RT, many silicocarnotite grains were identified as rims around larger quartz grains and within the β-TCP matrix in direct contact with larnite (Figure 12). In both experiments TQC-2 and TQC-3, the upper stability limit of silicocarnotite was not reached.

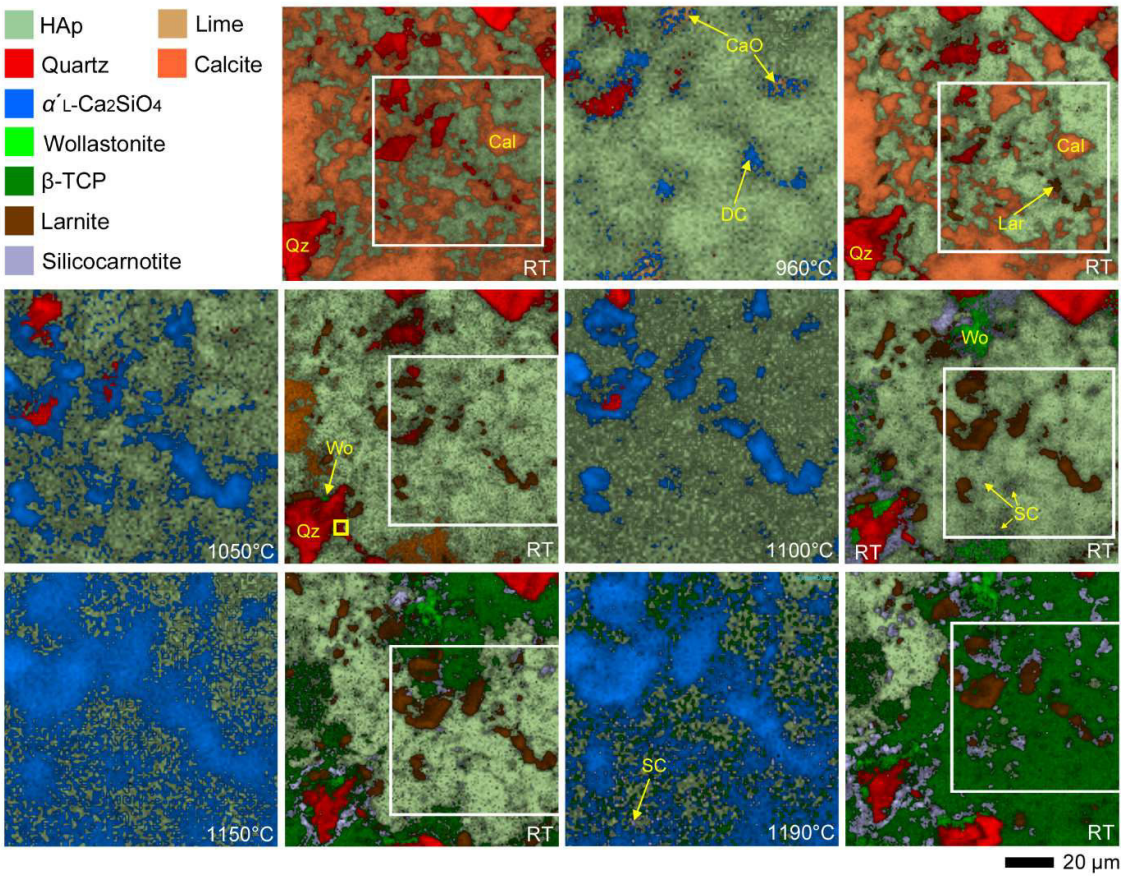

Figure 12: False-colored hyperspectral Raman images of the mineral distribution of a 100 x 100 µm² surface area of a green body containing HAp, lime, and quartz at different temperatures and after cooled to room temperature (experiment TQC-3). Note that a larger area was measured at RT. The white frame marks the corresponding area at HT. The imaged area varies slightly due to the shrinkage and expansion of the sample. The yellow arrows hint to the newly formed mineral phases dicalcium silicate (DC), wollastonite (Wo), and silicocarnotite (SC) within the HAp matrix which transformed to β-TCP during the experimental process. Dicalcium silicate crystallized in contact to lime in the expense of quartz. The high-temperature polymorph α´L-Ca2SiO4 crystallized to larnite during cooling to room temperature (RT) and recrystallized during firing. The formation of silicocarnotite started after cooling from 1050 ± 5 °C (8 vol.-% within the 5 x 5 µm² large yellow box) in contact to larnite and wollastonite, respectively. The crystallization of silicocarnotite within the HAp/β-TCP matrix started after cooling from 1100 ± 5 °C.

4 Discussion

4.1 The stability of HAp and the formation of β-TCP

HAp crystallizes in two different space groups: monoclinic ($P2_1/b$, C_{2h}, no. 14) and hexagonal ($P6_3/m$, C_{6h}, no. 176 or $P6_3$, C_6, no. 173, respectively). Although the monoclinic form is thought to be thermodynamically more stable, it appears that a hexagonal phase is the most common one [61,64,74,78–81]. The hexagonal form allows atomic substitutions (e.g., Na^+, Mg^{2+}, Si^{2+}, K^+, Zn^{2+}, Sr^{2+}, Ba^{2+}, Cl^-, F^-, CO_3^{2-} [23]), balanced by disordered hydroxyl groups as also observed in bones [e.g., 22–24]. However, the structural definition of HAp is still intensively discussed with regard to the hexagonal space groups $P6_3/m$ and $P6_3$ as well as to biological and theoretical considerations [23,61,64,82–84]. A group theoretical analysis for the C_{6h} factor group yields only 62 Raman active modes for space group $P6_3/m$ ($14A_g + 14^2E_{2g} + 10^1E_{1g} + 14^1E_{2g} + 10^2E_{1g}$) [74,75,85], where the OH stretching mode is not involved [61]. In the $P6_3$ symmetry, there is only one hydroxyl group per Ca^{2+} ion triangle to circumvent the non-physical doubling of each hydroxyl group by the mirror plane [83]. In contrast to the C_{6h} factor group, 110 Raman bands ($22A + 22E_1 + 22E_2$) are expected for the C_6 factor group [83–86].

Using crystal structure data published by Ikoma and co-authors [87], a group theoretical analysis for the monoclinic phase reveals that 126 ($63A_g + 63B_g$) among 249 expected optical modes are Raman active [85]. However, the crystal symmetries $P2_1/b$, $P6_3/m$, and $P6_3$ are very similar and the number of expected bands differs due to the order of OH^- ions, which changes during heating. We note in this context that the band near 630 cm^{-1}, which has been assigned to the liberation of OH^- ions within the $P6_3$ symmetry [61,66,84], was not observed in our Raman spectra.

In general, the temperature-dependent decomposition of HAp may operate via three possible reactions, whereby TCP and other calcium phosphates are formed and H_2O is released into the atmosphere:

$$Ca_{10}(PO_4)_6(OH)_2 \rightarrow 2Ca_3(PO_4)_2 + Ca_2P_2O_7 + 2CaO + H_2O \quad (2a)$$

$$Ca_{10}(PO_4)_6(OH)_2 \rightarrow 2Ca_3(PO_4)_2 + Ca_4P_2O_9 + H_2O \quad (2b)$$

$$Ca_{10}(PO_4)_6(OH)_2 \rightarrow 3Ca_3(PO_4)_2 + CaO + H_2O \quad (2c)$$

In the case of equations 2a and 2c, lime is also formed as an intermediate product that has only a weak second order Raman spectrum and is thus difficult to detect [57]. The HT Raman study of pure, nanocrystalline HAp reveals significant spectral changes due to the alteration of P–O bonds within the PO_4 units. By using the empirical correlation between Raman wavenumbers of PO_4 tetrahedra and their P–O bond lengths in crystalline phosphates [88], we obtain a shortest bond length of 152.3 pm for the highest frequency (1076 cm^{-1}) and a longest bond length of 155.6 pm for the lowest frequency (961 cm^{-1}) of HAp. P–O bond lengths of 151.9 and 156.0 pm were calculated for β-TCP indicating a shortening of the P–O bond of the assigned $v_3(PO_4)$ band and an expansion of the P–O bond of the assigned $v_1(PO_4)$ mode during the transformation of HAp to β-TCP. Some authors claim a dehydration of HAp by a gradual release of its OH^- ions at temperatures over 1000 °C [28–30]. However, our observations suggest a complete loss of structural OH groups between a relative narrow temperature interval between 770 and 850 °C (Table 2). Loss of hydroxyl groups bound to the surface of the HAp nanocrystals, however, occurs in distinct overlapping stages below about 600 °C. The first step is the loss of adsorbed water below 200 °C [23,68], which can be followed by (i) the first mass loss in the TG curve and the first peak in the QM (m: 18) curve (Figure 8), (ii) the decrease of OH bands in the frequency range 3500–4000 cm^{-1}, in particular the disappearance of the OH bands (5-7) (Figure 3a and 3c), and (iii) the abrupt shift to higher frequencies of the main band position of HAp during firing (Figure 5), i.e., the average P–O bonds shortened.

Previous studies have indicated that another type of water in addition to adsorbed surface molecular water, surface, and structural OH groups occurs within the HAp structure, which has been defined as lattice water [68,89], structural intra-crystalline water [90], structurally incorporated water [91], or dissociated water [92]. All terms refer to inner-surface-bound water that fills the empty space in the crystal lattice channels of HAp. The fact that the OH bands (2-7) are found only in the pressed tablet but not in the powder suggests a surface-bound origin, possibly favored by the nanocrystallinity of the sample material. Thus, the OH bands (2-4) are assigned to surface-bound OH groups, which can be removed by heating to above 200 °C [90]. Indeed, these OH bands disappear in the temperature range 400–600 °C. Moreover the TG data agree well with studies on carbonated HAp, except for an additional weight loss for CO_2 [89–91]. In agreement with Pasteris and colleagues, we obtained about 3 % mass loss due to the loss of structurally incorporated water [91].

The loss of surface-bound molecular water and hydroxyl groups can cause a contraction of the HAp unit cell in the *a*-axis dimensions [68] and possibly a reversal of the ordered hydroxyl groups [80,93] which could be responsible for the observed spectral changes in the frequency range 300–1200 cm^{-1} between 380 and 770 °C. The position and intensity of all stretching and bending modes changed significantly (Figure 4). At 480 °C, a monoclinic to hexagonal phase transition is predicted [23,93–96], which could explain the spectral changes above 380 °C and the anomalies in our DTA at about 450 °C (Figure 8), respectively. However, the most dramatic changes happened between 770 and 850 °C (Figure 4), where the HAp structure broke down leading to the formation of β-TCP (Equations 2a-c). The peak at about 770 °C in the QM (m = 18) curve indicates a release of H_2O during the decomposition of HAp. At nearly the same temperature, the $\nu(OH)_{HAp}$ band disappears (Figure 3c), suggesting the formation of oxyapatite ($Ca_{10}(PO_4)_6O$) [28]. In fact, new Raman bands at about 350 and 720 cm^{-1} (HT) can be assigned to pyrophosphates (Ca/P < 1.5) [69,70,97], which were produced during the transformation from HAp to β-TCP by changing the Ca/P ratio from 1.667 to 1.5 [71,72]. This is in good agreement with observations made by Coelho and co-workers [31]. These authors also observed a band in the 700–750 cm^{-1} frequency range in Raman spectra of HAp samples heated at 700 and 900 °C and measured ex situ. They assigned the new bands, that were observed after sintering HAp at 700 °C, to other calcium phosphates and suggested that the formation of β-TCP occurs between 700 and 900 °C [31]. The latter basically agrees with our observations (Figure 5 and Figure 7b) as the new band at 545 cm^{-1} (HT) can clearly attributed to anti-symmetric bending modes of the PO_4 units of β-TCP [67]. Our data, however, allows us to more accurately define the transformation temperature for pure HAp to β-TCP, which occurs between 800 and 810 °C (determined inflection point: 808 °C), while the bulk decomposition starts at about 770 °C with the loss of structural OH, which is accompanied by the formation of pyrophosphates, likely at the surface of the nanocrystallites.

However, within the ternary system $Ca_{10}(PO_4)_6(OH)_2$-SiO_2-CaO, the breakdown of nanocrystalline HAp and formation of β-TCP proceeded at significant higher temperatures. Although it is very difficult to distinguish HAp and β-TCP in situ at high temperatures due to spectral similarities, the changes of bending modes (Figure 4b) can be used for unambiguous identification of β-TCP. In experiment TQC-1, the temperature-series Raman images reveal that the decomposition of HAp started at 820 ± 5 °C and pyrophosphates were likely formed (Figure 9). In contrast, in experiment TQC-2, where much more quartz and lime were present, β-TCP crystallized at 1050 ± 5 °C (Figure 10). Thus, quartz and/or lime appear to affect the rate and likely the activation energy for early thermal decomposition of HAp to β-TCP. Raman images acquired during the in situ/quench experiment (TQC-2, Figure 12) show that, although β-TCP could clearly be identified in situ between 960 and 1100 ± 5 °C, HAp formed during quenching. It is known that α-TCP can be hydrolyzed to Ca-deficient HAp at temperatures as low the human body temperature [98]. The hydrolysis of β-TCP with water from the furnace environment could possibly have led to the formation of Ca-deficient HAp. However, no evidence, for example a weak band at 872 cm^{-1} or a broadening of the ν_1 band [98], was found. In general, the observation that β-

TCP was first identified at RT after cooling down from 1150 ± 5 °C indicates that a long sintering period is needed to decompose HAp at lower temperatures so to obtain β-TCP at RT.

4.2 The β- to α-TCP and the α- to α'-TCP transformation

The β- to α-TCP polymorphic phase transformation has previously been observed between 1125 and 1130 °C [32–34]. However, Serena and co-authors [35] observed that the presence of MgO stabilize the β-TCP phase, leading to a phase transition at a significantly higher temperature of 1230 °C. However, impurities (> 0.02 wt.-%) could be excluded and yet both the DTA and HT Raman studies of HAp/β-TCP sample reveal a β-TCP to α-TCP transformation at temperatures above 1220 °C. The α-phase crystallizes in the monoclinic space group $P2_1/a$ (C_{2h}, no. 14) with 24 formula units (312 atoms) per unit cell [99], reflecting the complexity of the high-temperature polymorph. A group theoretical analysis for the C_{2h} factor group yields 468 Raman active modes ($234A_g + 234B_g$) based on published crystal structure data [99]. However, due to the low intensity and large broadening of the bands at HT, the number and positions of the bands were difficult to determine. However, the significant shift of $v_1(PO_4)$ to higher frequencies between 1220 and 1260 ± 1 °C clearly suggests a phase transition within this temperature range, which is further confirmed by the endothermic DTA peaks with onsets slight above 1270 °C during heating. During cooling the reverse reaction α → β-TCP was observed at lower temperatures than on heating. The hysteresis effect during cooling defined by the exothermic peak at 1080 °C indicates a 1st order phase transition, which, however, depends on the heating and cooling rates, respectively. For the physico-chemical conditions of our experiments (heating/quenching rate, holding time, composition etc.), we can assume an upper stability temperature of 1220 ± 1 °C with a transition zone to about 1270 ± 5 °C for β-TCP, which then remained metastable during cooling to RT. In our experiments, the RT Raman spectra clearly identify the β-polymorph of TCP. We can further state that the new band at 1089 cm^{-1} for the fired HAp/β-TCP matches well with the shortest P–O bond length calculated for β-TCP.

The onset of the α → α'-TCP transformation was observed at 1454 ± 5 °C and is consistent with other studies [32–35]. During cooling the reverse reaction α' → α-TCP was observed at nearly the same temperature as on heating (onset: 1444 ± 5 °C).

4.3 The formation of silicocarnotite

Within the ternary system HAp-SiO_2-CaO, dicalcium silicate (α'_L-Ca_2SiO_4) already formed at temperatures below 960 °C by a reaction between quartz and lime (Figures 10 and 12). During quenching, the α'_L-phase reversibly transforms to the β-phase (larnite), as reported in detail in our previous study [56]. The identification of silicocarnotite is based on the published data on the $v_1(PO_4)$ and $v_1(SiO_4)$ frequencies, varying between 950 and 964 cm^{-1} and 845 and 854 cm^{-1}, respectively (see Table 3).

Table 3: Published data on $v_1(PO_4)$ and $v_1(SiO_4)$ frequencies of silicocarnotite at room temperature.

Reference	[45]	[35]	[47]	[53]	[48]	**This study**
$v_1(PO_4)$ [cm^{-1}]	954	964	959-963	957	953	950-952
$v_1(SiO_4)$ [cm^{-1}]	847	854	854	850	848-850	845

It is well-known that silicocarnotite can be synthesized by a solid-state reaction between dicalcium silicate and tricalcium phosphate as described by following equation:

$$Ca_3(PO_4)_2 + Ca_2SiO_4 \rightarrow Ca_5(PO_4)_2SiO_4 \quad (3)$$

It has been proposed that a so-called R solid solution phase is formed as reaction product of the high-temperature polymorphs α'-$Ca_3(PO_4)_2$ and α-Ca_2SiO_4 at temperatures above 1450 ± 20 °C [32–35]. During cooling down to RT, the R phase was found to transform to silicocarnotite at about 1370 °C [33] or 1310 °C [35] by DTA of stoichiometric mixtures.

The material used for the Raman heating study is the same as investigated by Galuskin and co-authors [53]. Compared to our data, the number of identified bands varies and there are some differences in band assignments. For example, the authors assigned a band at 584 cm^{-1} to anti-symmetric bending modes of both the SiO_4 and PO_4 units, although they occur in different frequency ranges, i.e., 520–570 and 570–620 cm^{-1}, respectively [56,61–64]. On the other hand, we can confirm that the band at 633 cm^{-1} can be assigned to a $v_4(PO_4)$ mode. The bands at frequencies above 1010 cm^{-1} can be unambiguously assigned to $v_3(PO_4)$ vibrations, whereas anti-symmetric stretching modes of the SiO_4 tetrahedra occur at much lower frequencies (~880 cm^{-1}) [56].

The $v_1(PO_4)$ frequency of silicocarnotite recorded at RT after quenching the multi-component experiments is in good agreement with the $v_1(PO_4)$ position of 951 ± 1 cm^{-1} observed from the natural silicocarnotite sample. Using the HT reference spectra, we were able to identify silicocarnotite even at high temperatures. The time- and temperature-series Raman images of the in situ experiment TQC-2 and the in situ/quench experiment TQC-3 reveal that silicocarnotite was first identified as small grains located close to large α'$_L$-Ca_2SiO_4 grains within the HAp/β-TCP matrix. After cooling to RT, silicocarnotite crystallized further as rims around dicalcium silicate grains. Grains of wollastonite appear to have reacted with the adjacent β-TCP to silicocarnotite. With reference to previous results, we note that wollastonite cannot only form by a reaction between quartz and lime [e.g., 93], but could also be a breakdown product of dicalcium silicate at temperatures higher than 1020 °C [54–56,101]. Here, we propose that silicocarnotite can form by the reaction between tricalcium phosphate and wollastonite which yields additional silica:

$$Ca_3(PO_4)_2 + 2CaSiO_3 \xrightarrow{T \sim 1050\,^{\circ}C} Ca_5(PO_4)_2SiO_4 + SiO_2 \quad (3)$$

In fact, silicocarnotite and wollastonite usually occurred together in contact with large quartz grains (Figures 10 and 12). While the wollastonite concentration decreased the silicocarnotite content increased. It is possible that newly formed silica reacted with dicalcium silicate and new wollastonite was formed, which is confirmed by the observation that the quartz concentration remained stable (Figure 12).

In experiment TQC-2, silicocarnotite was first identified at 1150 ± 5 °C after a dwell time of two hours. This observation suggests that a long sintering time can activate the formation of silicocarnotite by the supply of more β-TCP by the decomposition of HAp or that the diffusion of $Ca_3(PO_4)_2$ into Ca_2SiO_4 appears to be very slow [35]. Quenching, in turn, seems to trigger the nucleation and growth of silicocarnotite. In experiment TQC-3, silicocarnotite was first identified at RT after cooling from 1050 ± 5 °C, i.e., about 250 °C below the expected R phase-to-silicocarnotite phase transition. Nurse and co-authors postulated that increasing the dicalcium silicate content in the starting mixture promotes the crystallization of silicocarnotite, which is accompanied by another unknown silicate phase (A phase), at lower temperatures than observed for stoichiometric mixtures [32]. However, no A phase could be identified in our experiments. Moreover, our in situ and in operando experiments show that the formation of silicocarnotite is not only possible above 1450 °C by the reaction between the high-temperature polymorphs α'-$Ca_3(PO_4)_2$ and α-Ca_2SiO_4, but also at significant lower temperatures (approx. 1050–1150 °C) through either a reaction between the high-temperature polymorphs β-$Ca_3(PO_4)_2$ and α'$_L$-Ca_2SiO_4 or from the reaction between β-$Ca_3(PO_4)_2$ and $CaSiO_3$ with additional formation of quartz.

5 Conclusion

The in situ Raman heating experiments with pure nanocrystalline HAp and β-TCP and the TG/DTA measurements gave new insights into the breakdown process of nanocrystalline HAp and the formation of tricalcium phosphate polymorphs, which are summarized in Table 2. The main observations are:

- The loss of surface hydroxyl groups bound to HAp nanocrystals is a stepwise process which is completed at about 570 °C. To study the behavior of structural OH during heating future studies should use larger HAp crystals.
- Between 770 and 850 ± 1 °C and 1220 to 1270 ± 5 °C, the reconstructive HAp → β-TCP and β-TCP → α-TCP transformations, respectively, were observed.
- At a heating rate of 10 °C/min, the onset temperature of the likewise reconstructive α → α'-TCP transformation was observed at about 1450 °C.
- With the same quenching rate, β-TCP remained metastable down to RT.

In addition, HT Raman spectra of a natural silicocarnotite sample were recorded for the first time up to 1200 °C in 50 °C-steps and a heating rate of 10 °C per minute. This experiment revealed, for instance, that the position of the $v_1(PO_4)$ band shifted from 951 ± 1 cm^{-1} to approx. 930 cm^{-1} at 1200 ± 1 °C. The HT Raman spectra were also used to identify silicocarnotite in experiments in the ternary system $Ca_{10}(PO_4)_6(OH)_2$-SiO_2-CaO, which gave additional information about solid-state silica-/calcium phosphate reactions:

- HAp decomposed at higher temperatures (960–1050 ± 5 °C), indicating that quartz and/or lime stabilize HAp during firing.
- The in situ formation of silicocarnotite was observed after a dwell time of two hours in direct contact to α'_L-Ca_2SiO_4 grains located within the initially nanocrystalline HAp/β-TCP matrix.
- During quenching, silicocarnotite was first identified at RT after cooling from 1050 ± 5 °C, i.e., about 250 °C below the previously observed R phase-to-silicocarnotite phase transition zone.
- Silicocarnotite crystallized in the temperature range between 1050 and 1150 °C, either from the reaction between β-$Ca_3(PO_4)_2$ and α'_L-Ca_2SiO_4 or from the reaction between β-$Ca_3(PO_4)_2$ and $CaSiO_3$, which additionally involve the formation of quartz.

In conclusion, we would like to state that hyperspectral in situ Raman imaging is a unique tool to study high-temperature solid-state reactions in multi-component systems in situ and in operando, i.e., while the solid-state reactions are running. In return, the work shows how important the availability of HT reference Raman spectra is in order to be able to correctly identify mineral phases in multi-phase systems in situ and at high temperatures.

Funding: This research was financially supported by the RWE Power AG, Kraftwerk Niederaußem, Bergheim, Germany, and the German Research Foundation (DFG, grant number GE1094/22-1).

Acknowledgements: Many thanks go to B. Hofmann of the Museum of Natural History in Bern for providing the natural silicocarnotite sample.

Conflicts of Interest: The authors declare no conflict of interest.

Data availability: RT/HT Raman data are available to readers by contacting the corresponding author.

References

[1] Albee FH, Morrison HF. Studies in bone growth - Triple calcium phosphate as a stimulus to osteogenesis. *Ann Surg* 1920;71:32–9. doi:10.1097/00000658-192001000-00006.

[2] Lange TA, Zerwekh JE, Peek RD, Harrison BH. Granular Tricalcium Phosphate in Large Cancellous Defects. *Ann Cinical Lab Sc*i 1986;16:467–72. PMDI:3541772.

[3] Hench LL. Bioceramics : From Concept to Clinic. *J Am Ceram Soc* 1991;74:1487–510. doi:10.1111/j.1151-2916.1991.tb07132.x.

[4] Suchanek W, Yoshimura M. Processing and properties of hydroxyapatite-based biomaterials for use as hard tissue replacement implants. *J Mater Res* 1998;13:94–117. doi:10.1557/JMR.1998.0015.

[5] Vallet-Regí M. Ceramics for medical applications. *J Chem Soc, Dalt Trans* 2001:97–108. doi:10.1039/b007852m.

[6] LeGeros RZ. Properties of Osteoconductive Biomaterials: Calcium Phosphates. *Clin Orthop Relat Res* 2002;395:81–98. doi:10.1097/00003086-200202000-00009.

[7] Dorozhkin S V, Epple M. Biological and Medical Significance of Calcium Phosphates. *Angew Chem Int Ed* 2002;41:3130–46. doi:10.1002/1521-3773(20020902)41:17<3130::AID-ANIE3130>3.0.CO;2-1.

[8] de Aza PN, de Aza AH, de Aza S. Crystalline Bioceramic Materials. *Bol Soc Esp Ceram V* 2005;44:135–45. doi:10.1002/chin.200629272.

[9] Xie Y, Chopin D, Morin C, Hardouin P, Zhu Z, Tang J, Lu J. Evaluation of the osteogenesis and biodegradation of porous biphasic ceramic in the human spine ceramic in the human spine. *Biomaterials* 2006;27:2761–7. doi:10.1016/j.biomaterials.2005.12.011.

[10] Dorozhkin S V. Calcium orthophosphate cements for biomedical application. *J Mater Sci* 2008;43:3028–3057. doi:10.1007/s10853-008-2527-z.

[11] Chow LC. Next generation calcium phosphate-based biomaterials. *Dent Mater J* 2009;28. doi:10.4012/dmj.28.1.

[12] Vassilev S V, Baxter D, Andersen LK, Vassileva CG. An overview of the composition and application of biomass ash . Part 1 . Phase – mineral and chemical composition and classification. *Fuel* 2013;105:40–76. doi:10.1016/j.fuel.2012.09.041.

[13] Miles TR, Miles Jr TR, Baxter LL, Bryers RW, Jenkins BM, Oden LL. Alkali Deposits Found in Biomass Power Plants: A Preliminary Investigation of Their Extent and Nature. Report, NREL Subcontract TZ-2-11226-1, Colorado, USA: 1995.

[14] Vamvuka D, Pitharoulis M, Alevizos G, Repouskou E, Pentari D. Ash effects during combustion of lignite / biomass blends in fluidized bed. *Renew Energy* 2009;34:2662–71. doi:10.1016/j.renene.2009.05.005.

[15] Vamvuka D. Comparative fixed/fluidized bed experiments for the thermal behaviour and environmental impact of olive kernel ash. *Renew Energy* 2009;34:158–64. doi:10.1016/j.renene.2008.04.032.

[16] Yakaboylu O, Harinck J, Smit KGG, de Jong W. Supercritical water gasification of manure : A thermodynamic equilibrium modeling approach. *Biomass and Bioenergy* 2013;59:253–63. doi:10.1016/j.biombioe.2013.07.011.

[17] Vamvuka D, Kakaras E. Ash properties and environmental impact of various biomass and coal fuels and their blends. Fuel Process Technol 2011;92:570–81. doi:10.1016/j.fuproc.2010.11.013.

[18] Tan Z, Lagerkvist A. Phosphorus recovery from the biomass ash : A review. *Renew Sustain Energy Rev* 2011;15:3588–602. doi:10.1016/j.rser.2011.05.016.

[19] Ovsyannikova E, Arauzo PJ, Becker GC, Kruse A. Science of the Total Environment Experimental and thermodynamic studies of phosphate behavior during the hydrothermal carbonization of sewage sludge. *Sci Total Environ* 2019;692:147–56. doi:10.1016/j.scitotenv.2019.07.217.

[20] Falk J, Skoglund N, Grimm A, Öhman M. Fate of Phosphorus in Fixed Bed Combustion of Biomass and Sewage Sludge. *Energy Fuels* 2020;34:4587–94. doi:10.1021/acs.energyfuels.9b03976.

[21] Zheng X, Ye Y, Jiang Z, Ying Z, Ji S, Chen W, Wang B, Dou B. Science of the Total Environment Enhanced transformation of phosphorus (P) in sewage sludge to hydroxyapatite via hydrothermal carbonization and calcium-based additive. *Sci Total Environ* 2020;738:139786. doi:10.1016/j.scitotenv.2020.139786.

[22] LeGeros RZ. Apatites in Biolocical Systems. *Prog Cryst Growth Charact* 1981;4:1–45. doi:10.1016/0146-3535(81)90046-0.

[23] Elliot JC. Structure and Chemistry of the Apatites and Other Calcium Orthophosphates. Amsterdam: Elsevier; 1994. ISBN: 0-4444-81582-1.

[24] Akram M, Ahmed R, Shakir I, Ibrahim WAW, Hussain R. Extracting hydroxyapatite and its precursors from natural resources. *J Mater Sci* 2014;49:1461–75. doi:10.1007/s10853-013-7864-x.

[25] Ferraz MP, Monteiro FJ, Manuel CM. Hydroxyapatite nanoparticles : A review of preparation

methodologies. *J Appl Biomater Biomech* 2004;2:74–80. doi:10.1177/228080000400200202.
[26] Yao J, Tjandra W, Chen YZ, Tam KC, Ma J, Soh B. Hydroxyapatite nanostructure material derived using cationic surfactant as a template. *J Mater Chem* 2003;13:3053–7. doi:10.1039/b308801d.
[27] Li Y, Tjandra W, Tam KC. Synthesis and characterization of nanoporous hydroxyapatite using cationic surfactants as templates. *Mater Res Bull* 2008;43:2318–26. doi:10.1016/j.materresbull.2007.08.008.
[28] Liao C, Lin F, Chen K, Sun J. Thermal decomposition and reconstitution of hydroxyapatite in air atmosphere. *Biomaterials* 1999;20:1807–13. doi:10.1016/S0142-9612(99)00076-9.
[29] Lin F, Chun-Jen L, Ko-Shao C, Jui-Sheng S. Thermal reconstruction behavior of the quenched hydroxyapatite powder during reheating in air. *Mater Sci Eng* C 2000;13:97–104. doi:10.1016/S0928-4931(00)00182-X.
[30] Zhou J, Zhang X, Chen J, Zeng S, De Groot K. High temperature characteristics of synthetic hydroxyapatite. *J Mater Sci Med* 1993;4:83–5. doi:10.1007/BF00122983.
[31] Coelho JM, Moreira JA, Almeida A, Monteiro FJ. Synthesis and characterization of HAp nanorods from a cationic surfactant template method. *J Mater Sci Mater Med* 2010;21:2543–9. doi:10.1007/s10856-010-4122-5.
[32] Nurse RW, Welch JH, Gutt W. High-temperature Phase Equilibria in the System Dicalcium Silicate-Tricalcium Phosphate. *J Am Ceram Soc* 1956:1077–83.
[33] Martínez IM, Velásquez P, De Aza PN. The Sub-System α-TCP_{ss}-Silicocarnotite Within the Binary System $Ca_3(PO_4)_2$-Ca_2SiO_4. *J Am Ceram Soc* 2012;95:1112–7. doi:10.1111/j.1551-2916.2011.05031.x.
[34] Fix W, Heymann H, Heinke R. Subsolidus Relations in the System $2CaO{\cdot}SiO_2$-$3CaO{\cdot}P_2O_5$. *J Am Ceram Soc* 1969;52:346–7. doi:10.1111/j.1151-2916.1969.tb11948.x.
[35] Serena S, Sainz MA, Caballero A. Single-phase silicocarnotite synthesis in the subsystem $Ca_3(PO_4)_2$ – Ca_2SiO_4. *Ceram Int* 2014;40:8245–52. doi:10.1016/j.ceramint.2014.01.022.
[36] Carlisle EM. Silicon: A Possible Factor in Bone Calcification. *Science* 1970;167:279–80. doi:10.1126/science.167.3916.279.
[37] Schwarz K, Milne DB. Growth-promoting Effects of Silicon in Rats. *Nature* 1972;239:333–4. doi:10.1038/239333a0.
[38] Balas F, Pérez-Pariente J, Vallet-Regí M. In vitro bioactivity of silicon-substituted hydroxyapatites. *J Biomed Mater Res* 2003;66A:364–75. doi:10.1002/jbm.a.10579.
[39] Vallet-Regí M, Arcos D. Silicon substituted hydroxyapatites. A method to upgrade calcium phosphate based implants. *J Mater Chem* 2005;15:1509–16. doi:10.1039/b414143a.
[40] Pietak AM, Reid JW, Stott MJ, Sayer M. Silicon substitution in the calcium phosphate bioceramics. *Biomaterials* 2007;28:4023–32. doi:10.1016/j.biomaterials.2007.05.003.
[41] Duan W, Ning C, Tang T. Cytocompatibility and osteogenic activity of a novel calcium phosphate silicate bioceramic : Silicocarnotite. *J Biomed Mater Res Part A* 2013;101A:1955–61. doi:10.1002/jbm.a.34497.
[42] Dickens B, Brown WE. The Crystal Structure of $Ca_5(PO_4)_2SiO_4$ (Silico-Carnotite). *TMPM Tschermaks Miner Petrogr Mitt* 1971;16:1–27. doi:10.1007/BF01099075.
[43] Pliego-Cuervo Y, Glasser FP. Phase relations and crystal chemistry of apatite and silicocarnotite solid solutions. *Cem Concr Res* 1978;8:519–24.
[44] Li H, Ng BS, Khor KA, Cheang P, Clyne TW. Raman spectroscopy determination of phases within thermal sprayed hydroxyapatite splats and subsequent in vitro dissolution examination. *Acta Mater* 2004;52:445–53. doi:10.1016/j.actamat.2003.09.046.
[45] Gomes S, Nedelec J, Jallot E, Sheptyakov D, Renaudin G. Silicon Location in Silicate-Substituted Calcium Phosphate Ceramics Determined by Neutron Diffraction. *Cryst Growth Des* 2011;11:4017–26. doi:10.1021/cg200587s.
[46] Lu W, Duan W, Guo Y, Ning C. Mechanical Properties and In Vitro Bioactivity of $Ca_5(PO_4)_2SiO_4$ Bioceramic. *J Biomater Appl* 2012;26:637–50. doi:10.1177/0885328210383599.
[47] Serena S, Caballero A, De Aza PN, Sainz MA. New evaluation of the in vitro response of silicocarnotite monophasic material. *Ceram Int* 2015;41:9411–9. doi:10.1016/j.ceramint.2015.03.319.
[48] Rincón-López JA, Hermann-Muñoz JA, Cinca-Luis N, López-Conesa L, Fernández-Benavides DA, García-Cano I, Guilemany-Casadamon JM, Boccaccini AR, Muñoz-Saldaña J, Alvarado-Orozco JM. Apatite Mineralization Process from Silicocarnotite Bioceramics: Mechanism of Crystal Growth and Maturation. *Cryst Growth Des* 2020;20:4030–3045. doi:10.1021/acs.cgd.0c00322.
[49] Bulina N V, Chaikina M V, Gerasimov KB, Ishchenko A V, Dudina D V. A novel approach to the synthesis of silicocarnotite. *Mater Lett* 2016;164:255–9. doi:10.1016/j.matlet.2015.10.047.
[50] Bouregba A, Diouri A. Silicocarnotite Synthesis and Bioactivity in Artificial Saliva Medium. *J Biomim Biomater Biomed Eng* 2018;38:38–46. doi:10.4028/www.scientific.net/JBBBE.38.38.
[51] Carnot A, Richard J. Silico-phosphate cristallin produit dans la déphosphoration des fontes. *Bull La Société*

Minéralogique Fr 1983;6,7:316–20.
[52] Riley DP, Segnit ER. An optical and X-ray examination of the basic-slag mineral silicocarnotite. *Miner Mag* 1949;28:496–504.
[53] Galuskin E, Galuskina I, Gfeller F, Krüger B, Kusz J, Vapnik Y, Dulski M, Dzierzanowski P. Silicocarnotite, $Ca_5[(SiO_4)(PO_4)](PO_4)$, a new ,,old'' mineral from the Negev Desert, Israel, and the ternesite-silicocarnotite solid solution: indicators of high-temperature alteration of pyrometamorphic rocks of the Hatrurim Complex, Southern Levant. *Eur J Mineral* 2016;28:105–23. doi:10.1127/ejm/2015/0027-2494.
[54] Stange K, Lenting C, Geisler T. Insights into the evolution of carbonate-bearing kaolin during sintering revealed by in situ hyperspectral Raman imaging. *J Am Ceram Soc* 2018;101:897–910. doi:10.1111/jace.15209.
[55] Böhme N, Hauke K, Neuroth M, Geisler T. In situ Raman imaging of high-temperature solid-state reactions in the $CaSO_4$–SiO_2 system. *Int J Coal Sci Technol* 2019;6:247–259. doi:10.1007/s40789-019-0252-7.
[56] Böhme N, Hauke K, Neuroth M, Geisler T. In Situ Hyperspectral Raman Imaging of Ternesite Formation and Decomposition at High Temperatures. *Minerals* 2020;10:287. doi:10.3390/min10030287.
[57] Hauke K, Kehren J, Böhme N, Zimmer S, Geisler T. In situ Hyperspectral Raman Imaging: A new Method to investigate Sintering Processes of Ceramic Material at High Temperature. *Appl Sci* 2019;9:1–23. doi:10.3390/app9071310.
[58] Suchanek K, Bartkowiak A, Perzanowski M, Marszałek M. From monetite plate to hydroxyapatite nanofibers by monoethanolamine assisted hydrothermal approach. *Sci Rep* 2018;8:15408. doi:10.1038/s41598-018-33936-4.
[59] Mihara N, Kuchar D, Kojima Y, Matsuda H. Reductive decomposition of waste gypsum with SiO_2, Al_2O_3, and Fe_2O_3 additives. *J Mater Cycles Waste Manag* 2007;1:21–6. doi:0.1007/s10163-006-0167-4.
[60] Lafuente B, Downs R T, Yang H SN. The power of databases: the RRUFF project. In: Armbruster T, Danisi RM, editors. Highlights Mineral. Crystallogr., Berlin, Germany: De Gruyter; 2015, p. 1–30.
[61] Nelson DGA, Williamson BE. Low-Temperature Laser Raman Spectroscopy of Synthetic Carbonated Apatites and Dental Enamel. *Aust J Chem* 1982;35:715–27. doi:10.1071/CH9820715.
[62] Remy C, Reynard B, Madon M. Raman Spectroscopic Investigations of Dicalcium Silicate: Polymorphs and High-Temperature Phase Transformations. *J Am Ceram Soc* 1997;80:413–23. doi:10.1111/j.1151-2916.1997.tb02846.x.
[63] Frost RL, Weier ML, Mills SJ. A vibrational spectroscopic study of perhamite, an unusual silico-phosphate. *Spectrochim Acta Part A* 2007;67:604–10. doi:10.1016/j.saa.2006.07.044.
[64] Tsuda H, Arends J. Orientational Micro-Raman Spectroscopy on Hydroxyapatite Single Crystals and Human Enamel Crystallites. *J Dent Res* 1994;73:1703–10. doi:10.1177/00220345940730110501.
[65] Jillavenkatesa A, Condrate RA. The Infrared and Raman Spectra of β- and α-Tricalcium Phosphate ($Ca_3(PO_4)_2$). *Spectrosc Lett* 1998;31:1619–34. doi:10.1080/00387019808007439.
[66] Blakeslee KC, Condrate RA. Vibrational Spectra of Hydrothermally Prepared Hydroxyapatites. *Am Ceram Soc* 1971;54:559–63. doi:10.1111/j.1151-2916.1971.tb12207.x.
[67] de Aza PN, Santos C, Pazo A, de Aza S, Cuscó R, Artús L. Vibrational Properties of Calcium Phosphate Compounds. 1. Raman Spectrum of ß-Tricalcium Phosphate. *Chem Mater* 1997;9:912–5. doi:10.1021/cm960425d.
[68] LeGeros RZ, Bonel G, Legros R. Types of "H_2O" in Human Enamel and in Precipitated Apatites. *Calcif Tiss Res* 1978;26:111–8.
[69] Cornilsen BC, Condrate Sr. RA. The vibrational spectra of β-$Ca_2P_2O_7$ and γ-$Ca_2P_2O_7$. *J Inorg Nucl Chem* 1979;41:602–5. doi:10.1016/0022-1902(79)80457-1.
[70] de Fátima Gimenez I, Mazali IO, Alves OL. Application of Raman spectroscopy to the study of the phase composition of phosphate based glass-ceramics. *J Phys Chem Solids* 2001;62:1251–5. doi:10.1016/S0022-3697(01)00017-8.
[71] Raynaud S, Champion E, Bernache-Assollant D, Thomas P. Calcium phosphate apatites with variable Ca/P atomic ratio I . Synthesis, characterisation and thermal stability of powders. *Biomaterials* 2002;23:1065–72. doi:10.1016/S0142-9612(01)00218-6.
[72] Quillard S, Mellier C, Gildenhaar R. Raman and Infrared Studies of Substituted β-TCP. *Key Eng Mater* 2012:225–30. doi:10.4028/www.scientific.net/KEM.493-494.225.
[73] Yashima M, Sakai A, Kamiyama T, Hoshikawa A. Crystal structure analysis of β-tricalcium phosphate $Ca_3(PO_4)_2$ by neutron powder diffraction. *J Solid State Chem* 2003;175:272–7. doi:10.1016/S0022-4596(03)00279-2.
[74] Hughes JM, Cameron M, Crowley KD. Structural variations in natural F, OH, and Cl apatites. *Am Mineral* 1989;74:870–6.
[75] Wilson RM, Elliott JC, Dowker SEP. Rietveld refinement of the crystallographic structure of human dental

enamel apatites. *Am Mineral* 1999;84:1406–14. doi:10.2138/am-1999-0919.
[76] de Aza P, Guitián F, Santos C, de Aza S, Cuscó R, Artús L. Vibrational Properties of Calcium Phosphate Compounds. 2. Comparison between Hydroxyapatite and β-Tricalcium Phosphate. *Chem Mater* 1997;9:916–22. doi:10.1021/cm9604266.
[77] Reynard B, Remy C, Takir F. High-pressure Raman spectroscopic study of Mn_2GeO_4, Ca_2GeO_4, Ca_2SiO_4, and $CaMgGeO_4$ olivines. *Phys Chem Miner* 1997;24:77–84. doi:10.1007/s002690050019.
[78] Posner A., Perloff A, Diorio AF. Refinement of the hydroxyapatite structure. Acta Cryst 1958;11:308. doi:10.1107/S0365110X58000815.
[79] Ma G, Liu XY. Hydroxyapatite : Hexagonal or Monoclinic? *Cryst Growth Des* 2009;9:2991–4. doi:10.1021/cg900156w.
[80] Kay MI, Young RA. Crystal structure of hydroxyapatite. *Nature* 1964;204:1050–2. doi:10.1038/2041050a0.
[81] Elliott JC, Mackie PE, Young RA. Monoclinic Hydroxyapatite. *Science* 1973;180:1055–7. doi:10.1126/science.180.4090.1055
[82] Iqbal Z, Tomaselli VP, Fahrenfeld O, Möller KD, Ruszala FA, Kostiner E. Polarized raman scattering and low frequency infrared study of hydroxyapatite. *J Phys Chem Solid*s 1977;38:923–7. doi:10.1016/0022-3697(77)90132-9.
[83] Corno M, Busco C, Ugliengo P. Periodic ab initio study of structural and vibrational features of hexagonal hydroxyapatite $Ca_{10}(PO_4)_6(OH)_2$. *Physi Chem Chem Phys* 2006;8:2464–72. doi:10.1039/b602419j.
[84] Fowler B. Infrared Studies of Apatites. I. Vibrational Assignments for Calcium, Strontium, and Barium Hydroxyapatites Utilizing Isotopic Substitution. *Inorg Chem* 1974;13:194–207. doi:10.1021/ic50131a039.
[85] Kroumova E, Aroyo MI, Perez-Mato JM, Kirov A, Capillas C, Ivantchev S, Wondratschek H. Bilbao Crystallographic Server : Useful Databases and Tools for Phase-Transition Studies. *Phase Transitions* 2003;76:155–70. doi:10.1080/0141159031000076110.
[86] Ulian G, Valdrè G, Corno M, Ugliengo P. The vibrational features of hydroxylapatite and type A carbonated apatite : A first principle contribution. *Am Mineral* 2013;98:752–9. doi:10.2138/am.2013.4315.
[87] Ikoma T, Yamazaki A, Nakamura S, Akao M. Preparation and Structure Refinement of Monoclinic Hydroxyapatite. *J Solid State Chem* 1999;144:272–6. doi:10.1006/jssc.1998.8120.
[88] Popović L, de Waal D, Boeyens JCA. Correlation between Raman wavenumbers and P — O bond lengths in crystalline inorganic phosphates. *J Raman Spectrosc* 2005;36:2–11. doi:10.1002/jrs.1253.
[89] Suchanek WL, Shuk P, Byrappa K, Riman RE, TenHuisen KS, Janas VF. Mechanochemical – hydrothermal synthesis of carbonated apatite powders at room temperature. *Biomaterials* 2002;23:699–710. doi:10.1016/S0142-9612(01)00158-2.
[90] Kaflak A, Kolodziejski W. Complementary information on water and hydroxyl groups in nanocrystalline carbonated hydroxyapatites from TGA, NMR and IR measurements. *J Mol Struct* 2011;990:263–70. doi:10.1016/j.molstruc.2011.01.056.
[91] Pasteris JD, Yoder CH, Wopenka B. Molecular water in nominally unhydrated carbonated hydroxylapatite: The key to a better understanding of bone mineral. *Am Mineral* 2014;99:16–27. doi:10.2138/am.2014.4627.
[92] Kebede GG, Mitev PD, Broqvist P, Kullgren J, Hermansson K. Hydrogen-Bond Relations for Surface OH Species. *J Phys Chem* C 2018;122:4849–4848. doi:10.1021/acs.jpcc.7b10981.
[93] Suda H, Yashima M, Kakihana M, Yoshimura M. Monoclinic Hexagonal Phase Transition in Hydroxyapatite Studied by X-ray Powder Diffraction and Differential Scanning Calorimeter Techniques. *J Phys Chem* 1995;99:6752–4. doi:10.1021/j100017a068.
[94] Takahashi H, Yashima M, Kakihana M, Yoshimura M. A differential scanning calorimeter study of the monoclinic ($P2_1/b$) - hexagonal ($P6_3/m$) reversible phase transition in hydroxyapatite. *Thermochim Acta* 2001;371:53–6. doi:10.1016/S0040-6031(01)00431-2.
[95] Slepko A, Demkov AA. Hydroxyapatite : Vibrational spectra and monoclinic to hexagonal phase transition. *J Appl Phys* 2015;117:074701. doi:10.1063/1.4908001.
[96] Hochrein O, Kniep R, Zahn D. Atomistic Simulation Study of the Order/Disorder (Monoclinic to Hexagonal) Phase Transition of Hydroxyapatite. *Chem Mate*r 2005;17:1978–81. doi:10.1021/cm0401903.
[97] Pemberton JE, Latifzadeh L, Fletcher JP, Risbud SH. Raman Spectroscopy of Calcium Phosphate Glasses with Varying CaO Modifier Concentrations. *Chem Mater* 1991:195–200. doi:10.1021/cm00013a039.
[98] Durucan C, Brown PW. α-Tricalcium phosphate hydrolysis to hydroxyapatite at and near physiological temperature. *J Mater Sci Mater Med* 2000;11:365–71. doi:10.1023/a:1008934024440.
[99] Mathew M, Schroeder LW, Dickens B, Brown WE. The Crystal Structure of α-$Ca_3(PO_4)_2$. *Acta Crys*t 1977;B33:1325–33. doi:10.1107/S0567740877006037.

[100] Tschegg C, Ntaflos T, Hein I. Thermally triggered two-stage reaction of carbonates and clay during ceramic firing - A case study on Bronze Age Cypriot ceramics. *Appl Clay Sc*i 2009;43:69–78. doi:10.1016/j.clay.2008.07.029.

[101] Ptáček P, Opravil T, Šoukal F, Havlica J, Holešinský R. Kinetics and mechanism of formation of gehlenite, Al-Si spinel and anorthite from the mixture of kaolinite and calcite. *Solid State Sci* 2013;26:53–8. doi:10.1016/j.solidstatesciences.2013.09.014.

Appendix

Table A1: Observed (Raman shift), widths, given as a full width at half maximum (FWHM) and intensity ratios between the $v_1(PO_4)$ and the $v_1(SiO_4)$ modes of the silicocarnotite sample. The normalized intensity ratio of the $v_1(PO_4)$ band to the $v_1(SO_4)$ band is also given.

Temperature [°C]	**$v_1(PO_4)$** [cm^{-1}]	**FWHM $v_1(PO_4)$** [cm^{-1}]	**$v_1(SiO_4)$** [cm^{-1}]	**FWHM $v_1(SiO_4)$** [cm^{-1}]	**Intensity ratio $v_1(PO_4)$/ $v_1(SiO_4)$**	**Intensity ratio (norm.) $v_1(PO_4)$/ $v_1(SO_4)$**
30	950.3	12.1	843.4	19.1	5.1	9.7
100	949.4	12.8	843.2	17.3	5.4	9.6
150	948.6	14.0	842.2	20.7	5.0	9.0
250	947.9	14.9	841.1	19.8	5.6	7.7
300	946.8	16.2	840.2	20.9	5.2	8.2
350	945.9	16.6	838.7	21.2	5.3	7.3
400	945.2	17.3	838.2	19.1	5.6	6.5
450	944.7	18.8	837.7	23.1	5.5	7.3
500	944.0	20.6	837.1	27.1	4.8	7.6
550	943.0	20.9	837.0	28.6	4.4	5.4
600	942.0	21.8	835.3	27.2	4.7	6.7
650	940.6	22.2	835.0	28.3	4.5	6.2
700	939.4	21.1	834.8	26.9	4.5	6.1
750	938.5	22.2	834.5	27.3	4.6	5.5
800	937.9	23.4	833.4	31.5	4.3	5.7
850	936.8	24.3	832.6	31.2	4.1	6.5
900	936.3	24.6	831.9	31.7	4.4	7.5
950	935.6	26.3	830.9	29.1	4.4	6.8
1000	934.5	26.0	830.6	34.6	4.2	5.9
1050	934.2	28.8	829.6	31.0	4.5	3.9
1150	930.9	29.6	826.9	38.4	4.6	0
1200	929.8	30.9	824.5	45.6	3.4	0
	δv/δT	δFWHM/δT	δv/δT	δFWHM/δT	Ø	
	-0.0127	0.0156	-0.0104	0.0186	4.8	
	± 0.001	± 0.0005	± 0.0016	± 0.0017		
	$r^2 > 0.99$	$r^2 > 0.98$	$r^2 > 0.98$	$r^2 > 0.85$		

EPILOGUE

Compared to the first and the second study, which were carried out to examine the anhydrite-quartz and anhydrite-quartz-lime system, respectively, the third study replaced the sulfate component with a phosphate phase. The HAp-quartz-lime system was investigated and gave new insights into the formation of silicocarnotite ($Ca_5(PO_4)_2SiO_4$) at high temperatures. Silicocarnotite crystallized in the temperature range between 1050 and 1150 °C, either from the reaction between β-TCP and α'_L-Ca_2SiO_4 or between β-TCP and wollastonite with the additional formation of quartz. Furthermore, quartz and/or lime were found to stabilize HAp during firing within the multi-phase experiments.

The heating studies of nanocrystalline HAp and β-TCP revealed that the loss of surface water bound to the HAp nanocrystals is a stepwise process until 770 °C. Between 770 and 850 °C, structural OH was lost during HAp transformed to β-TCP. In addition, the β-TCP–to–α-TCP and the α–to–α'-TCP transformation temperatures could be determined. In both single- and multi-phase experiments, β-TCP remained metastable at RT.

Further Raman studies with larger HAp crystals are planned for the future to obtain more information on the behavior of structural hydroxyl groups and possible differences compared to the nanocrystalline material during heating.

5 Investigations of calcium silicates and calcium phosphates in a waste wood ash – an alternative fuel

5.1 Introduction

Fuels derived from biomass and waste are attractive and sustainable sources of energy. In the context of the debate on coal combustion, these alternative fuels gain increasing attention [7,58–60].
From an economic point of view, the possibility of co-firing biomass/waste with coal in power plants is an interesting option as it widens the range of acceptable fuels, especially coals, avoids seasonal difficulties, and allows the use of existing infrastructure. An important environmental aspect is that the combustion of these residues can reduce the volume of waste, allowing energy recovery [60]. Furthermore, the use of biomass/waste is considered carbon neutral, as the CO_2 released during its use is an integral part of the carbon cycle [e.g., 7]. Waste wood ash is the residue produced when wood waste is incinerated for energy. Recent investigations have shown that waste wood ash can be used as a cement substitute in the building industry [61–63]. However, the quality and composition of wood ash can vary depending on the combustion temperature, combustion technology, and type of wood used [61,64], as well as the addition of coal or other fuels [65]. During the combustion process, sinter reactions of containing minerals can lead to deposit formation inside the furnace. Therefore, a detailed analysis of the properties of wood ash before its technical use is of utmost importance.

In the present study, a waste wood ash was investigated using various analytical means. The aim was to analyze the chemical and mineralogical composition in detail. Furthermore, initial heating experiments were carried out with samples of waste wood ash to evaluate the application potential of HT Raman imaging on real waste wood ashes, i.e., to study whether it is possible to also visualize inorganic phase reactions at high temperatures by hyperspectral Raman imaging.

5.2 Material and methods

The waste wood ash used in this study was produced from waste wood by combustion in a furnace at about 550 °C. The chemical analysis of the main elements in the waste wood ash was carried out with a Bruker S8 Tiger X-ray fluorescence spectrometer (XRF, Bruker AXS, Madison, WI, USA) at the Mineralogical Laboratory of the RWE Power AG, Niederaußem, Germany. The spectrometer is equipped with a rhodium tube and a scintillation counter tube as detector. The measurements were carried out under vacuum with a collimator mask (34 mm) and a sample rotation of 30 revolutions per minute. The installed crystals used for analysis, the respective generator settings, and the associated analyzable elements are listed in Table 3. The measurements were carried out on melting tablets (1050 °C). The evaluation of the recorded spectra was automatically carried out with the SPECTRAplus software (Bruker AXS).

Table 3: Crystals used in the XRF measurement with the respective generator settings and the elements to be measured.

Crystal	Generator settings	Elements
PET	30 kV, 135 mA	Al, Si
LiF200	50 kV, 81 mA	Ba, Ca, K, Ti
XS-Ge-C	30 kV, 135 mA	Cl, P, S
LiF220	60 kV, 67 mA	Fe
XS-55	30 kV, 135 mA	Mg, Na
LiF200	60 kV, 67 mA	Mn, Sr, Zn

The mineralogical analysis of the waste wood ash was conducted with a Bruker D5000 X-ray powder diffractometer (XRD, Bruker AXS, Madison, WI, USA) with a theta-theta-goniometer geometry, Cu-Kα radiation, and a graphite monochromator. The X-ray tube operated at 40 kV and 40 mA. The XRD scans were performed between 4 and 70 °2θ, with a step size of 0.02°/s and an acquisition time of 40 s per step. The software systems DIFFRAC.EVA and DIFFRAC.TOPAS by Bruker AXS were used for qualitative identification and quantitative analysis of crystalline components, respectively. In addition, the XRD results were verified and complemented by Raman measurements. Furthermore, two sintering experiments were performed with the same starting material using a Horiba Scientific HR800 Evolution Raman spectrometer (Horiba Scientific*,* Kyōto, Japan*)* equipped with an electron-multiplier charge-coupled device (EM-CCD) detector, an Olympus BX41 microscope, and a Nd:YVO_4 laser (λ = 532.11 nm). A LINKAM TS1500 heating stage was mounted onto the automated x-y-z stage below the microscope objective of the Raman microscope as shown and described in detail in Chapter 1. Both instruments are located at the Institute of Geoscience of the University of Bonn, Germany.

For Raman measurements, ~20 mg of the sample material was pressed with 10 kPa into cylinders with a diameter of 3 mm and a height of about 1.5 mm to produce a flat sample surface for high-quality Raman images as described in Chapter 1.2.1. Several representative areas (160 x 160 μm^2) of the sample surface were selected to record hyperspectral Raman images at RT. Afterwards the samples were fired to the first temperature step with a heating rate of 10 °C/min. Then, two Raman images were taken in succession (total acq. time: ~4 h) before the sample was further heated to the next temperature (~50 °C-steps). After recording the last image at the maximum temperature, the sample was cooled down to RT (10 °C/min) and a final Raman image (200 x 200 μm^2) was recorded. The individual Raman spectra were collected during continuous x-y stage movement with a scanning speed of 1.6 µm/s (SWIFT© mode) in the wavenumber range from 100 to 1730 cm^{-1}. For the evaluation of Raman images, all Raman spectra were corrected for any possible spectrometer shift that can occur during long-time image acquisition using the position of the intense Ne line at 1707.06 cm^{-1}. The data reduction and creation of hyperspectral false-color Raman images were carried out using the LabSpec software. The images show the 2-dimensional, micrometer-scale distribution of mineral phases identified within the area. The dominant mineral phase in a given Raman spectrum was determined by the classical least-squares (CLS) fitting procedure as described in Chapter 1.3.2.

5.3 Results and discussion

5.3.1 Chemical and mineralogical composition of waste wood ash

In contrast to the experiments of previous studies, the present investigations were not carried out on synthetically produced samples. Therefore, the composition of the material was not known and the focus was on identifying the minerals in the waste wood ash and, generally, to evaluate the application potential of HT Raman imaging on real waste wood ashes. First, the contents of inorganic elements

were measured by XRF (Figure 14). Ca is the predominant element (~43 wt.-% CaO) in the present waste wood ash. It also contains about 13 wt.-% K_2O and other critical elements such as Si and P in major concentrations. Al, Na, Mg, Fe, Mn, Ti, Zn, Ba, Sr, S, and Cl were detected in trace concentrations. The measured inorganic chemical composition agrees well with results of other chemical investigations of waste wood ashes [60,61,64]. Wood ash usually contains high amounts of heavy metals due to the longer rotation time of wood, which increases accumulation and may explain the lower pH value of forest soils [60]. However, the higher the incineration temperature, the lower the content of light metals (K, Na, Zn, etc.) [64], i.e., more volatile elements are released into the atmosphere. The combustion temperature significantly affects the chemical and the mineralogical composition of waste wood ashes. At a combustion temperature below 500 °C, calcite ($CaCO_3$) predominates in waste wood ash, whereas at higher incineration temperatures in the order of 1000 °C, oxide compounds such as quicklime (CaO) are found in waste wood ashes [61] due to the decomposition of calcite. The generally high calcium content of wood ash is due to its high content naturally occurring in wood. Furthermore, Si is commonly found in significant amounts in waste wood ashes [60,61]. However, the present chemical analysis revealed only a moderate silica concentration, but a high K content. Both the Ca and Si content as well as other components depend on the type of wood [61].

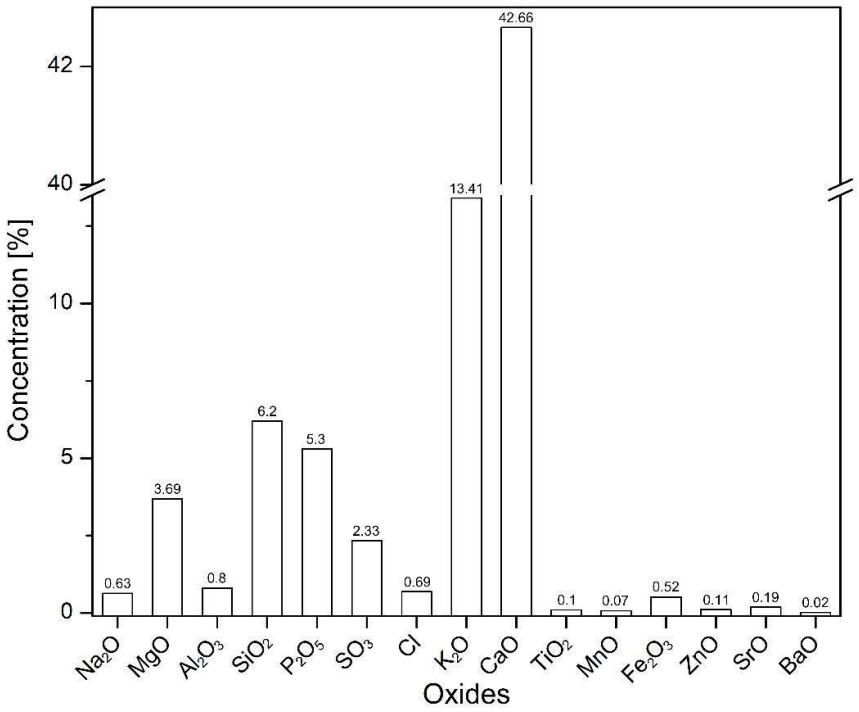

Figure 14: Chemical analysis of the waste wood ash produced from incinerating waste wood in a furnace at ~550 °C. The main oxides are CaO, K_2O, SiO_2, and P_2O_5.

Ash behavior and deposition tendencies during the combustion process are normally predicted through the use of empirical indices. These indices can give indications of possible contamination or sintering reactions during firing. One simple index is the base-to-acid ratio $R_{b/a}$ (Equation 3), where the data for each compound refers to its weight concentration in the ash [60].

$$R_{b/a} = \frac{wt.-\%\ (Fe_2O_3 + CaO + MgO + K_2O + Na_2O)}{wt.-\%\ (SiO_2 + Al_2O_3 + TiO_2 + P_2O_5)} = 4.91 \qquad (3)$$

In general, P_2O_5 is not considered in this equation. Nevertheless, it is commonly a major component of biogenic fuels such as waste wood ash. The chemical composition of the present wood ash yields a $R_{b/a}$ value of 4.91, indicating a medium deposition tendency. However, the base-to-acid ratio only considers aluminosilicate networks. Also, the possibility of the occurrence of sulfidic or sulfatic melts is neglected [66]. Other empirical indices are the iron-calcium and silica-aluminum ratio, which were found to be 0.01 and 7.75, respectively, for the present wood ash. These values are outside the critical range (0.31-3.00), which is associated with a low deposition tendency [60].

However, more mineralogical details are essential to predict fouling and sintering reactions of waste wood ash. The mineralogical characterization was performed by both XRD and Raman spectroscopic studies. In general, XRD data provide information about the total content of mineral phases contained in the investigated sample material, but not about the localities or, in particular, about the grain boundary reactions during or after sintering. In addition, the detection limit of XRD analysis is in the order of 0.1 to 5.0 vol.-%, i.e., phases that occur in minor amounts cannot be detected. However, both qualitative and quantitative analysis is possible, which also helps to identify mineral phases in Raman studies. The diffractogram with identified mineral phases is shown in Figure 15. The main mineral phases in the present waste wood ash are calcite ($CaCO_3$) with 61.5 vol.-% and apatite ($Ca_5(PO_4)_3(OH, F, Cl)$ with 15.3 vol.-%. In addition, 7.4 vol.-% arcanite (K_2SO_4), 5.6 vol.-% albite ($NaAlSi_3O_8$), 3.8 vol.-% microcline ($KAlSi_3O_8$), and 3.2 vol.-% periclase (MgO) and quartz (SiO_2) were detected. Notably, the peaks that identify hydroxylapatite (HAp) match very well with XRD data of Sr-substituted HAp. Natural apatite has the chemical composition $Ca_5(PO_4)_3(OH, F, Cl)$, but also the Ca atoms can be substituted by a number of cations including Na^+, Mg^{2+}, K^+, Mn^{2+}, Fe^{2+}, Zn^{2+}, Sr^{2+}, Ba^{2+} [67–69]. The apatite diffraction peaks from the wood ash are shifted to lower °2θ values with respect to the peaks of pure, end member HAp, indicating an increase in the lattice constants, i.e., the incorporation of other elements into the apatite structure.

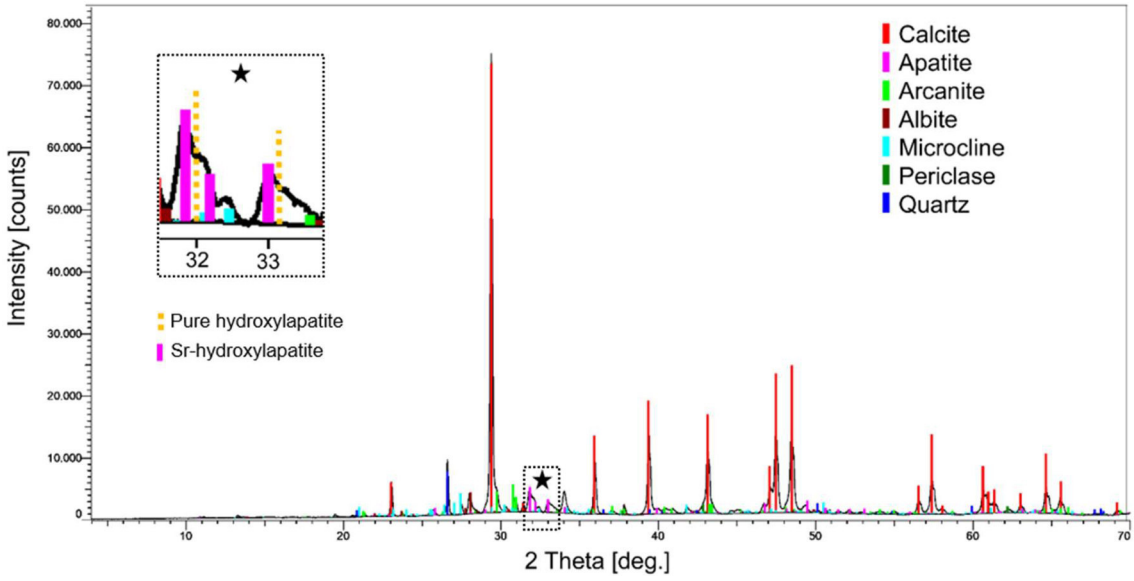

Figure 15: : X-ray diffraction pattern of the waste wood ash with identified mineral phases based on the ICDD PDF 2-2016 database [70]. *The inset shows diffraction peaks that identify Sr-substituted hydroxyapatite (HAp). Compared to diffraction peak positions of pure HAp, the corresponding diffraction peaks of Sr-HAp are shifted to lower 2θ angles.*

Three false-colored Raman images taken from different localities on the sample surface are shown in Figure 16. The Raman spectroscopic measurements confirm that calcite and apatite are the main mineral phases in the present waste wood ash. The most intense Raman band of apatite was identified

in a frequency range from 938 to 962 cm^{-1} measured at different localities on the sample surface (Figure 17a). Compared to the $v_1(PO_4)$ mode obtained from pure hydroxylapatite at 961 cm^{-1}, the main band shifted to lower wavenumbers, indicating longer P-O bond length, which could reflect the substitution of Ca by other elements in the apatite crystal structure [67,71]. Chlorapatite can be identified by the $v_1(PO_4)$ being located at 959 cm^{-1} [71], whereas in Sr- and Ba-substituted hydroxylapatite this band is shifted to 948 and 935 cm^{-1}, respectively [67]. Referring to the chemical analysis, the incorporation of the identified elements (Cl, Sr, Ba, etc.) into the apatite crystal structure is possible.

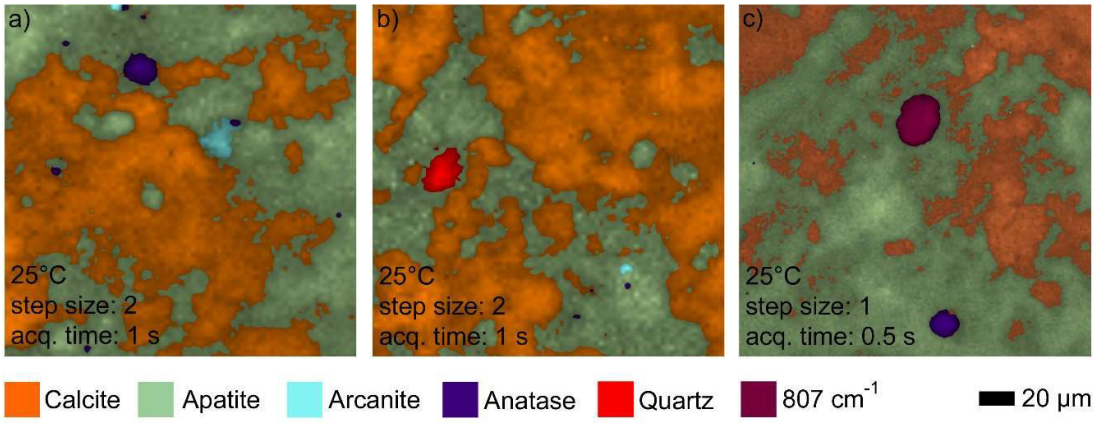

Figure 16: False-colored Raman images of the mineral distribution of three 160 x 160 µm²-sized surface areas of a sample body made of waste wood ash taken at RT.

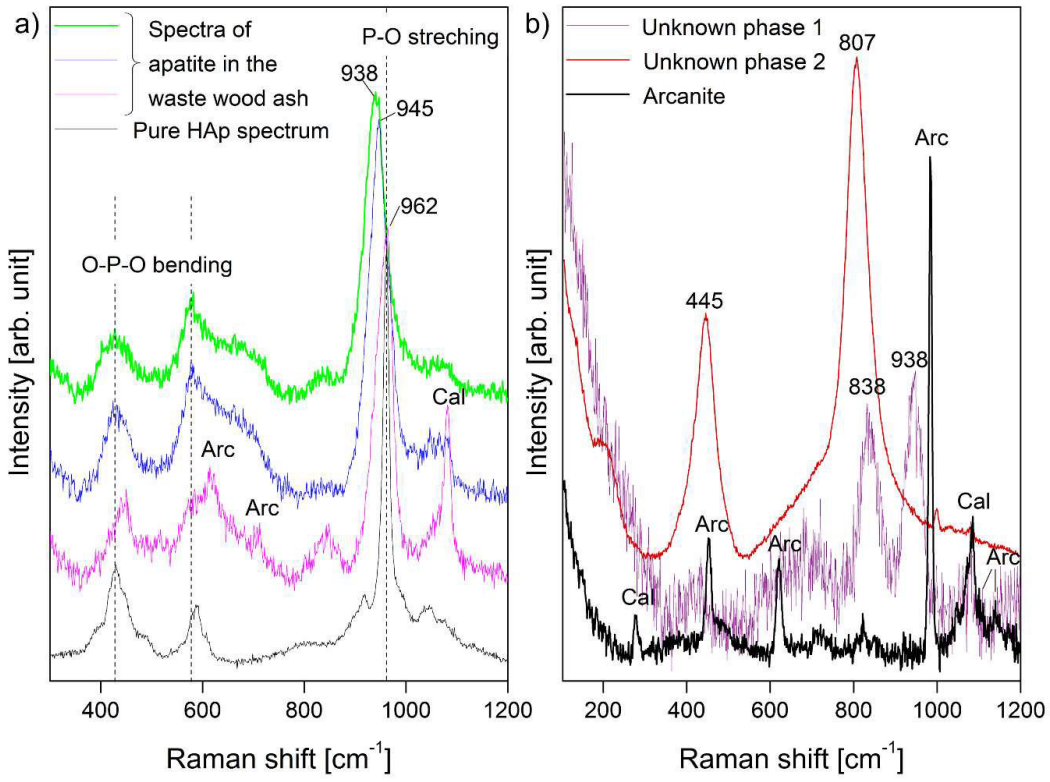

Figure 17: (a) RT Raman spectra of apatite recorded at three different localities on a wood ash sample surface compared to a representative spectrum of pure, but nanocrystalline hydroxylapatite (HAp) [57]*. Note the significant differences in the frequency of the $v_1(PO_4)$ band of the apatite of the wood ash sample, which varies between 938 and 962 cm^{-1}. (b) Representative RT Raman spectra of arcanite and two currently unidentified phases.*

Due to the limit of detection of XRD analyses, the TiO_2 identified by XRF could not be detected by XRD. In contrast, Raman images confirm the presence of TiO_2 within the waste wood ash. More precisely, anatase could be identified in all three imaged areas at RT (Figure 16). Arcanite (K_2SO_4) was identified by its most intense Raman band at 983 cm^{-1}, which is assigned to the v_1 stretching mode of the SO_4 tetrahedra [72,73]. The two medium intense bands at 453 and 620 cm^{-1} are assigned to the $v_2(SO_4)$ and $v_4(SO_4)$ bending modes, respectively. The weak bands at 1104 and 1145 cm^{-1} are attributed to the v_3 stretching modes of the SO_4 tetrahedra. Possibly, a third $v_3(SO_4)$ mode appeared near 1090 cm^{-1} as claimed in other studies [72,73], but was overlain by the main band of calcite (Figure 17b).

Two unknown mineral phases were found as small grains within the waste wood ash. The first unknown phase is characterized by a broad band at 838 cm^{-1}. Unfortunately, only mixed Raman spectra, possibly including apatite signals (938 cm^{-1}), could be recorded (Figure 17b). The second unknown phase with two intense bands at 445 and 807 cm^{-1} was identified within a 160 x 160 μm^2 area (Figure 16c). A representative spectrum of this phase is shown in Figure 17b. Possibly, both unknown phases are dicalcium silicates, which certainly occur in wood ash [65] and show relative broad and intense $v_1(SiO_4)$ bands between 800 and 860 cm^{-1} [74,75]. On the one hand, the Raman band at 807 cm^{-1} may indicate γ-Ca_2SiO_4 [74,75], which could have formed by the reaction between quartz and calcite during the firing process. On the other hand, the band at 445 cm^{-1} cannot be attributed to dicalcium silicate. However, the incorporation of Mg^{2+}, Fe^{2+}, Sr^{2+}, Ba^{2+} cations into the dicalcium silicate structure is possible [74,76], which may result in additional Raman bands.

Two heating experiments with cylindrical sample bodies of waste wood ash were conducted. For the first experiment, an area with calcite and arcanite was selected. During firing to 820 °C, calcite decomposed to CaO and CO_2, but recrystallized during the following quenching step. Arcanite remained stable during firing and was also identified at RT (Figure 18a). Thus, the Raman images at high temperatures (not shown here) reveal no phase reactions between arcanite and calcite. For the second experiment, an area with calcite and apatite as main phases was therefore selected. The sample was first fired to 870 °C and after the image acquisition time of four hours, it was heated up to the second temperature step of 960 °C. After taking the last image, the sample was cooled down to RT. The HT images at both temperature steps show no phase reactions, except the calcite decomposition (not shown here). During cooling calcite recrystallized and was again identified at RT, as were apatite, arcanite, and the unknown phase at 838 cm^{-1} (Figure 18b).

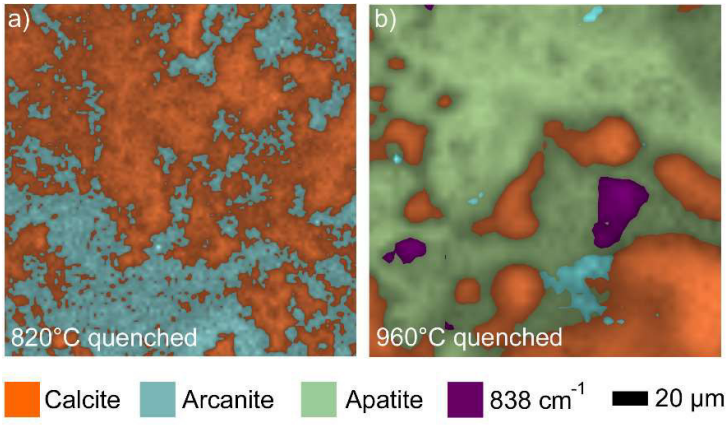

Figure 18: False-colored Raman images of samples of waste wood ash after firing (a) 4 hours at 820 °C and (b) 4 hours at 870 °C and 4 hours at 960 °C, respectively, recorded at RT. Both images were acquired with an acquisition time of 0.5 s per spectrum. The step size was 2 pixels for the first image and 4 pixels for the second image.

5.4 Conclusion

The major aims were to gain detailed information on the chemical and mineralogical composition of waste wood ash produced during the combustion of waste wood in a kiln at about 550 °C and to explore the potential of in situ and in operando Raman imaging of mineral reactions in natural wood ash. Both XRD and Raman measurements were performed, which allowed the identification of the main mineral phases, which are calcite, apatite, and arcanite. This mineralogical paragenesis is well-reflected by the chemical composition of the ash. Accessory phases are alkali feldspars, periclase, and quartz. Also anatase and minor amounts of dicalcium silicate phases were detected. The chemical analysis also revealed trace elements (e.g., Cl, Sr, and Ba) which are most likely located in the apatite phase. The XRD pattern identifies Sr-substituted HAp as the main apatite phase in the waste wood ash. In addition, the Raman data show that Ca is also substituted by Ba, reflected by a distinctly lower $v_1(PO_4)$ frequency.

The results of the heating experiments demonstrate that firing of waste wood ash containing calcite, apatite, and arcanite to 960 °C does not lead to considerable sinter/melting reactions between these phases. However, it must be considered that predictions of ash behavior and deposition tendencies during the combustion process based on composition or empirical indices of fuel ashes are always sample-specific and cannot always be generalized.

6 Summary discussion

6.1 Advantages and limits of high-temperature, in situ Raman spectroscopy and imaging

6.1.1 High-temperature Raman spectroscopy

High-temperature in situ Raman spectroscopy enables to identify mineral phases during firing and cooling processes, in particular (i) crystalline and amorphous phases, (ii) various polymorphs, and (iii) metastable phases are detectable. The identification of minerals at high temperatures is more complicated due to the fact that all available reference Raman spectral databases solely contain RT spectra that usually differ significantly from their HT counterparts. Therefore, heating studies on pure mineral phases, covering all the minerals that are potentially present in the multi-phase experiments, were performed to acquire high-temperature Raman spectra (cf. Section 1.2.1). In addition, these studies using point measurements provided valuable results on (i) structural changes, e.g., loss of sulfur/OH-groups, (ii) thermal stability limits, and (iii) phase transformation processes during firing. For instance, the heating studies of the sulfate- and phosphate-containing end members of a solid solution series ternesite [52] and silicocarnotite, and the heating studies with hydroxylapatite (HAp) and tricalciumphosphate (TCP) [57] are presented in Chapters 3 and 4, respectively.

The temperature dependence of integrated intensity ratios of Raman bands delivers information about thermal stability limits of a single phase. For instance, the ratio between the $v_1(PO_4)$ and $v_1(SiO_4)$ band intensities (A) was found to not significantly change with increasing temperature up to ~1200 °C, reflecting a high temperature stability of silicocarnotite. In contrast, the integrated intensity ratio between both v_1 bands, $A_{v1(SO4)}/A_{v1(SiO4)}$, of ternesite as a function of temperature revealed a significant change at about 730 °C, when the transformation from ternesite to dicalcium silicate begins.

6.1.2 High-temperature Raman imaging: In operando study of solid-state mineral reactions

Confocal hyperspectral Raman imaging at high temperatures allows the study of solid-state or solid-melt reactions in operando and in situ, i.e., while the reactions are in progress and without the need to quench the sample before analysis. In addition, spatially resolved information on phase composition and textures at micrometer-scale can be obtained at high temperatures. The generation of kinetic information on various reaction processes leading to the formation of new mineral phases and the quantification of grain growth and decay in situ and at high-temperature are also possible [24]. Note that all this information is limited to the extract (~100–200 µm x ~100–200 µm x ~15 µm) that is examined, i.e., no bulk information representative of the whole volume of the green body is given. Despite the short acquisition time per spectrum (0.5 s), the total exposure time for a single HT image was still about two hours. Therefore, an image is not always an accurate snapshot, since processes are still running during image generation. In addition, information about some minerals with low Raman cross sections may be hidden because the phase with the highest partial intensity within a Raman spectrum is displayed with a color assigned to that phase. However, when taking all these facts into

account while interpreting the hyperspectral Raman images, in situ Raman imaging is a unique tool to study high-temperature solid-state reactions in multi-component systems.

6.2 Mineral reactions during firing and cooling

The major aim of this project was to apply in situ HT Raman spectroscopy to study the thermodynamics and kinetics of solid-state and melt-crystal interactions of calcium (alumina) silicates and silica-/calcium sulfates/phosphates. Their formation and decomposition reaction mechanisms were studied in multi-phase Raman experiments at high-temperature. All starting mixtures contained quartz and CaO supplying minerals, but varied in composition and phase proportions to investigate possible influences on textural and phase evolution.

Understanding the kinetics of sintering reactions helps to systematically control manufacturing processes, but also to understand metamorphic rock formation processes in nature. Even if a mineral transformation is thermodynamically favored, it is not guaranteed that the transformation will occur at any measurable rate. The rate of reaction is highly dependent on the mechanisms involved in the reaction process and can change with time and temperature. In general, solid-state reactions involve diffusion-based processes, such as grain boundary diffusion of elements, their adsorption at interfaces, migration through the product layer, and nucleation and growth of a new phase from the solid without the formation of a melt phase. Melting is considered as a grain boundary controlled dissolution process, which is controlled by the diffusion of elements through the continuously increasing melt phase and it is mainly associated with fluxes such as alkalis [77]. However, all mineral crystallizations observed in the present multi-phase experiments are solid-state reactions and no evidence for a partial melt has been found.

Diffusivities depend on several factors, including temperature, pressure, composition, physical state and structure of the phase, and sometimes oxygen fugacity [78]. The chemical mass transfer and the localized reactions proceed simultaneously producing reaction fronts between the educts. Both processes may be rate-limiting, and the coupling between the two processes determines the overall reaction kinetics [79]. So far there are two approaches to identify the rate-limiting component and to identify the direction of the migration front: (i) experiments with isotopically doped reactants [80,81] that is conceivable with ^{18}O-labeled reactants and (ii) the rim growth approach that was followed by in situ Raman imaging in the present project.

6.2.1 The formation of calcium silicates in the systems $CaSO_4$-SiO_2, $CaSO_4$-SiO_2-$Ca_2Al(AlSi)O_7$, and $CaSO_4$-SiO_2-CaO

The first multi-phase experiments were performed with anhydrite and quartz (AQ-experiments, Chapter 2), which were then added with gehlenite (AQG-experiments, Chapter 2) and calcium oxide (AQC-experiments, Chapter 3), respectively. In these multi-phase experiments, three different wollastonite-forming reactions could be identified at different temperatures and from different precursor materials. It is well-known that wollastonite can be synthesized at about 1000 °C by a reaction between quartz and calcite, whereby CO_2 is released into the atmosphere and lime (CaO) is formed as an intermediate product [e.g., 68]. The decomposition of anhydrite also produces lime, which is then available to react with quartz to form wollastonite, according to the following reactions:

$$CaSO_4 \xrightarrow{T \sim 660 - 1000\ ^\circ C} CaO + SO_3 \quad \text{(a)}$$

$$CaO + SiO_2 \rightarrow CaSiO_3 \quad \text{(b)}$$

Thus, in all two-phase experiments with anhydrite and quartz, wollastonite was the first calcium silicate, which crystallized along anhydrite-quartz interfaces involving diffusion-based chemical mass transfer of Ca/Si ions. From the Raman images of the AQ-experiments, it appears that wollastonite layers grew simultaneously in both interfacial directions, inwardly replacing quartz and outwardly replacing anhydrite, i.e., the inward diffusion of CaO and the outward diffusion of SiO_2. Here, the formation of wollastonite depends on the thermal decomposition of anhydrite, which is further influenced by the quartz content. In performed experiments, where more quartz was available, anhydrite decomposed at lower temperatures (~920) than in experiments with lesser quartz content (~1000 °C) [48]. In the AQ-experiments, the transformation of wollastonite to its high-temperature polymorph pseudowollastonite was observed at about 1000 °C, which is 125 °C below the known wollastonite stability temperature [49]. It is noteworthy that in one experiment with an even higher quartz content, anhydrite decomposed already at about 660 °C, and both wollastonite and pseudowollastonite crystallized contemporaneously (AQG-2, Epilog Chapter 2). The formation of both polymorphs at the same temperature has already been observed in in situ Raman experiments performed by Stange and co-workers [26]. These authors suggested that the local conditions must have been different, perhaps due to different crystallographic structures or orientations of the reactants, which favored the formation of either a single-chain inosilicate (Wo) or a cyclosilicate (PWo) [26].

In experiment AQ-2.1, the high-temperature phase α'_L-Ca_2SiO_4 could be identified at about 1100 °C related to the solid-state reaction between wollastonite and lime:

$$CaSiO_3 + CaO \xrightarrow{T\ \sim 1100\ °C} Ca_2SiO_4 \qquad (c)$$

During quenching, α'_L-Ca_2SiO_4 transformed to β-Ca_2SiO_4 (larnite) and remained metastable at RT [48]. The RT data of experiment AQ-1 revealed that after a total sintering time of 9 h at 1093 ± 5 °C, larnite was identified as rims around anhydrite and near to pseudowollastonite crystallized around quartz grains [48]. It is possible that initially quartz and lime (from decomposition of anhydrite) formed rims around anhydrite grains. Then more CaO reacted with wollastonite to form dicalcium silicate (Equation c). Alternatively, the formation of wollastonite could have occurred while dicalcium silicate formed in regions with high anhydrite content, i.e., more CaO was available. However, it can be concluded that the formation of dicalcium silicate is more bound to CaO supplying minerals, in this case anhydrite.

The formation of wollastonite by a reaction of dicalcium silicate with free SiO_2 (Equation d) was observed in various in situ experiments (AQC-1.2, AQG-2) at different temperatures depending on the local chemistry [48,52].

$$Ca_2SiO_4 + SiO_2 \rightarrow 2CaSiO_3 \qquad (d)$$

The Raman images of experiment AQC-1.2, for instance, show the growth of wollastonite at the expense of a quartz grain in a dicalcium silicate matrix as time and temperature increased (1020–1100 °C). When quenched to RT, α'_L-Ca_2SiO_4 completely transformed to larnite and only a quartz relic remained in the center of the wollastonite grain.

In both AQG-experiments, gehlenite appeared to be replaced by wollastonite (cf. [48], Epilogue Chapter 2) at about 830 °C, which was also observed by Stange and colleagues [26]. It follows that additional gehlenite in the CaO-SiO_2 system enhances the formation of wollastonite because, first, it may be a breakdown product of gehlenite and, second, released CaO is available to react with free SiO_2 to form additional wollastonite.

In contrast to that, in all multi-phase experiments performed with lime and quartz as precursor materials, α'_L-Ca_2SiO_4 was the first newly formed mineral phase during firing indicating dicalcium

silicate is thermodynamically favored compared to wollastonite. The addition of free CaO allows the formation of dicalcium silicate at lower temperatures, since calcium oxide is directly available:

$$2CaO + SiO_2 \rightarrow Ca_2SiO_4 \quad \text{(e)}$$

Already at the first heating step at about 660 °C, small grains of dicalcium silicate could be identified within the CaO matrix (AQC-1.2) [52]. In this case, the required SiO_2 was derived from small invisible quartz particles, which are more reactive than the larger particles due to their larger surface area [24]. In addition, α'_L-Ca_2SiO_4 crystallized at the interface between quartz and lime/anhydrite by growing around large quartz grains (e.g., AQC-1.1). Such reaction rims separated the reactants by forming a barrier between lime/anhydrite and quartz. The further crystallization of α'_L-Ca_2SiO_4 thus had to take place by diffusion of Ca^{2+} ions through this barrier layer. With increasing time and temperature, the fraction of dicalcium silicate increased at the expense of SiO_2 and CaO supplying minerals [24,82]. The same reaction was followed during isothermal sintering at about 850° C for 24 hours performed by Hauke and co-workers [24]. A linear increase of α'_L-Ca_2SiO_4 over time was observed. Accordingly, the fraction of the educts CaO and quartz also decreased linearly. The average grain size of the newly formed α'_L-Ca_2SiO_4 grains also increased linearly with time. A pseudo-zero order behavior of mineral growth was observed in the system, which is most likely due to a CaO excess [24].

6.2.2 The formation of ternesite and silicocarnotite

Ternesite and silicocarnotite represent the sulfate- and phosphate-containing end member of a solid solution series. Experiments with anhydrite, quartz, and CaO as precursor materials (AQC-experiments, Chapter 3), were mainly performed to observe the formation and decomposition of ternesite [52]. As mentioned, the first newly crystallized mineral phase during firing was dicalcium silicate, which is able to react with anhydrite to form ternesite. At about 930 °C, ternesite started to nucleate in the interior of dicalcium silicate grains and from this point on it continued to grow outwards. However, ternesite not only displaced individual α'_L-Ca_2SiO_4 grains within the CaO matrix in contact with anhydrite grains, but also began to crystallize with increasing time at the expense of a large quartz grain (AQC-1.1). It appears that the reaction must have proceeded very fast, as dicalcium silicate was not detected as an intermediate phase after two hours at ~930 °C to ~970 °C. With increasing temperature, this large quartz grain was more and more replaced by ternesite, while the grain boundary migrated inwards due to the solid-state reaction between the reactants. In addition, smaller quartz grains were pseudomorphically replaced completely. Noticeably, at about 1020 °C, α'_L-Ca_2SiO_4 formed new reaction rims around ternesite, producing a layered texture with quartz in the center, ternesite in the middle, and α'_L-Ca_2SiO_4 in the outer layer. Between 1016 and 1060 ± 5 °C, the content of the three phases seems to have been stable. The single-phase heating study of natural ternesite confirms that both ternesite and dicalcium silicate domains co-exist at high temperatures up to about 1120 °C. In fact, at 1104 ± 5 °C, large ternesite grains decomposed and were almost completely replaced by dicalcium silicate, which later transformed to larnite on cooling to RT. Some smaller dicalcium silicate grains recrystallized to ternesite. However, whether ternesite or larnite was observed after quenching to RT depends on the course of the reaction.

Experiments with HAp, quartz, and CaO as precursor materials (TQC-experiments, Chapter 4), were performed to observe the formation of silicocarnotite [57]. Previously, silicocarnotite was thought to be formed by a reaction between high-temperature polymorphs of dicalcium silicate and TCP during cooling down from temperatures above 1450 ± 20 °C [83,84]. However, in the multi-phase experiments silicocarnotite was identified as small grains located close to large α'_L-Ca_2SiO_4 grains within the HAp/β-TCP matrix at 1150 ± 5 °C after a dwell time of two hours. After cooling to RT, silicocarnotite crystallized further as rims around dicalcium silicate grains. The in operando observations demonstrate that silicocarnotite can furthermore form by a reaction between

wollastonite and β-TCP with the additional formation of quartz at rather low temperatures (~1050 °C). Both the formation of silicocarnotite involving dicalcium silicate and wollastonite appear to be controlled by grain boundary diffusion of TCP components.

The single-phase experiment with nanocrystalline HAp revealed that between 770 and 850 ± 1 °C and 1220 to 1270 ± 5 °C, the reconstructive HAp to β-TCP and β-TCP to α-TCP transformations occurred, respectively. The complex process of the loss of surface hydroxyl groups bound to HAp nanocrystals up to about 570 °C is described in detail in Chapter 4. In the TCP-experiments, HAp decomposed at higher temperatures (960–1050 ± 5 °C). Obviously, the reaction kinetics of the HAp decomposition can change due to the addition of other minerals, i.e., quartz and/or lime were found to stabilize HAp during firing [57].

6.2.3 Temperature stability fields of mineral phases

The diversity of reaction pathways to form calcium silicates makes the mineral phases stable within a wide range of temperature. Figure 19 gives an overview of observed temperature stability fields of calcium silicates and other minerals that occurred in the $CaO\text{-}SiO_2(\text{-}SO_3/Al_2O_3/P_2O_5)$ system and subsystems studied in this project.

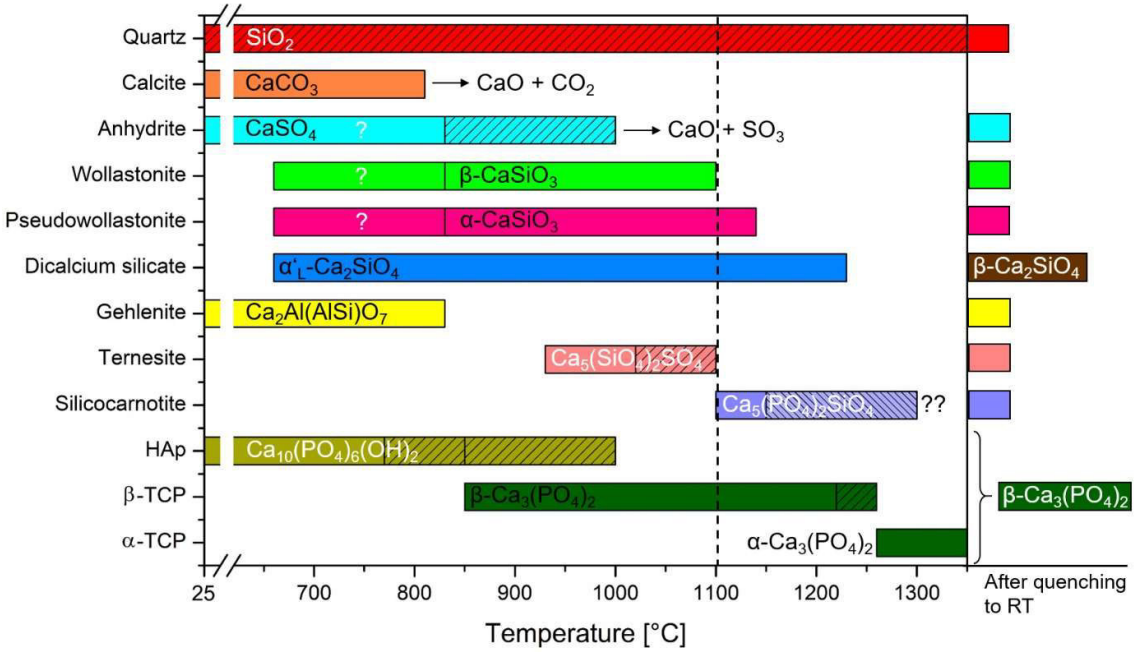

Figure 19: Temperature stability fields of minerals that occurred during the in situ Raman experiments. Quartz was stable within the entire temperature range, but reacted with other minerals, e.g., lime to form calcium silicates. The areas striped diagonally to the right mark the decomposition zones of anhydrite, ternesite, HAp, and β-TCP. Question marks were used to hint to one experiment (AQG-2), where anhydrite decomposed already at 660 °C and wollastonite/pseudowollastonite crystallized. The first decomposition zone of HAp is the transformation to β-TCP, and the second zone was determined from the multi-phase TQC-experiments. Both anhydrite and HAp were affected by the quartz content in the system. Note that most experiments were monitored up to ~1100 °C, which is indicated by the dashed line. Silicocarnotite was observed up to 1150 ± 5 °C, in this case the maximum sintering temperature, but the upper stability limit of silicocarnotite was not reached. After recording the last image at the maximum temperature, each sample was cooled down to RT and a last Raman image was recorded. During cooling, $\alpha'_L\text{-}Ca_2SiO_4$ transformed to β-Ca_2SiO_4 (larnite). After firing HAp to 1350 ± 5 °C and cooling down to RT, β-TCP remained metastable.

6.3 To what extent are observations from the synthetic system transferable to real systems?

6.3.1 Combustion and cement industry

The use of materials containing CaO and SiO_2 in the operation of industrial furnaces, such as in quicklime and cement production or coal combustion, leads to sinter deposits consisting mainly of calcium silicates, which cause problems during kiln operation [3–6]. Moreover, silica-/calcium phosphates are involved when biomass and/or sewage sludge is fired. However, deposited minerals can serve as a temperature indicator once their thermal stability field is known, which can help kiln operators to optimize the combustion temperatures. In addition, calcium silicates are well-known phases in the cement industry [10–12]. Interest in their high-temperature properties, particularly those of the sulfate-containing product ternesite, has increased recently. The so-called belite calciumsulfo-aluminate ternesite (BCT) technology combines the early age strength of calcium sulfoaluminate cements with the durability of belite-bearing cements. In this system, ternesite bridges the reactivity gap between the rapid aluminate reaction and the late strength development of belite. Due to its lower firing temperature, the CO_2 emissions of the BCT clinker can be reduced compared to those of conventional clinker production.

The here presented in situ Raman experiments at high temperatures gave detailed information about solid-state reactions within the large field of the CaO-SiO_2(-SO_3/Al_2O_3/P_2O_5) system and subsystems as well as of pure phases, which can help to extend their technical advantages and predict sintering reactions in industrial processes at a given temperature.

Coal, biomass, as well as cements are very complex materials and the experiments with synthetic samples show only parts of chemical and mineralogical reactions that may occur at high temperatures, which can be further influenced by several factors of the firing process, such as (i) combustion rate, (ii) duration of firing, (iii) gas fugacity and composition in the furnace, and maybe (iv) furnace size; and factors of the materials used, such as (v) chemical and mineralogical composition, (vi) particle size distribution, (vii) surface properties, and (viii) natural origin. For instance, Ward [85] summarized the results of several works concerning to the mineral matter of coal and refers to the link between the minerals in coal and the concentration of particular trace elements. Associations include As, Cd, Se, Tl, Hg, Pb, Sb, and Zn with sulfide minerals, Rb, Ti, Cr, Zr, Hf, and a number of other elements with aluminosilicate components, and Sr and Ba with carbonates or aluminophosphate minerals. In addition, several trace elements, including Ge, Ga, Cl, and B, appear not to be bound to minerals in some coals and in such cases may occur as part of the organic matter [85]. Furthermore, trace elements incorporated into the apatite structure were found in biomasses, especially in the ash of waste wood (Chapter 5). These alternative fuels are also used as a cement additive, where, for example, insoluble salts significantly retard cement hydration and highly soluble salts can act as accelerators, affecting mechanical properties in both cases [86]. It is also possible that trace elements influence the mineralogical interactions of phases at high temperatures, or that the properties of minerals change as elements are incorporated into the crystal structure. Therefore, multi-phase sintering experiments with both natural/original materials and synthetic samples with systematically added elements are required to estimate the potential extent of their influence.

First studies have already been performed on natural coal samples fired at 815 °C before analysis. For instance, one experiment with a coal ash added with quartz sand is shown in Figure 20. The XRD results revealed anhydrite, quartz, and periclase as the main phases (Figure 20a). However, only quartz could be identified by Raman spectroscopy and studies of the mineral matter of the coal

yielded no results due to interfering factors caused mainly by severe fluorescence effects, which are more significant at lower temperatures (cf. Section 1.3.1.1). When firing to 838 ± 5 °C, wollastonite was formed according to a reaction between quartz and lime supplied by the decomposition of anhydrite (Figure 20b). Moreover, a large akermanite ($Ca_2MgSi_2O_7$) grain was identified near quartz, crystallized by a reaction between lime, quartz, and magnesium oxide. The Raman spectra assigned to the matrix around the wollastonite and quartz grains do not show clearly discernible bands, resulting in a mixed and blurred appearance of the matrix color in the image. During cooling down to RT, pseudowollastonite was formed within the wollastonite matrix (Figure 20c). Merwinite ($Ca_3Mg(SiO_4)_2$) crystallized in contact to akermanite, apparently due to an increased oxygen concentration, possibly from the decomposition of anhydrite, which was not identified at RT. Furthermore, an unknown phase with the main Raman band at 862 cm^{-1} could be identified near quartz. The white areas in the Raman images are interference zones that could be due to fluorescent cations. On the other hand, it is also possible that residues of organic substances have caused interference during the measurement.

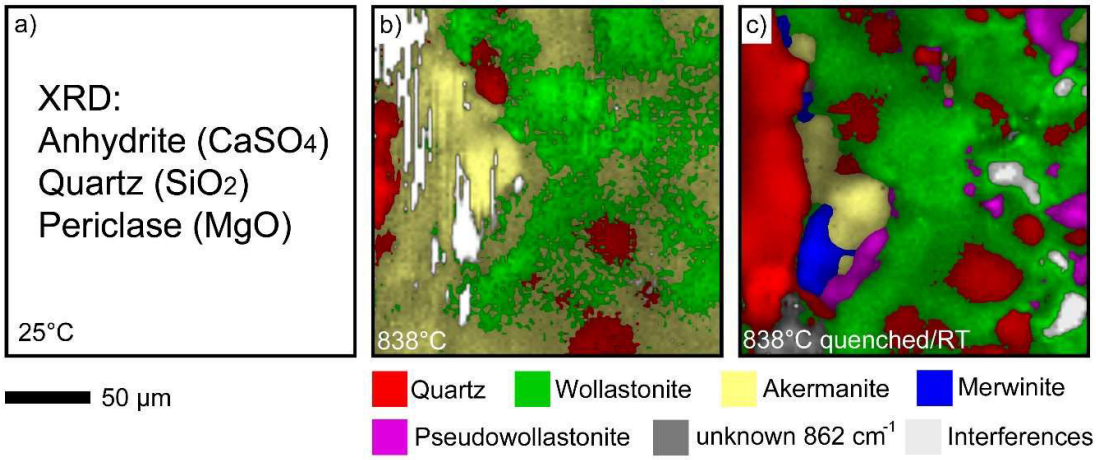

Figure 20: (a) A natural coal sample fired at 815 °C before analysis and added with quartz sand was analyzed by XRD at 25 °C. (b, c) Hyperspectral Raman images (200 µm x 200 µm) at about 838 °C and after quenching to RT. The total recording time for one image was about 4 h. Obviously, anhydrite decomposed during firing, and the released lime reacted with quartz to form wollastonite.

In general, mineral reactions identified in the Raman experiments with synthetic samples, e.g., crystallization of wollastonite by a reaction between anhydrite and quartz (Equations a and b in Section 6.2.1), could also be observed in real samples. At a high quartz content, anhydrite decomposed already at about 838 °C and CaO was available to form wollastonite, which partially transformed to pseudo-wollastonite during quenching. However, interfering factors generally complicated the evaluation of the Raman analysis. In addition, natural/real samples usually consist of many different minerals. The more mineral phases the material to be analyzed contains, the more reactions can occur that influence each other. In the future, HT reference spectra from other relevant phases have to be collected.

Nevertheless, in situ experiments at given conditions such as (i) sample composition and properties, (ii) temperature rate and range, (iii) heating and quenching rate (iv) dwell and recording time, and (v) gas fugacity can help to predict sintering reactions within the defined system and to be able to better model the thermodynamics and kinetics of these reactions.

6.3.2 Ceramic industry

The application of the results of the present experiments within the $CaO\text{-}SiO_2(\text{-}SO_3/Al_2O_3/P_2O_5)$ system and subsystems to industrial processes depends on the complexity or purity of the system. Well-defined systems can be found in the production of glass or ceramic products, especially for medical

applications. Here, the insights into the high-temperature solid-state reactions gained by hyperspectral Raman imaging can help to extend the technical advantages of the identified minerals and ensure their synthesis under optimal conditions. For instance, the formation of silicocarnotite was studied in the model system $Ca_{10}(PO_4)_6(OH)_2$-SiO_2-CaO [57]. Recently, highly promising studies with silicon-substituted calcium phosphates have shown that silicon is an essential trace element for bone mineralization and can improve the bioactivity of calcium phosphate materials [18–23]. The wide range of CaO, SiO_2, and P_2O_5 solid solutions varies with temperature and makes silicocarnotite ($Ca_5(PO_4)_2SiO_4$) [87–92] an excellent ceramic with great potential for medical applications [23,92–95]. The results of the in situ Raman experiments demonstrate that silicocarnotite can form from a reaction between β-TCP and α'_L-Ca_2SiO_4, but also by a reaction of β-TCP and $CaSiO_3$ with the additional formation of quartz in the temperature range between 1050 and 1150 °C [57], i.e., well below 1340 ± 30 °C, the proposed temperature at which the so-called R solid solution phase transforms to silicocarnotite when cooling from 1450 °C to RT [83,84]. This information offers new possibilities for the synthesis of ceramic products at lower temperatures, i.e., to reduce energy costs.

7 Conclusion and outlook

The Raman spectrometer system with integrated heating stage used in this project allows the visualization of mineral reactions and textures even at high temperatures with a spatial resolution of a few micrometers and without the need to quench the sample to room temperature before analyzing it. Therefore, solid-state reactions can be studied in operando, i.e., while they are running. In general, the present experiments focused on thermal stability fields of calcium silicates and silica-/calcium sulfates/phosphates and their solid-state mineral reactions in both single- and multi-phase systems, which varied in composition and phase proportion to investigate their possible influence on textural and phase evolution. These minerals are of great interest due to their use in industry. Moreover, they have been identified as sinter deposits in industrial kilns, which may affect the kiln operation. However, they can serve as reliable temperature indicators or their formation during kiln operation can be avoided if their thermodynamic and kinetic parameters are known. The present results remarkably demonstrate the power and diverse possibilities of in situ high-temperature Raman spectroscopy. The most noticeable findings of this study were that

(1) the decomposition of anhydrite is significantly influenced by the quartz content, i.e., in performed experiments, where more quartz was available, anhydrite decomposed at lower temperatures than in experiments with lesser quartz content,

(2) three different reaction pathways were identified to form wollastonite in a wide range of temperature,

(3) wollastonite and pseudowollastonite can crystallize simultaneously,

(4) when calcium oxide is directly available, it reacts with quartz and preferably dicalcium silicate is formed,

(5) during cooling, α'_L-Ca_2SiO_4 transforms to β-Ca_2SiO_4 (larnite) and remains metastable at RT,

(6) while ternesite transforms to α'_L-Ca_2SiO_4 during firing, both the ternesite and dicalcium silicate domains co-exist at high temperatures, and it depends on the reaction progress whether ternesite or larnite is identified after quenching to RT,

(7) the loss of surface hydroxyl groups bound to HAp nanocrystals is a stepwise process,

(8) quartz and/or lime stabilize HAp during firing,

(9) two reaction pathways are found to form silicocarnotite at temperatures more than 300 °C lower than previously proposed, and

(10) in general, quenching and heating periods have a significant effect on the final sintering products.

Isothermal in situ experiments in the CaO-SiO_2 system added with sulfate and phosphate components are necessary to investigate in more detail the kinetics of the formation of calcium silicates and silica-/calcium sulfates/phosphates and grain growth during firing. Detailed knowledge about the kinetic parameters of the mineral reactions at high temperatures can help to monitor and control important technical properties including densification and grain growth during sintering of the studied materials. Such information is of great importance for their synthesis, but also of great use for the combustion and refractory industries, thus would complement the present results.

In situ high-temperature Raman imaging is currently the only analytical tool to visualize mineral reactions in multi-component systems during firing at high temperatures and/or cooling with a high time and spatial resolution. This powerful method can give new insights into solid-state and solid-melt mineral reactions, and therefore also potentially offers the industry a wide range of possibilities to fully exploit and expand the technical application of refractory materials.

REFERENCES

[1] Taylor J, Dinsdale A. Thermodynamic and phase diagram data for the CaO-SiO_2 system. *Calphad* 1990;14:71–88. doi:10.1016/0364-5916(90)90041-W.

[2] Hillert M, Sundman B, Wang X. An Assessment of the CaO-SiO_2 System. *Metall Mater Trans* 1990;21B:303–12. doi:10.1007/BF02664198.

[3] Nankervis JC, Furlong RB. Phase changes in mineral matter of North Dakota lignites caused by heating to 1200 °C. *Fuel* 1980;59:425–30. doi:10.1016/0016-2361(80)90196-9.

[4] Vuthaluru HB, Zhang DK. Effect of Ca- and Mg-bearing minerals on particle agglomeration defluidization during fluidized-bed combustion of a South Australian lignite. *Fuel Process Technol* 2001;69:13–27. doi:10.1016/S0378-3820(00)00129-6.

[5] Kostakis G. Mineralogical composition of boiler fouling and slagging deposits and their relation to fly ashes: The case of Kardia power plant. *J Hazard Mater* 2011;185:1012–8. doi:10.1016/j.jhazmat.2010.10.006.

[6] Li J, Zhu M, Zhang Z, Zhang K, Shen G, Zhang D. The mineralogy, morphology and sintering characteristics of ash deposits on a probe at different temperatures during combustion of blends of Zhundong lignite and a bituminous coal in a drop tube furnace. *Fuel Process Technol* 2016;149:176–86. doi:10.1016/j.fuproc.2016.04.021.

[7] Vassilev S V, Baxter D, Andersen LK, Vassileva CG. An overview of the composition and application of biomass ash. Part 1. Phase – mineral and chemical composition and classification. *Fuel* 2013;105:40–76. doi:10.1016/j.fuel.2012.09.041.

[8] Bartels M, Lin W, Nijenhuis J, Kapteijn F, van Ommen JR. Agglomeration in fluidized beds at high temperatures: Mechanisms, detection and prevention. *Prog Energy Combust Sci* 2008;34:633–66. doi:10.1016/j.pecs.2008.04.002.

[9] Rashid AR, Shamsudin R, Abdul Hamid MA, Jalar A. Low temperature production of wollastonite from limestone and silica sand through solid-state reaction. *J Asian Ceram Soc* 2014;2:77–81. doi:10.1016/j.jascer.2014.01.010.

[10] Beaudoin J, Ramachandran V. A new perspective on the hydration characteristics of cement phases. *Cem Concr Res* 1992;22:689–94. doi:10.1016/0008-8846(92)90021-M.

[11] Low N, Beaudoin J. Mechanical properties of high performance cement binders reinforced with wollastonite micro-fibres. *Cem Concr Res* 1992;22:981–9. doi:10.1016/0008-8846(92)90122-C.

[12] Azarov GM, Maiorova EV, Oborina MA, Belyakov AV. Wollastonite raw materials and their applications (a review). *Glas Ceram* 1995;52:237–40. doi:10.1007/BF00681090.

[13] Dienemann W, Schmitt D, Bullerjahn F, Ben Haha M. Belite-Calciumsulfoaluminate-Ternesite (BCT) – a new low-carbon clinker technology. *Cem Int* 2013;11:100–9.

[14] Liu X, Tao S, Ding C. Bioactivity of plasma sprayed dicalcium silicate coatings. *Biomaterials* 2002;23:963–8. doi:10.1016/s0142-9612(01)00210-1.

[15] de Aza P, Guitián F, de Aza S. Bioactivity of wollastonite ceramics: In vitro evaluation. *Scr Metall Mater* 1994;31:1001–5. doi:10.1016/0956-716X(94)90517-7.

[16] Mohammadi H, Hafezi M, Nezafati N, Heasarki S, Nadernezhad A, Ghazanfari SMH, Sepantafar M. Bioinorganics in bioactive calcium silicate ceramics for bone tissue repair: Bioactivity and biological properties. *J Ceram Sci Technol* 2014;5:1–12. doi:10.4416/JCST2013-00027.

[17] LeGeros RZ. Properties of Osteoconductive Biomaterials: Calcium Phosphates. *Clin Orthop Relat Res* 2002;395:81–98. doi:10.1097/00003086-200202000-00009.

[18] Carlisle EM. Silicon: A Possible Factor in Bone Calcification. *Science* 1970;167:279–80. doi:10.1126/science.167.3916.279.

[19] Schwarz K, Milne DB. Growth-promoting Effects of Silicon in Rats. *Nature* 1972;239:333–4. doi:10.1038/239333a0.

[20] Balas F, Pérez-Pariente J, Vallet-Regí M. In vitro bioactivity of silicon-substituted hydroxyapatites. *J Biomed Mater Res* 2003;66A:364–75. doi:10.1002/jbm.a.10579.

[21] Vallet-Regí M, Arcos D. Silicon substituted hydroxyapatites. A method to upgrade calcium phosphate based implants. *J Mater Chem* 2005;15:1509–16. doi:10.1039/b414143a.

[22] Pietak AM, Reid JW, Stott MJ, Sayer M. Silicon substitution in the calcium phosphate bioceramics. *Biomaterials* 2007;28:4023–32. doi:10.1016/j.biomaterials.2007.05.003.

[23] Duan W, Ning C, Tang T. Cytocompatibility and osteogenic activity of a novel calcium phosphate silicate bioceramic : Silicocarnotite. *J Biomed Mater Res Part A* 2013;101A:1955–61. doi:10.1002/jbm.a.34497.

[24] Hauke K, Kehren J, Böhme N, Zimmer S, Geisler T. In situ Hyperspectral Raman Imaging: A new Method to investigate Sintering Processes of Ceramic Material at High Temperature. *Appl Sci* 2019;9:1–23. doi:10.3390/app9071310.

[25] Linkam Scientific Instruments Ltd. Linkam Scientific Instruments TS1500, UK, 2018.

[26] Stange K, Lenting C, Geisler T. Insights into the evolution of carbonate-bearing kaolin during sintering revealed by in situ hyperspectral Raman imaging. *J Am Ceram Soc* 2018;101:897–910. doi:10.1111/jace.15209.

[27] Lafuente B, Downs R T, Yang H SN. The power of databases: the RRUFF project. In: Armbruster T, Danisi RM, editors. Highlights Mineral. Crystallogr., Berlin, Germany: De Gruyter; 2015, p. 1–30.

[28] Chaigneau M, Picardi G, Girard H, Arnault J-C, Ossikovski R. Laser heating versus phonon confinement effect in the Raman spectra of diamond nanoparticles. *J Nanopart Res* 2012;14:955. doi:10.1007/S11051-012-0955-9.

[29] Yuan X, Mayanovic RA, Zheng H. Determination of pressure from measured Raman frequency shifts of anhydrite and its application in fluid inclusions and HDAC experiments. *Geochim Cosmochim Acta* 2016;194:253–65. doi:10.1016/j.gca.2016.09.002.

[30] Neuville DR, de Ligny D, Henderson GS. Advances in Raman spectroscopy applied to earth and material sciences. *Rev Miner Geochem* 2014;78:509–41. doi:10.2138/rmg.2013.78.13.

[31] Sharma SK, Simons B, Yoder HSJ. Raman study of anorthite, calcium Tschermak's pyroxene, and gehlenite in crystalline and glassy states. *Am Mineral* 1983;68:1113–25.

[32] Sharma SK, Yoder HS, Matson DW. Raman study of some melilites in crystalline and glassy states. *Geochim Cosmochim Acta* 1988;52:1961–7. doi:10.1016/0016-7037(88)90177-9.

[33] Krishnan RS. The Raman spectrum of rocksalt and its interpretation. *Proc Indian Acad Sci* 1947;26:419–31. doi:10.1007/BF03170899.

[34] Schlecht RG, Böckelmann HK. Raman scattering from microcrystals of MgO. *Phys Rev Lett* 1973;31:930–2. doi:10.1103/PhysRevLett.31.930.

[35] Ishikawa K, Fujma N, Komura H. First-order Raman scattering in MgO microcrystals. *J Appl Phys* 1985;57:973. doi:10.1063/1.334701.

[36] Everall NJ. Depth Profiling With Confocal Raman Microscopy, Part I. *Spectroscopy* 2004;19:22–8.

[37] Everall NJ. Modeling and measuring the effect of refraction on the depth resolution of confocal Raman microscopy. *Appl Spectrosc* 2000;54:773–82. doi:10.1366/0003702001950382.

[38] Everall NJ. Confocal Raman microscopy: Why the depth resolution and spatial accuracy can be much worse than you think. *Appl Spectrosc* 2000;54:1515–20. doi:10.1366/0003702001948439.

[39] Everall NJ. Confocal Raman microscopy: common errors and artefacts. *Analyst* 2010;135:2512. doi:10.1039/c0an00371a.

[40] Juang C-B, Finzi L, Bustamante CJ. Design and application of a computer-controlled confocal scanning differential polarization microscope. *Rev Sci Instrum* 1988:2399–408. doi:10.1063/1.1139918.

[41] Tian H, Wachs IE, Briand LE. Comparison of UV and Visible Raman Spectroscopy of Bulk Metal Molybdate and Metal Vanadate Catalysts. *J Phys Chem B* 2005;109:23491–9. doi:10.1021/jp053879j.

[42] Zouboulis E, Renusch D, Grimsditch M. Advantages of ultraviolet Raman scattering for high temperature investigations Advantages of ultraviolet Raman scattering for high temperature investigations. *Appl Phys Lett* 1998;72:1–3. doi:10.1063/1.121437.

[43] Nasdala L, Beyssac O, Schopf JW, Bleisteiner B. Application of Raman-based Images in the Earth Sciences. Raman Imag. Berlin, Germany: Springer Series in Optical Sciences; 2012. doi:10.1007/978-3-642-28252-2.

[44] Saloman EB, Sansonetti CJ. Wavelengths, energy level classifications, and energy levels for the spectrum of neutral neon. *J Phys Chem Miner* 2004;33:1113–58. doi:10.1063/1.1797771.

[45] Ming H, Ren Z, Hua X. Characterization and analysis of $CaO–SiO_2–B_2O_3$ ternary system ceramics. *J Mater Sci Mater Electron* 2011;22:389–93. doi:10.1007/s10854-010-0148-1.

[46] Jia D, Kim D, Kriven W. Sintering Behavior of Gehlenite. Part I: Self-Forming, Macro-/ Mesoporous Gehlenite—Pore-Forming Mechanism, Microstructure, Mechanical, and Physical Properties. *J Am Ceram Soc* 2007;90:1760–73. doi:10.1111/j.1551-2916.2007.01704.x.

[47] Jia D, Kriven W. Sintering Behavior of Gehlenite, Part II. Microstructure and Mechanical Properties. *J Am Ceram Soc* 2007;90:2766–70. doi:10.1111/j.1551-2916.2007.01835.x.

[48] Böhme N, Hauke K, Neuroth M, Geisler T. In situ Raman imaging of high-temperature solid-state reactions in the $CaSO_4–SiO_2$ system. *Int J Coal Sci Technol* 2019;6:247–259. doi:10.1007/s40789-019-0252-7.

[49] Osborn EF, Schairer JF. The ternary system pseudowollastonite-akermanite-gehlenite. *Am J Sci* 1941;239:715–763.

[50] Ptáček P, Opravil T, Šoukal F, Havlica J, Holešinský R. Kinetics and mechanism of formation of gehlenite, Al-Si spinel and anorthite from the mixture of kaolinite and calcite. *Solid State Sci* 2013;26:53–8. doi:10.1016/j.solidstatesciences.2013.09.014.

[51] Pryce MW. Calcium sulphosilicate in lime-kiln wall coating. *Mineral Mag* 1972;38:968–71. doi:10.1180/minmag.1972.038.300.09.

[52] Böhme N, Hauke K, Neuroth M, Geisler T. In Situ Hyperspectral Raman Imaging of Ternesite Formation and Decomposition at High Temperatures. *Minerals* 2020;10:287. doi:10.3390/min10030287.

[53] Dorozhkin SV. Calcium orthophosphates. *Biomater* 2011;1:121–64. doi:10.4161/biom.18790.

[54] Dorozhkin SV. Amorphous Calcium Orthophosphates: Nature, Chemistry and Biomedical Applications. *Int J Mater Chem* 2012;2:19–46. doi:10.5923/j.ijmc.20120201.04.

[55] Carnot A, Richard J. Silico-phosphate cristallin produit dans la déphosphoration des fontes. *Bull La Société Minéralogique Fr* 1983;6,7:316–20.

[56] Riley DP, Segnit ER. An optical and X-ray examination of the basic-slag mineral silicocarnotite. *Miner Mag* 1949;28:496–504.

[57] Böhme N, Hauke K, Dohrn M, Neuroth M, Geisler T. High-temperature phase transformations of hydroxylapatite and the formation of silicocarnotite in the hydroxylapatite - quartz - lime system studied in situ and in operando by Raman spectroscopy. *J Mater Sci* 2022. Submitted.

[58] Anthony E. Fluidized bed combustion of alternative solid fuels; status, successes and problems of the technology. *Prog Energy Combust Sci* 1995;21:239–68. doi:10.1016/0360-1285(95)00005-3.

[59] Chirone R, Salatino P, Scala F, Solimene R, Urciuolo M. Fluidized bed combustion of pelletized biomass and waste-derived fuels. *Combust Flame* 2008;155:21–36. doi:10.1016/j.combustflame.2008.05.013.

[60] Vamvuka D, Kakaras E. Ash properties and environmental impact of various biomass and coal fuels and their blends. *Fuel Process Technol* 2011;92:570–81. doi:10.1016/j.fuproc.2010.11.013.

[61] Chowdhury S, Mishra M, Suganya O. The incorporation of wood waste ash as a partial cement replacement material for making structural grade concrete: An overview. *Ain Shams Eng J* 2015;6:429–37. doi:10.1016/j.asej.2014.11.005.

[62] Vu V-A, Cloutier A, Bissonnette B, Blanchet P, Duchesne J. The Effect of Wood Ash as a Partial Cement Replacement Material for Making Wood-Cement Panels. *Materials* 2019;12:2766. doi:10.3390/ma12172766.

[63] Tamanna K, Raman SN, Jamil M, Hamid R. Utilization of wood waste ash in construction technology: A review. *Constr Build Mate*r 2020;237:117654. doi:10.1016/j.conbuildmat.2019.117654.

[64] Etiégni L, Campbell AG. Physical and Chemical Characteristics of Wood Ash. *Bioresour Technol* 1991;37:173–8. doi:10.1016/0960-8524(91)90207-Z.

[65] Steenari B, Lindqvist O. Fly ash characteristics in co-combustion of wood with coal, oil or peat. *Fuel* 1999;78:479–88.

[66] Schimpke R, Klinger M, Krzack S, Meyer B. Determination of the initial ash sintering temperature by cold compression strength tests with regard to mineral transitions. *Fuel* 2017;194:157–65. doi:10.1016/j.fuel.2016.12.066.

[67] Blakeslee K, Condrate R. Vibrational Spectra of Hydrothermally Prepared Hydroxyapatites. *Am Ceram Soc* 1971;54:559–63. doi:10.1111/j.1151-2916.1971.tb12207.x.

[68] Filippelli GM, Delaney ML. The effects of manganese(II) and iron(II) on the cathodoluminescence signal in synthetic apatite. *J Sediment Petrol* 1993;63:167–73. doi:10.1306/D4267AB9-2B26-11D7-8648000102C1865D.

[69] Elliot JC. Structure and Chemistry of the Apatites and Other Calcium Orthophosphates. Amsterdam: Elsevier; 1994.

[70] Gates-Rector S, Blanton T. The Powder Diffraction File: a quality materials characterization database. *Powder Diffr* 2019;34:352–60. doi:10.1017/S0885715619000812.

[71] Tsuda H, Arends J. Orientational Micro-Raman Spectroscopy on Hydroxyapatite Single Crystals and Human Enamel Crystallites. *J Dent Res* 1994;73:1703–10. doi:10.1177/00220345940730110501.

[72] Martínez-Arkarazo I, Angulo M, Zuloaga O, Usobiaga A, Madariaga JM. Spectroscopic characterisation of moonmilk deposits in Pozalagua tourist Cave (Karrantza, Basque Country, North of Spain). *Spectrochim Acta Part A* 2007;68:1058–64. doi:10.1016/j.saa.2007.05.026.

[73] Buzgar N, Buzatu A, Sanislav IV. The Raman study of certain sulfates. *Analele Stiint Ale Univ Al I Cuza Iasi* 2009;55:5–23.

[74] Remy C, Reynard B, Madon M. Raman Spectroscopic Investigations of Dicalcium Silicate: Polymorphs and High-Temperature Phase Transformations. *J Am Ceram Soc* 1997;80:413–23. doi:10.1111/j.1151-2916.1997.tb02846.x.

[75] Reynard B, Remy C, Takir F. High-pressure Raman spectroscopic study of Mn_2GeO_4, Ca_2GeO_4, Ca_2SiO_4, and $CaMgGeO_4$ olivines. *Phys Chem Miner* 1997;24:77–84. doi:10.1007/s002690050019.

[76] Sokol EV, Seryotkin YV, Kokh SN, Vapnik Y, Nigmatulina EN, Goryainov SV. Flamite, $(Ca,Na,K)_2(Si,P)O_4$, a new mineral from ultrahightemperature combustion metamorphic rocks, Hatrurim Basin, Negev Desert, Israel. *Mineral Mag* 2015;79:583–96. doi:10.1180/minmag.2015.079.3.05.

[77] Tschegg C, Ntaflos T, Hein I. Thermally triggered two-stage reaction of carbonates and clay during ceramic firing - A case study on Bronze Age Cypriot ceramics. *Appl Clay Sci* 2009;43:69–78. doi:10.1016/j.clay.2008.07.029.

[78] Zhang Y. Diffusion in Minerals and Melts: Theoretical Background. *Rev Mineral Geochemistry* 2010;72:5–59. doi:10.2138/rmg.2010.72.2.

[79] Gaidies F, Milke R, Heinrich W, Abart R. Metamorphic mineral reactions: Porphyroblast, corona and symplectite growth. *EMU Notes Miner* 2017;16:469–540. doi:10.1180/EMU-notes.16.14.

[80] Milke R, Wiedenbeck M, Heinrich W. Grain boundary diffusion of Si, Mg, and O in enstatite reaction rims: a SIMS study using isotopically doped reactants. *Contrib Miner Pet* 2001;142:15–26. doi:10.1007/s004100100277.

[81] Milke R, Heinrich W. Diffusion-controlled growth of wollastonite rims between quartz and calcite: Comparison between nature and experiment. *J Metamorph Geo*l 2002;20:467–80. doi:10.1046/j.1525-1314.2002.00384.x.

[82] Fierens P, Picquet P. Kinetic Studies of the Thermal Synthesis of Calcium Silicates Above 1400°C: I, Dynamic Thermal Synthesis of Ca_2SiO_4. *J Am Ceram Soc* 1975;58:50–1. doi:10.1111/j.1151-2916.1975.tb18982.x.

[83] Martínez I, Velásquez P, De Aza P. The Sub-System α-TCP_{ss}-Silicocarnotite Within the Binary System $Ca_3(PO_4)_2$-Ca_2SiO_4. *J Am Ceram Soc* 2012;95:1112–7. doi:10.1111/j.1551-2916.2011.05031.x.

[84] Serena S, Sainz MA, Caballero A. Single-phase silicocarnotite synthesis in the subsystem $Ca_3(PO_4)_2$ – Ca_2SiO_4. *Ceram Int* 2014;40:8245–52. doi:10.1016/j.ceramint.2014.01.022.

[85] Ward C. Analysis and significance of mineral matter in coal seams. *Int J Coal Geol* 2002;50:135–68. doi:10.1016/S0166-5162(02)00117-9.

[86] Horsley C, Emmert MH, Sakulich A. Influence of alternative fuels on trace element content of ordinary portland cement. *Fuel* 2016;184:481–9. doi:10.1016/j.fuel.2016.07.038.

[87] Nurse RW, Welch JH, Gutt W. High-temperature Phase Equilibria in the System Dicalcium Silicate-Tricalcium Phosphate. *J Am Ceram Soc* 1956:1077–83.

[88] Fix W, Heymann H, Heinke R. Subsolidus Relations in the System $2CaO{\cdot}SiO_2$-$3CaO{\cdot}P_2O_5$. *J Am Ceram Soc* 1969;52:346–7. doi:10.1111/j.1151-2916.1969.tb11948.x.

[89] Dickens B, Brown WE. The Crystal Structure of $Ca_5(PO_4)_2SiO_4$ (Silico-Carnotite). *TMPM Tschermaks Miner Petrogr Mitt* 1971;16:1–27. doi:10.1007/BF01099075.

[90] Pliego-Cuervo Y, Glasser FP. Phase relations and crystal chemistry of apatite and silicocarnotite solid solutions. *Cem Concr Res* 1978;8:519–24.

[91] Li H, Ng BS, Khor KA, Cheang P, Clyne TW. Raman spectroscopy determination of phases within thermal sprayed hydroxyapatite splats and subsequent in vitro dissolution examination. *Acta Mater* 2004;52:445–53. doi:10.1016/j.actamat.2003.09.046.

[92] Gomes S, Nedelec J, Jallot E, Sheptyakov D, Renaudin G. Silicon Location in Silicate-Substituted Calcium Phosphate Ceramics Determined by Neutron Diffraction. *Cryst Growth Des* 2011;11:4017–26. doi:10.1021/cg200587s.

[93] Lu W, Duan W, Guo Y, Ning C. Mechanical Properties and In Vitro Bioactivity of $Ca_5(PO4)_2SiO_4$ Bioceramic. *J Biomater Appl* 2012;26:637–50. doi:10.1177/0885328210383599.

[94] Serena S, Caballero A, De Aza P, Sainz M. New evaluation of the in vitro response of silicocarnotite monophasic material. *Ceram Int* 2015;41:9411–9. doi:10.1016/j.ceramint.2015.03.319.

[95] Rincón-López JA, Hermann-Muñoz JA, Cinca-Luis N, López-Conesa L, Fernández-Benavides DA, García-Cano I, Guilemany-Casadamon JM, Boccaccini AR, Muñoz-Saldaña J, Alvarado-Orozco JM. Apatite mineralization process from Silicocarnotite bioceramics: Mechanism of crystal growth and maturation. *Cryst Growth Des* 2020;20:4030–3045. doi:10.1021/acs.cgd.0c00322.

LIST OF FIGURES

LIST OF TABLES

ACKNOWLEDGEMENTS

This work could not have been realized without the support of many people. I would like to take this opportunity to express my deepest gratitude.

First of all, I thank my supervisor Thorsten (Prof. Dr. Geisler-Wierwille), who always gave me the freedom to create the project myself and supported my ideas. It was nice to be back in the "Schloss" and to be part of your working group. Many thanks for your careful review and valuable comments on the manuscripts, which always helped the project to move forward and improved the quality of the work.

The RWE Power AG is thanked for the financial support. In particular, I thank Manu (Dr. Manuela Neuroth) for the opportunity to carry out this great project. Thank you very much for your support, the constructive discussions, and the provision of sample materials.
I would also like to thank my second reviewer Prof. em. Dr. Michael Raith and the other members of my doctoral committee Prof. Dr. Barbara Reichert and Prof. Dr. Robert Glaum.

In addition, many thanks go to Thomas Schulz for the technical support with the heating stage and to Nils Jung for sample preparation.

I like to thank my colleague Kerstin for her input and her enthusiasm for Raman spectroscopy with which she infected me in no time☺. I would like to thank my colleagues Moritz, Milan, and Hans-Henning, who always helped me with technical problems. Furthermore, I thank my friend Dana for her help in finding special minerals, but even more for her good coffee and her open ear.

Finally, my great thanks go to my family. I would especially like to thank my husband Stephan for his endless patience, his support, and his unconditional love. I cannot imagine a better partner, friend, and father ♡. I am happy that we will soon be four.